Dynamics of Neural Systems: From Intracellular Transport in Neurons to Network Activity

by

Ehsan Mirzakhalili

A dissertation submitted in partial fulfillment
of the requirements for the degree of
Doctor of Philosophy
(Mechanical Engineering)
in the University of Michigan
2018

Doctoral Committee:

Professor Bogdan I. Epureanu, Chair
Associate Professor Victoria Booth
Assistant Research Scientist Eleni Gourgou
Assistant Professor Allen P. Liu
Professor Michal R. Zochowski

Ehsan Mirzakhalili

mirzakh@umich.edu

ORCID iD: 0000-0002-1926-0035

Acknowledgements

First and foremost, I would like to thank my mentor Dr. Bogdan Epureanu for giving the opportunity to study at University of Michigan. I thank you for providing me the privilege to pursue different subjects during my Ph.D., and for teaching me greatly in the process. I always felt encouraged after our meetings and felt treated more as colleague than a student.

I thank my doctoral committee, Drs. Victoria Booth, Eleni Gourgou, Allen Liu, and Michal Zochowski. Their mentorship and advice have made this dissertation possible. I had my very first class at University of Michigan with Allen. I learned a lot from his class. More importantly, I thank him for his welcoming approach, which helped me greatly when I started my studies. I thank Eleni for always being a great advocate for me. I appreciate all her efforts in teaching me about biology and how to communicate with people outside my discipline. My journey as a Ph.D. student would have been a lot harder without her. I thank Victoria without whom I would have abandoned many of the ideas that are now part of this thesis. I thank her for all our meetings and answering my questions about mathematical and computational neuroscience. I thank Dr. Zochowski whose research has inspired me. Even though I never had a class with him, I have followed his research at University of Michigan by reading his papers, and attending his presentations or presentations by his students. I always walked away full of ideas from such presentations that I used in my own research.

I am also grateful to my colleagues and friends of Applied Nonlinear Dynamics of Multi-Scale Systems Laboratory, including Kiran D’Souza, Woochul Nam, Seunghoon Baek, Kiyoung Oh, Jauching Lu, Mainak Mitra, Weihan Tang, Adegbenga Odofin, Chenyu Yi, Kejie Chen, Andrea Lupini, Mert Egilmez Mohammad Khodabakhsh, Amin Ghadami, and Mohammad Ravandi, for their insights and suggestions.

My years of Ph.D. would have been a lot more stressful and a lot less fun without my partner Caroline. I thank her for going to all the crazy concerts with me and watching my favorite movies and shows. Her support and trust have been essential to my success. I also thank her cats for adopting me.

I am thankful to my family for their support and for always believing in me. None what I have achieved would have been possible without parents. They did not have higher education but they made sure their children faced no obstacle to have the opportunities they never had. I would not be who I am if it was for their dedication and sacrifice. I am also thankful to my brothers. They always made sure their younger brother is supported and no one is allowed to mess with me except for them! Many of the decisions I made in my life was by looking up to them.

Table of Contents

List of Figures

List of Appendices

Abstract

Neurodegenerative diseases such as Alzheimer's disease (AD) are all results of neurons losing their normal functionality. However, the exact mechanics of neurodegeneration remains obscure. Most of the knowledge about this class of diseases is obtained by studying late stage patients. Therefore, the mechanism proceeding the late stages of such diseases are less understood. Better understanding of respective mechanisms can help developing in early diagnostic tools and techniques to enable more effective treatment methods. Analyzing the dynamics of neural systems can be the key to discover the underlying mechanisms, which lead to neurodegenerative diseases. The dynamics of neural systems can be studied in different scales.

At subcellular level, dynamics of axonal transport plays an important role in AD. In particular, anterograde axonal transport conducted by kinesin-1, known conventionally as kinesin, is essential for maintaining functional synapses. The stochastic motion of kinesin in the presence of magnetic nanoparticles is studied. A novel reduced-order-model (ROM) is constructed to simulate the collective dynamics of magnetic nanoparticles that are delivered into cells. The ROM coupled with the kinesin model allows the quantification of the decrease in processivity of kinesin and in its average velocity under external loads caused by chains of magnetic nanoparticles. Changes in the properties of transport induced by perturbations have the potential to decipher normal transport from impaired transport in the state of disease.

In single-cell level analysis, Ca^{2+} transients in ASH neuron of *C. elegans* model organism is studied in the context of biological conditions such as aging and oxidative stress. A novel mathematical model is established that can describe the unique Ca^{2+} transients of ASH neuron in *C. elegans* including its "on" and "off" response. The model provides insight into the mechanism that governs the observed Ca^{2+} dynamics in ASH neuron. Hence, the proposed mathematical model can be utilized as a tool that offers explanation for changes induced by aging or oxidative stress in the neuron based on the observed Ca^{2+} dynamics.

Network level analysis of neurons does not require methods of extremely high spatial and temporal resolution compared to the analysis in subcellular and cellular level. Yet, malfunction in smaller scales can manifest themselves in dynamics of larger scales. In particular, impairment of synaptic connections and their dynamics can jeopardize the normal functionality of the brain in pathological conditions such as AD. The impact of synaptic deficiencies is investigated on robustness of persistence activity (essential for working memory, which is adversely affected by AD) in excitatory networks with different topologies. Networks with rich-clubs are shown to have higher robustness when their synapses are impaired. Hence, monitoring changes in the properties of the neural network can be utilized as a tool to detect defects in synaptic connections. Moreover, such defects are shown to be more devastating if they occur in synapses of highly active neurons. Impairments of synapses in highly active neurons can be directly linked to subcellular processes such as depletion of synaptic resources. Using stochastic firing rate models, the parameters that govern synaptic dynamics are shown to influence the capability of the model to possess memory. The decrease in the release probability of synaptic vesicles, which can be caused by loss of axonal transport, is shown to have a detrimental effect on memory represented by the firing rate of population models.

Chapter 1

Introduction

Advances in neuroscience constantly improve our understanding of the brain's complexity and functionality. However, many aspects of the nervous system including the brain itself are elusive such as brain-related diseases. Unfortunately, the brain displays limited self-repairing capabilities when faced with stroke, severe traumatic injury or neurodegeneration [1]. Neurodegenerative diseases such as Alzheimer's disease (AD) are now more important than ever due to the increase in life expectancy and an aging population [2]. Significant progress has been achieved in the understanding of the underlying mechanisms of such diseases, as for instance the involvement of tau proteins, Aβ amyloids, and impaired axonal transport [3] and synaptic deficiencies [4] that are linked to AD. Investigating dynamical characteristics of neurons can be the key to decipher the mechanisms that govern neurodegenerative diseases and lead potentially to early diagnosis.

The dynamics of neural systems ranges from nanoscale of intracellular transport to mesoscale population activity of neurons. However, dynamical processes in different scales are not independent of each other. Understanding the link between dynamics of different scales and connecting them can be the key to better understanding of neural systems in normal and pathological conditions. For instance, detecting defects in a subcellular process requires extremely high spatial and temporal resolution. However, such subcellular malfunctions may have a magnified impact in the dynamics of larger scales where they are more tractable.

Such a multiscale study cannot be conducted without adequate knowledge of each individual scale. Therefore, this dissertation first studies the intracellular transport in neurons before attempting to establishing connections between the dynamics in small scales and larger scales. Axonal transport supplies newly synthesized proteins from the cell body of the neuron along the axons toward the presynaptic area [5]. Such transport has been shown to decline during normal aging or AD [6–8]. Therefore, understanding the mechanism that regulates axonal transport is crucial [9]. Moreover, experimental data shows that defects in transport is present earlier than other neural abnormalities [10]. Therefore, axonal transport deficiencies potentially occur in the early stages of neurodegeneration. Defects in axonal transport can be attributed to many factors including cargo-motor deficiencies [11]. Impaired motor protein mediated transport of cargos is related to variety of pathological conditions [12].

Motor proteins are energy consuming protein carriers that moving along the cytoskeleton. Among motor proteins, kinesin transport cargos from the cell body to the periphery whereas other motor proteins such as dyneins perform the transport in the opposite direction [13]. Advances in cell imaging techniques led to direct observation of organelle transport and discovery of the kinesin family of motor proteins [14].

Kinesin motion on microtubules has been characterized previously [15]. Loads and directionality affect motion of kinesin greatly. For instance, loads opposing motion of kinesin has been shown to decrease motility of kinesin while assisting force increases binding affinity of ADP (adenosine diphosphate) for kinesin [16]. Moreover, the effects of load and ATP (adenosine triphosphate) concentration on the motion of kinesin transport has been measured experimentally

[17]. For instance, the distance traveled by kinesin decreases as the opposing force increases or ATP concentration decreases. Such experiments and measurements have paved the way for the development of mathematical models that can describe motion of kinesin and its stochasticity [18,19]. Detailed models are extremely important when mechanisms that represent impairment of axonal transport are studied. For instance, microtubule-associated proteins such as tau protein have been shown to be related to neurodegenerative diseases [3,20]. Tau protein has been reported to cause traffic jams [21] and such traffic jams have been suggested to be related to neurodegenerative diseases [22,23]. Moreover, tau protein has been shown to regulate dynamics of motor proteins by changing their properties such as their binding and unbinding rates [24,25]. Therefore, mechanistic models that can also demonstrate effects of binding and unbinding of kinesin to microtubules are crucial [26]. Indeed, such models [27,28] have been helpful to study phenomena like traffic jams in the axonal transport [29,30].

The interruption of the dynamics of the axonal transport by various mechanisms such as the traffic jams can affect dynamics of neural systems in larger scales. Kinesin axonal transport is necessary for synaptic components such as synaptic vesicle precursors [31]. Therefore, defects in motors proteins and intracellular transport are expected to cause failure of synaptic efficiency and subsequently to neurodegeneration [9,32]. Hence, synaptic dynamics is the bridge that connects the dynamics of intracellular process of the axonal transport to larger scale dynamics of neural networks.

There are several factors to consider in modeling of neural networks. First, there are many choices for modeling of neurons [33]. Models with several compartments are capable of reproducing physiological behavior of neurons faithfully [34] but they are computationally expensive for many network applications. Simpler models such as integrate-and-fire models [35] are computationally more efficient but less biologically plausible compared to Hodgkin-Huxley based models since they do not model individual channels [36].

The effect of network topology and its structure on its dynamics (neural networks here) is apparent but less studied [37]. Small-world network [38] is a popular choice and networks with such properties have been studied extensively. For example, the properties of small-world network have been shown to influence dynamics of activity patterns in epilepsy [39,40]. However, properties of neural networks are not limited small-world. Examples of structured topologies in neural networks are many, ranging from humans [41] to simpler organisms such as *C. elegans* nematode [41]¸ the first organism to have its connectome fully mapped [42,43]. Such advancements in mapping neural networks have revealed static network metrics in neural system such as presence of rich-clubs [41], scale-free or aforementioned small-world networks [44]. The non-random structure of the neural networks in the brain is the common conclusion of all such studies [45]. However, understanding how the non-random topology of neural networks influences their dynamics is limited. Such understanding can be the key to reveal how neuronal malfunctions affect the dynamics of neural network.

The dynamics of neural networks can be studied in various details and contexts. In a high-fidelity model, detailed models of neurons and synapses in the network will be simulated individually. One the other hand, low-fidelity models will consider population of neurons as one entity and model their collective behavior without tracking dynamics of individual neurons. Both of these approaches are considered in this dissertation. High-fidelity and low fidelity models of neural networks are studied when the neural system is exposed to various impairments, which can mimic biological and pathological conditions (mainly defects in the axonal transport). The context that such neural systems are studied is related to AD because AD is known to be adversely affected by loss of synapses [4]. However, AD is a disease with broad range of conditions and symptoms. Here, the focus is on working memory, which is shown to deteriorate in patient with AD [46]. Working memory is the ability of the brain to store some information for a short period of time. For instance, remembering a sequence of number such as a phone number for seconds. Such ability of the brain has been shown be related to persistent activity of neural networks in the brain [47]. The persistent activity of a neural network can be considered as the ability of the network to sustain its activity after the initial stimulus is withdrawn [48]. Moreover, the capability of the network to show bistability has been shown to be essential to working memory [49]. This dissertation aims to study neural systems with such properties subjected to impairments.

Chapter 2 explores subcellular dynamics of axonal transport. Intracellular dynamic of kinesin mediated cargo transport is studied in neurons. The stochastic kinesin model is perturbed by forces exerted on the cargo by magnetic nanoparticles that are delivered into the cell. The magnetic nanoparticles form chain-like structures in the presence of external magnetic field that oppose movement of the cargo by kinesin. A reduced-order-model (ROM) is developed to enable fast simulation of the particle dynamics. Then, the ROM and kinesin model are coupled to explore the impact of spatial forces on the dynamics of kinesin. The tool developed in Chapter 2 enables fast and accurate modeling of kinesin transport in the presence of temporal and spatial varying forces. Such tool can be utilized to study dynamics of healthy and impaired transport. Then, detection methods can be established based on the comparison between the dynamics of impaired and healthy transport due to their dissimilar response to the same external force.

Chapter 3 studies dynamics of a single neuron a cellular level. Namely, Ca^{2+} dynamics in ASH neuron of *C. elegans* model organism is investigated. A mathematical model is developed based on experimental data [50] that can capture unique features of Ca^{2+} dynamics in ASH neuron.

Such features include the “on” and “off” responses of ASH neuron. Moreover, the mathematical model can be utilized to predict response of ASH neuron to complex stimuli, which is challenging in experiments. However, the main contribution of the developed model with regard to this dissertation is the ability of the model to suggest potential subcellular variations in the cell machinery that can explain changes in Ca^{2+} dynamics induced by aging or oxidative stress. The results in Chapter 3 demonstrate how changes in small scale dynamics in neurons (here, components of the models such as pumps and channels) can contribute to dynamics of the neurons in larger scales (here, Ca^{2+} transients).

Chapter 4 studies dynamics of neural systems in a network level. Dynamics of neural networks are explored when subjected to synaptic impairments. Excitatory networks that show persistent activity are created. The degree distribution of the networks is used to construct networks with desired metrics such as having high rich-club coefficient. Then, dynamical metrics are introduced to investigate robustness of networks when synapses are weakened. Different scenarios of impairments are introduced that can represent biological and pathological conditions, especially those related to defects in the axonal transport. The results of Chapter 4 shows how the dynamics of neural networks can provide monitoring guidelines for detection of synaptic failure by monitoring dynamics of the network.

Chapter 5 introduces the method and tools for studying stochastic dynamical systems, which will be exploited in Chapter 6. The Fokker-Planck equation is used to find the probability distribution associated with stochastic dynamical systems. Mainly, probabilistic bifurcation diagrams are introduced based on stationary solution the Fokker-Planck equation. Such probabilistic bifurcation diagrams are powerful tools that allow detailed analysis of stochastic dynamical systems in the presence of additive and multiplicative noise.

Chapter 6 studies dynamics of population of neurons. Firing rate models are used to explore population activities in the presence of noise. Noise is added to the firing rate models to represent stimulus, which is necessary for recalling of a memory. Then, using the methods and tools introduced in Chapter 5, stochastic firing rate models are studied. Namely, the ability of the system to hold and recall memory is related to bistability of the firing model. Then, changes in the probability distribution of the model, which leads to loss of bistability is used to explore effects of impairment on the model. The model of impairment ranges from synaptic weights to parameters that are connected to synaptic dynamics. The parameters related to synaptic dynamics are directly linked to dynamics of the axonal transport in neurons. Hence, changes in population activity with defects in axonal transport is explored.

Finally, chapter 7 provides the summary of the dissertation and main conclusions. Then, future direction is suggested with regard to the topics covered in each chapter.

Chapter 2

Reduced-Order Models for the Dynamics of Superparamagnetic Nanoparticles Interacting with Cargoes Transported by Kinesins

2.1 Introduction

Magnetic nanoparticles have been used *in vivo* for many different purposes such as drug delivery [51], image contrast [52], localized heating [53], and many more [54]. Complimentary to the experimental work, nanoparticles have also attracted computational scientific community to develop mathematical models to study dynamics of magnetic nanoparticles [55]. However, such models are computationally expensive because they consist of many particles with highly nonlinear dynamics. Such high-fidelity models become a burden when they need to be integrated with highly stochastic biological systems since many realizations are needed to draw statistically relevant conclusions from systems with such high variability.

Reduced order models (ROMs) can be utilized as an alternative method to high-fidelity models to decrease the computational cost associated with running many long simulations. However, conventional methods of constructing ROMs [56–58] are not completely applicable for multibody dynamics of particles that are also subjected to external magnetic fields. ROMs

---

The results presented in this chapter is published as:

Mirzakhalili E, Nam W, Epureanu BI. Reduced-order models for the dynamics of superparamagnetic nanoparticles interacting with cargoes transported by kinesins. Nonlinear Dyn 2017:1–18. doi:10.1007/s11071-017-3673-0.

developed for discrete element methods [59] are the most similar system to the one developed in this chapter. However, such model reductions are developed by assuming an infinite number of particles [60] while such assumption is not accurate for biological systems. For example, aside from technical difficulties in delivering nanoparticles into cells, excessive numbers of nanoparticles have adverse effects on cells [61–63]. Hence, we develop a novel ROM for limited finite/moderate number of magnetic nanoparticles based on the dynamics of the magnetic nanoparticles and their interaction with nanotransport inside cells.

In the absence of an external magnetic field, superparamagnetic nanoparticles have random magnetization and therefore have zero net magnetic moment [64]. Hence, they can be coated as to not agglomerate in the absence of external magnetic fields [64,65]. However, in the presence of an external magnetic field, superparamagnetic nanoparticles can form aggregates. These are most frequently chain-like structures [66]. Models based on first principles can predict the behavior of superparamagnetic nanoparticles under a variety of conditions [67]. We use such models to develop our novel ROM to be combined with models for intracellular transport by motor proteins such as kinesins.

Kinesin-1, also known as conventional kinesin [68], performs anterograde transport inside cells, including neuronal axons by walking on microtubules [14,69,70]. Motor proteins such as kinesin convert chemical energy in the form of adenosine triphosphate (ATP) into mechanical energy to transport cargoes inside cells. Advances in single molecule techniques [71] have enabled detailed studies of motor proteins [15,72–74]. With the help of experimental data, stochastic models for kinesin nanotransport have been developed and validated [26]. Such models can predict features of kinesin-mediated nanotransport that have not yet been studied experimentally, and can be used to design new experiments to investigate further the intracellular nanotransport [75]. Such an example is provided in this chapter, where kinesin models are used to predict the effects of superparamagnetic particles on the kinesin-mediated intracellular nanotransport. In experiments, the external force is directly applied to the cargo (typically a latex bead) carried by kinesins [76–78]. However, extending such single-molecule methods from *in vitro* to *in vivo* has had only partial success. Here, we propose and examine an alternate method, possible to apply *in vivo*, to influence kinesin transport by indirectly applying external loads on cargoes using superparamagnetic nanoparticles. We study such nanotransport using novel models.

The strength of the attractive forces between adjacent superparamagnetic nanoparticles depends on the properties of the particles as well as the intensity of the magnetic field. Therefore, altering the magnetic field can be used as a means to control dynamically the properties of the medium in which the nanoparticles are present [79]. Such features of magnetic nanoparticles can be used for many different applications. In this chapter, we examine how superparamagnetic nanoparticles and the chains they form inside cells can influence transport of cargos transported by kinesins. The simulation of even small numbers of superparamagnetic nanoparticles requires intensive computations, and a large number of simulations are necessary to characterize the average nanotransport because it is stochastic. Thus, performing full-order computations is ineffective. To address this issue, we develop a novel ROM to determine the interaction of chains of superparamagnetic nanoparticles with cargoes without having to solve the motion of each individual nanoparticle. The ROM is then coupled with kinesin models to allow the quantification of the decreases in processivity of kinesin and in its average velocity under the external loads caused by chains of magnetic nanoparticles.

2.2 Modeling

In this section, we present the mathematical models we use to describe dynamics of the different components of the system explored in this chapter. To that end, the forces that act on different components in the system are provided. The dynamics of superparamagnetic nanoparticles is described by the interaction forces between them due to the external magnetic field, their interaction with the cargo, and viscous forces. The dynamics of the cargo is described by the interaction forces between the cargo and the superparamagnetic nanoparticles, viscous forces, and the pulling force generated by the motion of kinesin motor proteins. Finally, we present the mechano-chemical model that describes the motion of kinesin motor proteins and the forces it generates.

2.1.2 Dynamics of the Superparamagnetic Nanoparticles and the Cargo

Superparamagnetic nanoparticles are assumed to be spheres of the same radius. They have a uniform steric layer coating which prevents them from creating collides [64]. In the absence of an external magnetic field, they do not have interacting forces between them. However, in the presence of an external magnetic field, superparamagnetic nanoparticles are magnetized and have their magnetic moment aligned with the direction of the external magnetic field. This leads to magnetic interaction forces. The thermal fluctuation forces that lead to the Brownian motion of the superparamagnetic nanoparticles are negligible compared the strong magnetic interaction forces. The interaction of two particles i and j, and the interaction force with the external magnetic field is characterized using three energy terms [80] as follows

(a) the energy of particle-to-particle interaction due to the magnetic field, which can be expressed as

$$u_{ij}^{m} = \frac{\mu_0 m_0^2}{4\pi r_{ij}^3}\left[\mathbf{n}_i \cdot \mathbf{n}_j - 3(\mathbf{n}_i \cdot \mathbf{t}_{ij})(\mathbf{n}_j \cdot \mathbf{t}_{ij})\right], \tag{2.1}$$

where μ_0 is the magnetic permeability in vacuum, m_0 is the magnetic moment of a particle, $\boldsymbol{r}_{ij}$ is the relative position vector between the two particles ($\boldsymbol{t}_{ij} = \boldsymbol{r}_{ij} / r_{ij}$ is the unit vector along $\boldsymbol{r}_{ij}$), $\boldsymbol{n}_i$ is the direction of magnetic moment on particle i.

(b) the energy of particle-to-particle interaction due to the steric overlap, which can be expressed as

$$u_{ij}^{v} = 2kT\lambda_v \left[1 - \frac{r_{ij}}{dt_\delta} \ln\left(\frac{d\left(1+2t_\delta\right)}{r_{ij}} \right) - \frac{r_{ij}-d}{dt_\delta} \right], \tag{2.2}$$

where d is the diameter of the particle, k is the Boltzmann constant, T is the temperature, λ_v is a non-dimensional parameter related to d and to the number of surfactant molecules on the surface of each particle, and $t_\delta = \delta / d$ is the ratio of the thickness δ of the steric layer.

(c) the energy of particle-to-field interaction, which can be expressed as

$$u_i^H = -\mu_0 m_0 \boldsymbol{n}_i \cdot \boldsymbol{H}, \tag{2.3}$$

where $\boldsymbol{H}$ is the applied external magnetic field.

Most studies of magnetic nanoparticles focus on predicting the final structure formed by the particles [67,80–82] instead of their dynamics under forces. Hence, these studies can use energy-based methods in Monte Carlo simulations [67,80–82], where the structure/formation is determined by the minimization of potential energy. However, our study focuses on the dynamics of the nanoparticles. Therefore, we use the force between magnetic particles calculated as the gradient of the potential energy fields in Eqs. (2.1)-(2.3)Thus, the interaction forces between two superparamagnetic nanoparticles [83] can be expressed in three components as follows

(a) the particle-to-particle interaction due to the magnetic field, which can be expressed as

$$\boldsymbol{F}_{ij}^{m} = -\frac{3\mu_0 m^2}{4\pi r_{ij}^4} \left\{ -\left(\boldsymbol{n}_i \cdot \boldsymbol{n}_j\right)\boldsymbol{t}_{ij} + 5\left(\boldsymbol{n}_i \cdot \boldsymbol{t}_{ij}\right)\left(\boldsymbol{n}_j \cdot \boldsymbol{t}_{ij}\right)\boldsymbol{t}_{ij} - \left[\left(\boldsymbol{n}_j \cdot \boldsymbol{t}_{ij}\right)\boldsymbol{n}_i + \left(\boldsymbol{n}_i \cdot \boldsymbol{t}_{ij}\right)\boldsymbol{n}_j\right] \right\}, \tag{2.4}$$

(b) the particle-to-particle interaction due to the steric overlap, which can be expressed as

$$\boldsymbol{F}_{ij}^{v} = \frac{kT\lambda_v}{\delta}\boldsymbol{t}_{ij}\ln\left(\frac{d}{r_{ij}}\right) = L_v\,\boldsymbol{t}_{ij}\ln\left(\frac{d}{r_{ij}}\right),\ \ d/r_{ij} \geq 1, \tag{2.5}$$

where $L_v = \dfrac{kT\lambda_v}{\delta} = 150\,\mathrm{pN}$ is a constant that acts like a penalty term and controls the small numerical penetration between contacting particles.

(c) the particle-to-field interaction, which can be expressed as

$$\boldsymbol{F}_{ij}^{H} = 0, \tag{2.6}$$

Of course, Eq. (2.6) reflects the fact that interaction of a nanoparticle with the applied magnetic field does not create any force because the magnetic filed is constant in space.

The motion of the superparamagnetic nanoparticles in a fluid is also affected by viscous fluid forces. The Reynolds number of nanoparticles is very small. Hence, the fluid force for a spherical particle is a drag force that can be calculated using Stokes' law as

$$\boldsymbol{F}_{i}^{d} = -3\pi\mu d\boldsymbol{v}_i, \tag{2.7}$$

where $\mu = 10^{-3}\,\mathrm{Pa.\,s}$ is the viscosity of the fluid, and $\boldsymbol{v}_i$ is the velocity of particle i.

The interaction force between a cargo (i.e., a non-magnetic and larger particle) and superparamagnetic nanoparticle i can be expressed similar to Eq. (2.5) as

$$\boldsymbol{F}_{i}^{c} = L_v\boldsymbol{t}_i\ln\left(\frac{d+D}{2r_i}\right),\ \ \frac{d+D}{2r_i} \geq 1, \tag{2.8}$$

where $\boldsymbol{r}_i$ is the relative position vector between the cargo and particle i ($\boldsymbol{t}_i = \boldsymbol{r}_i / r_i$ is the unit vector along $\boldsymbol{r}_i$), D is the diameter of the cargo.

The equation of motion for each superparamagnetic particle i can be expressed as

$$m_i \boldsymbol{a}_i = \sum_{j=1,\ j\neq i}^{n} \left(\boldsymbol{F}_{ij}^{m} + \boldsymbol{F}_{ij}^{v} \right) + \boldsymbol{F}_i^{c} + \boldsymbol{F}_i^{d}, \tag{2.9}$$

where n is the total number of superparamagnetic nanoparticles, m_i is the mass of superparamagnetic particle i, and $\boldsymbol{a}_i$ is its acceleration. Since the inertia of the particles is negligible compared to the viscous and magnetic forces (at the nanoscale), the equation of motion can be reduced to

$$\boldsymbol{F}_i^{c} + \boldsymbol{F}_i^{d} + \sum_{j=1,\ j\neq i}^{n} \left(\boldsymbol{F}_{ij}^{m} + \boldsymbol{F}_{ij}^{v} \right) = 0, \text{ which leads to} 3\pi\mu d\boldsymbol{v}_i = \boldsymbol{F}_i^{c} + \sum_{j=1,\ j\neq i}^{n} \left(\boldsymbol{F}_{ij}^{m} + \boldsymbol{F}_{ij}^{v} \right). \tag{2.10}$$

Similarly, the inertia of the cargo is negligible compared to the viscous forces and the forces generated by the kinesin motors. Therefore, the sum of all forces acting on the cargo can be expressed as

$$\boldsymbol{F}_c^{d} + \sum_{i=1}^{n} \boldsymbol{F}_i^{c} + \boldsymbol{F}_k = 0, \text{ which leads to} 3\pi\mu D\boldsymbol{V}_c = \sum_{i=1}^{n} \boldsymbol{F}_i^{c} + \boldsymbol{F}_k, \tag{2.11}$$

where $\boldsymbol{F}_c^{d}$ is the drag force created by the fluid onto the cargo, $\boldsymbol{F}_k$ is the force generated by the kinesin, which will be described in the next section, and $\boldsymbol{V}_c$ is the velocity of the cargo.

Equation (2.10) provides the velocity $\boldsymbol{v}_i$ of particle i, and can be integrated over time using, for example, a well-known forward Euler formula, to obtain the position $\boldsymbol{x}_i^t$ of the particle i at time t.

2.2.2 Mechano-chemical Model of Kinesins and the Force They Generate

The walking motion of a kinesin molecule and its unbinding from the microtubule determine the transport velocity and the run length. Importantly, the motion of kinesin is affected by the loads acting on its cargo linker. In this work, we use a model which captures these phenomena [19,26,84].

The model includes the chemical reaction between the kinesin heads and ATP, the change in the kinesin structure induced by ATP binding to kinesin, and the Brownian motion of the free kinesin head (i.e., a head when is not bound to the microtubule). The influence of the load on the unbinding is introduced into the model with a Boltzmann's relation, which can predict the changes in the unbinding probability as a function of the strain energy generated by the force in the molecule. This model uses a single-molecule kinetics [85] to account for the chemical reaction [26] as

$$\mathrm{K} + \mathrm{ATP} \underset{k_{1b}}{\overset{k_{1f}}{\leftrightarrow}} \mathrm{K.ATP} \xrightarrow{k_{2f}} \mathrm{K} + \mathrm{ADP} + \mathrm{Pi}, \tag{2.12}$$

where K denotes kinesin molecule, $k_{1f} = 2\,\mu\mathrm{M}^{-1}\mathrm{s}^{-1}$ and k_{1b} are the forward and backward rates for the binding of ATP to kinesin, $k_{2f} = 100\,\mathrm{s}^{-1}$ is the rate constant for hydrolysis of ATP molecule [26]. ADP is adenosine diphosphate, and Pi is phosphate.

$$\frac{d}{dt} P_{K+ATP} = -k_{1f}\left[ATP\right] P_{K+ATP} + k_{1b} P_{K.ATP}, \tag{2.13}$$

$$\frac{d}{dt} P_{K.ATP} = k_{1f}\left[ATP\right] P_{K+ATP} - k_{1b} P_{K.ATP} - k_{2f} P_{K.ATP}, \tag{2.14}$$

$$\frac{d}{dt} P_{K+ADP+Pi} = k_{2f} P_{K+ATP}, \tag{2.15}$$

where P_{K+ATP}, $P_{K.ATP}$, and $P_{K+ADP+Pi}$ denote the probabilities of chemical states of kinesin. These probabilities are calculated by solving the coupled relations in Eqs. (2.13)-(2.15). The effect of the load on the chemical reaction is modeled as a load-dependent transition rate constant in the backward reaction of ATP binding to kinesin. Specifically, the rate constant is a function of the strain energy in the kinesin structure generated by the external load [86] as

$$k_{1b} = k_{1b,0} \exp \frac{\frac{1}{2}\kappa\left(\frac{F_k}{\kappa} - \Phi_c\right)^2}{kT}, \tag{2.16}$$

where $\kappa = 3.964\,\text{pN/nm}$ (implicitly affected by the potential and stress in of the molecule configuration of the motor protein) and $\Phi_c = 1.009\,\text{nm}$ (related to optimal configuration of the motor protein) are parameters determined by using experimental data [26]. These parameters consider the effects of strain energy in the kinesin structure on the chemical reaction. $k_{1b,0} = 43\ \text{s}^{-1}$ is the minimum backward reaction rate. F_k is the force acting on kinesin molecule, as shown in Figure 2.1.

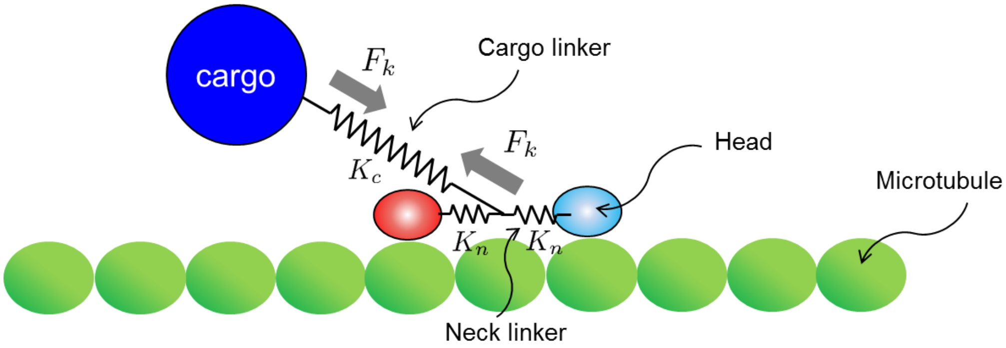

Figure 2.1- Schematic of kinesin molecule. $K_c = 0.3\text{pN}/\text{nm}$ and $K_n = 3.8\text{pN}/\text{nm}$ [26] are the stiffness of the cargo linker and the neck linker.

The force F_k is calculated using the position of the kinesin and the cargo, and the stiffness of the cargo linker and the neck linker. Details and the values of the parameters are provided in [26].

The time required for the conformational change and the Brownian motion are significantly short compared to the duration of the chemical reaction cycle [26,86]. Thus, the rear (free) head of kinesin is assumed to move instantaneously to the next binding site after ATP attaches to the leading head. In addition, the backward motion is modeled by using the probability of backward steps measured experimentally [86]. The unbinding probability of kinesin from the microtubule is constant over steps if the load and ATP concentration do not change. However, each mechanochemical state has a different unbinding probability. The highest unbinding probability is when a kinesin takes a step. The unbinding probability is low during the dwell time (time when a kinesin waits for ATP to bind). After a kinesin takes a step, the likelihood of unbinding is negligible because both its heads are tightly bound to the microtubule. Thus, the unbinding probabilities are calculated depending on the current state of kinesin. In addition, in time marching simulations, three different uniformly distributed random numbers between 0 and 1 are generated at every time step to characterize the three types of stochastic behavior in the model, namely the duration of the current dwell time, the direction of walking, and the occurrence of unbinding. The methods used to calculate the probability of each event and more details can be found in [26].

2.3 Modeling Results

In this section, we present first the general behavior of superparamagnetic nanoparticle dynamics in the presence of an external magnetic field. Then, we describe the likely scenarios that the cargo interacts with chains of superparamagnetic nanoparticles, and show the results for such scenarios. In Sec. 3, we use such scenarios to build our novel ROM.

2.3.3 Nanoparticle Chains

The size of the superparamagnetic nanoparticles used in the study is very important for several reasons. First, if nanoparticles are too small, the magnetic moment they create under feasible external magnetic fields is not strong enough to create strong chains, and thus the resisting force the chains apply to cargoes is too small. Second, if nanoparticles are too large, it is difficult to deliver them inside cells. Moreover, large particles may have greater side effects in the cell because they are more likely to interact with other intracellular proteins [61–63]. Thus, the resisting forces created by nanoparticle chains were calculated for commercially available nanoparticles with a diameter of 40nm and a saturated magnetization of 30 emu/g. Such particles are commercially available, are small enough to be used inside cells, and they can form chains that exert large enough resisting forces on cargoes to alter the transport.

The integration of the equations of motion in Eq. (2.10) from random initial conditions shows that superparamagnetic nanoparticles form chain-like structures in the y direction which is the direction of the applied external magnetic field (Figure 2.2). The formation of chains of superparamagnetic nanoparticles has been shown experimentally (in the presence of thermal fluctuations) [66]. Therefore, our modeling approach is able to predict the formation of nanoparticle chains even with considering simplifying assumptions such as neglecting the Brownian motion of the nanoparticles. Moreover, we are only interested in the mean displacement of the chains. Therefore, the fast and small motion of superparamagnetic nanoparticles can be neglected compared to the slow and large motion of the cargo.

Initially, chains are very short and have different lengths as shown in Figure 2.2-A. Over time, small chains slowly join each other in the y direction, and form longer structures as shown in Figure 2.2-B-F. Therefore, long chains are formed in the fluid when there are enough nanoparticles. Figure 2.2 also shows that longer chains tend to stay away from each other in the x direction. When the external magnetic field is applied, chains of superparamagnetic nanoparticles repel each other in the horizontal direction. Thus, chains are generally not close to each other, as shown in Figure 2.2-D-F.

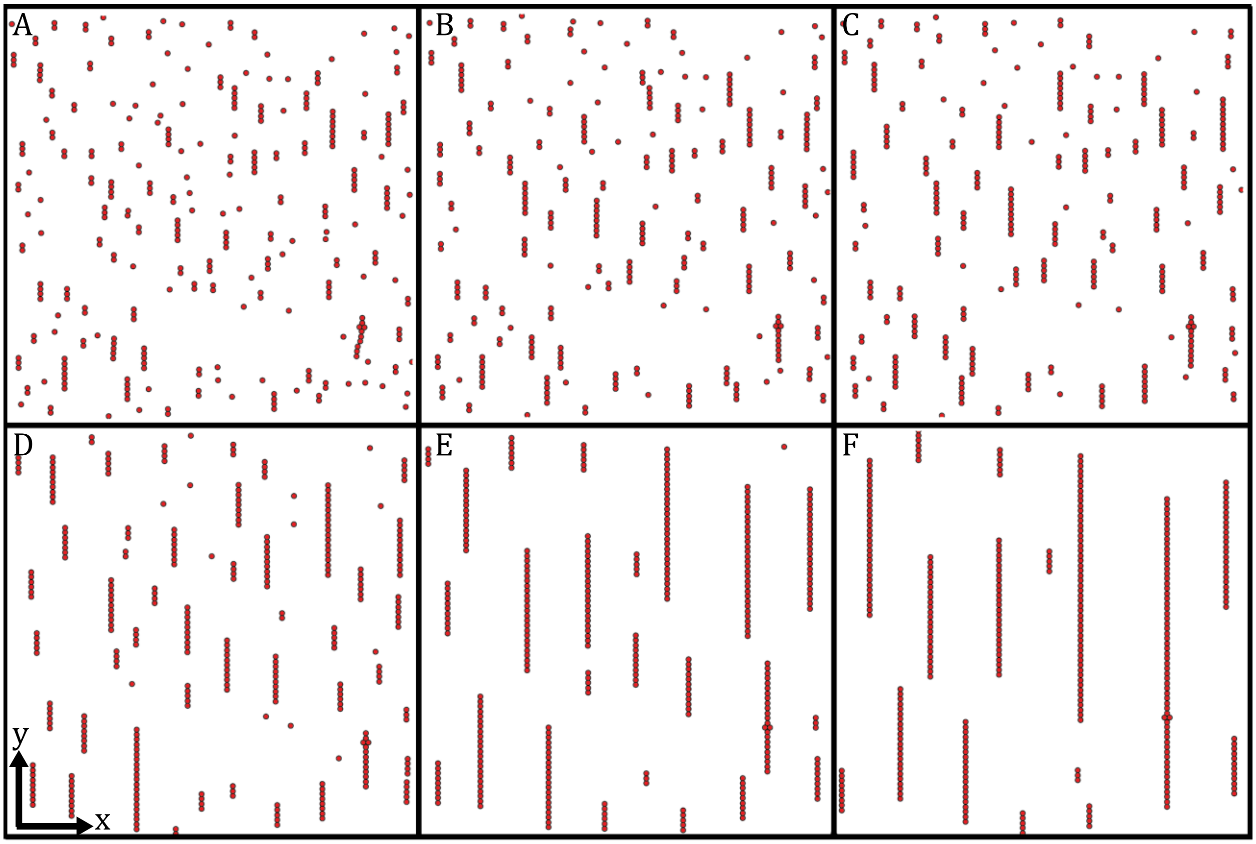

Figure 2.2- The formation of chains is shown. Dots show superparamagnetic nanoparticles. Frames are in chronological order with frame A being the earliest. Initially, the superparamagnetic nanoparticles are randomly positioned. The external magnetic field is applied in the y direction. Frames A through F show the structures superparamagnetic nanoparticles form when time advances. Initially, small chains are formed in the direction of applied magnetic field (frames A-C). Next, the short chains of particles join each other and form longer chains (frames D and E). As longer chains are formed (frame F), the chains also tend to repel each other in the direction perpendicular to the direction of applied magnetic field (x direction).

2.4.3 Cargo Transport

We consider a cargo with a diameter of 1µm, which is similar to cellular cargoes such as mitochondria. When the cargo encounters a single chain of magnetic nanoparticles in its path, it pushes against the chain. The attractive forces between the nanoparticles in the chain are much stronger than the repulsive force between the cargo and the nanoparticles in the chain. In addition, chains are aligned in the direction of the external magnetic field. Thus, our computational model shows that in the absence of any other obstacles, chains slide in front of cargoes remaining relatively straight and not significantly bending as cargoes push them. However, experimental results [87] show that the intracellular environment where the transport occurs is crowded by other structures of the cytoskeleton that do not allow molecules to move freely. For example, experimental and computational results show that the porosity of the cytoskeleton restricts the free diffusion of protein in cells [88]. Therefore, we assume that the chains of nanoparticles will not remain straight because of their interaction with the cytoskeleton structure while they slide because of the cargo motion. We model the interaction between chains and the other structures in the cytoskeleton as constraints or obstacles on the motion of the chains (as shown in Figure 2.3). These obstacles resemble the porosity of the cytoskeleton and do not allow chains to slide, but they act as anchors for the chains (Figure 2.3-A). Thus, chains start to bend when pushed by cargoes (Figure 2.3-B and D) and eventually break (Figure 2.3-C and E). The force applied by an anchored chain on a cargo during the breaking process is much larger than the force of a free chain.

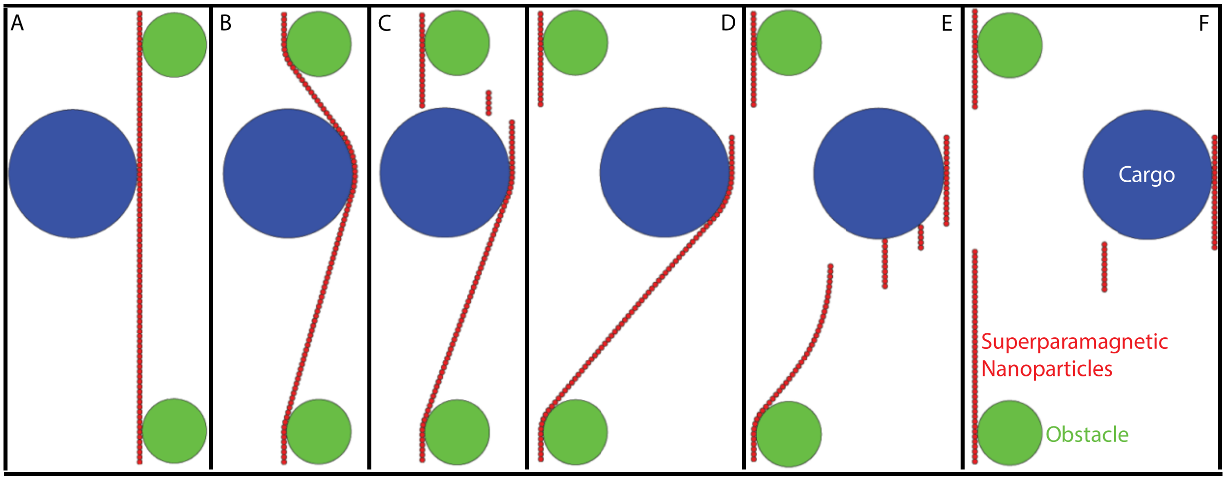

Figure 2.3- The process of a cargo breaking a chain is shown. Frame A shows the cargo aproaching a chain of superparamagnetic nanoparicles that are anchored by two obstacles. Frame B shows the cargo bending the chain of superparamagnetic nanoparicles. Frame C shows the cargo breaking the chain of superparamagnetic nanoparicles. Frame D shows the cargo pushing the reminder of the chain that is still anchored by one of the obstacles. Frame E shows the cargo breaking the chain for the second time. Frame F shows the cargo pushing/sliding the broken chain. Also, similar to the nanoparticles that formed longer chains in Figure 2.2, the small broken chains shown in frame E are attracted to the larger broken chain in front of the cargo to form a longer broken chain seen in frame F.

Next, several features regarding the interaction between cargoes and chains are considered. First, the resisting force exerted on a cargo by an anchored chain depends on the attractive force acting between the nanoparticles. Thus, the motion of the cargo is slowed down or terminated when the attractive force between particles increases considerably. Second, the distance between the obstacles that anchor chains play an important role. Hence, the kinesin-mediated transport of the cargo strongly depends on the distance between chain anchors. This distance is a stochastic variable, which we examine in detail. The chain of nanoparticles only exerts considerable force on the cargo when they are anchored at their both ends. However, chains may not be anchored at both their ends when they are pushed by the cargo. Hence, we modeled chains that extend beyond the anchors. The length of the chains beyond the anchors does not influence the resisting force considerably. This is the reason why we use the distance between the anchors in our model instead of the length of the chains. Third, the interaction between a cargo and a chain is affected by the relative position of the cargo with respect to the anchors. As shown in Figure 2.3, the cargo does not always encounter the chain at the middle point between two anchors. We refer to the distance between the center of the cargo and the middle point between two anchors as the offset of the chain-cargo interaction. Since the location of the anchors and that of the cargoes is random, the probability of the cargo pushing a chain anywhere between two adjacent anchors is the same.

Although the chains of superparamagnetic nanoparticles repel each other, a cargo can push a complete chain or a portion of a previously broken chain. As a cargo encounters multiple chains in its path (as shown in Figure 2.3-F), it pushes these chains against each other. Through this process, chains that consist of more than a single row of nanoparticles are formed. These multiple chains create larger resisting forces that can stall the cargo. It is much harder for a cargo to break such multiple chains.

2.4 Reduced-order Model (ROM)

Computing the dynamics of the superparamagnetic nanoparticles is computationally intensive because very small time-scales are needed for numerical convergence. In addition, the system contains a significantly large number of particles, and calculating the interaction between all of them increases the computational effort even further. However, forces between particles that are far from each other are weak and can be neglected without significant loss of accuracy. Therefore, a common approach is to use a cutoff radius chosen to limit the calculation to the neighboring nanoparticles inside a sphere with that radius, and hence reduce the computational effort. Nonetheless, the remaining computational effort is still prohibitively large, especially for performing stochastic simulations with many nanoparticles and over long durations of time. Therefore, to overcome this challenge, instead of using a cutoff radius, a unique reduced-order model (ROM) is developed in this section. The ROM can estimate the interaction force between the superparamagnetic nanoparticles and cargoes without having to solve the high-fidelity model of the nanoparticle dynamics. After our ROM is constructed, we discuss how the ROM can be used to study the dynamics of a cargo transported by a kinesin motor protein.

2.5.4 ROM Construction

Based on the results shown in the previous section, nanoparticle chains are the dominant structures that are formed. Hence, the ROM is developed for chains of nanoparticles. The ROM is dynamic. Its construction requires several components as described next. Quasi-static simulations can be used instead of dynamic simulations to construct the ROM to characterize the interaction forces between a cargo and chains of nanoparticles. At each step of the quasi-static motion, the cargo is incrementally displaced by $d/20$, where d is the diameter of the nanoparticles, and the final position of the nanoparticles is computed. This position is computed over time and updated until the nanoparticles reach a steady-state location. Then, the force between the cargo and the magnetic nanoparticles is recorded. Thus, the velocity of the nanoparticles and the cargo are not parameters of the ROM because the interaction forces do not depend on these velocities. In addition, the repulsive penalty forces between the particles (Eq. (2.5)) and those between the particles and the cargo (Eq. (2.8)) are automatically accounted for in the ROM because the ROM is constructed using quasi-static simulations which account for these forces (i.e., it prevents particles from penetrating each other especially when the penalty terms are large enough). Therefore, size of the cargo (value that only appears in Eq. (2.8)) does not influence the ROM significantly. The size of the cargo only affects how many particles are in contact with the cargo simultaneously when the chain is highly bent and near breaking (Figure 2.3-B). Thus, we do not consider size of the cargo as one of the parameters of the ROM. Moreover, the size of the nanoparticles does not appear explicitly in any of the equations except for Eqs. (2.5) and (2.8). However, considering Eq. (2.4), the distances between nanoparticles, that are a function of the particle size, are important in determining the forces between particles. Hence, even though we do not use the size of the nanoparticles as a parameter in the ROM, the particle size is accounted for in the distance between the nanoparticles. The magnetic moment of the particles is the other determining factor that appears in Eq. (2.4) for the forces between particles. Hence, the magnetic moment of the nanoparticles and the distance between them are used as the main parameters in building the ROM in this chapter.

Consider first the interaction between a cargo and a chain. To characterize this interaction, quasi-statically move a cargo against a chain with zero, one or two anchors. The motion of the cargo results in the deformation of the chain. At the beginning of the motion, the resisting force is small. The chain deforms and the force increases as the cargo moves, as shown in Figure 2.4-A. The deformation continues until the chain breaks. The sudden drop in the resisting force (near a displacement of 400nm in Figure 2.4-A) indicates the rupture of the chain, and the resisting force after the breakage of the chain is negligibly small. The main goal in constructing the ROM is predicating force-position curves such as the one shown in Figure 2.4-A for different scenarios without the need for simulations using high-fidelity models.

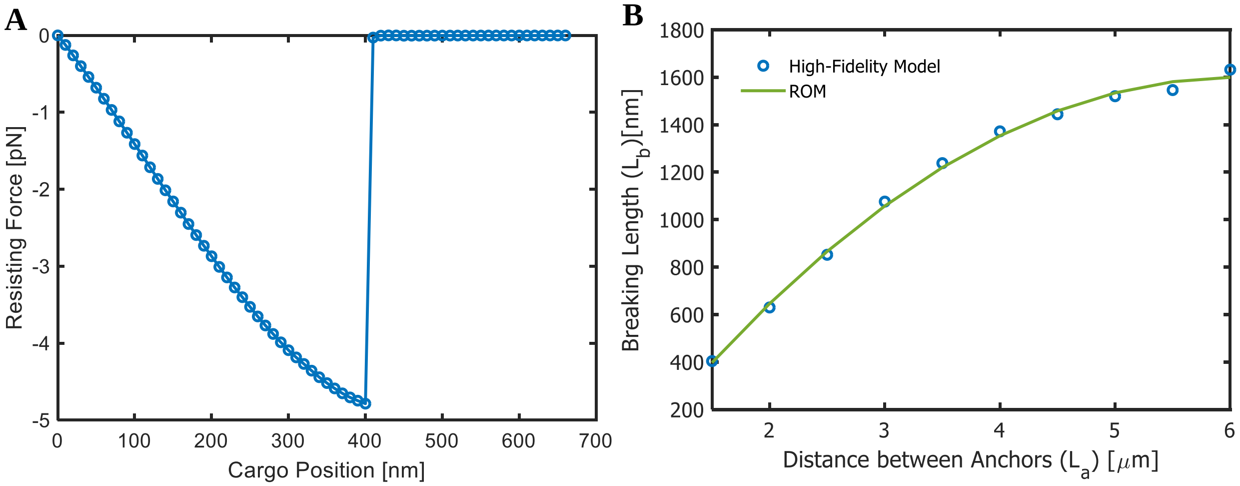

Figure 2.4- Variation of the resisting force versus the cargo position for a sample quasi-static simulation in which the cargo breaks a single chain of superparamagnetic nanoparticles (as shown in A). Breaking length L_b of superparamagnetic nanoparticle chains for different distances between the two anchors L_a follows a quadratic polynomial as shown in Eq. (2.17) and B).

Interactions between a cargo and several different chains with different distances between anchors were performed to obtain a series of force-displacement curves such as the one shown in Figure 2.4-A. We refer to the distance that the cargo travels between the moment when it encounters a chain to the moment when it breaks the chain as the breaking length (L_b). When the chains are not anchored by the obstacles, no matter how strong the magnetic forces are between the particles, the chains do not break and the cargo only slides/pushes the chain (such as the situation shown in Figure 2.3-F). Therefore, it is expected that L_b must be correlated with the length L_a of the chain between the two anchors. This correlation can be observed in Figure 2.4-B; it is a quadratic polynomial relation given by

$$L_b = a_L + b_L L_a + c_L L_a^2, \tag{2.17}$$

where $a_L = -522.15$, $b_L = 699.44$, and $c_L = -57.63$ are constants. The existence of this correlation is one of the reasons why constructing a ROM is possible. Similar analyses can be performed when the cargo encounters multiple chains in its path. In this chapter, we analyzed encounters with double and triple chains since chains with higher multiplicity create resisting forces over 6pN; strong enough to completely stall cargoes transported by single kinesins. As expected, we discovered correlations between L_a and L_b for multiple chains similarly to single chains. These correlations were the same as in Eq. (2.17), with different coefficients a_L, b_L, and c_L, of course.

To create the ROM, the maximum resisting force F_b at breaking must be determined. As Eq. (2.4) suggests, the breaking force depends on the distance between the nanoparticles and on the magnetic moment m of the particles. As discussed earlier, the correlation between L_b and L_a includes the distance between particles because L_a accounts for that distance. Therefore, the dependences of F_b on the distance L_a and on m are investigated.

We assume that the effects of L_a on F_b and the effects of m on F_b are cumulative and independent of each other. First, the magnetic moment appears as a quadratic term in Eq. (2.4). Thus, it is expected that the relation between F_b and m has a quadratic form. To check this hypothesis, we fixed the length L_a of the chain and performed simulations of cargoes quasi-statically moving and breaking chains over different magnetic moments, as shown in Figure 2.5-B. The results of these simulations showed that the variation of F_b with m follows a quadratic polynomial. However, unlike the magnetic moment – that is the same for all the particles in Eq. (2.4) and can be factored during summation of forces between the particles – the distance between the particles in Eq. (2.4) cannot be generalized especially when the chains are bent. Therefore, predicting the correlation between F_b and L_a is more challenging compared to the correlation between F_b and m. Nonetheless, we discovered that such a correlation exists between F_b and L_a, and can be captured by a quadratic polynomial for a fixed magnitude of m (as shown in Figure 2.5-A). Hence, the complete dependence of F_b on m and L_a can be expressed as

$$F_b = \left(a_m + b_m m + c_m m^2\right)\left(a_b + b_b L_a + c_b L_a^2\right), \tag{2.18}$$

where $a_b = -0.9606$, $b_b = -0.0192$, $c_b = 0.0021$, $a_m = 0$, $b_m = 0$, and $c_m = 0.003$ are constants. The fact that $a_m = 0$ and $b_m = 0$ in Eq. (2.18) is because m is involved only as m^2 in the expression of the forces between particles in Eq. (2.4). The existence of these correlations is another reason why constructing a ROM is possible. Similar analyses can be performed when the cargo encounters multiple chains in its path. We discovered correlations between F_b and L_a for multiple chains similarly to single chains. These correlations were the same as in Eq. (2.18), with different coefficients a_b, b_b, c_b, and c_m.

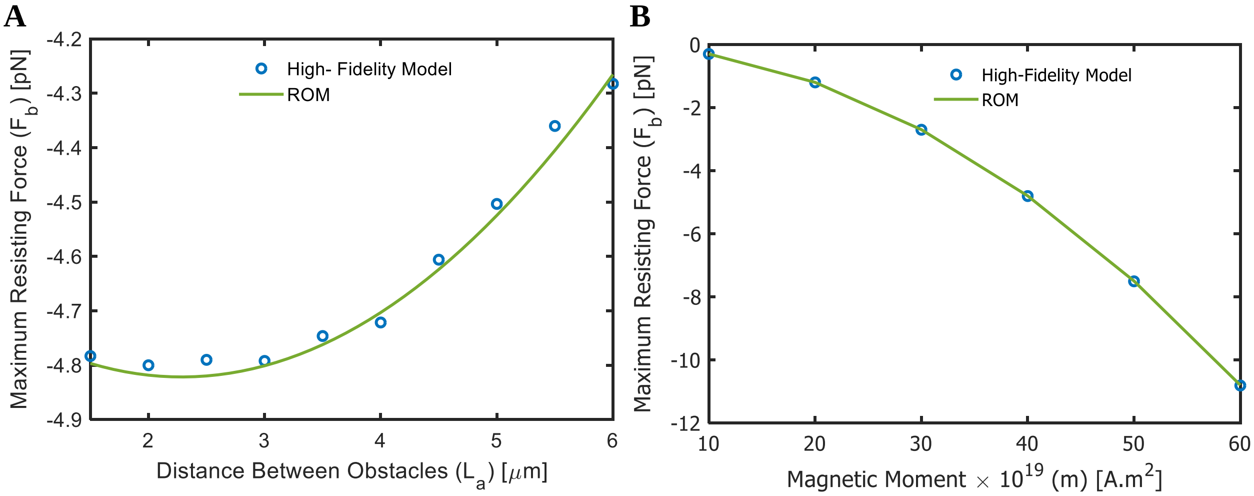

Figure 2.5- Maximum resisting force F_b that occurs at the breaking point of superparamagnetic nanoparticle chains follows a quadratic polynomial with respect to the distance L_a between the two anchors for a fixed magnitude of magnetic moment (as shown in A). Maximum resisting force F_b increases with respect to the magnetic moment m of the superparamagnetic nanoparticles for a fixed length L_a of the chain, and follows a quadratic polynomial (as shown B).

Equations (2.17) and (2.18) allow the prediction of the breaking length and maximum resisting force. However, to use the ROM to create the force-position curves such as the one shown in Figure 2.4-A, the value of the resisting force for each cargo displacement before the chain breaks is needed. The force-displacement curves for various distances between the obstacles are shown in Figure 2.6-A. All these curves appear different although they start from the origin and terminate each at a different breaking point. To analyze whether a correlation exists between the force and the cargo displacement, we nondimensionalize the cargo displacement of different chains by their corresponding breaking length $\left(x^* = x / L_b\right)$, and nondimensionalize the force by their corresponding breaking force $\left(F^* = F / |F_b|\right)$. The nondimensionalization revealed that all the different curves in Figure 2.6-A approximately collapse onto a single curve (as shown in Figure 2.6-B). This suggests that the nondimensionalized force F^* is strongly correlated with the nondimensionalized displacement x. This correlation can be expressed using a cubic polynomial as

$$F^* = a_F x^* + b_F x^{*2} + c_F x^{*3}, \tag{2.19}$$

where $a_F = -1.52$, $b_F = 0.25$, and $c_F = 0.27$ are constants. This correlation shows that the force-displacement relation for all chains of magnetic nanoparticles with different lengths and magnetic moment is the same. Similar analyses can be performed when the cargo encounters multiple chains in its path. We discovered correlations between F^* and x^* for multiple chains similarly to single chains. These correlations have the same form with Eq. (2.19)). However, the values of the coefficients a_F, b_F, and c_F are different, as expected.

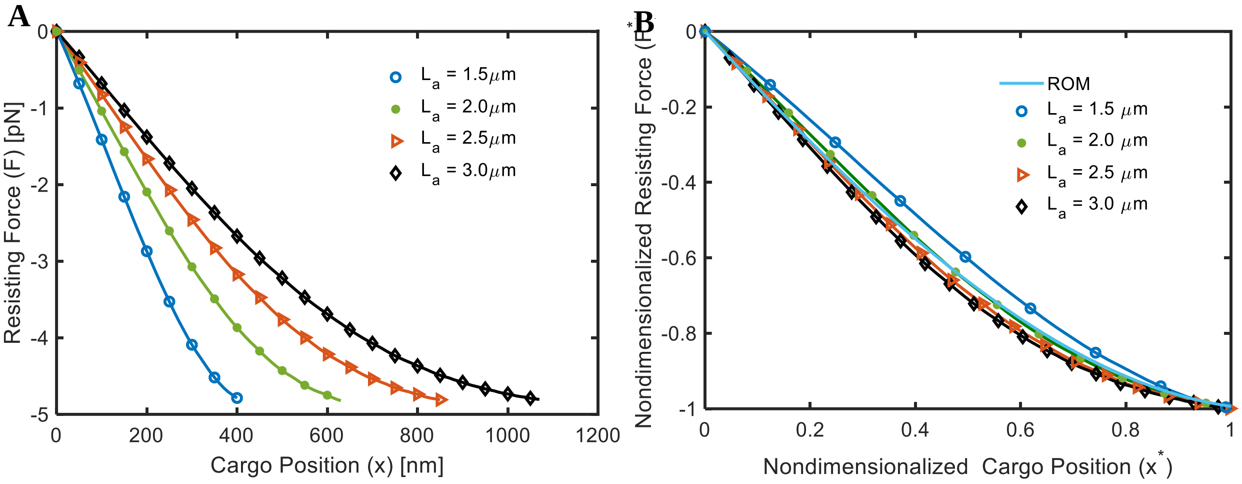

Figure 2.6- The absoulte value of the resisting force is shown as the cargo moves until the chain of superparamagnetic particles is broken. The varation of the resisting force with the cargo position (shown in A) depends on the distance L_a between the two anchors. However, if the resisting forces are nondimensionalized by the resisting force at the breaking instant, and the cargo position is nondimensionalized by the breaking length , then all curves can are similar (as shown in B), and can be approximated by a cubic polynomial as shown in Eq. (2.19)).

In the results above, we focused on scenarios where the cargo encounters chain of the particles in the middle. When there is an offset, the cargo breaks the chain in two steps. First, the chain breaks near the obstacle what is closer to the cargo (as shown in Figure 2.3-C). Next, the cargo pushes the reminder of the chain (as shown in Figure 2.3-D) and breaks it at a location near the cargo (as shown in Figure 2.3-E). However, only the resisting force before the first breaking point is significant. The resisting forces of the remaining chain are negligibly small. Thus, the offset reduces both of the maximum resisting force and the breaking length for chains of all lengths. We nondimensionalized the breaking length at all offset values using the value of at zero offset $\left(L_o = L_b / L_b\left(y=0\right)\right)$. Similarly, we nondimensionalized the maximum resisting force F_b at all offset values using the value of F_b at a zero offset $\left(F_o = F_b / F_b\left(y=0\right)\right)$. Figure 8 shows that a linear approximation can be used to describe the variation of the nondimensionalized breaking length L_o and the nondimensionalized maximum resisting force F_o with the offset y_o as

$$L_o = a_{o,L} + b_{o,L} y_o, \tag{2.20}$$

$$F_o = a_{o,F} + b_{o,F} y_o, \tag{2.21}$$

where $a_{o,L} = 0.9527$, $b_{o,L} = 0.3355$, $a_{o,F} = 1$, and $b_{o,F} = -0.1673$.

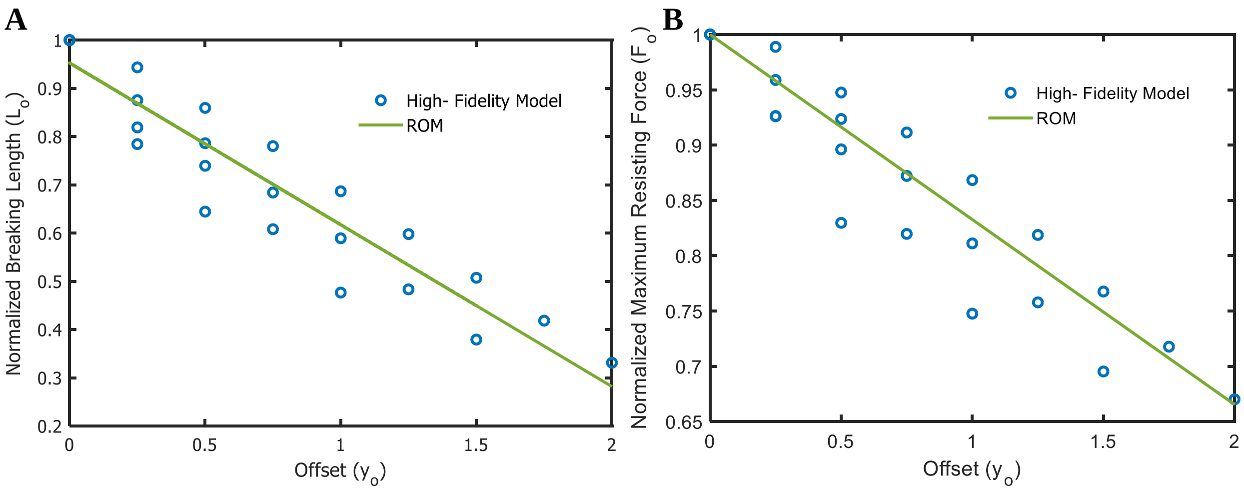

Figure 2.7- The values of the breaking length L_o and the breaking force L_b are smaller when the cargo encounters the chain of superparamagnetic nanoparticles with an offset compared with the case when the cargo faces the middle of the chain. The nondimensionalized breaking length L_o and the nondimensionalized maximum resisting force F_o when there is an offset can be estimated by linear approximations as shown in Eqs. (2.20) and (2.21).

In summary, the force-position curves can be predicted without solving the full-order system. This estimation requires a small set of 14 parameters, and is achieved by combining Eqs. (2.17)-(2.21) to obtain

$$F = \left(c_m m^2\right)\left(a_b + b_b L_a + c_b L_a^2\right)\left(a_{o,F} + b_{o,F} y_o\right)$$
$$\begin{bmatrix} a_F\left[\left(a_L + b_L L_a + c_L L_a^2\right)\left(a_{o,L} + b_{o,L} y_o\right)(x)\right] + \\ b_F\left[\left(a_L + b_L L_a + c_L L_a^2\right)\left(a_{o,L} + b_{o,L} y_o\right)(x)\right]^2 + \\ c_F\left[\left(a_L + b_L L_a + c_L L_a^2\right)\left(a_{o,L} + b_{o,L} y_o\right)(x)\right]^3 \end{bmatrix}, \tag{2.22}$$

where Eq. (2.19) was used along with the term $L_b\, L_o = \left(a_L + b_L L_a + c_L L_a^2\right)\left(a_{o,L} + b_{o,L} y_o\right)$ (the breaking length when the offset is also considered) to convert the nondimensionalized x^* to actual displacement, and the term $F_b F_o = \left(c_m m^2\right)\left(a_b + b_b L_a + c_b L_a^2\right)\left(a_{o,F} + b_{o,F} y_o\right)$ (the maximum resisting force when offset is also included) to convert F^* to actual resisting force.

Equation (2.22) allows a very fast estimation of the force-position curves over different lengths of chains and over different magnitude of magnetic moment when there are single, double or triple chains for quasi-static cases. The ROM does not need to be re-constructed when the velocity or the size of the nanoparticles and the cargo change because they do not directly contribute to the ROM. In addition, the ROM does not need to be re-constructed if one changes the magnetic moment of the particles or the lengths and numbers of the chains or the offset; these are inputs for the ROM. Specifically, the magnetic moment m, the length of the chain encountered by the cargo L_a and the value of offset y_o are inputs for the ROM in Eq. (2.22) while the output of the ROM is the quasi-static force-position curve which can be used in a statistical simulation (Monte-Carlo or any other sample-based statistical approach) to obtain results such as those shown in Figure 2.6-A. However, the ROM must be re-constructed only when the characteristics of the chains are changed. These characteristics can change if, for example, the magnetic particles have different geometry or internal properties, or if the external magnetic field is not constant in space. Figure 2.8 provides a schematic overview of procedure to construct and use the ROM.

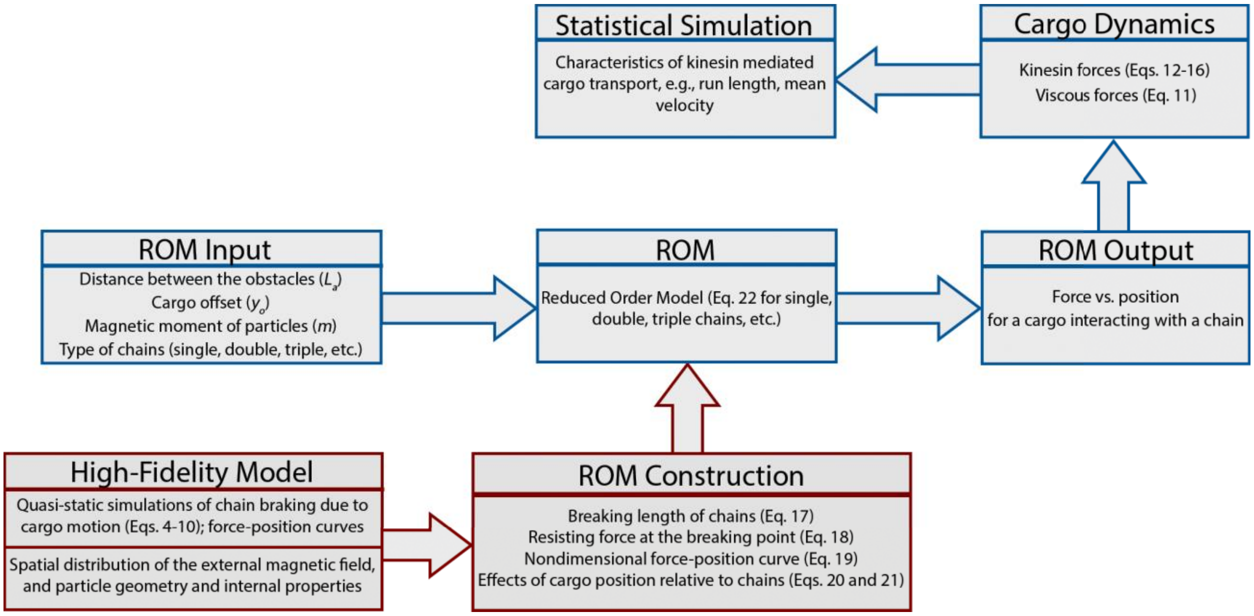

Figure 2.8- Schematic of the reduced order model (ROM) construction, usage and relationship to the high-fidelity model

2.6.4 ROM Application

The transport of the cargo by kinesin is a dynamic process, and the motion of the cargo affects the force-position curve. During the dwell time, the cargo does not move and the resisting force caused by the chain of the magnetic nanoparticles can be found using the results of quasi-static simulations. However, as kinesin steps forward or backward, the cargo changes its position quickly. Therefore, the quasi-static force-position simulations can no longer be used to estimate the resisting force during this rapid process. Nevertheless, it is possible to enhance the quasi-static model to resolve the swift dynamics of the cargo in the presence of kinesin. When kinesin steps, a sudden change in the resisting force is observed. The amount of sudden force increase depends on the acceleration of the cargo. When the acceleration of the cargo is positive, the absolute value of the resisting force starts to increase from the baseline (quasi-static curve) to a maximum value. When the acceleration is negative, the absolute value of the resisting force starts to decrease and recovers to the value of the baseline when the cargo stops moving. Therefore, the resisting force oscillates between the baseline and a lower curve (where the acceleration of the cargo is zero) during the motion. In the ROM, the upper curve for the force corresponds to the quasi-static case. We found that the lower bound for the force can be constructed similar to the upper curve by using different coefficients in Eq. (2.19). Moreover, the oscillations between the upper curve and the lower curve are assumed proportional to the acceleration of the cargo.

The comparison between the results obtained using a high-fidelity model (Figure 2.9-A) and those from the ROM (Figure 2.9-B) shows that the ROM is capable of reproducing the force-position curves with acceptable detail and accuracy. There are several occasions where the actual forces are smaller than even the quasi-static motion (in both graphs of Figure 2.9). Such decrease in the force is caused by backward steps of kinesin. When no external load is applied to kinesins, they tend to move toward the plus end of microtubules. However, the probability of moving backward increases as the external load becomes larger. Therefore, when the resisting force is high (the magnetic moment is high and the chains are near breaking), a backward stepping and consequently, a sudden drop in the resisting force may be observed. Backward steps take place at different locations for the high-fidelity model compared to the ROM, as can be observed in Figure 2.9 because the backward steps are not a deterministic phenomenon and they have a probability proportional to the external load. Therefore, even for the same simulation parameters, the location where backward steps occur is highly variable.

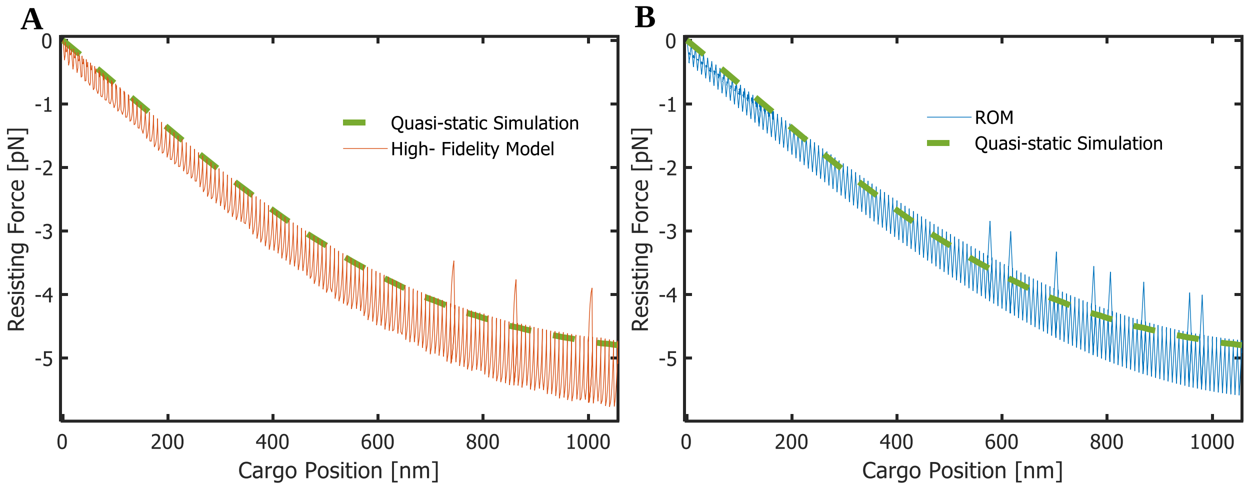

Figure 2.9- Force-position curves show oscillations between two curves because the cargo has a pulsatile motion due to the walking nature of kinesin motor proteins. The ROM can successfully predict the force-position curves for the motion of the cargo. The drop in the value of the forces is due to backward steps of kinesin. The backward motion occurs at different locations in the ROM compared to the high-fidelity model since the walking of kinesin is stochastic.

Using the ROM, we have investigated the nanotransport of cargoes by kinesin in the presence of superparamagnetic nanoparticles with various magnetic moments. We chose random lengths of the chains that the cargoes encounter. The position of the cargoes was initialized randomly behind or in front of the kinesin heads such that the cargo linkers are not in a stall condition. The nanotransport in the presence of superparamagnetic nanoparticles was predicted until the kinesin unbinds from the microtubule. Since the transport by kinesin is stochastic and the chains are chosen randomly, many simulations are needed to calculate the average velocity and run length for each magnetic moment. To show the stochastic nature of the nanotransport, we first present histograms of run length and velocity for two situations: (a) no external magnetic field, and (b) maximum external magnetic field.

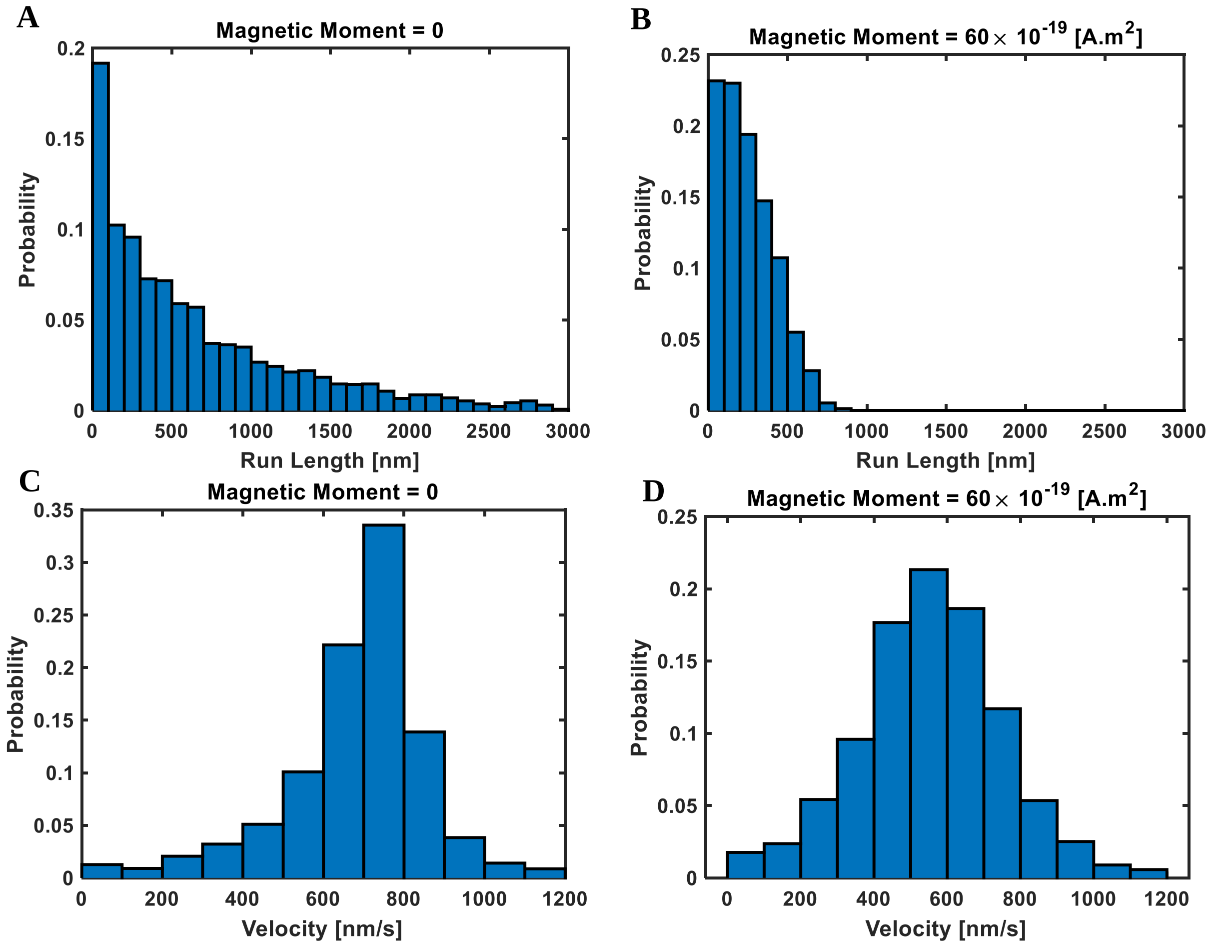

Figure 2.10- The force exerted on the cargo by chains of superparamagnetic nanoparticles reduces the maximum run length of kinesin (A and B). The force exerted on the cargo by chains of superparamagnetic particles changes the velocity distribution of the cargo by decreasing the mean velocity and increasing the variability in the velocity (C and D). These results are obtained using 3000 random realizations

Figure 2.10-A and B show that applying an external magnetic field changes the probability distribution of the run length dramatically. First, when there is no external magnetic field, kinesin can walk distances longer than 1,000nm before detaching from the microtubule. However, for a strong external magnetic field, long run lengths are not observed. However, the number of very small run length (less than 100nm) does not change significantly. This behavior can be explained by examining the force-position curves such as the ones shown in Figure 2.9. When the run length is small, the chain of superparamagnetic nanoparticles is not deformed considerably. Hence, the resisting force is small regardless of the intensity of the external magnetic field. Therefore, for

small displacements of the cargo, the run length is not affected considerably by the external magnetic field, and the stochastic nature of the simulation determines the number of events that have small run lengths. However, comparing probability of events for run lengths larger than 100nm, we observe that the external magnetic field encourages early unbinding of kinesin. Figure 2.10-C and D show that the velocity for different events is also affected by the external magnetic field. In the absence of an external magnetic field, the number of events at which the velocity is low is lower than the number of similar events in the presence of an external magnetic field. The resisting force created by the magnetic field decreases the kinesin velocity in two ways: (a) by increasing the dwell time, and (b) by causing backward steps. For the same reason, the value of the maximum velocity in the distribution also decreases due to the presence of external magnetic field.

The results presented in Figure 2.10 as histograms can be obtained for other magnetic moments, and the information can be summarized by averaging the results as shown in Figure 2.11.

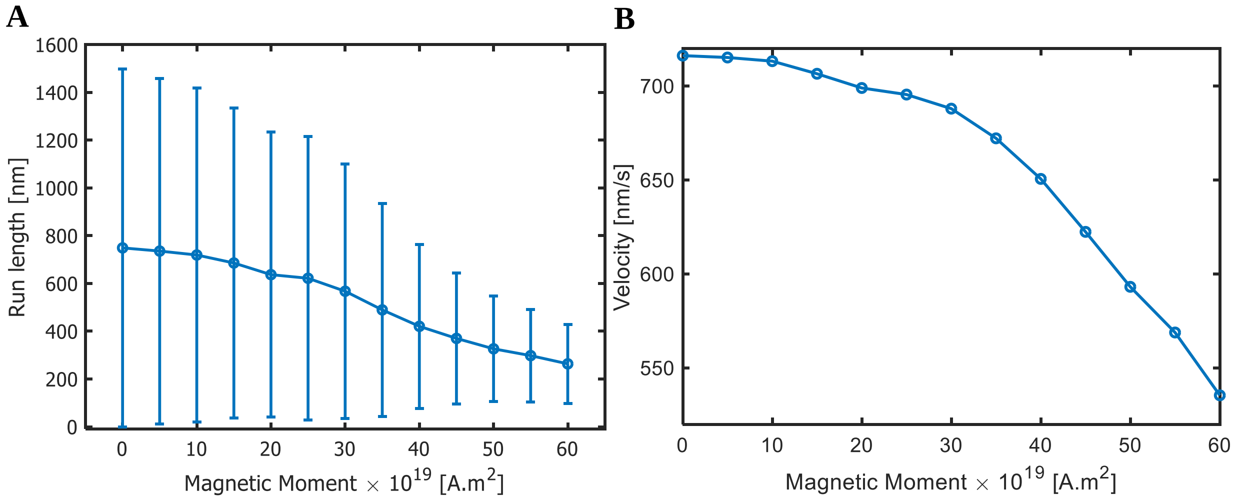

Figure 2.11- Mean value and standard deviation of the run length decrease as the magnetic moment of the superparamagnetic nanoparticle increases (as shown in A). The mean velocity of the cargo decreases as the magnetic moment increases (as shown in B). These results are obtained using 3,000 realizations.

Figure 2.11-A shows how average run length changes with the magnetic moment of the nanoparticles. As the distribution of run lengths in Figure 2.10- A and B also suggests, the average run length decreases with the magnetic moment. The error bars in Figure 2.11-A represent the standard deviation of run lengths obtained for 3,000 random simulations. The standard deviations decrease over the magnetic moment of the nanoparticles. When the external magnetic field is weak, the resisting force is small, and the run lengths are longer. However, there are always instances when the run lengths are short and near zero. Long run lengths are also more frequent when the magnetic field is weak. Hence, the difference between the average run length and the minimum and maximum values of the run length is greater for weak external magnetic fields. On the contrary, when the magnetic moment is high, the resisting force by the chains of magnetic nanoparticles is stronger. Therefore, kinesin has a higher chance of detachment, which decreases the average run length. Moreover, instances when the run length is long are less frequent. Therefore, the difference between the average run length and the minimum and maximum values of the run length is smaller for strong external magnetic fields. Hence, the standard deviation of the run length decreases as the magnetic moment of the nanoparticles increases.

For high magnetic moments, the velocity distribution is closer to the normal distribution but it deviates from the normal distribution for smaller magnetic moments (as shown in Figure 2.10-C and D). Therefore, simply averaging the velocities for all the events does not reflect the proper average velocity. Therefore, instead of averaging the velocities for all the events, we calculate the average velocity by dividing the sum of all run lengths by the sum of all times for transport. This method of averaging gives more weight to velocities that are distributed near the peak value. The downside of calculating the average velocity with this method is that it does not allow calculating the standard deviation of velocities. Figure 2.11-B shows that the average velocity decreases when the magnetic moment increases. The increase in the magnetic moment is equivalent to the increase in the resisting force acting on the cargo when it is carried by kinesin. The curve in Figure 2.11-B is very similar to the velocity-force curves observed in other studies [17,76,89,90]. The main difference is in the method used to apply a resisting force to the cargo; by chains of nanoparticles in our study. In previous studies [17,76,89,90], single-molecule methods such as optical tweezers are used to exert forces on the cargo transported by kinesin. Such methods are designed to control and measure the applied force on the cargo *in vitro*, but their applicability *in vivo* is challenging. One alternative is to use magnetic nanoparticles to influence intracellular transport. This method has the potential to be used *in vivo* studies by passively controlling the *in vivo* transport system by manipulating the environment with magnetic nanoparticles and magnetic fields. The effective ROM technique developed in this chapter contributes to this magnetic-based method by reducing long computation time to calculate the effects of nanoparticles on kinesin-mediated transport.

2.5 Conclusions

Magnetic nanoparticles have been used for variety of applications in cells. Most such research for biological systems only includes experimental studies. The simulation of magnetic nanoparticles is time consuming because of the small time-scales associated with their dynamics and the dynamics involves interactions between many nanoparticles. Moreover, integrating the model for the dynamics of the nanoparticles with the dynamics of highly stochastic biological phenomena inside cells adds to the computational cost of simulating the whole system. Hence, in this chapter, we developed a novel ROM for dynamics of superparamagnetic nanoparticles to be implemented in studying nanotransport inside cells.

The nanoparticles were shown to create elongated chains in the direction of the applied external magnetic field. Therefore, our novel ROM was developed to predict dynamics of such chains inside cells. Moving cargos such as organelles inside cells interact with the chains of nanoparticles, and that leads to the deformation of these chains. The deformed chains create resisting forces on the cargo. Force-position curves associated with the deformation of the chains are the necessary information needed to study nanotransport inside cells. By examining several scenarios and introducing a few parameters, a ROM was developed which was capable of generating almost identical force-position curves compared to high-fidelity models of the same superparamagnetic nanoparticles.

For an application of the developed ROM, we focused on kinesin-mediated cargo transport by using a stochastic model of the kinesin previously developed. The resisting forces that chains of nanoparticles exert on the cargo are of interest because they can be used to influence intracellular transport, and can be utilized for *in vivo* experiments where the transport is deliberately interrupted. Nanoparticles with higher magnetic moments attract each other more strongly, and form chains that are difficult to deform or break. Therefore, the external magnetic field can be used to affect dynamically the force exerted on the cargo carried by motor proteins. Using the ROM, we investigated features of the nanotransport that were affected by the space-varying forces created by the superparamagnetic nanoparticles chains. The ROM enabled us to characterize the stochastic motion of the cargo by using many realizations for different values of the magnetic field intensity.

The results showed that increasing the external magnetic field reduces the average velocity and the run length of kinesin. The resisting forces created by the chains of superparamagnetic nanoparticles increases the dwell time and the frequency of backward steps, which in turn decreases the velocity of kinesin. In addition, the run length decreases because kinesin detaches from the microtubule faster under higher loads. Moreover, we observed that the decrease in the average velocity and the run length did not occur uniformly, and their probability distribution changes. For small external magnetic fields, kinesin is more processive, i.e. walks longer distances before detaching. However, when the magnetic field becomes stronger, the kinesin unbinds sooner. The number of events at which the kinesin unbinds right after the start of the simulation is almost independent of the strength of the external magnetic field. For the average velocity, when the resisting force is small, the probability distribution of velocities is higher around the mean value. However, for stronger external magnetic fields, the probability distribution of velocities becomes more similar to normal distribution around the average value. Such results show the importance of forces acting on the cargo transported by kinesin especially when such forces vary in space.

Chapter 3

A Mathematical and Computational Model of Calcium Dynamics in *Caenorhabditis Elegans* ASH Sensory Neuron

3.1 Introduction

Voltage gated Ca^{2+} channels open when an action potential generated near the cell body reaches synapses. Then, the Ca^{2+} ions trigger release of vesicle containing neurotransmitters, which enable communication of presynaptic and postsynaptic neurons. Also, Ca^{2+} dynamics is known to regulate synaptic plasticity [91]. Synaptic plasticity is necessary for formation of memory and is shown to be highly affected by Ca^{2+} [92,93]. Moreover, Ca^{2+} dynamics and its effect on plasticity has been shown to be linked to Alzheimer's disease [94]. Furthermore, the use of Ca^{2+} transients to indirectly assess a neuron's activation is a well-established approach [95–97] despite its limitations and the caution needed when drawing conclusions about the neuron's concurrent depolarization [98–102]. *C. elegans* in particular has been proved ideal for applying imaging techniques to monitor stimulus-evoked Ca^{2+} transients in a variety of neurons [96,103–108], in freely moving [104,109] as well as in immobilized worms, by using either traditional approaches[97,98,110,111] or advanced methods [50,96,112–115]. The ASH polymodal neuron is the subject of numerous such studies [50,112,113,116], due to its key importance as a nociceptor for the worms' survival and also because it is the starting point for a plethora of downstream neuronal events. The use of microfluidic chips for worm immobilization and stimulus delivery has revealed a second peak in the ASH Ca^{2+} transients, occurring upon withdrawal of the stimulus (the "off" response) [113,117,118], in addition to the first peak, which occurs upon delivery of the stimulus (the “on” response).

The “on” and “off” responses that ensue in the ASH neuron upon its stimulation are the object of several studies, which explore the connection between Ca^{2+} transients, neuronal behavior [100,117,119] and synaptic output of the ASH neuron to downstream neurons [105,113,120]. In particular, the connection between Ca^{2+} transients in the ASH neuron and *C. elegans* behavior has been the object of several studies that suggest an interesting correlation not only between the "on" response and specific behaviors[121–123], but also between the "off" response and avoidance behavior [117]. This leads to the conclusion that all features of the Ca^{2+} dynamics in the ASH neuron participate in fine-tuning the worm's rich behavioral repertoire.

Ca^{2+} transients [97] have been studied in ASH neurons in the context of different biological or environmental conditions, including aging [112,116], oxidative stress [50,106], food availability [123] and oxygen concentration [124]. Extended efforts have been made to decipher the molecular players involved [97,98,117,119,125]. At the same time, mathematical modeling of Ca^{2+} dynamics has been performed in a variety of organisms and cells, but the literature is sparse and far from complete for mathematical modeling of Ca^{2+} response in *C. elegans* neurons [118,121,126]. Work conducted by Kato and colleagues [118] has focused on the temporal responses of ASH and AWC to flickering stimuli, developing a phenomenological model that explains selected features of Ca^{2+} dynamics using ordinary differential equations. However, that work does not include the ASH "off" response, and the model does not account for the dynamics of the molecular players involved.

We propose a mathematical and computational model that is based on biochemical pathways and for the first time encompasses the Ca^{2+} dynamics observed during both the "on" and "off" responses in the *C. elegans* ASH neuron. The approach integrates biophysical models that describe several aspects of the overall Ca^{2+} signaling mechanism and it merges them into an inclusive model forged by novel phenomenological adjustments and known biochemical motifs. Thus, the model succeeds in capturing the Ca^{2+} dynamics in ASH neuron with excellent fidelity. Moreover, we show how the model can be used to suggest potential changes in molecular components that can explain modifications in Ca^{2+} dynamics due to aging and oxidative stress to guide future experiments. Lastly, we demonstrate how the proposed model can be used to predict Ca^{2+} transients in ASH neuron when delivering arrays of complex stimuli.

3.2 Methods

The model is based on intracellular molecular events responsible for the generation of Ca^{2+} transients. Numerous molecules and pathways are involved in this process [127,128]. We focused on molecular players which are believed to dominate the dynamics [98,118,129–132], taking also into account that some of the remaining molecular players are not yet well understood in *C. elegans* neurons [133]. We modeled the dynamics of the secondary players using a coarse grain approach, similar to reduced order modeling. To this end, we introduced selected equivalent players (viewed as states in the model) whose dynamics captures the overall combined effects of most of the secondary players.

3.1.2 Mathematical Model of Ca^{2+} Dynamics

Assuming a cell with well-mixed free Ca^{2+}, the concentration of free Ca^{2+} in the cytoplasm and endoplasmic reticulum (ER) can be written as the following system of ordinary differential equations [134]:

$$\frac{dc}{dt} = J_{IPR} + J_{Leak,ER} - J_{PMCA} - J_{SERCA} + J_{TRPV} + J_{VGCC} + J_{Leak}, \tag{3.1}$$

$$\frac{dc_{ER}}{dt} = \gamma(J_{SERCA} - (J_{IPR} + J_{Leak,ER})), \tag{3.2}$$

where c and c_{ER} are the concentrations of free Ca^{2+} in the cytoplasm and in the ER. J_{PMCA} represents the Ca^{2+} efflux through plasma membrane Ca^{2+} ATPase (PMCA) pumps to the extracellular space (ES), and J_{SERCA} is the Ca^{2+} flux from the cytoplasm into ER through ER ATPase pumps. J_{TRPV} and J_{VGCC} denote the influxes of Ca^{2+} into cytoplasm from ES through transient receptor potential-vallinoid (TRPV) channels and through voltage gated Ca^{2+} channels (VGCC). J_{Leak} and $J_{Leak,ER}$ represent constant influxes of Ca^{2+} into the cytoplasm from ES and ER through other mechanisms. γ denotes the ratio of the cytoplasmic volume to the ER volume, which can also account for fast linear Ca^{2+} buffers in the ER [135].

The PMCA pumps are modeled following [134] as:

$$J_{PMCA} = G_{PMCA} \frac{c^2}{c^2 + K_{PMCA}}, \tag{3.3}$$

$$J_{SERCA} = G_{SERCA} \frac{c^2}{c^2 + K_{SERCA}}, \tag{3.4}$$

where G_{PMCA} and G_{SERCA} are the maximum fluxes through PMCA and SERCA pumps. K_{PMCA} and K_{SERCA} model the affinity of PMCA and SERCA for Ca^{2+}. Ca^{2+} in the cytoplasm and the ER is always at equilibrium before applying the stimulus. To that end, the leak parameters across the cell membrane and the ER need to be adjusted based on the parameter values for PMCA and SERCA, and on the initial concentration of Ca^{2+} in the cell and the ER. The necessary leak values for equilibrium can be found by setting the time derivatives in Eqs. (3.1) and (3.2) (for example, when PMCA is knocked out *in silico*, the leak across the membrane will be found equal to zero).

Even though TRP channels show weak voltage dependence [136], due to limited evidence regarding TRP voltage sensitivity in *C. elegans* neurons, this behavior is not included in the model. The Ca^{2+} influx through TRPV channels is modeled as:

$$J_{TRPV} = G_{TRPV} O.I(c_{ES} - c), \tag{3.5}$$

where G_{TRPV} is the maximum influx of Ca^{2+} through TRPV channels, and c_{ES} denotes the Ca^{2+} concentration in the ES, which is assumed to be constant and c_{ES} =2000 μM. O and I are the probabilities of TRPV channels to be activated and inactivated, and are governed by:

$$\frac{dO}{dt} = k_O P_1 (1-O) - k_O^- O, \tag{3.6}$$

$$\frac{dI}{dt} = k_I (1-I) - k_I^- P_2 I, \tag{3.7}$$

where k_O, k_I are forward and k_O^-, k_I^- are backward rate constants for the O and I states. P_1 and P_2 represent two molecular players that control activation and inactivation of TRPV channels with the following kinetics:

$$\frac{dP_1}{dt} = k_{P_1} P_0 - k_{P_1}^- P_1, \tag{3.8}$$

$$\frac{dP_2}{dt} = k_{P_2} \frac{P_0}{P_0 + K_{P_2}} - k_{P_2}^- P_2, \tag{3.9}$$

where k_{P_1}, k_{P_2} are forward and $k_{P_1}^-$, $k_{P_2}^-$ are backward rate constants for P_1 and P_2, and K_{P_2} is the affinity of P_2 for an equivalent player P_0 that coarsely represents the dynamic effects of the cascade of molecular players that are activated by the external stimulus. We model the dynamics of P_0 as:

$$\frac{dP_0}{dt} = k_{P_0} \frac{S}{S + K_{P_0}} - k_{P_0}^{-} P_0, \tag{3.10}$$

where S represents the strength of the stimulus, K_{P_0} is the affinity of P_0 for S, and k_{P_0}, $k_{P_0}^{-}$ are forward and backward rates for P_0.

Player P_0 coarsely accounts for the pathway that is triggered upon delivery of the stimulus, including the G-proteins which are coupled with the receptors [137,138] (ODR-3, EGL-30, Figure 3.1). Player P_1 coarsely represents the pathway downstream of EGL-30, which leads to activation of TRPV channels [137]. Player P_2 represents the cascade of events in which fatty acids participate, modulating TRPV channels [127,139] (Figure 3.1).

Experimental results [104,116,117] show that a stronger stimulus leads to a stronger Ca^{2+} response in ASH neuron, although this finding has been challenged [98,102]. Therefore, P_0, which in our model translates the stimulus input into sparking molecular cascades, increases with the strength S of the stimulus. However, the dependence of P_0 on S is not linear, to allow saturation of P_0 for very strong stimuli and reflect the reality that an infinitely strong response is not possible. Both P_1 and P_2 are promoted by P_0. Hence, a stronger stimulus leads to a larger P_0, which in turn produces larger P_1 and P_2. Larger P_1 leads to stronger activation of TRPV channels, while larger P_2 leads to stronger inactivation of TRPV channels. Activation needs to surpass inactivation (P_1 must respond more strongly to the stimulus compared to P_2) to observe a stronger Ca^{2+} influx when a stronger stimulus is applied, as dictated by the underlying assumption [104,116,117].

Therefore, P_2 in our model saturates with P_0 (see Eq. (3.9)) to allow for stronger activation with stronger stimulus.

The Ca^{2+} influx through IP$_3$ receptors (IP$_3$Rs) is modeled as:

$$J_{IPR} = G_{IPR} O_{IPR} (c - c_{ER}), \tag{3.11}$$

where G_{IPR} is the maximum Ca^{2+} flux through IP$_3$ receptors, and O_{IPR} is the probability of IP$_3$ receptors (IPRs) to be open, which is modeled using a reduced form [140,141] in the De Young-Keizer model [142], namely:

$$O_{IPR} = \left(\frac{pc(1-y)}{(p+K_1)(c+K_5)} \right)^3, \tag{3.12}$$

where p is the concentration of IP$_3$, and y is the faction of inhibited IPRs. The faction of inhibited IPRs is in turn governed by:

$$\frac{dy}{dt} = \phi_1 (1-y) - \phi_2 y, \tag{3.13}$$

where

$$\phi_1 = k_2^- c \frac{k_{42} K_2 K_1 + K_4 p}{K_4 K_2 (K_1 + p)}, \tag{3.14}$$

$$\phi_2 = k_2^- \frac{p + k_{42} K_3}{K_3 + p}, \tag{3.15}$$

with $K_i = k_i^- / k_i^+$ being the equilibrium constants for binding/unbinding of IP$_3$ or Ca^{2+} to IPRs, with their original values, as used by De Young and Keizer [142].

To model variations in p upon the delivery of the stimulus, we use players P_1 and P_2 together with c to create the following phenomenological model:

$$\frac{dp}{dt} = k_p \frac{P_1}{1 + (K_p P_2)^4} \frac{c^2}{c^2 + K_c^2} - k_p^- p, \tag{3.16}$$

where k_p and k_p^- are constants that represent forward and backward rates, while K_p and K_c are the affinities of p for P_2 and c. The relation between P_1 and P_2 in Eq. (3.16) follows an incoherent feed-forward network motif [143], which is also combined with a Hill equation [134] for Ca^{2+}. This part of the model plays an important role in the "off" response. IPRs are responsible for the release of Ca^{2+} from intracellular stores. IP3 concentration (p) is the only free parameter in the original model of IPRs dynamics [142]. One option is to introduce new molecular players to govern the dynamics of p. However, that approach adds states to the model. Instead, P_1 and P_2 (two molecular players already present in the model) are used to capture the dynamics of p. Players P_1 and P_2 coordinate the dynamics of p in a way that the surge of p occurs when the stimulus is withdrawn, to allow release of Ca^{2+} from stores. Such dynamics for p can be achieved using incoherent feed-forward motifs [143] for generation of p by P_1 and P_2. Moreover, the term in Eq. (3.16) that depends on c (Ca^{2+} concentration) accounts for the generation of p. This term saturates when the concentration of Ca^{2+} increases, to incorporate in the model the well-known phenomenon of Ca^{2+}-induced Ca^{2+} release from intracellular stores [144].

The Ca^{2+} influx through L-type voltage gated calcium channels (VGCCs) are modeled using the Goldman-Hodgkin-Katz [145] equation:

$$J_{VGCC} = G_{VGCC} m_\infty^2 V \frac{c - c_{ES} e^{\frac{-zFV}{RT}}}{1 - e^{\frac{-zFV}{RT}}}, \tag{3.17}$$

where G_{VGCC} is the maximum Ca^{2+} flux through VGCC, z is the valence of the respective ions ($z = 2$ for Ca^{2+}), F is the Faraday constant, R is the gas constant, T is the temperature, V is the membrane voltage, and m is the activation variable given by:

$$m_\infty(V) = \frac{\alpha(V)}{\alpha(V) + \beta(V)}, \tag{3.18}$$

where α and β are rates that vary with the membrane voltage for the L-type current as follows [146]:

$$\alpha(V) = \frac{1.6}{1 + e^{-0.072(V-5)}}, \tag{3.19}$$

$$\beta(V) = \frac{0.02(V - 1.31)}{e^{(V-1.31)/5.36} - 1}. \tag{3.20}$$

Finally, we model the dynamics of membrane potential V. Unfortunately, the available experimental data regarding changes in the membrane potential of the *C. elegans* ASH neuron is limited. Moreover, the ion currents, which are responsible for the voltage response of *C. elegans* neurons, are not completely understood. However, the available data suggests that many *C. elegans* neurons show a graded voltage response rather than the action potential response [147–149]. Therefore, we use a phenomenological approach to model a graded voltage response based on the only ionic current, namely the Ca^{2+} current, as follows:

$$V = \alpha'(V_{max} - V) - \beta'(V - V_{rest}), \tag{3.21}$$

where V_{max} is the maximum membrane potential that can be reached during the graded response of the ASH neuron, and $V_{rest} = -70\text{mV}$ is the resting membrane potential. α' and β' are forward and backward rates for Eq. (3.21), and are given by:

$$\alpha'(c) = \frac{-26c + 4}{e^{-26c+4} - 1}. \tag{3.22}$$

$$\beta'(c) = \frac{260c - 20}{e^{13c-1} - 1}. \tag{3.23}$$

Note that α' and β' are similar to α and β in Eqs. (3.19) and (3.20). However, they have different values, and are functions of c (concentration of free Ca^{2+} in the cytoplasm) instead of V .

3.2.2 Ca^{2+} Concentration to FRET Signal Conversion

The Ca^{2+} concentration obtained using the mathematical model can be related to signals measured in experiments [50,112]. Experimental signals obtained using TN-XL FRET (fluorescence resonance energy transfer) measurements [150] are the result of Ca^{2+} interaction with an indicator genetically encoded in the *C. elegans* ASH neuron. The relation between the Ca^{2+} concentration and the measured % FRET change signal R follows an empirical form [151] that can be expressed as:

$$\begin{aligned} \Delta R\% &= \frac{R-R_{min}}{R_{max}-R_{min}} = R_{max}\frac{c^n}{c^n+K_d'^{\,n}}, \\ FRET &= \frac{R-R_0}{R_0}\times 100, \end{aligned} \tag{3.24}$$

where the Hill coefficient is $n=1.7$, and the apparent affinity of R for Ca^{2+} is $K_d'^{\,n}=2.5$, as provided in [150].

Equation (3.24) can be used to convert measured % FRET changes into the corresponding Ca^{2+} concentration. The use of Eq. (3.24) a stronger stimulus leads of R_{min} , R_{max} and R_0 . To this end, we used the data in [150,151] to set the baseline Ca^{2+} concentration to 100nM. Also, we set R=5 in Eq. (3.24) for the baseline Ca^{2+} concentration [Suppl. Figure 2 of ref 22]. We set FRET ratio change = 10% when Ca^{2+} concentration equals 500nM [152]. Hence, we calculate R_{min} and R_{max} based on the Ca^{2+} that we set. set the baseline Ca^{2+} concentration to 100nM and the maximum Ca^{2+} concentration to 500nM when $\Delta R\%=10$ (for young unstressed worms), and then calculated

R_{min} and R_{max}. Next, we determined R_0 using Eq. (3.24) based on the initial value of the Ca^{2+} concentration in the mathematical model, which is set to 100nM for all cases.

3.3.2 Parameter Estimation

There are 23 parameters (Table S1) that need to be determined in order to use the mathematical model proposed. Ultimately, the mathematical model must capture the Ca^{2+} dynamics in four experimental data sets that are used in this chapter, namely measured Ca^{2+} transients for young unstressed, young stressed, aged unstressed and aged stressed worms. We chose the experimental data set for young unstressed worms as reference to determine all 23 parameters. Next, we modified the values of as few of these parameters as necessary to fit the data for the other three cases, one at a time. This approach allows us to suggest different possible pathways through which the parameters governing Ca^{2+} transients may change, to capture alterations in stimulus-evoked Ca^{2+} dynamics in aged worms or in worms previously exposed to oxidative stress.

We used a hybrid optimization approach, which consists of a genetic algorithm (GA) as a global minimizer, and trust-region-reflective nonlinear least squares (TRNLS) as a local optimizer, to determine the parameters of the mathematical model. The hybrid optimization algorithm starts with the GA, and the fittest individual found from the GA is passed to the TRNLS. The minimization problem is also subjected to constraints that ensure all parameter values are physical (namely that they are positive). The MATLAB optimization toolbox is used to perform these calculations. The maximum-likelihood of the experimental data is the objective function used in the TRNLS algorithm, namely:

$$Res = \frac{FRET_{model} - \mu_{exp}}{\sigma_{exp}}, \tag{3.25}$$

where Res is the residual at each measurement instant, $FRET_{model}$ is the data obtained from the model, μ_{exp} and σ_{exp} are the average and the standard deviation of experimental data at that same time instant. The objective function to be minimized in the GA is the sum of all residuals given by Eq. (3.25) over all time instants measured.

We determined first the parameters for young unstressed worms. The solution of the GA depends on the initial population. Thus, we first applied the GA as a multi-objective optimizer to all four sets of experimental data. We then used the resulting population as an initial population for the GA applied only to the data from the young unstressed worms. Among the optimum solutions suggested by the multi-objective GA, we chose the solution for which the sum of the residuals for all experimental cases was the minimum, even though there were other solutions in which the residual for individual cases was smaller than the chosen solution. This approach allowed us to select as initial population for the GA a vicinity in the parameter space that is near an optimum solution (minimum residual) for all four cases.

There are more than one parameter sets that can result in the measured Ca^{2+} dynamics for young unstressed worms. However, we sought a single set of parameters for young unstressed worms for which the sensitivity of the solution for the estimated parameters was small. To that end, we used the numerical Jacobian matrix that is obtained from TRNLS to approximate the Hessian matrix. Then, we used the Hessian matrix to construct the covariance matrix. We chose the solution that had the smallest diagonal elements of the covariance matrix. That corresponds to choosing the solution with the smallest variance of the parameters, indicating that small changes in the parameters (for that solution) do not lead to vast changes in the Ca^{2+} dynamics.

For the other three experimental cases, we start with the parameters found for young unstressed worms to create the initial population for the GA in the hybrid optimization. Next, we limit the algorithm to change only 13 selected parameters of the total of 23. These 13 parameters (listed with bold in S1 Table) include strength and rates related to key players of the Ca^{2+} signaling mechanism – TRPV channels being activated/deactivated, IP_3, IPRs, PMCAs, SERCAs – and they have been selected based on discussions in the existing literature [153–156]. Then, we use the hybrid optimization algorithm to estimate the values of the 13 selected parameters, while the other parameters are kept constant. A similar procedure is performed separately for all possible combinations for the selected parameters. Next, the results from all the combinations are pooled together for each of the three experimental cases. Each combination of selected parameters is a potential pathway that can show effects of aging or oxidative stress on young unstressed worms. However, not all of the combinations are plausible. The first criterion used to select valid combinations of parameter sets, is the goodness of fit that the mathematical model provides, i.e. the residuals must be small. To make the comparison consistent among different cases, we sort the residual for all different combinations and only keep the combinations for which the residuals are smaller than 99% of all solutions. Next, we use a second criterion on the remaining combinations in which parameter changes that are detectable are selected. To that end, we compute changes in parameters as compared to young unstressed worms. If the absolute value of the changes for a parameter combination is larger than the sensitivity found using the covariance matrix, then we consider such combination plausible.

A component with more than one values for its parameters is still necessary in the model, even though different parameter sets can lead to same qualitative results. For instance, different combinations of parameters for PMCA and TRPV channels can provide relatively similar results. However, including PMCA cannot be claimed to be redundant just because several values can be suggested for it as the model breaks without PMCA (Figure 3.2-B).

3.4.2 Ca^{2+} Transients Experimental Data Analysis

All experimental results presented in Figure 3.2 and Figure 3.3 were acquired as described in Gourgou and Chronis, 2016 [50]. Briefly, using the TN-XL FRET sensor, the stimulus-evoked Ca^{2+} transients generated when the ASH neuron of stressed (exposed to oxidative stress) and unstressed *C. elegans* of various ages was stimulated by hyperosmotic solution of 1M glycerol [50,112] were recorded [50]. The FRET signal change was recorded in the microfluidic device [50], where each worm was introduced after growing in the presence of the oxidative stress-causing chemical paraquat [50]. Experimental data used in this chapter come from four populations of adult hermaphrodite *C. elegans*: i) young unstressed animals (control animals; reference case), ii) young oxidative-stressed animals, iii) aged unstressed animals, and iii) aged oxidative-stressed animals.

3.3 Results

The pathways and molecules included in the proposed model are portrayed in Figure 3.1 detailed description of their contribution in the generation of Ca^{2+} transients and their connection with the rest of the model components is given in the Discussion.

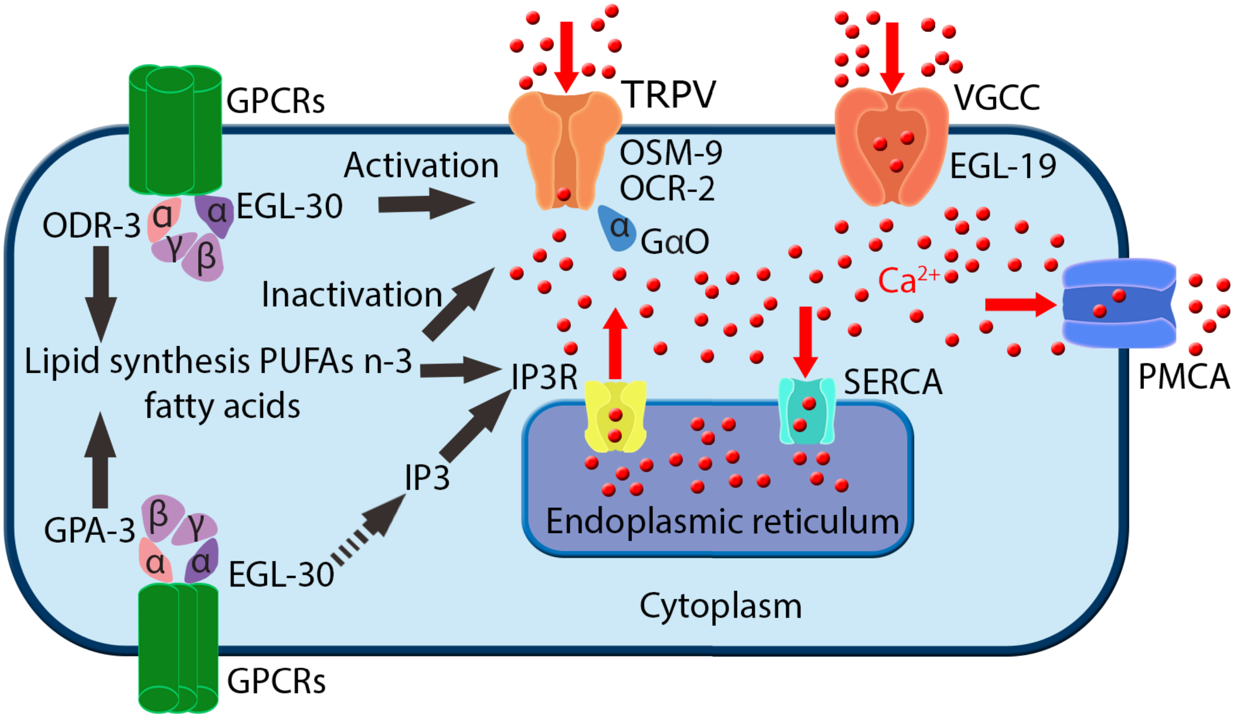

Figure 3.1- Molecular components of the Ca^{2+} homeostatic machinery that are included in the proposed mathematical model. GPCRs: G-protein coupled receptors, as the ones that are activated in ASH neuron by hyperosmotic stimuli; ODR-3, EGL-30, GPA-3: G-proteins coupled with the receptors, participating in signal transduction to downstream ion channels; OSM-9, OCR-2: molecular elements of the TRPV channels, the main cation channels through which Ca^{2+} flows into the neuron upon its stimulation; GαO: G-protein coupled with TRPVs; EGL-19: molecular component of the VGCCs, the L-type voltage gated Ca^{2+} channels, activated by the changed membrane potential due to ion influx upon neuronal activation; PMCA: plasma membrane Ca^{2+} ATPase, the main pump responsible for transporting Ca^{2+} into the extracellular space; SERCA: sarco-endoplasmic reticulum Ca^{2+} ATPase, which transports Ca^{2+} into the intracellular stores; IP3: 3-phopsho-inositol, secondary messenger participating in Ca^{2+} signaling events; IP3R: IP3 receptors, glycoprotein complex acting as a Ca^{2+} channel activated by IP3 , abundant on the endoplasmic reticulum (ER) membranes. GPCRs, ODR-3, EGL-30, GPA-3, OSM-9, OCR-2: not modeled individually; model parameters that account for these molecular components are P_0, P_1 and P_2, see Methods. Lipid synthesis, PUFAs, fatty acids, TRPV activation, TRPV inactivation events: modeled as O (activated) and I (inactivated) probabilities, see Methods. Included in the model and not depicted here: J_{Leak} and $J_{Leak,ER}$, which represent the constant influx of Ca^{2+} into the cytoplasm from extracellular space and ER, respectively, through other mechanisms, see Methods.

3.5.3 Accuracy and Effects of Knocking Out Components of the Model

As a first step, we explore whether our model can capture the dynamics of the Ca^{2+} transients which occur when the ASH neuron of young unstressed worms is stimulated by a hyperosmotic solution (Figure 3.2-A). Our results show that the model matches well the special and critical features of the Ca^{2+} transients, including magnitude and time of peaks, rising and decaying slopes for both “on” and “off” responses. The representation of the stimulus as a square pulse corresponds to the way the hyperosmotic solution is delivered to the worm’s nose in the microfluidic device [50,96,112,113].

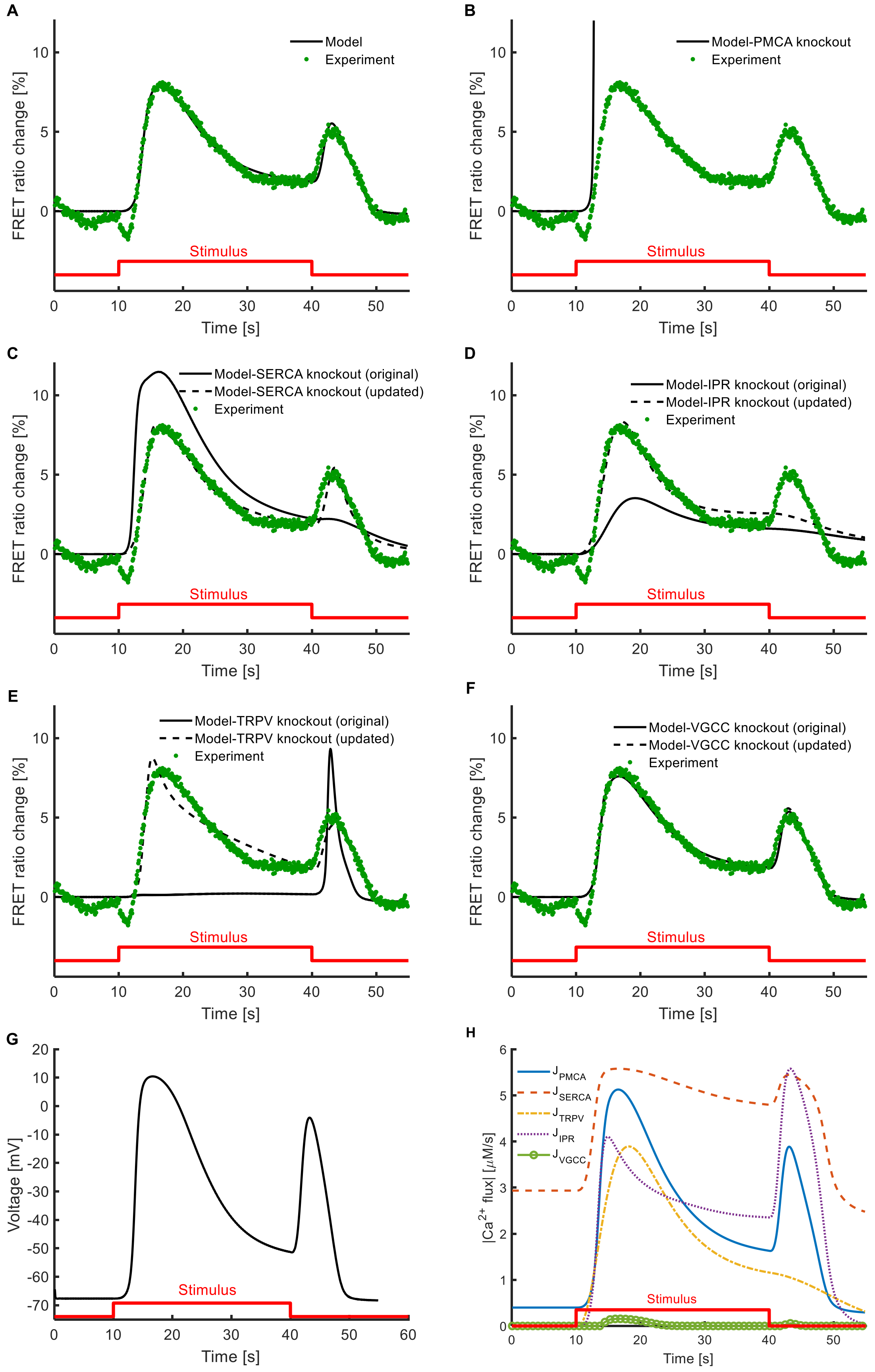
A
Model
Experiment
FRET ratio change [%]
Stimulus
Time [s]
B
Model-PMCA knockout
Experiment
C
Model-SERCA knockout (original)
Model-SERCA knockout (updated)
Experiment
D
Model-IPR knockout (original)
Model-IPR knockout (updated)
Experiment
E
Model-TRPV knockout (original)
Model-TRPV knockout (updated)
Experiment
F
Model-VGCC knockout (original)
Model-VGCC knockout (updated)
Experiment
G
Voltage [mV]
Stimulus
Time [s]
H
J_{PMCA}
J_{SERCA}
J_{TRPV}
J_{IPR}
J_{VGCC}
$|Ca^{2+}\ flux|\ [\mu M/s]$
Stimulus
Time [s]

Figure 3.2- The proposed mathematical model can capture the Ca^{2+} dynamics observed in young (Day 1) unstressed worms, when ASH sensory neuron is stimulated by hyperosmotic solution (glycerol 1M). (A) The model matches the Ca^{2+} transients, as recorded experimentally, including all key features (time and magnitude of peaks, rising and decay slopes) for the "on" response (upon delivery of the stimulus) and the "off" response (upon withdrawal of the stimulus). (B-F) Different components of the model are knocked out (in silico knock-out) to investigate their impact on the model-generated results. For the knockout results with original parameters (solid line), all the parameters are kept the same as in (A), except for the knockout component that is removed from the mathematical model. For the knockout results with updated parameters (dashed line), the hybrid optimization algorithm is run again trying to find an updated set of parameters which can explain the experimental Ca^{2+} dynamics, after the knocked-out component has been removed from the mathematical model. (B) When PMCA is removed, Ca^{2+} is not pumped out of the cell and the mathematical model fails. Changes in the parameters in any of the model components cannot compensate for PMCA knockout in the updated model. (C) When SERCA is removed, the original model fails to show the "off" response and features of the "on" response are also affected. Updating the parameters restores most of Ca^{2+} transients' features, except for the decaying slopes. (D) Removal of IPR affects all the features of "on" response and the "off" response completely vanishes. Updating the parameters restores the "on" response partly but fails to rescue the "off" response. (E) TRPV knockout for the original model does not show any "on" response, while "off" response is amplified. When the parameters are updated, both "on" and "off" responses are partially restored. (F) VGCC in silico knock-out does not affect significantly the results of the model, original or updated. The dashed and continuous lines coincide; the dashed line is distinguishable around the peak of the “on” response. (G) The phenomenological model used to describe the voltage response shows a graded response when the stimulus is applied. A weaker graded voltage response is also observed when the stimulus is removed. (H) The Ca^{2+} fluxes for different components in the original model show how much each component contributes to the overall dynamics. J_{PMCA} is the flux of Ca^{2+} by PMCA, plasma membrane Ca^{2+} ATPase, the main pump responsible for transporting Ca^{2+} into the extracellular space; J_{SERCA} is the flux of Ca^{2+} by SERCA, sarco-endoplasmic reticulum Ca^{2+} ATPase, which transports Ca^{2+} into the intracellular stores; J_{TRPV} is the flux of Ca^{2+} by TRPV, transient receptor potential-vallinoid channels that are responsible for initial influx of Ca^{2+} into the cell; J_{IPR} is the flux of Ca^{2+} IP3 receptors from the stores, which are the main contributor to the “off” response; and J_{VGCC} is the flux of Ca^{2+} through voltage gated Ca^{2+} channels.

One way to explore if a component of the model is necessary is to knock out that component and look for parameter sets that can still capture the complete response of the cell. To this end, we removed different components of the model, one at a time, to investigate their contribution to the predicted Ca^{2+} dynamics (Figure 3.2-B-F). For each of these *in silico* knockouts, two cases were considered: i) the original case, in which after the knockout component is removed the values for all parameters remain the same as in the model that generates the output shown in Figure 3.2-A, and ii) the updated case, in which after the knockout component is removed, we apply the hybrid optimization algorithm to estimate again the model parameters.

We use the case of PMCA, which leads to expected results, as the first knock out, to illustrate the purposefulness of the *in silico* knock out approach. We find that the model completely diverges without the PMCA (Figure 3.2-B), since all the Ca^{2+} that flows in upon delivery of the stimulus, remains in the neuron. Moreover, since the PMCA pump is the only component in the model that actively removes excessive Ca^{2+} out of the neuron, changing the value of any other parameter cannot compensate for the PMCA knockout; therefore, no updated solution can be reached when the PMCA is knocked out.

Next, when the SERCA pump is removed (Figure 3.2-C), Ca^{2+} that enters the cytoplasm is not pumped into the ER. The original model with a knocked out SERCA accounts for more Ca^{2+} in the cytoplasm, compared to the results shown in Figure 3.2-A, while at the same time the "off" response is absent. In the updated model, where the parameters of other components are adjusted, the overall results are improved. However, the final return of cytoplasmic Ca^{2+} to its initial levels is still not completely restored, and the rising slope of the "off" response is captured with a slight time lag.

Removing IPRs from the model (Figure 3.2-D) completely alters the features of the Ca^{2+} transients. The magnitude of the “on” response decreases dramatically, and the "off" response vanishes. The updated parameters can recover features of the “on” response, but they fail to yield the “off” response.

The “on” response completely disappears when TRPV channels are knocked out (Figure 3.2-E). Interestingly, the “off” response remains present and strong in the absence of TRPV channels. In the updated model, the adjusted parameters yield the “on” response, even without TRPV channels. However, the updated model without the TRPV channels accounts poorly for the magnitude of the "on" response and, most importantly, it fails to capture the dynamics of its decaying slope.

Elimination of VGCCs from the model (Figure 3.2-F) does not affect its predictions substantially. This is reflected equally in the outputs of the original and the updated version of the model, as shown in Figure 3.2-G.

We also explored the Ca^{2+} fluxes from each model component (Figure 3.2-H). The fluxes associated with PMCA and SERCA are not zero before applying the stimulus, because they need to keep Ca^{2+} flux in balance, despite the leaks across the cell membrane and ER membrane. TRPV channels respond quickly when the stimulus is presented, which leads to higher activity of pumps to balance the excessive Ca^{2+}. IPRs also follow TRPVs but their main contribution is to the “off” response when the stimulus is removed. VGCCs respond to the stimulus with a significant lag compared to the other components of the model, because they require a large amount of Ca^{2+} to enter the cell to induce their activation. Hence, VGCCs act like a secondary mechanism, with a weak contribution to total Ca^{2+} influx. Moreover, it is shown that TRPVs do not contribute to the “off” response at all (see also Figure 3.2-E). In addition, it takes time for most of the fluxes to return to or approach their initial equilibrium state after the stimulus is removed. Therefore, a different dynamical response is expected if the first stimulus is followed by a second pulse after a short interval. We explore such scenarios in Figure 3.6.

3.6.3 The model captures Ca^{2+} dynamics in aged and stressed worms

The parameters values in the parameter set found to capture the Ca^{2+} dynamics in young unstressed worms (Figure 3.2-A) are used as reference case. Using them as a starting point we can obtain different plausible parameter values that explain Ca^{2+} transients for young stressed (Figure 3.3-A), aged unstressed and aged stressed worms (Figure 3.3-B).

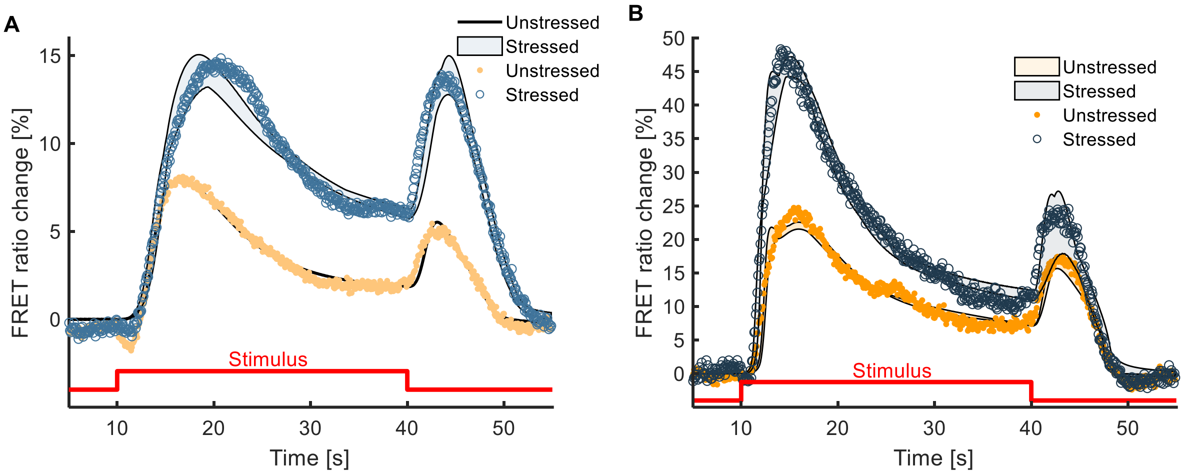

Figure 3.3- The proposed mathematical model can capture the stimulus-induced changes in the Ca^{2+} dynamics in the case of aged (Day 5) or previously exposed to oxidative stress (stressed) animals. (A) The parameter set for young (Day 1) unstressed worms is used as a reference point to detect changes in the parameters that can explain the stimulus-evoked Ca^{2+} dynamics in treated worms of the same age. The model results shown correspond to all plausible solutions. (B) Similar to (A), the parameter set for young (Day 1) unstressed worms is used to detect changes in the parameters that can explain the stimulus-evoked Ca^{2+} dynamics in aged (Day 5) unstressed and stressed worms. The modeling results correspond to all plausible solutions. Red line represents the stimulus pulse delivered (duration: 30sec). Experimental data originally presented in Gourgou and Chronis, 2016 [50].

We use the parameters for young unstressed worms to initiate the search for plausible solutions in the other three cases so that we can explore the impact of oxidative stress and age on the model parameters. The experimental data for young stressed worms lie well within the bounds of the results predicted by the mathematical model, except for the time right after the "on" response, as well as some time during the plateau (Figure 3.3-A). In these two short periods the model seems not to follow exactly the stabilization in Ca^{2+} concentration. In the case of aged worms, experimental data falls within the bounds of the results predicted by the mathematical model, with plausible parameter sets for both unstressed and stressed worms (Figure 3.3-B). Most of the model generated variations for aged worms occur around the "off" response, for both unstressed and stressed animals.

3.7.3 Parameters Contributing to the Modified Ca^{2+} Dynamics

Each plausible parameter set obtained from the multitude of possible initial populations in the hybrid optimization algorithm contains combinations of parameters that are different from the reference case (young unstressed worms). The times each parameter is present in a plausible parameter set for young stressed (total of 15 plausible sets), aged unstressed (total of 3 plausible sets) and stressed (total of 6 plausible sets) worms is shown in Figure 3.4-A, C, and E. The absence of a bar for a parameter (for example, VGCC is not present in Figure 3.4-A) does not indicate that the specific parameter remined unchanged at the condition studied (i.e., age and/or oxidative stress). Rather, it means that none of the different combinations that constitute plausible solutions for the specific case (e.g., regarding Figure 3.4-A, stress in young worms), contains this specific parameter. As shown in the dot plots in Figure 3.4-B, D, and F, the values of each parameter in all plausible sets in which it is included may vary substantially (e.g., k_O , Figure 3.4-F) or not (e.g., k_p , Figure 3.4-B). Notably, in the case of aged stressed worms (Figure 3.4-F) the parameters included in the plausible solutions that are changed compared to young unstressed worms, are increased hundreds of times (e.g., 4000% for k_o^- , 6000% or even 14000% for k_o Figure 3.4-F). In the case of young stressed and aged unstressed worms, the altered parameters increase only by up to ~350% (Figure 3.4-B, D), and sometimes they even decrease, compared to young unstressed animals (e.g. G_{SERCA} and k_O^- Figure 3.4-B, K_{SERCA} and k_I in Figure 3.4-D).

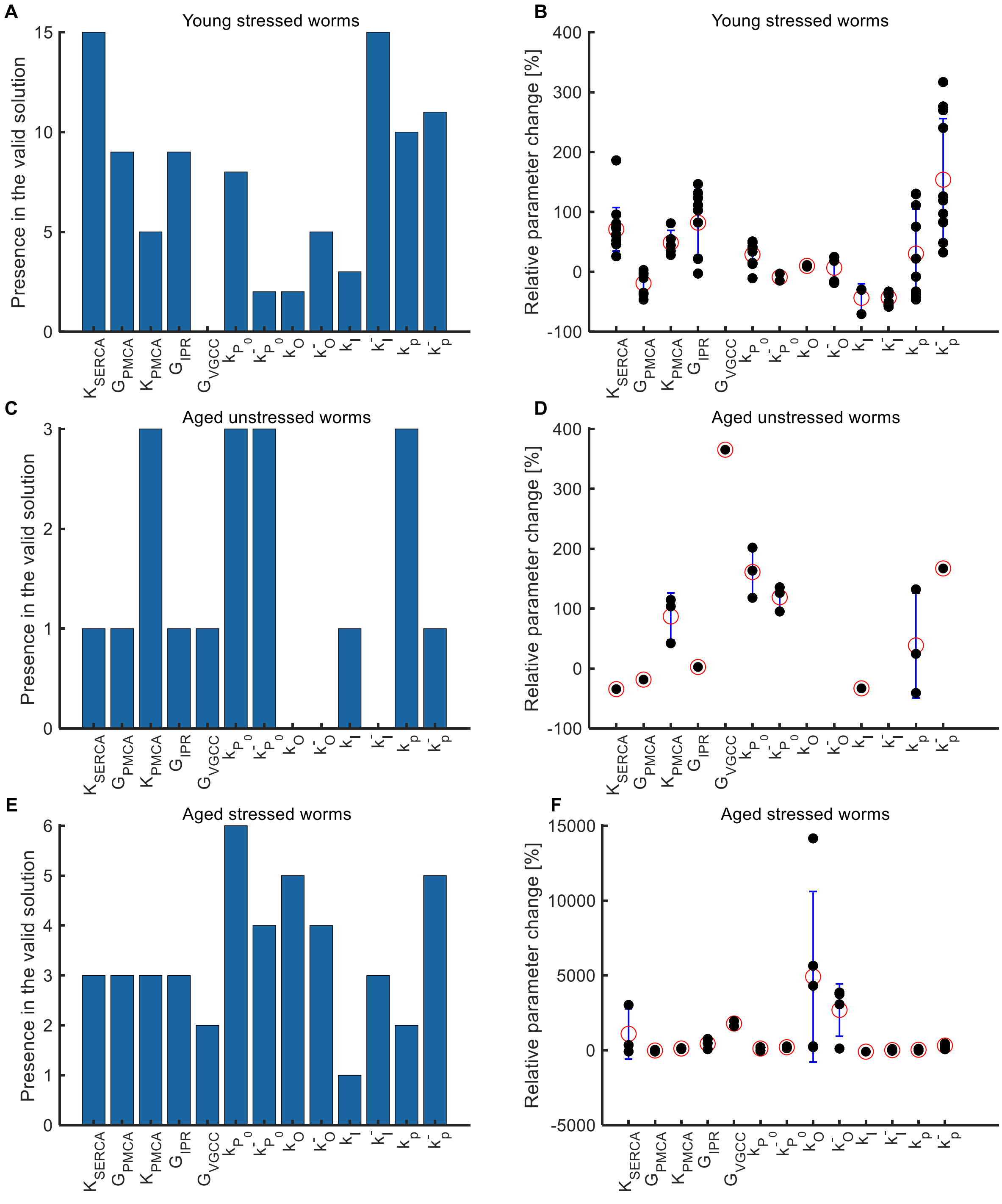

Figure 3.4- The effects of aging and oxidative stress treatment on stimulus-evoked Ca^{2+} transients can be explained by changing values of the parameter set for young unstressed worms (reference case). The frequency by which each of the selected parameters appears in all plausible combinations of solutions is shown in (A) for young stressed worms (15 plausible combinations), in (C) for aged unstressed worms (3 plausible combinations), and in (E) for aged stressed worms (6 plausible combinations). The dot plots in (B), (D), and (F) show the relative changes in the parameters compared to the respective parameters for young untreated worms. Each dot corresponds to a plausible solution; red circles indicate the mean; error bars represent standard deviation.

The overall sensitivity of the model parameters can be visualized by a sensitivity plot (Figure 3.5). For each of the plausible parameter sets, the parameter values are randomly perturbed by ±25%, and the peaks of the “on” and “off” responses are plotted. Results suggest that the model can predict the different behaviors observed in experiments, as shown by the approximate overlap between the model-generated and the experimental results. Moreover, the density of the model-generated data is high where the experimental data points are dense and is low where the experimental data points are sparse. This illustrates that the model generates more results in the regions where most experimental results are recorded.

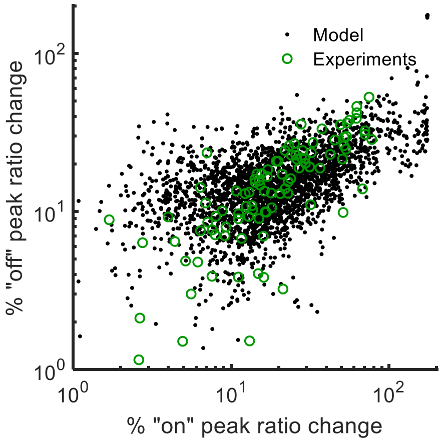

Figure 3.5- Sensitivity of transients on parameter models. Open green circles represent all the experimental results, including young unstressed, young stressed, aged unstressed, and aged stressed worms. For each plausible parameter set 100 samples are created, in which the parameter values are randomly perturbed by ±25%. For each sample, the maximum magnitudes of the “on” and “off” responses are recorded and plotted as filled black circles. The distribution of randomly perturbed model results shows that the mathematical model can capture the variations that are observed in experimental results. Moreover, the modeling results are observed to be dense/sparse where the experimental results are dense/sparse.

3.8.3 Using the Model to Predict Ca^{2+} Dynamics in the Case of Complex Stimuli

We used the model to explore how the ASH neuron would respond when activated by complex time-varying stimuli that would be challenging to implement in an experimental setup, yet it is possible for the worms to encounter in nature.

Figure 3.6 demonstrates selected examples of stimulus-evoked Ca^{2+} transients for such in silico experiments. In all panels, in addition to the %FRET ratio change, the Ca^{2+} concentration in the ER is also presented in order to show the long-lasting effects of the stimulus on the system. Compared to the changing Ca^{2+} concentration in the cytoplasm (represented by %FRET ratio change), the Ca^{2+} concentration in the ER has a slower dynamic, which affects the system's response especially during sequential stimuli. At rest, the Ca^{2+} concentration in the ER is equal to its equilibrium value. When the stimulus is delivered, a small increase in the ER Ca^{2+} concentration is observed due to influx of Ca^{2+} through TRPVs and VGCCs. This is followed by a rapid large decrease due to Ca^{2+} release from the ER through IPRs. Then, the Ca^{2+} concentration in the ER remains relatively constant while the stimulus is sustained, since the influx and efflux of Ca^{2+} balance each other. Finally, when the stimulus is withdrawn, a second rapid large decrease in the ER Ca^{2+} concentration is observed during the "off" response. Then, the Ca^{2+} concentration in the ER starts returning to its equilibrium. However, if a stimulus is delivered before the Ca^{2+} concentration in the ER reaches its equilibrium (this is the case for all the panels in Figure 3.6), the dynamics of the new cytoplasmic Ca^{2+} response are different. For instance, in all cases with sequential stimuli (Figure 3.6-A - D), the first "on" response is the strongest. When stimuli of equal strength and different durations are applied (10, 30 and 50 sec) Figure 3.6-A), the magnitude for all "off" responses are almost the same. The shortest stimuli (fourth and sixth pulse, 10sec) result in just one peak. The longest stimulus (fifth pulse, 50 sec) results in a longer plateau. When we apply stimuli with the same duration but different magnitudes (2α, α, $\alpha/2$, 4α) (Figure 3.6-B), the response to the first pulse, which has twice the magnitude of the first pulse in Figure 3.6-A, leads to stronger "on" and "off" responses. However, a stimulus with the same magnitude that is delivered later (fourth pulse) leads to weaker "on" and "off" responses.

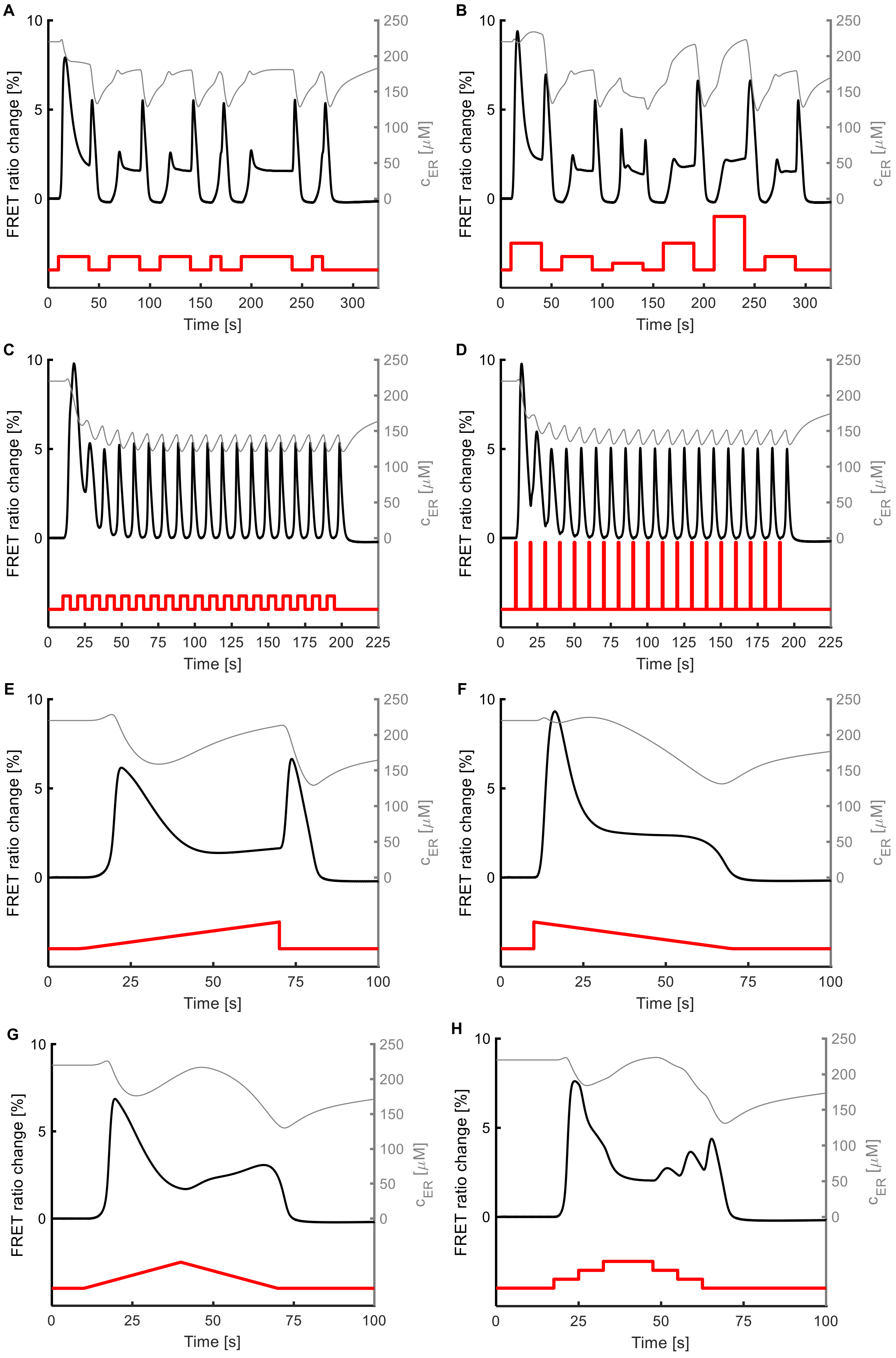
A
B
C
D
E
F
G
H
FRET ratio change [%]
c_{ER} [μM]
Time [s]
10
5
0
250
200
150
100
50
0
0
50
100
150
200
250
300
0
25
50
75
100
125
150
175
200
225
0
25
50
75
100

Figure 3.6- The proposed mathematical model can be used to investigate in silico the Ca^{2+} transients which would occur due to complex stimuli, challenging to implement experimentally. The parameters for young (Day 1) unstressed worms (reference case) are used to generate all the results shown in this figure. The left y-axis shows % FRET ratio change and the right y-axis shows the Ca^{2+} concentration in ER. (A) A sequence of stimuli with the same magnitude and different durations is applied. Consecutive stimuli lead to weaker "on" response while the "off" response is less affected. (B) A sequence of stimuli with same duration and different magnitudes is applied. Stronger stimulus leads to larger "off" response for successive stimuli while the "on" response does not increase when the stimulus strength increases. (C) A flickering stimulus results in a Ca^{2+} transient in which an array of single consecutive peaks is observed. (D) A flickering stimulus with the same frequency as (C). The pulses are stronger than the ones in (C), but they are shorter so that the area underneath each plus is the same for each pulse in C and D. The Ca^{2+} transients in (C) and (D) are almost identical. (E) When delivering a rising ramp-shaped stimulus, ASH neuron appears to show both "on" and "off" responses, of similar magnitude. (F) When the stimulus is in the shape of a decaying ramp, it leads to a strong "on" response, whereas a distinct "off" peak is absent. (G) A rising followed by a decaying ramp stimulus (triangular pulse) results in an initial "on" response, followed by a second rise during decrease of stimulus magnitude, without the characteristic "off" response peak. (H) The continuous triangular pulse in (G) can be delivered in consecutive steps. The area underneath the pulses in (G) and (H) is the same. While the overall Ca^{2+} transients in both cases are comparable, delivering the stimulus in discrete steps leads to “off” responses. Red line represents the stimulus; black line indicates the model-generated results.

As a next step, we applied short, repetitive (flickering) pulses (Figure 3.6-C, D). When we apply a series of pulses with medium intensity (magnitude the same with the first pulse in Figure 3.6-A) and intervals of equal duration (Figure 3.6-C), then a strong first "on" response occurs, followed by a series of almost identical peaks, apart from the second one. No obvious difference between "on" and "off" responses is observed. Interestingly, when we implement a series of acute, very short and strong pulses (1/10 of the duration and 10 times the magnitude of the first pulse in Figure 3.6-A), the response recorded (Figure 3.6-D) is almost identical.

Lastly, we applied ramp pulses, where the stimulus intensity (magnitude) changes gradually over time (Figure 3.6-E - G). When the pulse is in the form of a rising ramp (Figure 3.6-E) both “on” and “off” responses are observed, but they are weaker compared to the rectangular stimulus (first pulse in Figure 3.6-A, for example). However, for a descending ramp pulse (Figure 3.6-F) a strong “on” response is generated (comparable to the “on” response for the first pulse in Figure 3.6-A), without any apparent “off” response. When the pulse is triangular, namely an ascending ramp followed by a descending one (Figure 3.6-G), the "on" response peak is like the one caused by a single rising ramp (Figure 3.6-E). Instead of a well-defined "off" response, though, we observe a relatively mild increase of the % FRET ratio change before the signal returns to the basal level. Interestingly, when we replace the ramped triangular pulse with a stepped triangular pulse (Figure 3.6-H), the overall shape of the change in the % FRET ratio is similar, but the system seems to respond also to the small steps, especially as the magnitude of the stimulus decreases.

3.4 Discussion

3.9.4 The Dynamics of the Ca^{2+} Transients Mechanism is Reflected in the Model

TRPVs are the first channels to be activated, and the Ca^{2+} that flows in leads to IPRs opening via Ca^{2+}-induced Ca^{2+} release, and to a voltage change that activates the VGCCs. The important role of TRPVs in the model is verified when they are *in silico* knocked out (Figure 3.2-E). Neither the original model, where parameters remain as estimated before omitting a component, nor the updated model, where parameters are re-estimated after removing a component, can successfully account for the Ca^{2+} dynamics once the TRPV channels are removed.

TRPV channels are the key contributors to the cytoplasmic Ca^{2+} increase during the “on” response, even though VGCCs and IPRs contribute as well. This is mirrored in the original model, since in the absence of TRPV-mediated Ca^{2+} influx the VGCCs are not activated. Moreover, the Ca^{2+} that is released from the ER, due to IP_3 activation via receptor-coupled EGL-30, may not be enough to trigger an "on" response.

The contribution of VGCCs to the ASH Ca^{2+} transients has been experimentally reported [98,118]. Their role in Ca^{2+} signaling in the neurons lies mainly in propagating the Ca^{2+} signal from the soma to the axon. Their contribution to the soma Ca^{2+} transients is mild [97,98]. The absence of constraints on the model parameters that control Ca^{2+} flux through these channels reflects the lack of experimental data on the relative contribution of TRPVs and VGCCs to the "on" response. In the absence of such constraints, the optimization algorithm determines the strength of each channel solely based on goodness of the fit. Thus, both the original model and the updated one can compensate for the omission of VGCCs (Figure 3.2-F).

In contrast, the "off" response takes place even without the TRPV channels and is in fact stronger when the TRPV channels are knocked out (Figure 3.2-E). The "off" response occurs mainly due to Ca^{2+} released from the ER, and the model takes into account the Ca^{2+}-induced Ca^{2+} release, since the rates controlling the opening probability of IPRs depend on the Ca^{2+} concentration, Eqs. (3.12)-(3.14). Thus, since no Ca^{2+} flows in through knocked out TRPVs during the "on" response, the Ca^{2+} release from the ER is minimized. Hence, ER stores remain full and release a high amount of Ca^{2+} into the cytoplasm, as they respond to EGL-30 mediated induction of IPRs opening during the "off" response.

In the updated model with knocked out TRPV channels (Figure 3.2-E), the remaining parameters change, so that IPRs and VGCCs yield the "on" response even without TRPV channels. The entire Ca^{2+} response is then similar to the normal transient (Figure 3.2-A) and it includes an "off" response. However, certain features are not accounted for, as for example the time needed for the "on" peak and the respective decaying slope, indicating that the presence of TRPVs in the model is indispensable. In reality, a neuron will not be capable of compensating for complete loss of TRPV channels by upregulation of VGCCs and IPRs mechanism, therefore the inability of the updated model to account for the full dynamics of the Ca^{2+} transients may reflect a real biological constrain.

At the same time, VGCCs are gated by voltage changes, which in the cell are not generated only due to the Ca^{2+} influx, but also due to other ions that enter the cytoplasm upon neuronal activation. We do not explicitly include the dynamics of each of the other ion transients in the model. However, we do include players that account for the combined effects of these ion transients. The experimental data available in the literature regarding voltage traces in the ASH neuron is limited to events related to the "on" response [98]. Therefore, we use a reduced order modeling approach to model the membrane potential to construct a phenomenological model that generates a graded voltage response (Figure 3.2-G), which matches measurements reported for other *C. elegans* neurons [147–149,157,158]. Hence, our model accounts for the contribution of voltage gated channels only coarsely.

PMCA is the main ion pump responsible for removing excess Ca^{2+} from the cytoplasm in *C. elegans* [159]. Therefore, *in silico* knockout of PMCA (Figure 3.2-B) results in partial (original model) or complete (updated model) inability for the model to compensate for the PMCA function. We choose not to include in the model the Na^{+}/Ca^{2+} exchanger, which also exports Ca^{2+} from the cytoplasm, although its presence has been reported in *C. elegans* [160,161].

In eukaryotic cells, there are pumps to facilitate the Ca^{2+} transport back into Ca^{2+} stores. The most prominent among them is the SERCA [161] which, depending on its isoform, is abundant on the sarcoplasmic and endoplasmic reticulum membrane of muscle cells and neuronal cells [162–165]. In *C. elegans*, functional SERCA homologs have been discovered [165,166]. One orthologue of SPCA, a Golgi-related Ca^{2+} - transport ATPase, functioning as Ca^{2+} transporter, has also been reported [167–169]. *C. elegans* neurons are known to have the typical eukaryotic Ca^{2+} signaling tools [170], including functional Ca^{2+} stores. In our model, all Ca^{2+} stores are considered as one entity, depicted as ER, and the respective pumps are modeled as one mechanism, herein referred to as SERCA.

SERCA's omission from the model (Figure 3.2-C) results in most of the ER Ca^{2+} being released without being replenished, during the “on” response. Therefore, in the original model, there is not enough Ca^{2+} left in ER to yield the “off” response. However, even without an active

SERCA pump, the modeled leak across ER can restore Ca^{2+}. In the updated model for SERCA knock out, the hybrid optimization algorithm takes into account that there has to be an "off"' response upon withdrawal of the stimulus. Therefore, the remaining parameters change to save Ca^{2+} in the ER for the "off" response. This leads to forced increased influx of Ca^{2+} through TRPV channels during the “on” response. This way there is enough Ca^{2+} stored in the ER to produce the “off” response later in the updated model, even with SERCA removed.

However, *in vivo* a cell does not upregulate *a priori* the TRPV-mediated influx of Ca^{2+} upon neuronal activation to afford an "off" response later. Moreover, without a SERCA pump, the "off" response could not possibly occur in case of sequential stimuli, as replenishment of intracellular stores would not take place. Hence, the original model illustrates better the consequences for the cell, should the SERCA pumps be impaired (Figure 3.2-C, continuous line). This highlights the way in which the model can be used in a biologically meaningful way, to make reasonable hypotheses that may guide targeted experimental efforts.

The IP_3 receptor, a major intracellular Ca^{2+} release channel, has been reported in *C. elegans* [153,171,172]. As shown in the original model (Figure 3.2-D), the magnitude of the “on” response decreases dramatically when IPRs are omitted. However, the updated model parameters rescue most features of the “on” response, by increasing the input of TRPVs and VGCCs. Nevertheless, since the “off” response is attributed mainly to the release of Ca^{2+} from the ER, even the updated parameters fail to capture it. This shows that certain molecular players are irreplaceable, even when other agents are artificially asked to compensate for them.

The characteristic "off" response of the ASH Ca^{2+} dynamics, is observed also in other *C. elegans* sensory neurons [96,173]. However, it has not been included so far in any mathematical model for *C. elegans* Ca^{2+} dynamics. Elucidating the respective physiological mechanisms is work in progress [105,117]. Based on experimental results, which show that the TRP channel OSM-9 is required for the "off" response [117], and on the results of our model, we claim that the ASH “off” response is attributed mainly to the efflux of Ca^{2+} from the intracellular stores. This is an event related to OSM-9, via the Ca^{2+}-induced Ca^{2+}release mechanism. Therefore, the proposed model encompasses and accounts for experimentally obtained results.

Additional improvements could be applied to the model, if more experimental and electrophysiological data were available. For example, in young stressed worms the model successfully captures the overall Ca^{2+} dynamics, except for a small region right after the “on” response. One possible explanation is that, as explained, the current model accounts for VGCCs only coarsely, thus it misses some features of Ca^{2+} transients related VGCCs. This is supported by the fact that *egl-19* mutant worms have less steep decaying slope after the "on" response [118]. The models’ variations around the “off” response of aged worms may be related to the high variation observed also experimentally in the "off" response of in this age cohort ([50] S2 Figure C, [113] S1 Figure).

The *in silico* knock outs are informative primarily about how the model works and illustrate its minimality and purposefulness. Moreover, the *in silico* knock outs can serve as indications and possibly guides to targeted experiments.

3.10.4 Effect of Age and Stress on Ca^{2+} Signaling Machinery

Potential intercellular interactions between ASH and other neurons are not considered in the present model. ASH might be affected by oxidative stress- or aging-induced changes in other cells. The proposed effects are intended to offer plausible explanations regarding the intracellular events. Nonetheless, the overall ability of our model to capture the Ca^{2+} dynamics in all four worm groups studied is excellent (Figure 3.2- A, Figure 3.3-A, Figure 3.3-B). The model accounts for variability in the experimental data, as shown in the sensitivity analysis (Figure 3.5) and shows the same variation observed in the experimental data, when the model parameters are perturbed. Yet, the model is robust enough not to lead to unreliable results away from what is experimentally anticipated.

There are more than one parameter sets that can equally explain the changes in Ca^{2+} dynamics. This is because of multiple possible ways that can lead to similar cell responses. For example, the correlation between different channels in neurons that produce similar electrical properties has already been established [174]. Our model reflects similar phenomena. For instance, the elevated Ca^{2+} response due to aging may occur because PMCA is weakened or because TRPVs are more sensitive or perhaps due to a combination of the two. In fact, even though the effect of aging on the Ca^{2+} response is approximately the same among worms of the same age, their biological cause may be different among individuals. As expected, such correlations introduce difficulties when searching for a unique parameter set in the model.

Each parameter may affect the outcome of the model in more than one way. For example G_{IPR} affects both the "on" and "off" responses (Figure 3.2-D), and G_{PMCA} affects the decaying slope of both responses and also the magnitude of the on response (Figure 3.2-B). Consequently, quantitative correlations of parameter values exclusive to one specific feature of the Ca^{2+} transient are precarious. However, qualitative connections between parameters and physiological changes in the Ca^{2+} transients can be articulated in combination with experimental results. Worms of Day 5 of their adult life used here are considered to be middle aged; therefore the effect of aging on their Ca^{2+} transients is expected to be mild [175].

G-protein coupled receptors (GPCRs), like the ones activated by osmotic stress in the ASH neuron [176,177], can be dysregulated by increased production of ROS [178,179]. The effect of aging on GPCRs depends strongly on how related molecules, especially kinases and G-proteins, are affected [180–182]. In our experimental data (Figure 3.3), aging affects the rising and decaying slope of both "on" and "off" responses, the latter in combination with stress. The slopes in the model could be correlated to the rates (i.e. P_0, k_{P_0}, $k_{P_0}^-$) of events related to the receptor-coupled G proteins. Moreover, oxidative stress results in faster "on" peak in aged worms. This could potentially be linked to the rates of cascades related to receptor-coupled proteins (i.e. k_{P_0}, $k_{P_0}^-$). These rates (k_{P_0}, $k_{P_0}^-$) appear changed in the plausible solutions for young stressed and aged unstressed worms (Figure 3.4-A-D). Therefore, the model can assist on choosing potential experimental targets, to explore biological events.

Although TRP channels are involved in lifespan regulation in *C. elegans* [183], changes in TRPV activation with respect to aging have not been reported yet. Studies in mammalian systems indicate that expression or distribution of TRPV channels is affected by aging [184,185]. Our experiments show that the magnitude of the "on" and the "off" responses increases with aging (Figure 3.3). This could be related to changes in the probability of TRPVs being activated (parameters k_o and k_0^-) in aged worms (Figure 3.4E and F) as well as to changed rates for the G protein related cascades (k_{P_0}, $k_{P_0}^-$) (Figure 3.4C and D). Thus, the model can suggest potential roles for molecular players involved in aging-driven changes in the Ca^{2+} transients.

Oxidative stress has a significant impact on TRPV channels, mainly through oxidation of cysteine residues in channels' subunits [186,187], resulting in TRPV sensitization [186,188]. Experiments show that oxidative stress affects the magnitude and rising slope of the "on" response in aged worms, and the magnitude of "off" response in younger worms (Figure 3.3). These features can be linked to changes in the rates for the G protein related cascades (k_{P_0}, $k_{P_0}^-$ in young worms) or the probability of activated TRPV channels (k_0 and k_0^-, in aged worms, Figure 3.4-C-F).

Therefore, the results of our model corroborate experimental findings in *C. elegans* and other systems.

VGCCs are known to be affected by oxidative stress [189] via oxidation of cysteine residues [190] and –SH groups [191]. In aged neurons, VGCCs show increased activity [129,192], and their contribution to Ca^{2+} influx rises in both cases [129,133]. Interestingly, we do not detect any significant change regarding VGCC channels in our model. This could be due to the fact that VGCCs contribute less than TRPVs to Ca^{2+} transients in the neuronal body, where our efforts are focused. Moreover, VGCCs are modeled coarsely in the present work, not allowing us to draw solid conclusions.

The effect of aging on neuronal IP$_3$ receptors [133] results in elevated flux of Ca^{2+} into the cytoplasm [130,131], partially through enhanced Ca^{2+}-induced Ca^{2+} release [132]. Age increases the rising and decaying slopes of the "on" and "off" responses in our experiments, the latter only in stressed animals (Figure 3.3). The slopes in the model may be related to the maximum ion flux though IPRs (G_{IPR}), and to the rates for IPRs (k_P and k_P^-). These parameters are indeed included in the plausible solutions for aged and for stressed worms (Figure 3.4-C - F). This indicates that the model can successfully account for experimentally detected physiological changes.

Oxidative stress leads to increased Ca^{2+} efflux from the stores into the cytoplasm [193,194] through IP$_3$ receptors, because of –SH groups oxidation [131] and increased production of IP$_3$ [193]. Experiments show that oxidative stress affects the magnitude and rising slope of "on" response in aged worms, and the "off" response peak in young worms (Figure 3.3). The responses magnitude can be linked to the maximum ion flux through IPRs (G_{IPR}), which changes in stressed worms (Figure 3.4-A and B). Oxidative stress also results in faster "off" peak in young worms (Figure 3.3), which could be related to altered maximum ion flux through IPRs (G_{IPR}) and to the rates for IPRs (k_p and k_p^-) (Figure 3.4-A and B). Hence, the model accounts satisfactorily for the role of intracellular Ca^{2+} channels described by experimental data.

In contrast to the increased activity of ion channels due to oxidative stress, the PMCA pump is inactivated by ROS [193], as a result of altered tyrosine and methionine residues [195]. Decreased efflux of Ca^{2+} through PMCAs occurs also in aged neurons [196,197]. SERCA pumps are affected in a similar way, since they are inhibited by oxidative stress [198] and are also impaired in aged neurons [199]. The magnitude of the "on" and the "off" response increases with aging (Figure 3.3) in *C. elegans*. This could be related to changed affinity of PMCAs and SERCAs for Ca^{2+} (K_{PMCA} and K_{SERCA}) in aged worms (Figure 3.4-C-F). Experiments show also that oxidative stress affects the peak and rising slope of the "on" response (Figure 3.3) in aged worms, and of the "off" response in young worms (Figure 3.3). The response magnitude can be linked to the changed affinity for Ca^{2+} of SERCAs (K_{SERCA}) in young stressed worms (Figure 3.4-A and B). Stress results in altered decaying slope after the "on" and "off" response of young worms (Figure 3.3), which could possibly be related to changed maximum ion flux through PMCAs (G_{PMCA}), as is suggested in the model (Figure 3.4-A and B). Therefore, the way aging and oxidative stress affect the function of major cell pumps is well captured by the proposed model.

To summarize, our model can be used to explore the effects of aging and stress on the ASH Ca^{2+} signaling machinery. The suggested correlations between the effect of aging and oxidative stress on physiological cascades and the model parameters are not the only possible explanation for the observed changes in Ca^{2+} dynamics and should be confirmed experimentally. Parameters that are not included in the plausible solutions may also play a role. However, the agreement of the model with the available experimental data strongly suggests that the model and the selected parameters capture successfully the physiological trend.

3.11.4 Complex Ca^{2+} Transients Can be Predicted by the Model

C. elegans sensory neurons respond differently to varying stimulus strengths [200]. Our model generates Ca^{2+} transients peaks of different magnitudes in ASH neuron, in both "on" and "off" responses, depending on the strength of the applied stimulus (Figure 3.6-B). However, hidden states with slower dynamics, i.e. ER Ca^{2+} dynamics, that are not easily measured in experiments but are captured by the mathematical model, may have an important impact (Figure 3.6-B, differences in sequential responses).

The response to gradient stimuli has been shown experimentally for *C. elegans* sensory neurons [200], especially for odor gradients[121,201,202]. The model-generated Ca^{2+} transients that occur in the presence of a ramp stimulus (Figure 3.6-E-G) indicate that the ASH neuron can detect smooth gradients via the "on" response and sharp decreases via the “off” response. Therefore, our model suggests that the “off” response may be a mechanism that detects acute changes.

A step-increasing pulse, instead of a continuous gradient, (Figure 3.6-G and H) does not affect significantly the overall shape of the Ca^{2+} transient (the area underneath both pulses is the same). However, the decreasing stimulus through stepped pulses results in different “off” responses, as has been reported experimentally (33). This suggests that the proposed model can encapsulate Ca^{2+} dynamics in the ASH neuron in alignment with the experimental data.

The ability of ASH to respond reliably to a sequence of identical stimuli has been shown experimentally [118], and interestingly, the neuron responds consistently, especially via the "off" response (Supplementary Figure 5 of [118]). Indeed, when arrays of sequential pulses are applied in the model, results account for the robustness of the "off" response (Figure 3.6-A and B).

In our experiments, the duration of the stimulus is 30 sec [50], as in other similar studies [112,113]. Previous work [112] suggests that a shorter hyperosmotic stimulus (15 sec) leads to a weaker “on” response and a stronger “off” response, compared to long stimulus delivery in the same study. When a short stimulus is applied in our model (Fig S1 A) the "off" peak is lower than the "on". We hypothesize that the stronger “off” response reported in [112] is a consequence of the weaker “on” response and not of the short stimulus duration. To test this hypothesis, we tried different values for the K_c parameter in Eq. (3.16), which affects the dynamics of IP_3 production, to change the magnitude of the “on” response (Fig S1). Indeed, a weaker “on” response leads to a stronger “off” response, without changing the duration of the stimulus, possibly due to full intracellular Ca^{2+}stores. In the paper by Chronis and colleagues [113], the reason behind the shape of the Ca^{2+} transient of the 15 sec pulse could be the small population examined (3 traces, Suppl. Data [113]). Therefore, our model can help interpret experimental variations in *C. elegans* populations.

In the study by Kato and colleagues [118], the ASH neuron is shown to respond with precision, through its Ca^{2+} transients, to flickering stimuli of 1 sec long pulses (Figure 1 of [118]). Our model is able to capture such a flickering response (Figure 3.6-C and D). Therefore, the model can be a reliable computational tool when exploring the response of *C. elegans* sensory neurons. Moreover, the model shows that the stimulus-evoked Ca^{2+} transient is the same when the total amount of stimulus-carrying solution delivered is the same (as indicated by the area under each pulse) and does not depend solely on the actual duration or magnitude of the pulse (Figure 3.6-C: 2units of stimulus/5sec; Figure 3.6-D: 10units of stimulus/1sec). This is an interesting finding, which can elucidate the details of the activation mechanism of the ASH neuron if corroborated by experimental data.

Note that the fast responses of the system (Figure 3.6-C and D) captured by our model require further validation, because the equations of the model have been developed based on slower dynamics (Figure 3.3). However, the capability of the proposed model to successfully account for *in silico* trials shows that it can serve as a preliminary tool for pre-experimental tests.

3.5 Conclusions

We propose a model for the Ca^{2+} dynamics in the *C. elegans* ASH polymodal neuron, based on intracellular events that unfold as part of the Ca^{2+} signaling machinery. Our model uses experimental data on stimulus-evoked Ca^{2+} transients upon neuronal activation and it captures efficiently for the first time the dynamics of both the “on” and “off” responses. Moreover, the model can account for changes in the ASH Ca^{2+} dynamics due to age and exposure to oxidative stress, reflecting, confirming and sometimes predicting the role of each molecular player modeled in the cellular mechanism that generates Ca^{2+} transients. We believe that the proposed model makes a contribution in *C. elegans* neurobiology because it i) suggests how molecular players that are known to be affected by aging and/or oxidative stress may be involved in generating the altered Ca^{2+} transients features (e.g. IP_3 receptors), ii) suggests a possible effect of aging and/or oxidative stress on molecular players not yet documented to play a role toward aging- or stress-driven modifications of the Ca^{2+} transients features (e.g. activation/inactivation of TRPV channels), and iii) can be used to propose and guide future experimental work, targeting specific molecular players involved in Ca^{2+} dynamics. Finally, the model can be used to predict Ca^{2+} transients in the ASH neuron in the case of complex stimuli. We envision the proposed model as a tool used to further elucidate the Ca^{2+} dynamics of *C. elegans* neurons and to pave the way for the development of more mathematical models for neuronal Ca^{2+} dynamics.

Chapter 4

Synaptic Impairment and Robustness of Excitatory Neuronal Networks with Different Topologies

4.1 Introduction

The network structure/topology of the brain plays an indisputable role in a wide variety of tasks the brain performs [203]. Knowledge of the function of brain networks enables the development of tools and methods to detect and treat pathological conditions related to network malfunction [204,205]. That is in part why building the human connectome has attracted vast efforts in the past few years [206,207].

Although the complete human connectome is not available yet, even mapping individual circuits of human's or other animals' central nervous system has provided researchers with enormous amounts of data to study the network structure/topology of the brain. The non-random structure of the brain networks is a common conclusion of all these studies [203]. Scale-free or small-world network structures of the brain have been proposed [44,208–210]. More recently, the neuronal network of C. elegans, the first organism to have its connectome fully mapped [42,43], has revealed the presence of hubs and rich clubs in its nervous system [41]. Although in less detail,

---

The results presented in this chapter is published as:

Mirzakhalili E, Gourgou E, Booth V, Epureanu B. Synaptic Impairment and Robustness of Excitatory Neuronal Networks with Different Topologies. Front Neural Circuits 2017;11:38. doi:10.3389/fncir.2017.00038.

mesoscale and macroscale studies in humans [211], mice [212] and cats [213] have shown similar findings. Additionally, such heterogeneity in the network structure has been observed in cultured cells, and emergence of small-world networks [214] or rich clubs [215] has been reported for in vitro experiments.

The number and the strength of connections that neurons make with each other, create a non-random spatial topology of neuronal networks [216]. Connections are not completely static even in normal conditions. For example, synaptic plasticity and neuromodulation can affect the dynamics of neuronal networks and change the brain's functional connectivity [217,218]. Malfunctions in synaptic connections and synaptic dynamics in pathological conditions can jeopardize the normal functionality of brain. For instance, studies have shown loss of synapses as a hallmark of Alzheimer's disease [4,219,220]. Random loss of synapses has already been used to simulate different stages of Alzheimer's disease [221]. However, there are biological or pathological conditions that can lead to nonrandom loss of synapses. For instance, recent studies have shown that oxidative stress related to neuronal activity may result in dysfunction of synapses in Alzheimer's disease [222].

EEG [223,224] and fMRI [225–227] data have revealed that the network topology of the brain changes even during normal aging. Therefore, the study of neurodegenerative diseases and their symptoms on the network level can be the key to better understanding of these disorders by monitoring the structure and dynamics of neuronal networks [228–230]. In the present study, we investigate the impact of synaptic deficiency, namely reduced effectiveness of the synaptic function, on the robustness of neuronal networks with different topologies. The biological process that leads to this deficiency can be attributed to many factors, ranging from functional decline during normal aging, to age-associated neurodegenerative diseases, such as Alzheimer's disease.

We focus on networks with only excitatory neurons to emphasize on the importance of topology on the robustness of networks, since inhibitory neurons are shown to increase networks' robustness [231]. Particularly, we focus on persistent activity of neuronal networks defined as the ability of the network to sustain its activity upon removal of the initial stimulation. Persistent activity has been linked to working memory, which is the ability to remember information for periods of time in the order of seconds [47,232,233]. One of the reasons why we are interested in persistent activity is because working memory is known to be adversely affected in patients with Alzheimer's disease [46,234,235]. Previously, network connectivity [48,236] and degree distribution of networks [237] has been shown to influence the self-sustained activity of neuronal networks under normal conditions. However, there are no studies where the sensitivity of persistent activity to synaptic failure is investigated. We show here that networks with rich clubs can be constructed systematically by using bimodal degree distributions. Then, we examine how networks with different topologies respond to different levels and types of impairment. Robustness and capability of the neuronal network to maintain activity are used to differentiate dynamics of networks with different topologies.

4.2 Methods

4.1.2 Neuron Model

We adopt a neuron model based on the Hodgkin-Huxley formalism. The model features a fast Na^+ current, a delayed rectifier K^+ current and a leakage current [238–240]. The current balance equation for cell i is:

$$C\frac{dV_i}{dt} = -g_{Na}m_\infty^3 h\left(V_i - E_{Na}\right) - g_{Kdr}n^4\left(V_i - E_K\right) - g_L\left(V_i - E_L\right) + I_{ext} - I_i^{syn}, \tag{3.26}$$

where $C = 1.0\ \mu\mathrm{F/cm^2}$, $g_{Na} = 24.0\ \mathrm{mS/cm^2}$, $g_{Kdr} = 3.0\ \mathrm{mS/cm^2}$, $g_L = 0.02\ \mathrm{mS/cm^2}$, $E_{Na} = 55.0\ mV$, $E_K = -90.0\ \mathrm{mV}$, $E_L = -60.0\ \mathrm{mV}$ [238,239,241]. I_{ext} is the external current (measured in $\mu\text{A}/\text{cm}^2$) that controls the firing frequency of the neuron. This current is chosen so that the firing frequency of the i^{th} cell is zero when I_i^{syn} (the synaptic current received by neuron i) is zero.

The Na$^+$ inactivation gating variable h, and the K$^+$ delayed rectifier activation gating variable n are governed by first order dynamic equations expressed as:

$$\frac{dh}{dt} = \frac{h_\infty - h}{\tau_h} \text{ and } \frac{dn}{dt} = \frac{n_\infty - n}{\tau_n}, \tag{3.27}$$

where the steady state values and the time constants are given by:

$$h_\infty = \frac{1}{1 + \exp\left(\frac{V + 53.0}{7.0}\right)}, \tag{3.28}$$

$$\tau_h = 0.37 + \frac{2.78}{1 + \exp\left(\frac{V + 40.5}{6.0}\right)}, \tag{3.29}$$

$$n_\infty = \frac{1}{1 + \exp\left(\frac{-\text{V} - 30}{10.0}\right)}, \tag{3.30}$$

The activation of Na$^+$ current is assumed instantaneous, and is modeled by the following function:

$$m_\infty = \frac{1}{1 + \exp\left(\frac{-V - 30}{9.5}\right)}. \tag{3.31}$$

4.2.2 Synaptic model

The synaptic current from the presynaptic neuron j received by the postsynaptic neuron i is modeled as:

$$I_{ij}^{syn} = g_{syn} W_{ij} s_{ij} \left(V_i - E_s\right), \tag{3.32}$$

where $g_{syn} = 0.005\ \mathrm{mS/cm^2}$ is the maximum synaptic conductance, and E_s is the reversal potential for the synaptic current, which is usually considered equal to zero for excitatory synapses. W_{ij} is the connectivity weight between the presynaptic neuron j and the post synaptic neuron i. a synaptic connection without any synaptic impairment has a weight of $W_{ij} = 1$. When $W_{ij} = 0$, the two neurons are not connected to each other. We defined synaptic deficiencies as any values of W_{ij} between 0 and 1. s_{ij} is the fraction of open receptors, which follows a simple first order kinetic equation given by:

$$\frac{ds_{ij}}{dt} = \alpha\left[T_j\right]\left(1 - s_{ij}\right) - \beta s_{ij}, \tag{3.33}$$

Here $\alpha = 1.1\ \mathrm{mM^{-1}ms^{-1}}$ and $\beta = 0.19\ \mathrm{ms^{-1}}$ [242] are constants and correspond to forward and backward rates. $\left[T_j\right]$ is the concentration of neurotransmitters released by the presynaptic neuron j that can be approximated by the following equation [242]:

$$\left[T_i\right] = \frac{T_{max}}{1 + \exp\left(-\frac{V_i - V_p}{K_p}\right)}, \tag{3.34}$$

where $T_{max} = 1\ \mathrm{mM}$ is the maximum concentration of released neurotransmitters by the presynaptic neuron. $K_p = 5\ \mathrm{mV}$ and $V_p = 2\ \mathrm{mV}$ are constants that determine the steepness and half-activation value of the neurotransmitter release [243].

The total synaptic current received by neuron i is the summation of all synaptic currents from its presynaptic neurons in the network.

4.3.2 Network Connectivity

We use the degree distribution of networks to construct networks with different topological metrics. While small world networks can be constructed systematically [38] without using the degree distribution of the network, authors are not aware of such methods to build networks that consist of rich clubs. Hence, we propose a method in which networks with rich clubs can be constructed provided that they are based on bimodal degree distributions.

The degree of a neuron is defined as the summation of its indegrees (number of its inputs) and outdegrees (number of its outputs). The indegree and outdegree of a neuron can be different since the connections are not necessarily bidirectional. To generate networks with different degree distributions, we chose to concentrate on bimodal distributions, because they are the simplest distributions that are not single modal. Without any constraints, the degree distribution of a purely random network, also known as an Erdős–Rényi model, follows a Poisson distribution [244]. The networks in this chapter have 200 neurons, with 5% probability of connectivity. The probability of connectivity is defined as the chance of having a unidirectional connection between two neurons in the network. For the above parameters, a totally random network has a single mode distribution of mean 20. To make a close comparison to single modal distributions, we create bimodal distributions that have the same mean. Taking this as a reference case, all other networks are created so as to have the same number of synapses but with different mode distributions. To this end, the following relation for the modes of networks with bimodal degree distribution must hold:

$$\omega_1 M_1 + \omega_2 M_2 = 20, \tag{3.35}$$

where ω_1 and ω_2 are weights of the modes and M_1 and M_2 are the mean degree values of the modes. Hence, if weights of the modes are equal, then their average must be equal to 20 (for example $M_1 = 10$ and $M_2 = 30$ are a valid pair when the weights are equal).

To generate networks with different degree distributions, first, two Poisson distributions with the desired mean values are generated. Then, each of the probability distributions is normalized and weighted as desired so that the integral of the combined bimodal probability distribution function (PDF) is equal to 1. Next, a bin size is chosen, and the combined probability distribution function is integrated over each bin. The result of the integration in each bin shows the number of neurons that must have degrees between limits of that bin. Next, the proper number of neurons is assigned randomly with degrees according to the limits of each bin. Thus, the probability distribution function is converted to a degree distribution for the anticipated network. The next step is constructing a network according to the established degree distribution. For this purpose, a scrambled list is created in which each neuron is repeated at a number of times equal to its degree [52]. Next, two non-identical members of the list are selected randomly, and a connection is created from the first to the second element. Then, these two elements are removed from the list, and the process is continued until the list is empty. With this approach, a directed graph without any self-loops is constructed with the desired degree distribution. Figure 4.1 shows the implementation of this method to construct a network with mean values of 5 and 35, with equal weights.

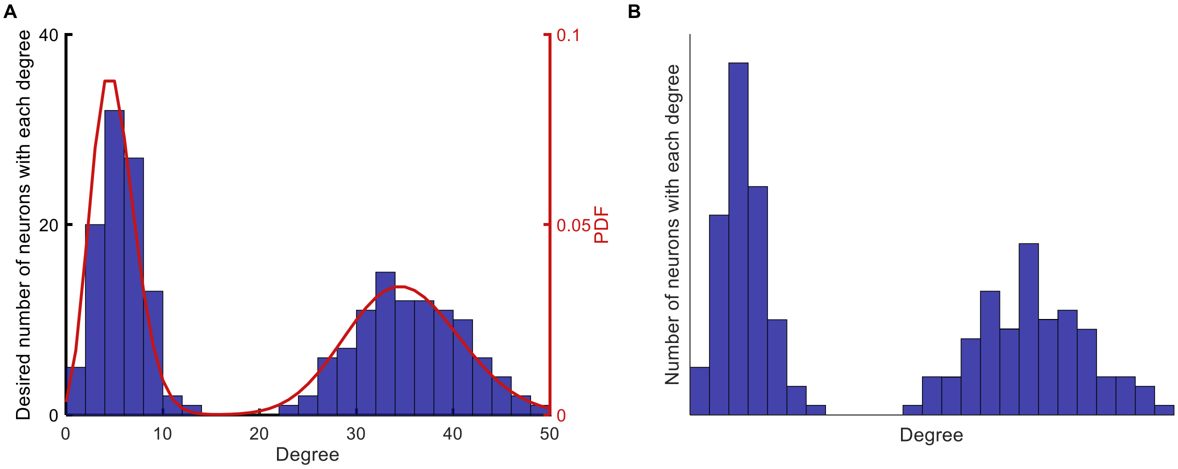

Figure 4.1- Implementation of network construction with desired degree (summation of indegree and outdegree) distribution. (A) A degree distribution that matches the desired probability distribution function (PDF) is randomly generated. (B) A network that matches the desired degree distribution described in (A), is randomly generated. The algorithm generates networks that match the desired degree distribution in a non-exact manner, since the process is random.

Figure 4.1 shows the steps that are taken to construct networks with different degree distributions. Figure 4.1-A shows the first two steps that are prescribing a probability distribution function and creating a random degree distribution according to that degree distribution. Figure 4.1-B shows the degree distribution of the actual network that is constructed based on the degree distribution in Figure 4.1-A. The degree distribution shown in Figure 4.1-A and B are different because the process of generating a network for a given degree distribution is random.

In addition to random networks with a single mode with mean degree value of 20, three bimodal degree distributions with pairs of {15,25}, {10,30}, and {5,35} are used in this chapter. Even though the two mean values used to build each distribution are imposed, the way that the lists are assembled and then networks are created is random. Therefore, the whole process of network construction is random, which leads to deviations in the number of synapses among different networks. Nevertheless, these deviations are small and negligible as the number of synapses is mainly a function of the network size and the probability of connectivity, which both remain unchanged in this chapter. However, to minimize the effects of stochasticity arising from the process of network construction on the system's dynamics, 50 realizations of each degree distribution are used to obtain the results.

4.4.2 Impairment Modeling

To quantify synaptic impairment of the network, we define two metrics: the level of impairment and the percentage of impairment. Impairments are implemented in the elements of the adjacency matrix W, which represent the synapses in the network. When the element W_{ij} is zero, then the two neurons i and j are not connected. When the element W_{ij} is nonzero, then the postsynaptic neuron i receives an input from the presynaptic neuron j. If the nonzero element is equal to 1, then the synapse between the two neurons is considered to be healthy, i.e., it has full strength. If the nonzero element is less than 1, then the synaptic connection is considered impaired, and the difference between the nonzero element and 1 is defined as the level of impairment. The percentage of impairment indicates what percentage of synapses in the network is weakened by the specific level of impairment. For example, a level of impairment of 0.6 and a percentage of impairment of 20% indicates that 20% of nonzero elements of the adjacency matrix of the network have $W_{ij} = 0.4$. For the same level and percentage of impairment, three possible scenarios of deficiency are used to study the effects of synaptic deficiency in the network.

In the first impairment scenario, synapses are randomly selected and weakened or removed, with equal probability. Conditions in which all neurons in a network can be affected equally may lead to random weakening of synapses. For example, aging may affect neurons in some regions of the brain with equal likelihood, and weakens the synapses randomly. Such method of synaptic weakening has been also used to model different stages of Alzheimer's disease [221]. Nonetheless, random impairments are analogues to normal heterogeneity in the strength of synapses in healthy neuronal networks. Furthermore, random impairments can be considered as the control scenario to determine if other impairment scenarios show different results.

In the second impairment scenario, neurons that have a higher number of synapses are more likely to be weakened or removed. The hypothesis for this type of defect is based on the significance of intracellular transport. We speculate that such impairment can be linked to pathologies where axonal transport is not functioning properly [9]. For instance, tau protein has been proposed to cause synapse loss induced by impaired axonal transport [20]. Axonal transport is required to provide precursor proteins that are essential for production and recycling of synaptic vesicles [5]. Therefore, the load on axonal transport is related to the number of functional synapses a neuron can maintain. For a neuron with few synapses, impaired axonal transport may still allow for synapses to be functional. However, if the number of synapses of the same neuron increases, the already impaired axonal transport becomes overloaded as well and thus it becomes more difficult for the neuron to perform. Hence, we propose that the synapses of neurons with large number of out-going synapses are more likely to be weakened in case of inefficient axonal transport. To implement this impairment scenario, the outdegree of all neurons in the network is calculated and sorted. Next, neurons with higher outdegree are selected and impaired first.

In the third impairment scenario, synapses of neurons that are highly active are more likely to be weakened or removed. Thus, this scenario considers the activity of neurons, not just the network topology. This contrasts the second scenario where neurons with more synapses are more likely to suffer from inefficient axonal transport. If such a neuron is not firing frequently, then even an impaired axonal transport might be capable of keeping synapses functional. Nevertheless, if such a neuron is highly active and fires frequently, then defective axonal transport will result in more ineffective synapses compared to a less active neuron which fires less frequently. In fact, synaptic fatigue has already been seen in experimental results even in healthy neurons for high-frequency stimulation [245].To this end, the third impairment scenario investigates how impairment of synapses of highly active neurons affects the activity of the whole network. To explore such synaptic weakening, the number of firings for each neuron in the unperturbed network is measured over a fixed period of time. Next, neurons are sorted based on their level of activity and those that are more active are selected first to have their synaptic weights reduced. Figure 4.2 shows an example of how each scenario affects the degree distribution of a network. The healthy/unperturbed network is constructed using mean values of 5 and 35 with equal weights. The level and percentage of impairments are 1 and 30% respectively for all impairment scenarios.

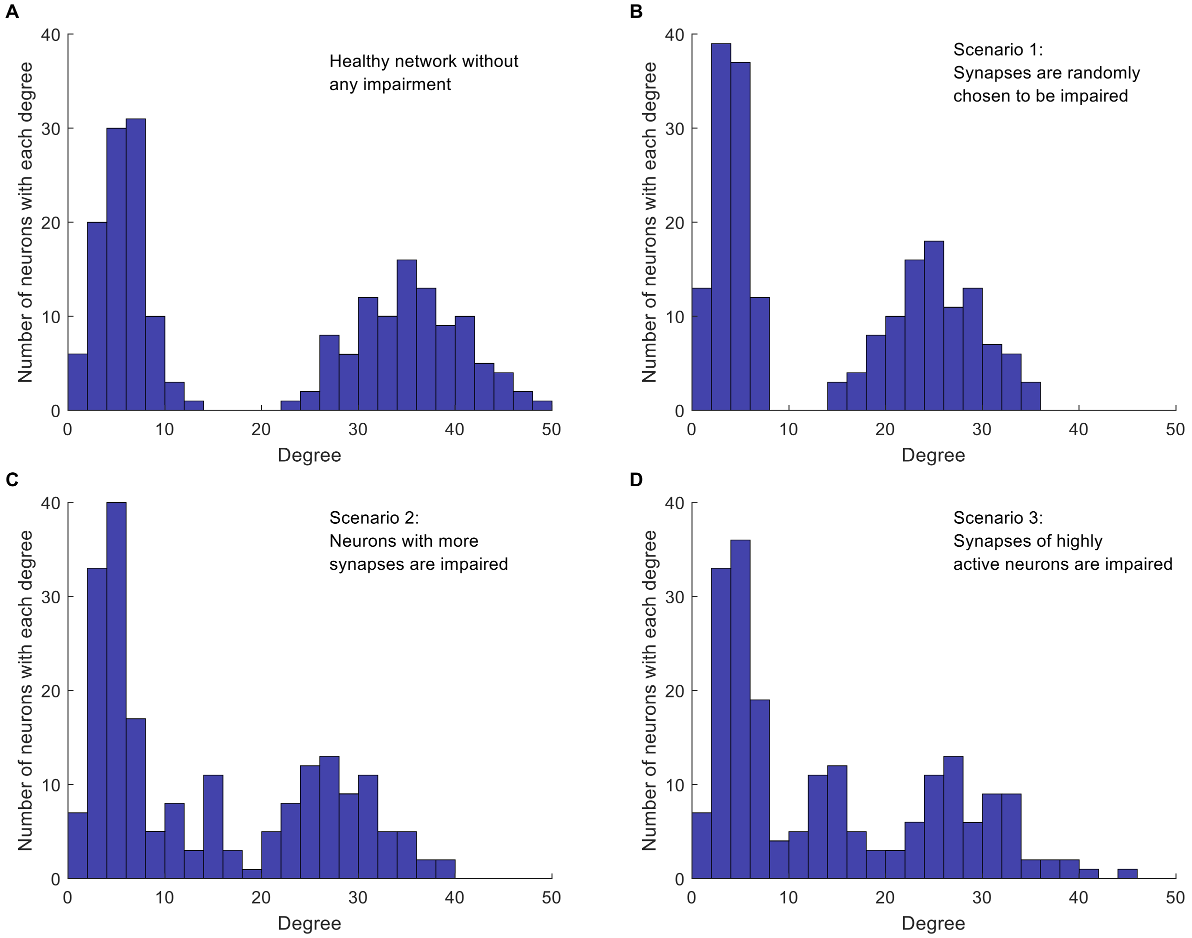

Figure 4.2- Implementation of the three cases of network impairment. Each graph shows how the original bimodal degree (summation of indegree and outdegree) distribution is affected in different impairment scenarios. Each method of impairment affects the original network degree distribution differently, leading to different network dynamics. Level of impairment and percentage of impairment are 1 and 30%, respectively, for all impairment scenarios. (A) Degree distribution in the original network, without any impairment. Network is constructed with mean values 5 and 35, with equal weights. (B) Random impairment of synapses. The shape of distribution and the general structure of the network are not affected. (C) Synaptic impairment based on the number of synapses per neuron. Neurons with more synapses are affected more. Shape of distribution and overall network structure are also affected. (D) Synaptic impairment based on neuron’s level of activity. More active neurons suffer more. Distribution and network structure are changed.

Comparing the degree distribution of the original network with the distribution in the first impairment scenario (Figure 4.2-B), we note that, as expected, the random selection affects neither the structure of the network nor the shape of the degree distribution. However, the mean degree value of each mode and consequently, the mean degree value of the whole network decrease because of the applied impairments. In the second impairment scenario (Figure 4.2-C), the mode with higher mean degree is affected more, since neurons with higher degrees are targeted first. Moreover, removing synapses from neurons with higher outdegree increases the number of neurons with lower degrees. Therefore, the height and width of the first mode increases in this scenario. In the third impairment scenario (Figure 4.2-D), neurons with higher degrees are still more likely to be affected since those with higher degrees are generally more active. However, comparing the degree distribution of the second and the third scenarios we notice that they are not equivalent. For instance, in the third impairment scenario, neurons with a degree of 45 still exist in the impaired network while such neurons are removed in the second impairment scenario. Importantly, the presence of such neurons in the third impairment scenario shows that neurons with a high degree are not necessarily more active. This is expected, because the activity of a neuron in the network depends on the dynamics of the whole network.

4.5.2 Topological Metrics

If a neuronal network is considered as a graph, each neuron is a node and the synaptic connection between each two neurons is an edge. Then, several metrics can be used to describe features of the network based on graph theory [246]. The degree of a node discussed above is the simplest of these metrics. Another metric is the characteristic path length defined as the average of path lengths (minimum number of edges between two nodes) over the whole network. Another metric is the clustering coefficient defined as the ratio of closed paths of length 2 over the total paths of length 2 in the whole network [247]. A network with a characteristic path length comparable to a random network but with a higher clustering coefficient is known to be a small world network [38]. Another metric is the rich club coefficient defined over degrees of the network [248–250]. For a chosen degree k, all of the nodes with smaller degrees than k and their corresponding edges are removed from the network. Then, the rich club coefficient is defined as the ratio of the edges in the remaining set over the number of edges in a fully connected network of the same size. The rich club coefficient is not a metric that can be defined for the whole network, since it depends on the chosen degree k, which varies between the lowest and highest degrees of nodes in networks. For each k, the size of the remaining network (club size) can be used to show how the rich club coefficient varies within a network. The network size and probability of connectivity can affect all of these metrics. Thus, the network metrics of a purely random network have been used to normalize these metrics for different network structures/topologies [250].

4.6.2 Dynamical Metrics

Unlike topological metrics, dynamical metrics depend on the activity of the neurons and their intrinsic properties, such as their excitability. Network synchronization is one of the most widely used dynamical metrics that has been used for the investigation of complex networks [251]. However, network synchronization is not an informative metric in our case because the neuron model used in this work is a type 1 neuron and networks that consist of such neurons are shown to have asynchronous behavior [241].

The first dynamical metric we use, is the presence of persistent activity. Persistent activity is a collective behavior of a network that indicates whether the network can sustain its activity for long periods of time, once the initial stimulus is removed. To quantify persistent activity, we declare that a network has persistent activity if even a single neuron has fired at least once during a time window (i.e., the last $200\ \mathrm{ms}$) at the end of a longer period (e.g., a period of $4,000\ \mathrm{ms}$).

All levels of impairment and percentages of impairment for each network need to be examined to determine the sensitivity of the persistent activity to impairments. However, this approach is computationally inefficient. A more effective approach is to estimate the boundary of persistent activity. This boundary is defined as the curve which separates networks without persistent activity (above the curve) from networks with persistent activity (below the curve)). To estimate the boundary of persistent activity, for a fixed percentage of impairment, we start from the highest level of impairment and observe the dynamics of the network. If the network activity is not persistent, then the level of impairment is decreased until a level of impairment with persistent activity is found (or the level of impairment reaches zero). Thus, for a fixed percentage of impairment, the boundary of persistent activity shows the maximum level of impairment that allows the network to have persistent activity. After the maximum level of impairment for a fixed percentage of impairment is found, the percentage of impairment is increased, and the networks are re-examined for persistent activity to find the maximum level of impairment for the new fixed percentage of impairment. This process continues until the percentage of impairment is 100%. The percentage of activity and the level of impairment are varied in increments of 10% and 0.1, respectively, to find the boundary of persistent activity.

The quality of the network activity is the second dynamical metric we introduce. We define it as the fraction of all neurons that fire at least once during a time window at the end of a longer period. Thus, this metric is useful for networks at the limit of persistent activity. Higher quality of activity means that more neurons participate in the activity of the network, during the time window used.

4.3 Simulations

All the neurons in the network are initially at rest. At time $t = 0$, they receive an external current with a random uniform distribution between 0 and 1 $\mu\mathrm{A}/\mathrm{cm}^2$. At $t = 100\ \mathrm{ms}$, the external current is removed and the dynamics of the network is observed until $t = 4000\ \mathrm{ms}$. All results presented are average values obtained from 50 realizations of the network with the same degree distribution. Error bars represent standard deviations of the measured values for these realizations.

All results are obtained using custom MATLAB codes and the numerical integration of the network is performed using the ODE45 function.

4.4 Results

First, we investigated how the topological metrics vary among the different network structures we have studied in this work. The topological metrics shown in Figure 4.3 explain why the dynamical metrics of different network structures vary.

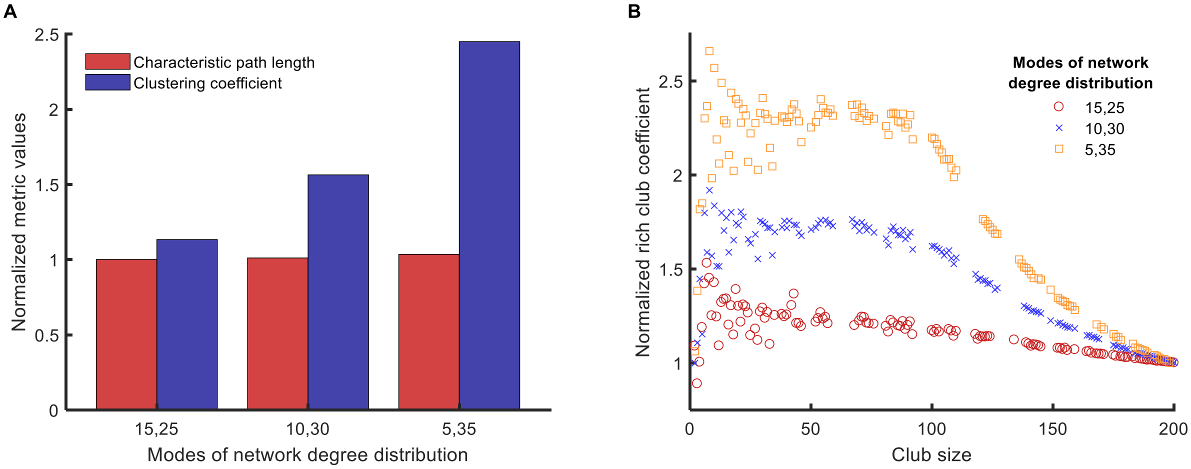

Figure 4.3- Comparison of clustering coefficients, characteristic path lengths, and rich club coefficients (the three topological metrics introduced in section 2.5) for three different network structures/topologies, each one with two modes of equal weight and mean degree values in pairs of {15,25}, {10,30} and {5,35}. The networks with distinct modes can resemble the structure of small world networks (high clustering coefficient, A) and can have rich clubs at the same time (rich club coefficient, B). the average of the two numbers is the same (20), and a network of {20,20} represents a single modal distribution with a mean of 20. The topological metrics for random networks (single mean degree value of 20) are used to normalize the same topological metrics for networks with bimodal degree distribution to avoid artifacts in results related to the size of the networks and the probability of connectivity. For example, if we denote clustering coefficient by C, normalized clustering coefficient of networks with {15,25} mean degree values is $C_{normalized} = C_{\{15,25\}} / C_{\{20\}}$.

Figure 4.3- A shows that the normalized characteristic path lengths of different networks are near 1, which means that all these networks have characteristic path lengths similar to a purely random network. However, the normalized clustering coefficients of these networks are larger than 1, and the value of this metric increases with the difference between the mean values of the bimodal distribution. Figure 4.3- B shows how the normalized rich club coefficients for different networks

change with the club size. The normalized rich club coefficient approaches 1 when the club size reaches the size of the original network, as expected for this metric. All networks with bimodal degree distribution have normalized rich club coefficients greater than 1 for many club sizes, which means that the nodes with larger degrees are connected to each other more in these networks compared to random networks. Moreover, for club sizes smaller than 100, the normalized rich club coefficients for networks with bimodal degree distributions is large and remains constant with small fluctuations. The value of this plateau region becomes higher as the distance between the modes of the degree distribution increases.

Figure 4.4 presents the raster plots for a sample case of network activity. Figure 4.4-A shows that the original network without any impairment continues its activity after the initial stimulus is removed, and therefore even though it consists of only excitatory neurons, it reaches a stable state. In addition, Figure 4.4-B shows that the same network structure loses persistent activity when its synapses are randomly impaired.

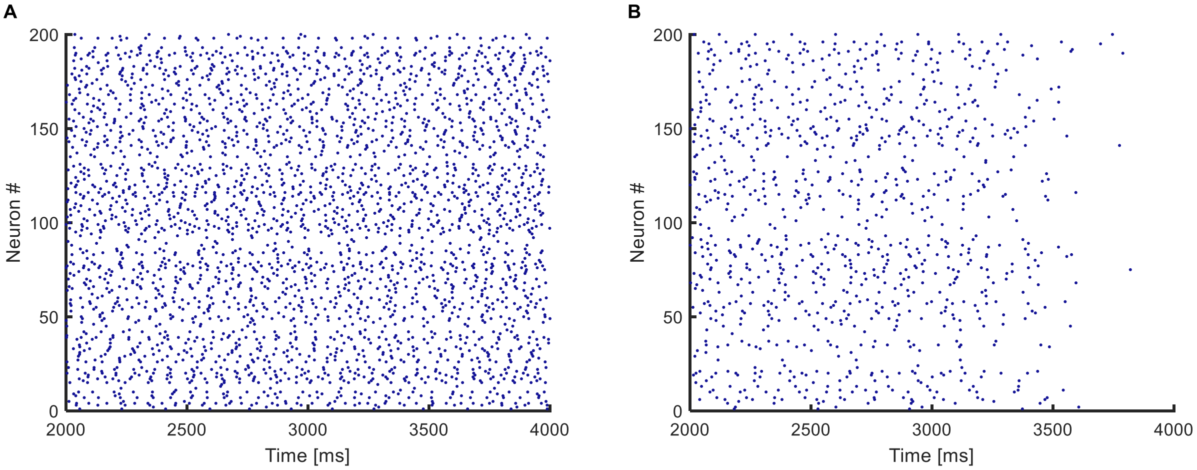

Figure 4.4- Raster plots for activity of a network with mean degree values of {10, 30}. (A) The original network, without any impairment, shows persistent activity. (B) The synapses of the original network are impaired randomly, and the network no longer shows persistent activity.

Next, we investigated how the network structure influences the dynamical metrics of the network by using four different degree distributions. The first degree distribution has only one mode with mean degree value of 20, which resembles a purely random network. The remaining three distributions have two modes with equal weights and have mean degree values in pairs of {15,25}, {10,30} and {5,35}. Figure 4.5 shows the boundary of persistent activity and the quality of activity when these networks are subjected to random impairments.

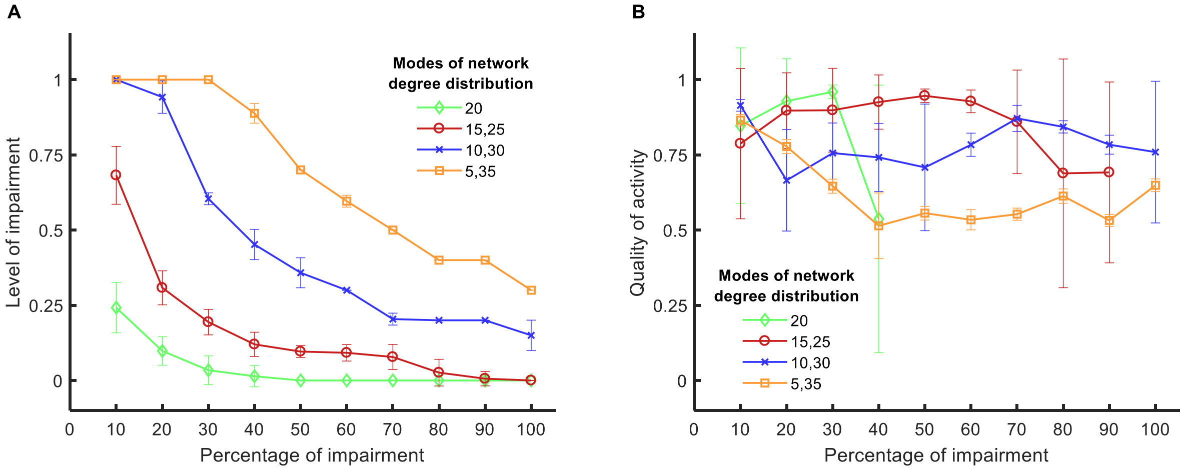

Figure 4.5- Boundary of persistent activity and quality of activity for four different network structures/topologies, when targets of impairments are chosen randomly. (A) The level of impairment (namely, the strength of an impaired synapse compared to a healthy synapse) implemented in the network, in relation to the applied percentage of impairment (namely, the percentage of synapses in the network that are weakened by the implemented level of impairment). The results show that random networks exhibit more vulnerability to synaptic loss compared to nonrandom networks. (B) The quality of activity (namely, the fraction of active neurons in the network), in relation to the percentage of applied impairment. Details for the definitions and the metrics can be found in Sections Impairment Modeling and Dynamical Metrics. Standard deviations from 50 separate realizations are shown by the error bars.

For each degree distribution, networks below the boundary have persistent activity (similar to Figure 4.4- A), and networks above the boundary have lost their persistent activity (similar to Figure 4.4- B). Figure 4.5-A clearly shows that the purely random network contains the smallest region in which the persistent activity is maintained when impairments are imposed. These results suggest that random networks are most vulnerable to random impairments, and they cannot withstand any level of impairment when more than 40% of the network is damaged. In contrast, networks with bimodal degree distributions endure impairments considerably better than random networks, as their boundary of persistent activity is well above the boundary of persistent activity for random networks.

When the difference between the two mean values of the degree distribution increases, the neurons start to form two clusters with one cluster having higher rich club coefficient than the other (Figure 4.3- B). The quality of activity can be used to determine whether neurons of only one of these clusters participate in the persistent activity of the networks. Since the weights of the two modes are equal, the number of neurons in each cluster is the same. Thus, if the quality of activity is above 0.5, then we can conclude that more than half the neurons are active (in the time window where the persistent activity was determined). Figure 4.5-B shows the quality of activity for each of the networks at their own boundary of persistent activity. Note that not all networks show persistent activity at all impairment levels up to 100%. Hence, the plots stop at lower values of impairment because the quality of activity is not defined for higher levels of impairment. For example, the quality of activity cannot be defined for impairments over 40% for networks with one mode of degree distribution (and mean degree value of 20) as shown in Figure 4.5-B. Similarly, the quality of activity cannot be defined for {15,25} networks for impairments over 90%. Note, however, that the quality of activity is over 0.5 for all cases, which shows that all networks have more than one active cluster. However, the networks with {5,35} modes, which have the largest region of persistent activity, have the poorest quality of activity compared to the rest of the networks. Therefore, the graphs in Figure 4.5 suggest that higher resistance to impairments has the downside of reducing the number of neurons that participate in the activity of the whole network. For instance, {15,25} networks have comparable quality of activity to {10,30} and {5,35} networks even though their self-sustained activity region is smaller.

Figure 4.6-A shows that the integrated persistent activity corresponding to random impairments of synapses (scenario 1) is always higher than the integrated persistent activity for the other impairment scenarios for all network structures/topologies. Moreover, the integrated persistent activity corresponding to impairments of synapses of highly active neurons (scenario 3) is always lower than the integrated persistent activity for the other scenarios, which means that the persistent activity of neuronal networks suffers the most in this scenario. However, the comparison between the scenarios of impairment in Figure 4.6-A does not hold for the quality of activity, as shown in Figure 4.6-B, except for {15,25} networks. Particularly, the quality of activity for {10,30} and {5,35} networks changes less than 4 between different impairment scenarios. All results in Figure 4.6 were analyzed in pairs by the unpaired two-tailed Student's t-test to determine if they are statistically significant (the performed t-test has 98 degrees of freedom for all the cases). For the results in Figure 4.6-A, all the comparisons showed p-values smaller than 0.001, except for the comparison between scenarios 1 and 2 for random networks which showed a p-value of 0.90. For the results in Figure 4.6-B, all the comparisons showed p-values smaller than 0.001, except for the comparison between scenarios 1 and 2 for random networks (p-value = 0.63), {15,25} networks (p-value = 0.002), {10,30} networks (p-value = 0.057) and {5,35} networks (p-value = 0.041).

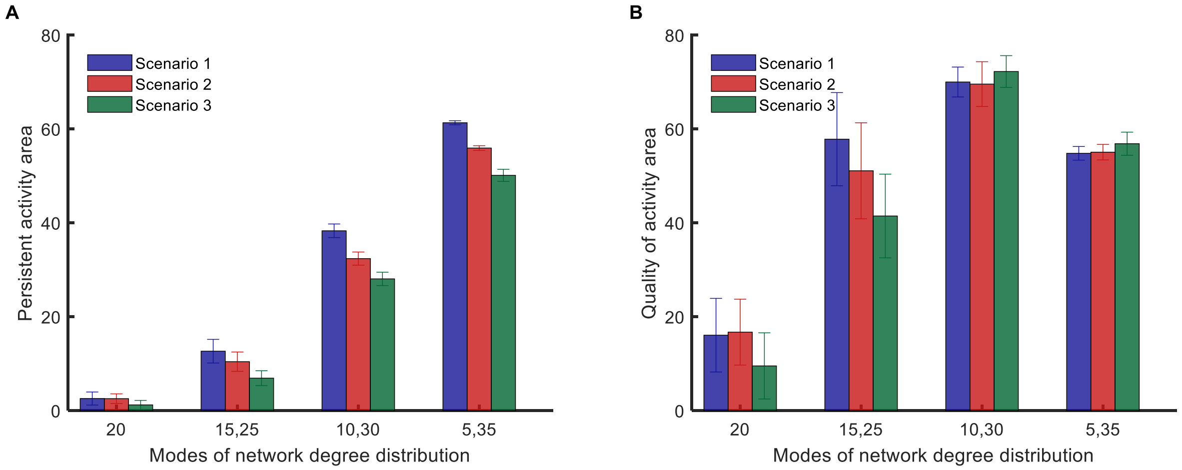

Figure 4.6- Comparison of persistent activity and quality of activity (the two dynamical metrics introduced in Section Dynamical Metrics), for different methods of impairment and network structures. In the first scenario, synapses are randomly impaired. In the second scenario, neurons with more synapses are preferably impaired. In the third scenario, synapses of most highly active neurons are preferably impaired. Details for the scenarios of impairment are provided in Section Impairment Modeling. (A) Persistent activity area suffers more from nonrandom impairment for all network structures. (B) Quality of activity area does not depend strongly on method of impairment for networks with distinct modes in their degree distribution. Standard deviations from 50 separate realizations are shown by the error bars.

All results presented above correspond to bimodal degree distributions with modes that have equal weights. However, different network structures can be constructed by keeping the mean value of one mode constant and varying the weights of each mode (sum of the weights must equal to 1). As the weight of the first mode becomes larger, the mean value of the second mode starts to increase to keep the total mean value constant. The results in Figure 4.6 show that {10,30} networks exhibit both a high level of persistent activity and a high quality of activity. Therefore, it is insightful to vary the weights and examine networks where one of the mean values is kept at 10 while the other mean value is fixed by the weights. Figure 4.7 shows how the weights affect the dynamical metrics of different networks. When the weights are equal to 0.5, the results are the same as {10,30} networks.

Figure 4.7-A shows that the area of persistent activity region increases monotonically when the weight of the first mode increases. Similar to the results shown in Figure 4.6-A, impairment scenario 1 inflicts less damage to the persistent activity compared to the other two scenarios. In

addition, scenario 3 has the most invasive effect. For low weights of the first mode, the integrated persistent activity for all impairment scenarios is similar - the lines corresponding to scenarios 1 and 2 are close to each other. However, they start to separate as the weight of the first mode increases. In contrast, the integrated persistent activity for scenarios 2 and 3 are separated for low weight of the first mode, but the distance between them decreases slightly as the weight increases.

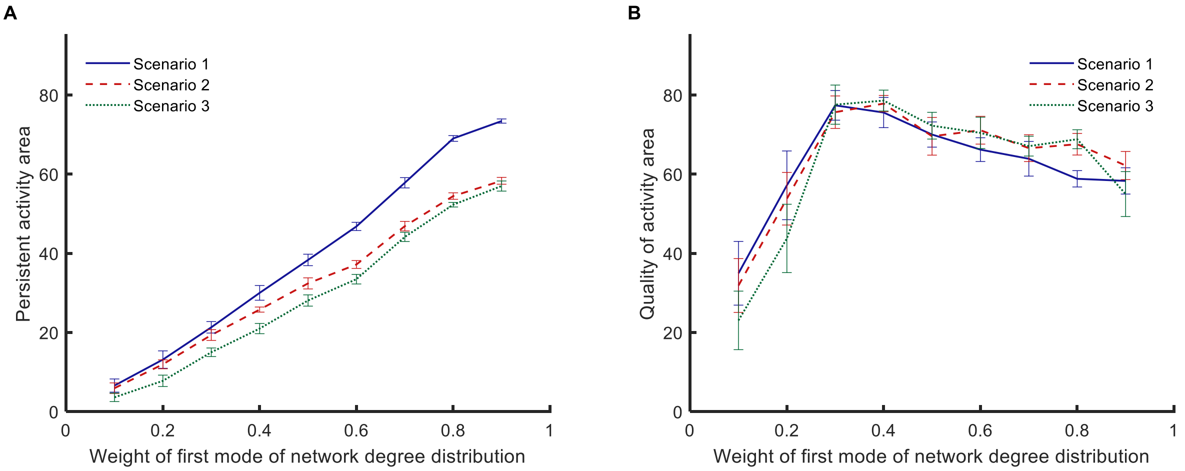

Figure 4.7- Comparison of persistent activity and quality of activity (the two dynamical metrics introduced in Section Dynamical Metrics), when the weights of degree distribution mode vary. In the first scenario, synapses are randomly impaired. In the second scenario, neurons with more synapses are preferably impaired. In the third scenario, synapses of most highly active neurons are preferably impaired. Details for the scenarios of impairment are provided in Section Impairment Modeling. (A) persistent activity area increases monotonically with weight of first mode of network degree distribution. (B) Quality of activity area initially increases with weight of first mode of network degree distribution, but it decreases with further increase of the weight. Standard deviations from 50 separate realizations are shown by the error bars.

Figure 4.7-B shows that the quality of activity changes nonlinearly with the weight of the first mode. Lines corresponding to different impairment scenarios cross each other several times. Therefore, unlike the persistent activity shown in Figure 4.7-A, a general statement cannot be made about how different impairment scenarios affect the quality of activity. For low weights of the first mode, the quality of activity is low because the network has low integrated persistent activity. The quality of activity improves as the integrated persistent activity increases. However, further increasing the weight of the first mode lowers the quality of activity even though the integrated persistent activity is still improving.

4.5 Discussion

Our results show the vulnerability of random networks to synaptic loss, compared to networks with bimodal degree distribution. The robustness of networks with bimodal degree distribution can be attributed to their topological metrics, and especially the presence of rich clubs. Our results also show that targeted synaptic loss, which may resemble different pathological or biological conditions, affects the dynamics of networks more, compared to random impairments. Therefore, monitoring the activity of networks has the potential to reveal underlying pathological or biological conditions earlier than symptoms detection methods.

We have used a model based on the Hodgkin-Huxley formalism that has been previously used successfully to simulate dynamics of neuronal networks [241]. One advantage of this model is its capability to be switched to a type 2 neuron with addition of a slow potassium current, which is ultimately responsible for the shift in neural excitability mediated by ACh [241]. Ca^{2+} dynamics have been shown to be related with persistent activity of neurons[252,253]. However, even though Ca^{2+} dynamics are not captured in this model, previous research has shown that persistent activity can be observed on the network level even when simple integrate-and-fire neurons have been used [48]. Like many other network simulations, details of simulations such as the values of dynamical metrics and boundary of persistent activity will change, because the elements of the network (neurons) will change. However, our main goal is to examine whether the network topology and pattern (or scenario) of impairment has significant counter-intuitive (or non-intuitive) effects on the network function. Hence, it is the relative robustness that we are mostly interested in; relative between different impairment scenarios or network topologies. Therefore, we believe that using other models such as the ones that include Ca^{2+} dynamics will not change the conclusions of this work about the influence of network structure on the activity of the network.

As a first step, we used the degree distribution of networks to construct networks with different topological metrics. While completely random connectivity topologies are usually the first choice made when studying the dynamics of neuronal networks, in vitro [214,215], in vivo [254] and even in silico [255] studies have revealed that neurons form structures/topologies which are correlated to their functionality. One simple way to explain the structure/topology of a network is through its degree distribution [247]. We built different network structures/topologies by combining Poisson distributions (the degree distribution of a random network) with two different mean values. This method of network generation creates networks with bimodal degree distributions, which consist of rich clubs with high clustering coefficients while their characteristic path lengths are almost equal to that of random networks. Networks with high clustering coefficients and path lengths comparable to random networks are known to have features of small world networks [38]. The characteristic path lengths of all the networks we studied are close to the characteristic path lengths of random networks. Therefore, networks with higher clustering coefficients are more similar to small world networks. Our results show that the clustering coefficient increases as the distance between modes of degree distribution increases (Figure 4.3). At the same time, the increased distance between modes of degree distribution leads to an increase in the persistent activity area. Hence, our results show that networks that have properties of small world networks are more robust. We define robustness as the ability of neuronal networks to maintain their persistent activity when exposed to impairments. Small world networks can tolerate impairments better than random networks since the connections between neurons in small world networks have more closed loops to sustain the activity of the whole network. Other studies [48,236], have also reported that the small world networks are more likely to have persistent activity. However, those studies are not parallel to our study since they do not consider impairment in synaptic connections. Moreover, their networks are constructed following the conventional method of constructing small world networks, so they do not consist of distinct rich clubs. However, features of small world networks are likely not enough to explain the higher robustness of networks with bimodal degree distribution because this topological metric does not describe the variation in the quality of activity for different networks.

The rich club coefficients can be used to describe both the persistent activity and the quality of activity for networks with bimodal degree distribution. When networks start to form rich clubs, hubs of highly connected neurons are created, which are interconnected to each other also. During impairments, these hubs can preserve the activity of the whole network. Having a core of highly connected neurons enables such network structures/topologies to maintain self-sustained activity when they experience loss of synapses. Moreover, for such networks, removal of connections between members of rich clubs and neurons outside the rich clubs does not influence the persistent activity significantly because neurons outside the rich clubs are not responsible for maintaining the persistent activity. Neurons in the rich club are also connected to the neurons outside the rich clubs. Hence, they distribute the activity to the whole network. This is the reason why high rich club coefficients coincide with high robustness in our results (Figure 4.3-B and Figure 4.6-A).

Our results suggest that there is a compromise between quality of activity and persistent activity of neuronal networks. Unlike the integrated persistent activity, the integrated quality of activity shows a nonlinear behavior when the distance between the modes of the degree distribution increases (Figure 4.6- B). Such behavior is more obvious when the weights of modes are changed (Figure 4.7-B). Initially, the quality of activity is low when the distance between the modes of degree distribution is small, because the integrated persistent activity is low. Such networks resemble random networks rather than networks with bimodal degree distributions.

When the distance between the modes of degree distribution increases, the integrated quality of activity and the integrated persistent activity both increase. In these networks, rich clubs sustain the activity of the whole network and since they are also connected to neurons outside rich clubs, they are able to keep neurons outside rich clubs active as well. However, as the distance between the modes of degree distribution increases, the robustness of networks continues to increase, whereas the quality of activity starts to decrease. At the same time, neurons outside rich clubs make few connections, either with each other or with members of rich clubs. In fact, the sharp transition in the normalized rich club coefficients of {5,35} networks (Figure 4.3-B) indicates that the core has weak connection with neurons outside the core. Therefore, neurons outside of rich clubs lose their activity even when a few of their synapses are removed. In this situation, rich clubs fail to act as a driving force for the rest of the network. Hence, the quality of activity for such networks is low even though highly connected hubs that form rich clubs can maintain the activity of the whole network.

The interplay between persistent activity and quality of activity can be considered as an optimization problem. To achieve higher robustness, our results suggest that the number of connections between neurons in rich clubs must increase. However, if the size of the neuronal network and its synapses are constrained to remain the same, then more connections between neurons in rich clubs mean fewer connections between neurons outside rich clubs. Therefore, even though such networks can endure impairments very well and can maintain persistent activity, only few neurons participate in the activity of the whole network and the quality of activity low. From this perspective, the network structure/topology can be viewed as a multi-objective optimization problem where the fitness of a network can be determined by both persistent and quality of activity, and the number of neurons and synapses are the constraints. Even though the network optimization can be regarded as an abstract mathematical problem, emergence of certain structures/topologies in networks can also be considered as evolution of these networks in reality [256]. However, a random network can evolve into different network structures/topologies to serve different tasks [257]. For example, Sporns and colleagues [258] have shown that based on differently imposed criteria, their graph selection algorithm leads to networks with different structures and capabilities. Although we have not solved such an optimization problem in the present work, our results show that networks with bimodal distributions have good fitness. Therefore, if a neuronal network requires high robustness to perform its tasks, a network with bimodal degree distribution can be the plausible solution. More precisely, networks with bimodal degree distributions with a moderate distance between distinct modes have high robustness and high quality of activity at the same time. Moreover, our results suggest that random networks are the least preferable neuronal network structure/topology for the metrics we have used, since such networks have neither high persistent activity nor high quality of activity.

In the present study, we have explored also how selective impairment of neurons can affect the dynamics of neuronal networks by investigating targeted weakening of synapses. We have explored how three different scenarios of synapses loss can affect the dynamical features of neuronal networks.

In the first impairment scenario, synapses are impaired randomly leading to the least impact on the persistent activity for all the network structures/topologies (Figure 4.6-A and Figure 4.7-A). The importance of all neurons and their synapses in the activity of the whole network is not the same, especially for the neuronal networks that do not have random connectivity. However, the reason why random impairments are the least damaging method is not the fact that synapses of more important neurons are not selected. Essentially, the likelihood of damaging such neurons is the same as any other neuron since the method of impairment is random. In fact, highly damaging effects of impairing critical neurons are compensated by impairing synapses of neurons that are less important to the activity of the whole network. Therefore, random impairments lead to overall less damaging effects compared to other impairment scenarios we have described in our study.

In the second impairment scenario, synapses of neurons with larger number of synapses are more likely to be impaired leading to more damaging effects to the persistent activity of neuronal networks than random impairments of neurons, for all network structures/topologies. The number of synapses a neuron has is a topological feature of a neuronal network. Therefore, if the wiring between neurons in a network is known, this wiring can be used to suggest where the impairments will occur in case of damaged axonal transport. Van den Heuvel and Sporns [213] have performed a similar analysis by observing the efficacy of neuronal networks. They have shown that targeted impairments that remove the links between members of rich clubs in the network induce a more dramatic change on the efficacy of neuronal networks than random impairments. The mechanism used for the targeted impairments in that study is not mentioned, but such impairments resemble our second scenario. Complimentary to our speculation about the links between the hub location and axonal transport deficiencies, experimental results have also shown that the hub locations correlate Aβ deposition in Alzheimer's disease [259]. Hence, hub locations can be monitored to detect abnormalities in neuronal networks earlier and with more efficiency.

In the third impairment scenario, synapses of highly active neurons are more likely to be impaired leading to the most destructive effect on the persistent activity of all neuronal networks when compared to the other impairment scenarios. The structure/topology of neuronal networks plays an important role, but the dynamics is important also. The dynamic map of activity in neuronal networks can also provide critical information about regions of interest. Other research has suggested also that regions of high activity and metabolism can be associated with cellular mechanism involved in Alzheimer’s disease [259]. Moreover, it has been proposed that, highly active neurons in the brain can be especially vulnerable to intrinsic oxidative stress, thus being susceptible to functional decline during normal aging or neurodegenerative diseases [260]. Therefore, monitoring the activity of neuronal networks can reveal the critical regions and neurons that influence the most the activity of the whole network. Consequently, we speculate that losses or changes in the activity of such regions can be used as an early sign of deficiencies in neuronal networks.

Altogether, we speculate that the transition in the network structure can be used as an indicator of neurodegenerative disease as the robustness of neuronal networks decreases when they lose their structured topology. Such transition of the brain network towards randomness has already been shown even in normal aging in several studies [261]. Therefore, monitoring alteration in the brain network structure has the potential to be used as an early diagnostic method in neurodegenerative diseases. Moreover, our results show that even though the topological metrics and maps of neuronal networks can provide valuable information, they should be accompanied by the dynamical metrics and maps of neuronal networks that are even more informative. Our results illustrate that such an argument is even stronger when neuronal networks are not randomly connected, and are instead topologically defined.

Chapter 5

Probabilistic Analysis of Bifurcations in Stochastic Nonlinear Dynamical Systems Using the Fokker-Planck Equation

5.1 Introduction

Dynamical systems have long been used to describe the behavior of physical systems. However, the analysis of dynamical systems is usually conducted in the absence of noise. While absence of noise can simplify the analysis of dynamical systems, such mathematical idealism is not physically realistic. Whether the source of the noise is from the environment, the nature of the physical system, or merely from observation, noise can dramatically change the behavior of dynamical systems [262,263]. Hence, stochasticity cannot be disregarded especially for nonlinear dynamical systems that their bifurcation leads to critical transitions with dramatic consequences [264].

Stochasticity is commonly encountered in biological systems. Hence, the mathematical models describing biological systems are subjected to noise. The noise is important in biological systems especially when the dynamical processes take place in smaller scales. Moreover, cell-to-cell variations is a common source of stochasticity in biological system such as cellular networks [265,266]. In this chapter, we develop a tool to analyze stochastic dynamical systems that will be used later in chapter 6 in which firing rate models [267] of neural networks are studied. Such probabilistic tool to study stochastic dynamical systems is necessary because noise can influence dynamics of neural systems greatly. For instance, noise can describe [267] spontaneous switching between states of neural networks in experimental data [268].

A single time evolution of stochastic dynamical systems is not representative of the system. However, the Monte Carlo simulation can estimate the probability density function (PDF) of stochastic nonlinear dynamical systems. However, even though The Monte Carlo simulation is easy to implement, numerous realizations are necessary to obtain PDFs from the Monte Carlo method since the initial conditions for the Monte Carlo simulations must span the physical space adequately. Such cumbersome simulations must be conducted each time the bifurcation parameter is changed because a previous Monte Carlo simulation cannot simply be the initial condition for the next simulation during the continuation of bifurcation parameter. Alternatively, the time evolution of PDFs of stochastic differential equations with white noise excitation can be obtained from the Fokker-Planck equation (FPE) [269]. The stationary solution of the FPE, provided it exists, can be used to construct probabilistic bifurcation diagrams of stochastic nonlinear dynamical systems. Such probabilistic bifurcation diagram demonstrates the probability of finding the dynamical system in space at each point on the bifurcation diagram. The probabilistic bifurcation diagram converges to the deterministic bifurcation diagram in the limit of noise going to zero. However, finding the closed-form analytical solution of the FPE is not trivial especially for higher-dimensional dynamical systems. Therefore, numerical solution of the PFE are often sought [270]. For example, finite element and finite difference methods have been used previously to obtain numerical solution of the FPE without showing any particular superiority for any of the methods [271,272]. Recently, more modern numerical methods have been utilized to address the curse of dimensionality associated with traditional numerical methods. For instance, meshless methods have been used to solve the FPE for four-dimensional dynamical systems [273]. Moreover, stationary and transient solution of the FPE for higher-dimensional dynamical has been obtained by utilizing tensor decomposition method [274–276]. Such methods highly relay on the validity of separating the dimensions in the FPE [277]. More recently, statistical methods have been used to approximate the solution of high-dimensional FPE [278]. Interestingly, the mentioned numerical studies of the FPE are performed for the case of additive noise and their authors have not included case studies with multiplicative noise. Moreover, none of the previous studies investigate the bifurcation diagrams of the systems they are presenting.

In this research, we find the stationary solution of the FPE for nonlinear dynamical systems in the presence of additive and multiplicative noise to construct their probabilistic bifurcation diagrams. We use the finite volume method to discretize the FPE to establish the numerical scheme. First, we compare our numerical solution with the analytical results for a one-dimensional system with subcritical pitchfork bifurcation. Then, we study the FitzHugh-Nagumo model as a two-dimensional system that exhibits limit cycle oscillations. Next, we study the three-dimensional Lorenz model as a system that displays chaotic behavior. Finally, we conclude by investigating dynamics of coupled Brusselators.

5.2 Numerical Solution

Consider a system of Ito stochastic differential equations for N variables [269]:

$$d\mathbf{x} = \mathbf{f}(\mathbf{x},t)dt + \mathbf{g}(\mathbf{x},t)d\mathbf{W}(t) \tag{4.1}$$

where $\mathbf{x} \in \mathbb{R}^N$ is the state vector of the general nonlinear dynamical system, $\mathbf{f}(\mathbf{x},t)$ is the drift vector describing the deterministic nonlinear dynamical system, $\mathbf{g} \in \mathbb{R}^{N \times M}$ is the diffusion matrix and $d\mathbf{W}(t) \in \mathbb{R}^M$ is the standard Weiner process. Then, the Fokker-Planck equation (FPE) is formed as [269]:

$$\frac{\partial p}{\partial t}(\mathbf{x},t) = -\sum_i \frac{\partial}{\partial_i}\left[f_i(\mathbf{x},t)\,p(\mathbf{x},t)\right] + \frac{1}{2}\sum_{i,j}\frac{\partial^2}{\partial_i \partial_j}\left[\left(\mathbf{g}(\mathbf{x},t)\mathbf{g}(\mathbf{x},t)^{\mathrm{T}}\right)_{i,j} p(\mathbf{x},t)\right], \tag{4.2}$$

where $p(\mathbf{x},t)$ is the time evolution of probability density function (PDF) associated with the stochastic system of equations in (4.1). Equation (4.2) can be written as a function of probability flux $\mathbf{J}(\mathbf{x},t)$:

$$\frac{\partial p}{\partial t}(\mathbf{x},t) = -\nabla.\mathbf{J}(\mathbf{x},t), \tag{4.3}$$

where each element of vector $\mathbf{J}(\mathbf{x},t)$ can be written as:

$$J_i(\mathbf{x},t) = f_i(\mathbf{x},t)\,p(\mathbf{x},t) - \frac{1}{2}\sum_j \frac{\partial}{\partial_j}\left[\left(\mathbf{g}(\mathbf{x})\mathbf{g}(\mathbf{x})^{\mathrm{T}}\right)_{i,j} p(\mathbf{x},t)\right]. \tag{4.4}$$

Next, we apply the finite volume method on Eq. (4.3) by integrating over a N-dimensional volume of Ω_k:

$$\int_{\Omega_k} \frac{\partial p}{\partial t}(\mathbf{x},t)dv = -\int_{\Omega_k} \nabla.\mathbf{J}(\mathbf{x},t)dv \Rightarrow V_k \frac{\partial \overline{p}}{\partial t}(\mathbf{x},t) = -\oint_{\partial\Omega_k} \mathbf{J}(\mathbf{x},t).\mathbf{n}dS, \tag{4.5}$$

where V_k is the volume, $\overline{p}$ is the volume average of PDF and the divergence theorem is applied on the flux terms. For the stationary solution we have $\frac{\partial \overline{p}}{\partial t}(\mathbf{x},t) = 0$, which leads to:

$$\oint_{\partial\Omega_k} \mathbf{J}(\mathbf{x},t).\mathbf{n}dS = 0. \tag{4.6}$$

Equation (4.6) shows that the finite volume method allows conservation of probability flux in each stencil in the domain. We have used a uniform structured grid to discretize the domain for all our cases. The fluxes are evaluated at the center of edges and cell average values are used to evaluate fluxes with second order accuracy. We have also assumed reflective boundary condition over the domain meaning the flux of probability is zero on the boundaries of the domain. Hence, assembling the discretized equations leads to a system of linear equations:

$$\mathbf{A}\bar{\mathbf{p}} = \mathbf{0}, \tag{4.7}$$

where $\mathbf{A}$ is the matrix of coefficients obtained from discretization of the domain, and $\bar{\mathbf{p}}$ (we denote $\bar{\mathbf{p}}$ as $\mathbf{p}$ for simplicity from now) is the vector of cell average PDF. Equation (4.7) has the trivial solution of $\mathbf{p} = \mathbf{0}$. However, such solution is not acceptable since $\mathbf{p}$ must satisfy the constraint for PDF as:

$$\int_{-\infty}^{+\infty} p(x)dx = 1. \tag{4.8}$$

Applying the constraint of Eq. (4.8) will not be necessary if transient form of Eq. (4.5) is solved with proper initial condition such as $p(\mathbf{x}_0, 0) = \delta(\mathbf{x} - \mathbf{x}_0)$ that already satisfies Eq. (4.8) at $t = 0$. Nonetheless, there are several methods to incorporate constraint in Eq. (4.8) into linear system of equations in (4.7). In the first approach, a vector $\mathbf{b}$ can be constructed such that $\mathbf{b}^{\mathrm{T}}\mathbf{p} = 1$. Then, an additional row is added to bottom of matrix $\mathbf{A}$ with elements of $\mathbf{b}^{\mathrm{T}}$ and the last row of right hand side in Eq. (4.7) will now be equal to 1. Therefore, matrix $\mathbf{A}$ is no longer a square matrix and the new linear system of equations must be solved by least-square methods. Alternatively, Eq. (4.7) can be solved with the constraint of Eq. (4.8) using optimization techniques and packages such as CVX [279] or CPLEX [280]. Also, Eq. (4.7) can be solved using an iterative method such as GMRES with a nonzero initial guess that can even satisfies Eq. (4.8) to obtain a nonzero solution. The final solution of the iterative solver will not necessarily satisfy Eq. (4.8) but it can be scaled so that the probability normalization can still hold. Such scaling is allowed because Eq. (4.7) is linear and the right-hand side is zero. We have applied the later approach in this work because it's the fastest compared to the other methods we have explained. We have used SciPy [281] library of iterative solvers for sparse systems of equations to obtain the stationary solution of the FPE.

5.3 Results and Discussion

In this section we present the probabilistic bifurcation diagrams for stochastic nonlinear dynamical systems of different dimension in the presence of additive and multiplicative noise and discuss how noise affects the dynamics of the systems.

5.1.3 Subcritical Pitchfork Bifurcation

We start with a one-dimensional nonlinear dynamical system for which we can find the analytic stationary solution of the FPE. Consider the following stochastic nonlinear dynamical system:

$$dx = (\mu x + x^3 - x^5)dt + g(x,t)dW, \tag{4.9}$$

where μ is the bifurcation parameter. When there is no noise $(g(x,t)=0)$, Eq. (4.9) shows the normal of a dynamical system with subcritical pitchfork bifurcation. First, we consider the stochastic differential equation with additive noise where $g(x,t)=\sigma$ in which σ is a constant determining the strength of the noise. Figure 5.1-(A) shows the time evolution of the stochastic process for $\mu=-0.1$ and $\sigma=0.5$. Clearly, the time evolution shows the dynamical systems oscillates between two extremums $(|x|=1)$ and also spend some short time in the between the extremums near $x=0$. However, such short simulation is not informative while the FPE can demonstrate what is the probability of being at each state.

Using Eq. (4.3) and (4.4), the stationary FPE associated with Eq. (4.9) with additive noise is:

$$-\frac{d}{dx}J(x) = -\frac{d}{dx}\left[(\mu x + x^3 - x^5)p(x) - \frac{1}{2}\sigma^2\frac{dp}{dx}(x)\right] = 0. \tag{4.10}$$

Integrating Eq. (4.10) once leads to:

$$J(x) = (\mu x + x^3 - x^5)\, p(x) - \frac{1}{2}\sigma^2 \frac{dp}{dx}(x) = \text{Constant}. \tag{4.11}$$

Assuming reflective boundary conditions, the constant in Eq. (4.11) becomes zero. Then, Eq. (4.11) can be integrated once more to find the stationary solution of the FPE associated with Eq. (4.9):

$$p(x) = \mathcal{C} \exp\left(\frac{2}{\sigma^2}\left(\frac{\mu}{2}x^2 + \frac{1}{4}x^4 - \frac{1}{6}x^6\right)\right), \tag{4.12}$$

where $\mathcal{C}$ is a normalization constant to make sure the constraint of Eq. (4.8) is satisfied. The PDF obtained from Eq. (4.12) as well as the numerical stationary solution of the FPE and the Monte Carlo simulation is depicted in Figure 5.1-(B). First, we can see that the numerical and analytical solutions of the FPE match well. Moreover, the PDF in Figure 5.1-(B) shows that the likelihood of finding the dynamical system is the same for both extremums at $x = \pm 1$. Such conclusion could not be simply reached from the time evolution of the system, which demonstrate why the probabilistic approach to stochastic differential equations is powerful and even necessary.

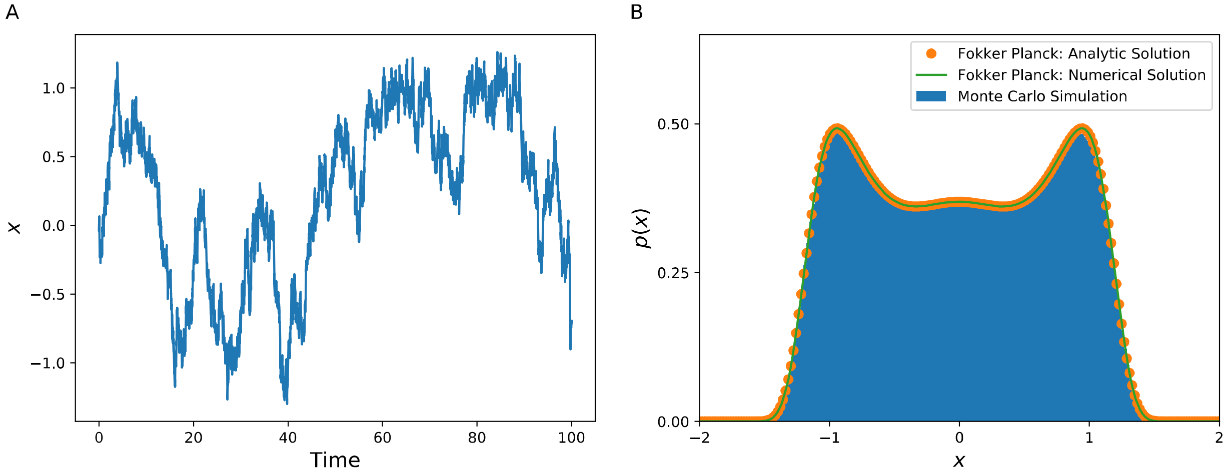

Figure 5.1- (A) time evolution of stochastic system of Eq. c. The system oscillates between extremums of $x = \pm 1$ and lingers in each one of them as well as a state between the two extremums at $x = 0$. (B) The PDF for system of Eq. (4.9) obtained from all three methods match well. The PDF shows that the system the likelihood of finding the system is equal and largest at the two extremums.

The bifurcation diagram of the dynamical system in Eq. (4.9) in the presence of additive noise can be constructed by varying μ in Eq. (4.12) or the numerical solution of the FPE must be found for each value of μ. The results for both methods is shown in Figure 5.2. The results of the numerical method match well with the results obtained from the analytic solution. The solid lines in Figure 5.2 corresponds to the deterministic bifurcation diagrams, which are obtained using MATCONT toolbox [282]. The black lines correspond to stable branches and white lines to unstable branches of the deterministic bifurcation diagram (the same color code for stable and unstable branches is used in the rest of the chapter).

For $\mu < -0.25$ there is only a single deterministic stable branch at $x = 0$. In the presence of additive noise, the PDF distribution is centered around this branch and becomes wider as the bifurcation parameter approaches $\mu = 0$ where the deterministic bifurcation occurs. However, in the presence of additive noise, the dynamical system visits the large amplitude branches before the deterministic bifurcation occurs as the probability of being near these branches is nonzero before $\mu = 0$. Such phenomenon occurs because the noise is strong enough to allow the dynamical system switch between the equilibria in the region of bistability in the neighborhood of $\mu = 0$. Hence, the effects of noise can have dramatic consequences in the system studied here, as the blow-up occur earlier than what the deterministic bifurcation predicts. Therefore, knowing the probability of finding the system at each point on the bifurcation diagram is invaluable.

For $\mu > 0$, the probability of finding the stochastic dynamical system around now unstable branch of $x = 0$ is nonzero. However, this probability approaches zero as μ becomes larger. For large μ, the probability of finding the system is largest around the deterministic large amplitude stable branches.

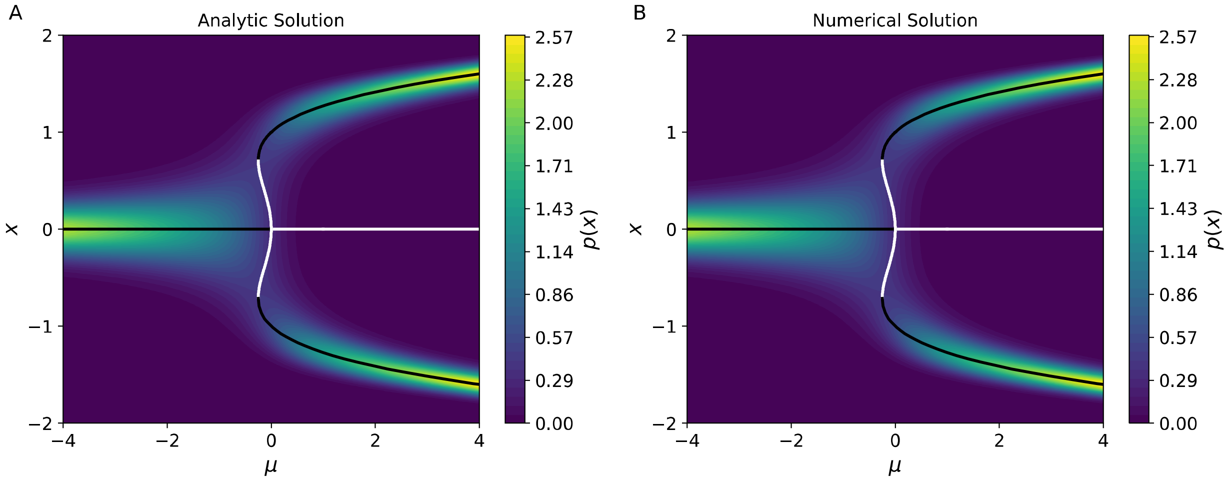

Figure 5.2- Analytic and numerical solution of the FPE for the dynamical system of Eq. (4.9) in the presence of additive noise $(\sigma = 0.5)$ match well. The black lines show the stable branches and the white lines correspond to unstable branches of the deterministic bifurcation diagram

For each value of μ in Figure 5.2, Eq. (4.8) still holds. Therefore, for example, the maximum value of $p(x)$ is smaller for $\mu = -2$ compared to the maximum value of $p(x)$ at $\mu = 2$ because the PDF distribution is wider when $\mu = -2$ compared to when $\mu = 2$. Such format of plotting where Eq. (4.8) holds for every μ can jeopardize interpretation of probabilistic bifurcation diagram. For instance, consider the extreme case in which the distribution for a certain bifurcation parameter is the delta function for which Eq. (4.8) clearly holds. However, no other distribution will be visible on the bifurcation diagram because the maximum value of the delta function dominates the colorbar of the graph. To avoid such issues and facilitate interpretation of results, we can normalize the PDF with its maximum at every bifurcation parameter. Therefore, the values of the colorbars in all graphs will be the same and vary between 0 and 1 for all bifurcation parameters. Also, the colorbars from all figures can be removed to make the representation of the results more concise.

Figure 5.3-(A) shows the same results as the one plotted in Figure 5.2 with the new format. The new representation allows tracking where the probability is the highest for each value of the

bifurcation parameter. Hence, we can deduce from Figure 5.3-(A) the bifurcation occurs in the stochastic dynamical system when the stable branches with large amplitude appear at $\mu = -0.25$. Next, we increase the strength of the additive noise as seen in Figure 5.3-(B). Increasing the noise does not change the trend of the probabilistic bifurcation diagram significantly and only widens the distribution.

Next, we introduce multiplicative noise into Eq. (4.9) by setting $g(x) = \sigma\left(1 + x^2\right)$. The analytic stationary solution of the FPE for such noise can be find similar to what we did for Eq. (4.12) as:

$$p(x) = \mathcal{C} \frac{\exp\left(-\frac{x^4 + x^2 + \mu - 2}{\sigma^2\left(x^2 + 1\right)}\right)}{\left(x^2 + 1\right)^{\frac{2\sigma^2 - 3}{\sigma^2}}}, \tag{4.13}$$

where $\mathcal{C}$ is again a normalization factor. Comparing Eq. (4.13) and (4.12), clearly shows that the multiplicative noise changes the PDF completely. The results for the probabilistic bifurcation diagram of Eq. (4.13) is shown in Figure 5.3-(C) and (D). The actual boundaries of the domain that the FPE is solved in is larger than the ones shown in Figure 5.3-(C) and (D) to ensure that the probability flux approaches zero on the boundaries. However, the bounds shown in Figure 5.3 are kept the same to allow easy comparison of results between different scenarios. Figure 5.3-(C) shows that for small noise, the bifurcation for the dynamical system with additive noise occurs for a larger μ compared to the system with just additive noise (Figure 5.3-(A)). Moreover, the probability around the for the multiplicative noise is no longer centered around the stable branches for large μ. Such deviation from deterministic bifurcation diagram is more evident for larger noise values as shown in Figure 5.3-(D). Figure 5.3-(D) shows that the bifurcation occurs for much larger values of μ compared with deterministic dynamical system. Moreover, examining Figure 5.3-(D) shows the bifurcation type has also changes from subcritical to supercritical. Hence, Figure 5.3-(D) shows the importance of the probabilistic approach for bifurcation of stochastic dynamical systems especially when the noise is multiplicative.

To emphasize the importance of multiplicative noise, we considered another case in which the multiplicative noise has the form of $g(x)=\sigma\left(1+x^{-2}\right)$. for which the analytic solution for the stationary FPE can be found as:

$$p(x)=\mathcal{C}\frac{x^4}{\left(x^2+1\right)^{\frac{2\sigma^2+2\mu-7}{\sigma^2}}}\exp\left(-\frac{2x^8-7x^6+\left(21-6\mu\right)x^4+\left(30-6\mu\right)x^2+6\mu}{6\sigma^2\left(x^2+1\right)}\right), \qquad (4.14)$$

where $\mathcal{C}$ is the normalization factor. Comparing Eq. (4.12)-(4.14), we can see the impact of multiplicate noise once more. The results of probabilistic bifurcation diagram of Eqs (4.14) are shown in Figure 5.3-(E) and (F). For both strength of noise, the probabilistic bifurcation diagram is almost similar. For large values of μ, the probabilistic bifurcation diagram follows the deterministic bifurcation diagram. However, for $\mu<-0.25$ the probabilistic bifurcation diagram does not follow the stable branch of the deterministic bifurcation diagram at $x=0$. Even though the system is attract to the fixed point at $x=0$, because the noise is proportional to x^{-2}, the noise becomes larger near the fixed point and is repelled from it. Therefore, a bifurcation does not happen in this case as the behavior of the system changes smoothly and continuously as the bifurcation parameter changes. Hence, introducing such multiplicative noise actually annihilate the bifurcation point.

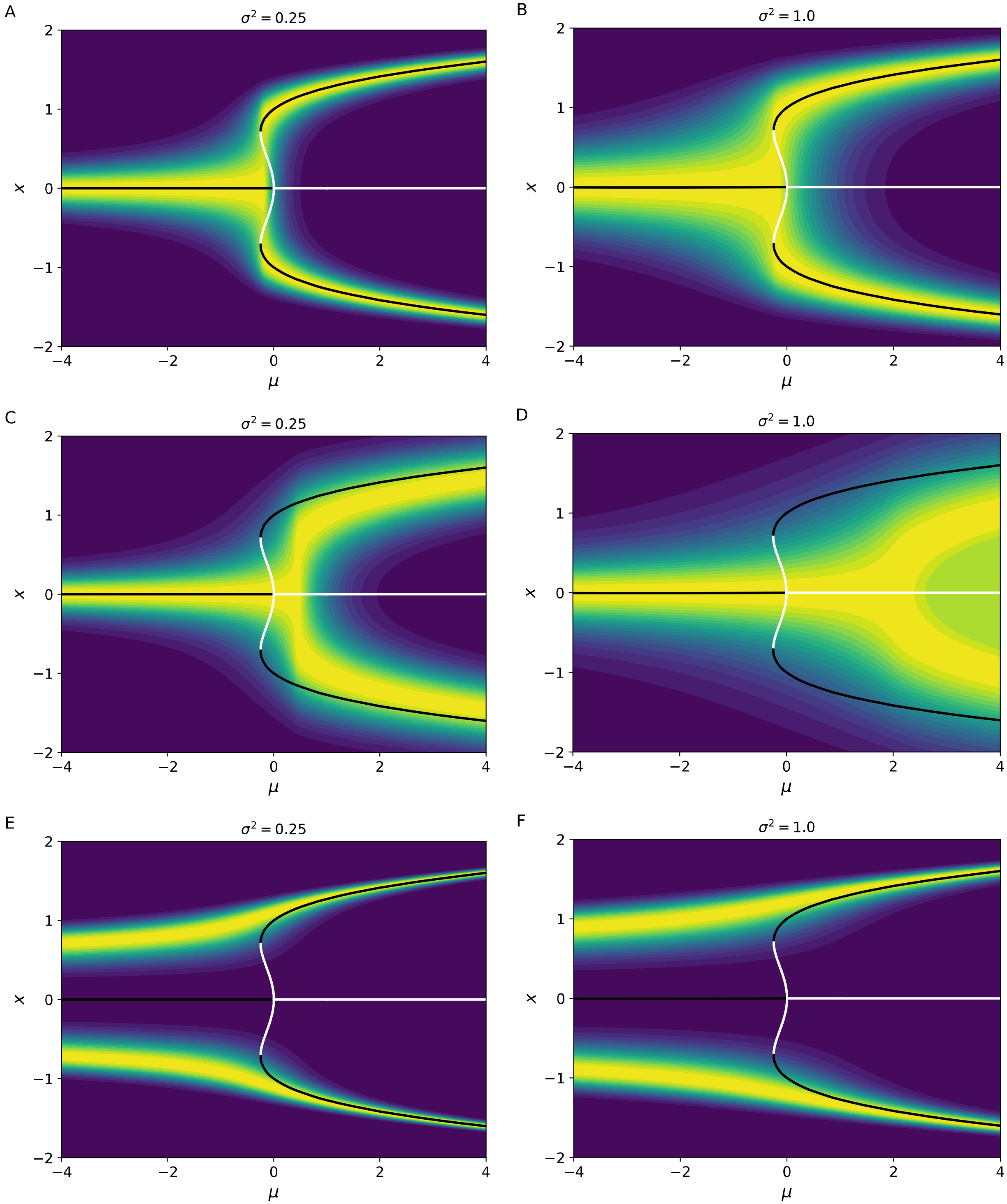

Figure 5.3- Probabilistic bifurcation diagram of the dynamical system of Eq. (4.9) in the presence of additive noise (A-B) and multiplicative noise. $g(x) = \sigma\left(1 + x^2\right)$ for (C-D) and $g(x) = \sigma\left(1 + x^{-2}\right)$ for (E-F). Black lines correspond to stable branches and white lines to unstable branches in the deterministic bifurcation diagram. The colorbars are removed because the values of the normalized PDF vary between 0 and 1 for all cases

5.2.3 FitzHugh-Nagumo Model

We have considered the FitzHugh-Nagumo (FHN) model as a two-dimensional nonlinear dynamical system. The FHN model is a simplified version of Hodgkin-Huxley neuron model [283]. The FHN model is also similar to van der Pol model and can be written as [284]:

$$\dot{V} = V(a-V)(V-1) - \omega + I, \tag{4.15}$$

$$\dot{\omega} = bV - c\omega, \tag{4.16}$$

where V mimics the membrane voltage, ω is a recovery variable, I resembles the injected current, and $a = 0.1, b = 0.075,$ and $c = 0.1$ are constant parameters. The stationary solution of the FPE for the FHN model has been previously investigated numerically in the presence of additive noise by Kostur and colleagues [285]. However, they did not construct the bifurcation of the dynamical system, which could have been used to explain some of the results they report in their study.

We choose the injected external current I , as the bifurcation parameter and assume it is noisy $I = I_0 + \mathcal{N}(0,\sigma^2)$. Here $\mathcal{N}(0,\sigma^2)$ is white noise with 0 mean and variance equal to σ^2 . Hence, there will be additive noise only in Eq. (4.15) and Eq. (4.16) will remain unchanged. Figure 5.4 shows the probabilistic phase plane analysis of the FHN model for three different values of external current.

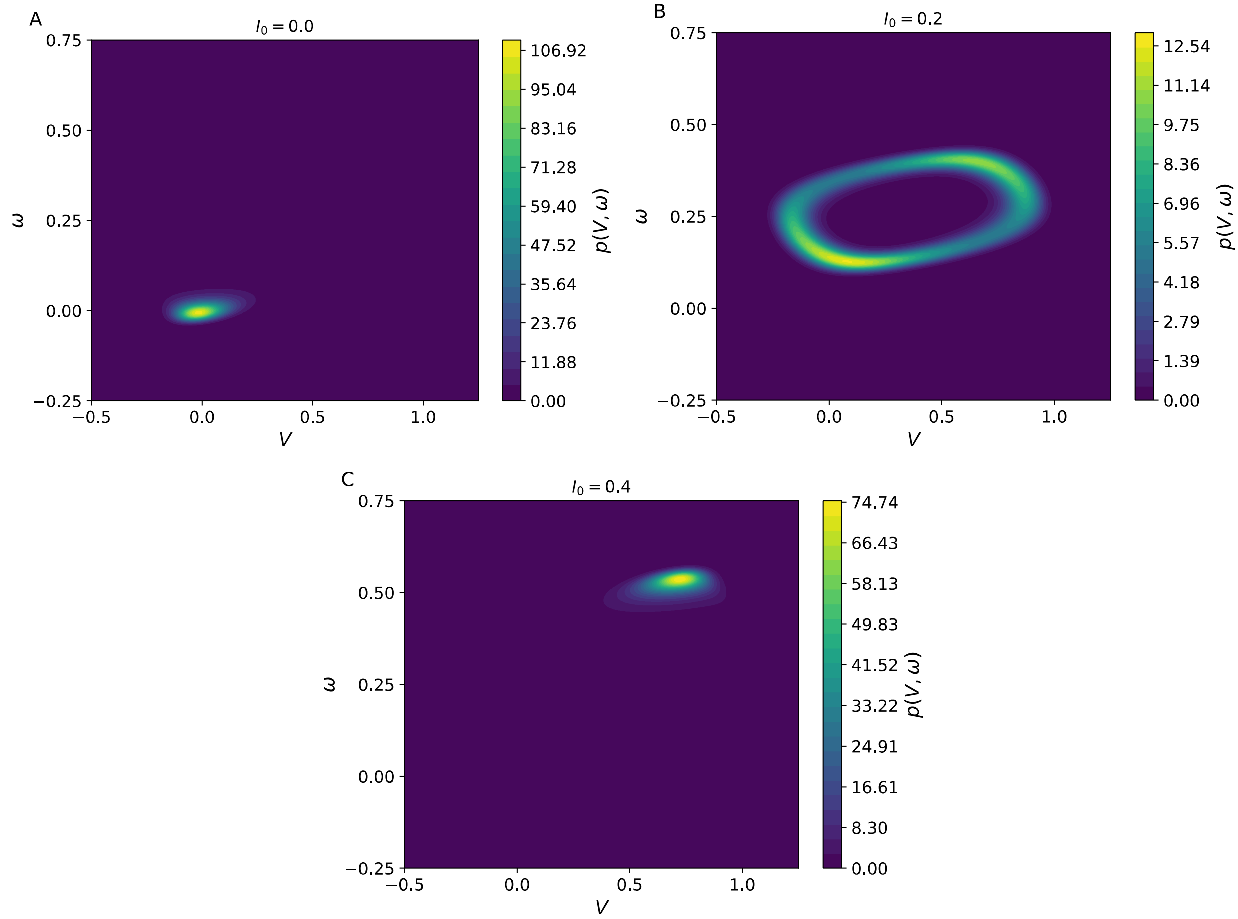

Figure 5.4- probabilistic phase planes of Fitzhugh-Nagumo (FHN) model when the external current has white noise $I = I_0 + \mathcal{N}(0,\sigma^2)$ with $\sigma^2 = 0.0025$.

Figure 5.4-(A) shows that for no injected current, the joint PDF for the states of the dynamical system is distributed around a fixed point meaning that the FHN neuron model is not firing and the membrane voltage is near the resting value. However, since the FHN model resembles a neuron model, increasing the injected current should lead to firing in the neuron model. Such behavior is demonstrated in Figure 5.4- (B) where we observe a limit cycle meaning that the membrane voltage oscillates between the resting value and a maximum value resembling firing of a neuron. Figure 5.4-(C) shows that increasing the injected current furthermore leads to the phenomenon known as the depolarization block meaning that the neuron stops firing while maintaining a high voltage due to the excessive injected current.

The complete behavior of the FHN in the presence of noisy injected current can be analyzed by constructing the probabilistic bifurcation diagram of the system. For systems that have more than one variable, we calculate the marginal probability density function (MPDF) for the variable that we want to construct its bifurcation diagram. For instance, the MPDF of membrane voltage, V , for the FHN model can be calculated as:

$$p(V) = \int p(V, \omega) d\omega. \tag{4.17}$$

The MPDF for systems with more than two dimensions can be found similar to Eq. 17 by calculating the multidimensional integral of the joint PDF. Again, we normalize the MPDF with its maximum value at each bifurcation parameter so that the MDPF varies between 0 and 1 for all values of the bifurcation parameter.

Figure 5.5-(A-D) demonstrate the probabilistic bifurcation diagram of the FHN model for two different magnitude of additive noise (white noise in the injected current). Again, the solid lines indicate the bifurcation diagram of the deterministic dynamical system. The black lines are the stable branches, the white lines are the unstable branches and the gray lines indicate the extremums of the limit cycles.

Even though noise is only introduced to Eq. (4.15), the recovery variable (ω) shows noisy behavior as expected because Eq. (4.15) and (4.16) are coupled. For the values of the bifurcation parameter where there is a stable branch, the probabilistic bifurcation diagram is almost centered around the stable deterministic branches when the noise is small (

Figure 5.5- (A) and (B)). However, when the noise becomes larger (

Figure 5.5-(C) and (D)) we observe that the probabilistic bifurcation diagram of voltage (V) deviates from the deterministic analysis especially near the bifurcation point where the limit

cycle appears. Hence, the deterministic bifurcation diagram does not represent dynamics of the FHN model when the noise in the injected current is large. Moreover, comparing

Figure 5.5-(A) and (C), we observe that the transition from finding the system around the stable branch to limit cycle oscillation is also affected by the magnitude of the noise. For small noise, such transition is more sudden compared to larger noise. When the system enters limit cycle regime, there is a probability of finding the system anywhere between the limits of the cycle. However, there are regions in the limit cycle regime that the probability is higher. The presence of such regions indicate that the dynamical system spends more time at such points during its cycle. In other words, the probabilistic bifurcation diagram can tell if the dynamical system is passing through a point in its cycle slowly or swiftly. Such information is also deducible from probabilistic phase plane analysis such as the one shown in Figure 5.4-(B). Points of higher probability in Figure 5.4-(B) indicate where the dynamical system is slow during its cycle.

Next, we study the FHN model in the presence of multiplicative noise. Here, we assume the membrane voltage is noisy $\left(V = V_0 + \mathcal{N}(0,\sigma^2)\right)$. Inserting such noise into Eq. (4.16) leads to:

$$d\omega = bV - c\omega + b\sigma dW, \tag{4.18}$$

where dW is the Wiener process again. However, implementing such noise in Eq. (4.15) is more complicated because of the nonlinearity in the voltage. When the voltage is noisy, Eq. (4.15) can be written in a more general form as:

$$dV = F\left(V + \mathcal{N}(0,\sigma^2), \omega, I\right)dt, \tag{4.19}$$

where $F\left(V,\omega,I\right) = V(a-V)(V-1) - \omega + I$. However, Eq. (4.19) does not have the standard form of stochastic differential equations as Eq. (4.1) in order to be converted to the FPE.

However, assuming the noise is small compared to the voltage, we can use the Taylor series expansion of $F\left(V+\mathcal{N}(0,\sigma^2)\right)$ to write Eq. (4.19) as:

$$dV = F\left(V,\omega,I\right)dt + \sigma\frac{\partial}{\partial V}F\left(V,\omega,I\right)dW. \tag{4.20}$$

Now, Eq. (4.20) has the same standard for as Eq. (4.1) and can be used to construct its associated FPE along with Eq. (4.18).

Figure 5.5-(E-H) demonstrate the bifurcation diagram of the FHN model in the presence of the multiplicative noise. Increasing the magnitude of noise does not change shape of the probabilistic bifurcation diagram in the multiplicative noise that is studied here. However, when the magnitude of noise increases, the injected current that leads to occurrence of limit cycle increases and the current that leads to depolarization block (the stable branch with large V) decreases. Therefore, increasing the magnitude of noise shortens the region where limit cycles exist. In other words, the multiplicative noise that is proportional to derivative of the drift as the one shown in Eq. (4.20) works towards keeping the system near its fixed points.

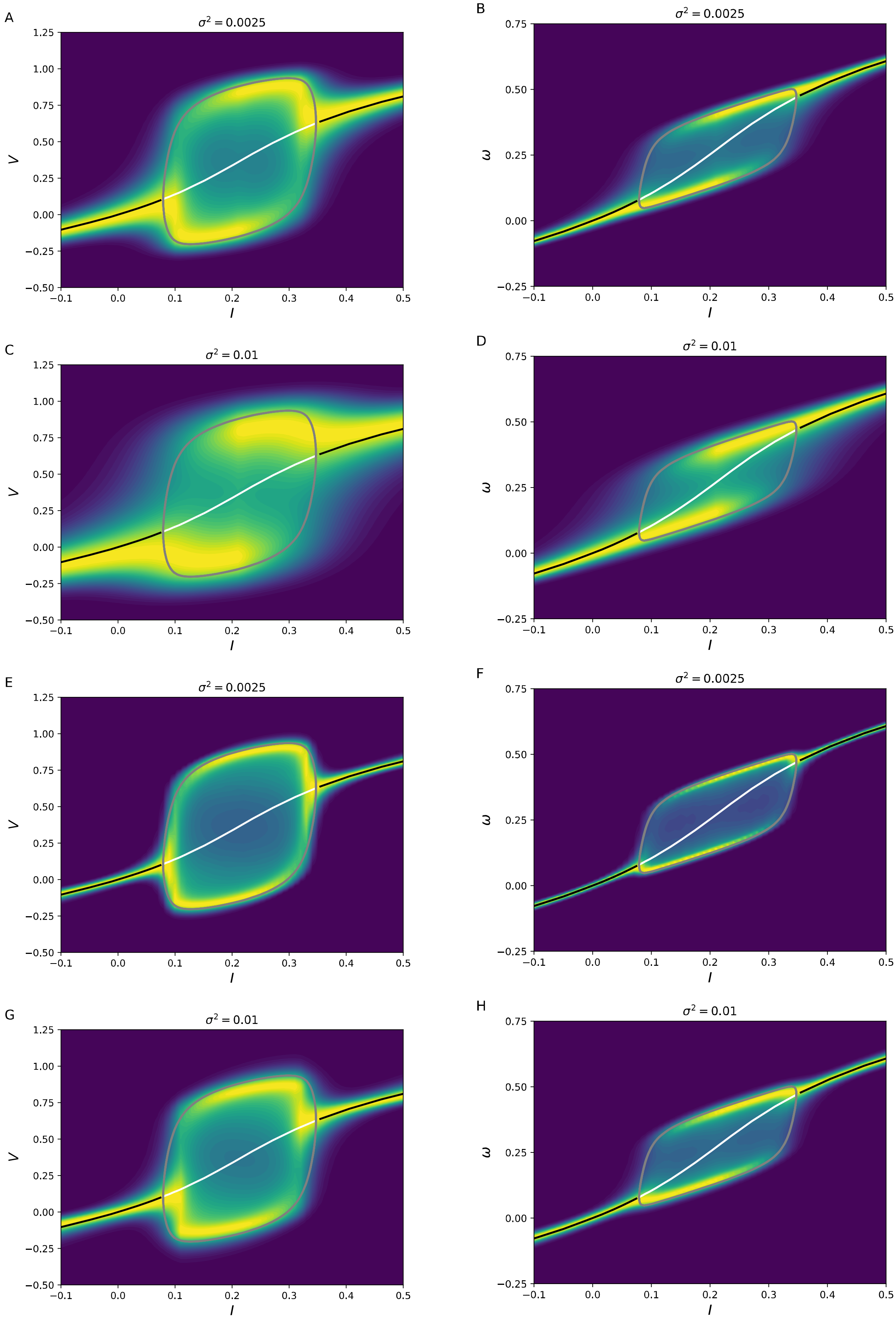
A
$\sigma^2 = 0.0025$
B
$\sigma^2 = 0.0025$
C
$\sigma^2 = 0.01$
D
$\sigma^2 = 0.01$
E
$\sigma^2 = 0.0025$
F
$\sigma^2 = 0.0025$
G
$\sigma^2 = 0.01$
H
$\sigma^2 = 0.01$
V
ω
I
1.25
1.00
0.75
0.50
0.25
0.00
−0.25
−0.50
−0.1
0.0
0.1
0.2
0.3
0.4
0.5

Figure 5.5- Probabilistic bifurcation diagrams of Fitzhugh-Nagumo (FHN) model in the presence of additive (A-D) and multiplicative (E-H) noise. The additive noise is associated with white noise in the injected current in Eq. (4.15). The multiplicative noise is due to white noise in the membrane voltage that leads to Eq. (4.18) and (4.20). Black lines correspond to stable branches, white lines to unstable branches, and gray lines to extremums of limit cycles in the deterministic bifurcation diagram. The colorbars are removed because the values of the normalized PDF vary between 0 and 1 for all cases.

5.3.3 Lorenz System

Next, we investigate dynamics of the Lorenz equations [286] in the presence of noise:

$$dx = \sigma(y - x)dt + g_1(x, y, z)dW, \tag{4.21}$$

$$dy = x(\rho - z) - y + g_2(x, y, z)dW, \tag{4.22}$$

$$dz = xy - \beta z + g_3(x, y, z)dW, \tag{4.23}$$

where x is related to the rate of convection, y and z are related to variation of temperature horizontally and vertically, respectively. We have set Prandtl number $\sigma = 5$, the geometrical parameter $\beta = 0.5$ and Rayleigh number ρ as the bifurcation parameter. The FPE for Lorenz equations has been investigated previously in the chaotic regime in the presence of additive noise [287,288]. However, previous studies did not investigate the bifurcation diagram of Lorenz system in the presence of noise or the influence of multiplicative noise.

First, we investigate the dynamics of Lorenz equations in the presence of additive noise. We have set $g_1 = g_2 = g_3 = \eta = 0.5$ in equations (4.21)-(4.23). Figure 5.6 shows the MPDFs of the Lorenz system when $\rho = 15$, which corresponds to chaotic dynamics. For the FHN model, we claimed that regions of high probability when there is a limit cycle indicate that the dynamical system passes through those points slowly. However, such conclusion cannot be made for the probabilistic phase planes shown in Figure 5.6. For a chaotic dynamical system, regions of high probability can merely mean that such points are visited more frequently rather than the dynamical system being slow at those points (or a combination of both).

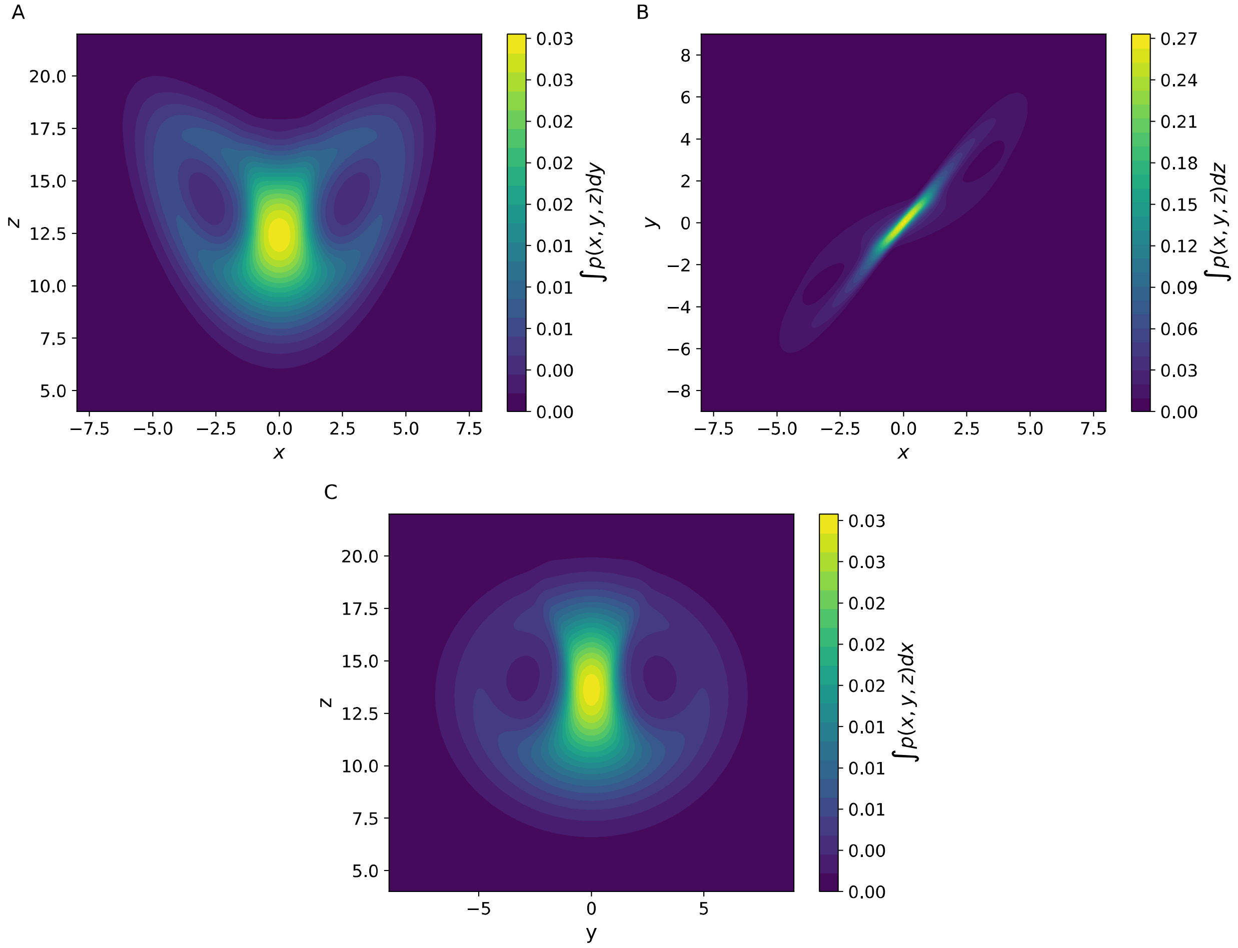

Figure 5.6- Probabilistic phase planes of Lorenz system in the presence of additive noise when $\rho = 15$. The two-dimensional projections show MPDFs.

Next, we construct the probabilistic bifurcation diagrams of the Lorenz equations in the presence of additive and multiplicative noise. Figure 5.7- (A-C) shows the probabilistic bifurcation diagrams for the case off additive noise where $g_1 = g_2 = g_3 = 0.5$. For another scenario, we assume there is white noise in y. Such white noise $\left(y = y_0 + \mathcal{N}(0,\eta^2) \right)$ will introduce additive noise in Eqs. (4.21) $(g_1 = \sigma \times \eta = 0.5)$ and Eq. (4.22) $(g_2 = \eta = 0.5)$ but multiplicative noise in Eq. (4.23) $(g_3 = \eta x = 0.5x)$. The results for such white noise is presented in Figure 5.7-(D-F). Again, the solid lines indicate the bifurcation diagram of the deterministic dynamical system. The black lines are the stable branches, the white lines are the unstable branches and the gray lines indicate the extremums of the limit cycles.

The supercritical pitchfork bifurcation occurs at $\rho = 1$ for the deterministic Lorenz equations. However, examining Figure 5.7-(A) and (B), the pitchfork bifurcation is delayed because of the additive noise. Figure 5.7-(D) and (E) also show delay in the pitchfork bifurcation in the case of multiplicative noise but the bifurcation occurs earlier compared to the case with additive noise. As ρ is increased, the dynamical system oscillates around the stable fixed points of the branches that occur after the pitchfork bifurcation. However, the dynamical system is also attracted by the unstable fixed point at $x = y = 0$ because the probability of finding the system there is not zero. In fact, the bounds of the unstable limit cycles approach fixed points at $x = y = 0$, which allows the stochastic system to switch between the stable branches. Hence, unlike the deterministic dynamical system that ultimately converges to either of the stable branches when $\rho < \rho_{chaos}$, the stochastic Lorenz system continue oscillating and switching between the stable branches. Further increase of ρ leads to chaotic behavior. The transition happens where the region of high probability occurs on the unstable branch even though stable fixed points are present. Comparing Figure 5.7-(A) and (B) with Figure 5.7-(D) and (E) shows that transition to chaotic behavior occurs faster when the noise is multiplicative in Eq. (4.23). The region of high probability near unstable fixed point at $x = y = 0$ in the chaotic regime indicates that the dynamical systems passes through that region of space more frequently. The width of probability distribution around $x = y = 0$ remains almost unchanged when the noise is additive unlike for the case where noise in multiplicative in Eq. (4.23).

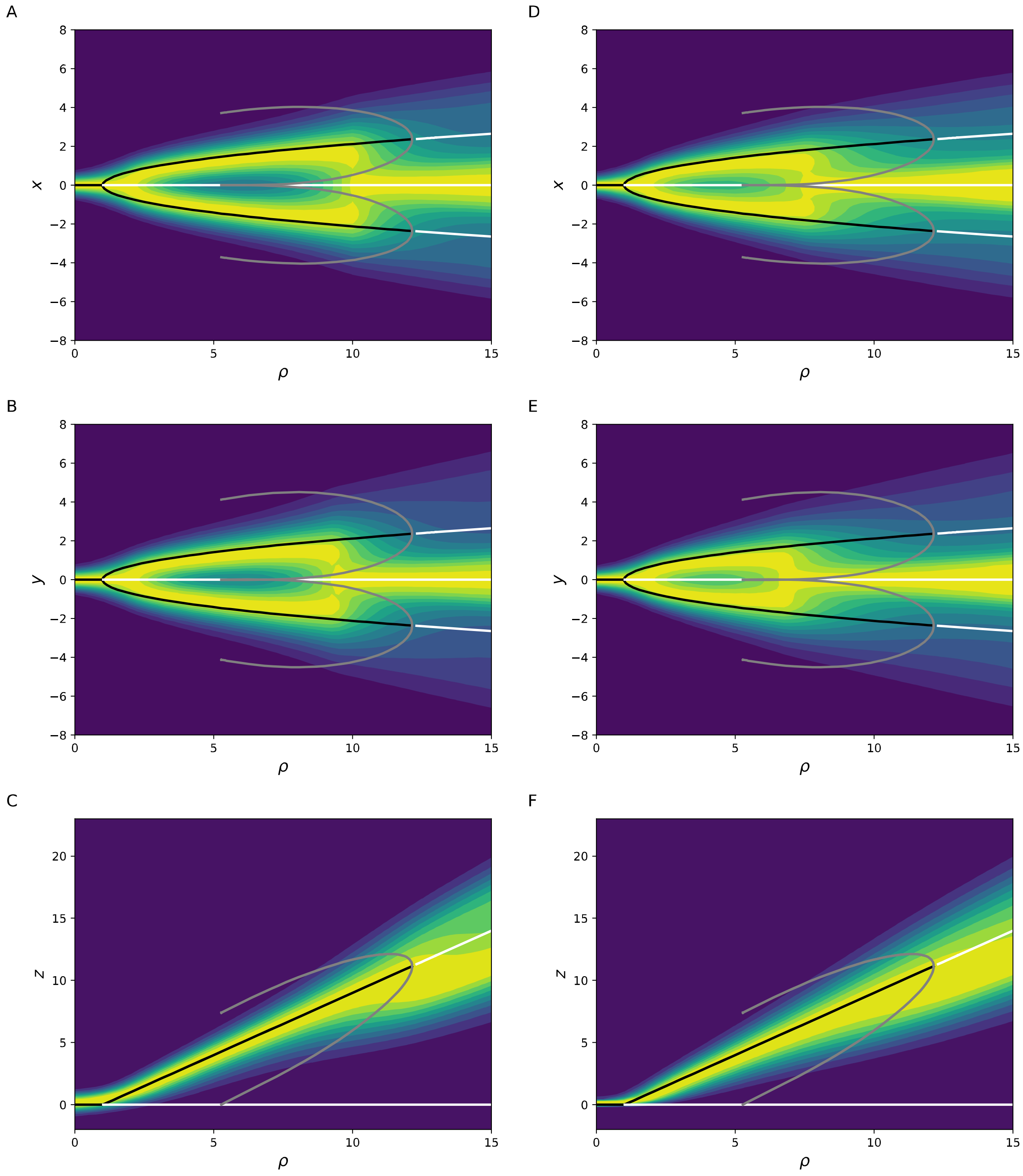

Figure 5.7- Probabilistic bifurcation digrams of Lorenz equations in the presence of additive (A-C) and multiplicative (D-F) noise. The multiplicative noise is due to white noise in y Black lines correspond to stable branches, white lines to unstable branches, and gray lines to extremums of limit cycles in the deterministic bifurcation diagram. The colorbars are removed because the values of the normalized PDF vary between 0 and 1 for all cases

5.4.3 Coupled Brusselators

We investigate dynamics of two Brusselators coupled together as a four-dimensional dynamical system. The Brusselator model [289] is a hypothetical chemical oscillator named after home of it inventors. Here, we study a system of coupled Brusselators in the presence of noise:

$$dX_1 = \left[A + X_1^2 Y_1 - BX_1 - X_1 + D_x \left(X_2 - X_1 \right) \right] dt + g_1(X_1, Y_1, X_2, Y_2) dW, \tag{4.24}$$

$$dX_2 = \left[A + X_2^2 Y_2 - BX_2 - X_2 + D_x \left(X_1 - X_2 \right) \right] dt + g_2(X_1, Y_1, X_2, Y_2) dW, \tag{4.25}$$

$$dY_1 = \left[BX_1 - X_1^2 Y_1 + D_y \left(Y_2 - Y_1 \right) \right] dt + g_3(X_1, Y_1, X_2, Y_2) dW, \tag{4.26}$$

$$dY_2 = \left[BX_2 - X_2^2 Y_2 + D_y \left(Y_1 - Y_2 \right) \right] dt + g_4(X_1, Y_1, X_2, Y_2) dW, \tag{4.27}$$

where A and B are constant supply of revivor chemicals [290], X_1, X_2, Y_1 and Y_2 are the concentration of intermediate reactants. The coupled model of Brusselators represents a system of two connected boxes (the subscript of reactants indicates which box the material is in) with D_x and D_y being the diffusion constants that control the exchange of material between the two boxes. Here, we choose B as the bifurcation parameter and have $A=1$ and $D_x = D_y = 0.5$. Moreover, we assume that there is white noise in both A and B. Such noise leads to multiplicative noise in Eq. (4.26) and (4.27) as $g_3 = \sigma_3 X_1$ and $g_4 = \sigma_4 X_2$. The noise also leads to a combination of additive and multiplicative noise in Eq. (4.24) and (4.25) as $g_1 = \sigma_1 + \sigma_3 X_1$ and $g_2 = \sigma_2 + \sigma_4 X_2$. We have set $\sigma_1 = \sigma_2 = \sigma_3 = \sigma_4 = \sqrt{0.1}$.

Interpretation of a four-dimensional system is less straightforward. We use MPDFs to present the results in two dimensions. Figure 5.8 shows the two-dimensional projection of MPDFs of the coupled Brusselators for $B = 2.5$. Solving PDEs in more than 3 dimensions is not common. Therefore, we use the symmetry in Eqs. (4.24)-(4.27) to show the validity of the solutions obtained here. Since the oscillators are identical, phase planes for $X_1 - Y_1$ and $X_2 - Y_2$ must look similar as shown in Figure 5.8-(A) and (D). Moreover, phase planes for $X_1 - Y_2$ and $X_2 - Y_1$ must look similar as shown in Figure 5.8-(C) and (F).

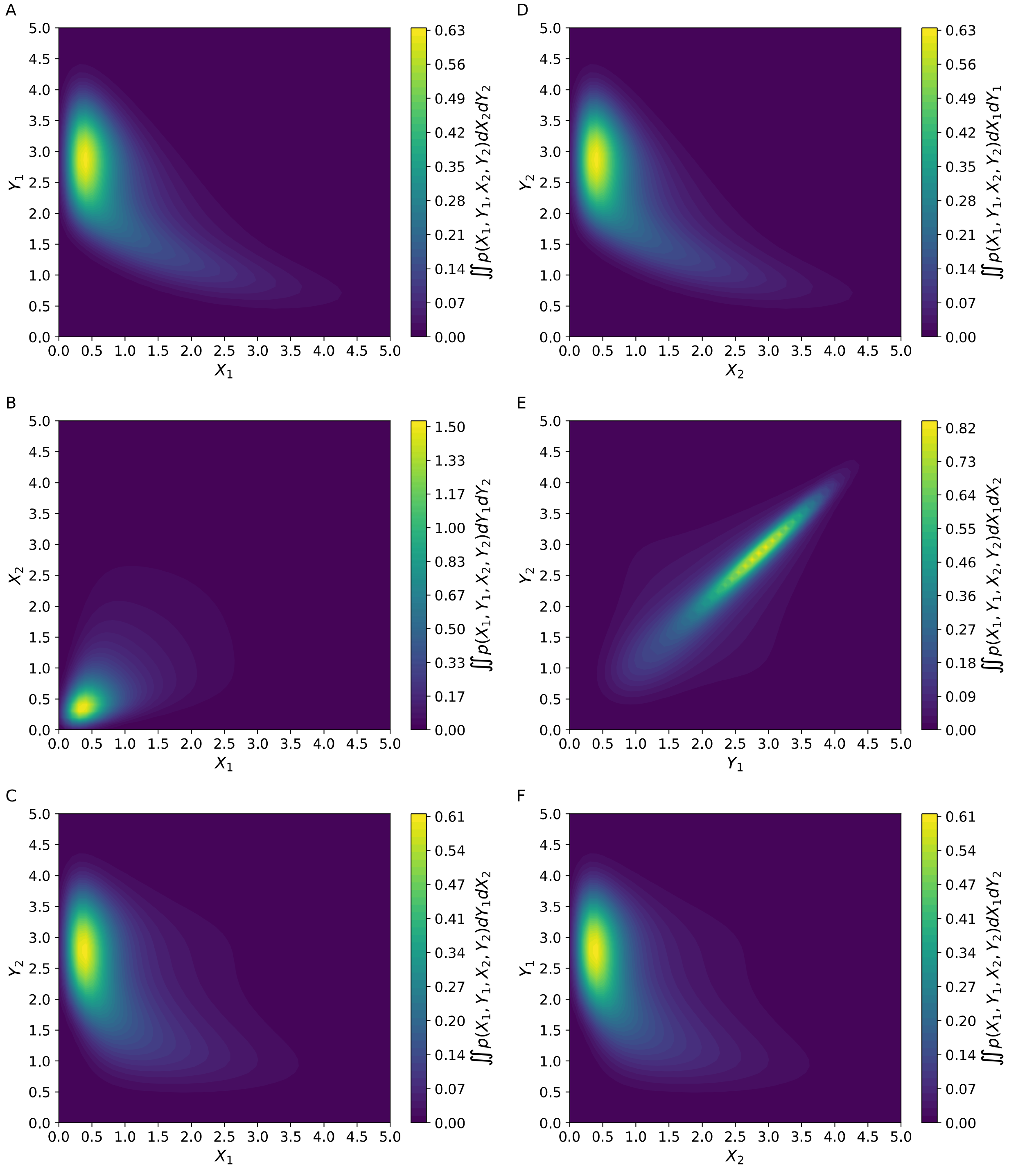

Figure 5.8- Probabilistic phase planes of coupled Brusselators in the presence of noise when $B = 2.5$. The two-dimensional projections show MPDFs.

$X_1 = X_2 = A = 1.0$ and $Y_1 = Y_2 = B / A = 2.5$ is a solution of Eqs. (4.24)-(4.27) in the absence of noise. Such solution loses stability when $B = 1 + A^2$ and a limit cycle appears in the deterministic equation. Figure 5.8 shows that the dynamical system has highest probability near the fixed points but the system is oscillatory because we can observe large deviations in the probability from the fixed point. The probabilistic bifurcation diagram of the coupled Brusselators is shown in Figure 5.9. Since the oscillators are identical, the bifurcation diagrams for X_1 and X_2 are similar as well as the diagrams for Y_1 and Y_2. Hence, we are only presenting the diagrams only for X_1 and Y_1. According to Figure 5.9-(A) the probabilistic bifurcation diagram has significant deviation from the deterministic bifurcation diagram before the bifurcation point at $X_1 = 2$. After the bifurcation point, X_1 follows one bound of the limit cycle meaning that the dynamical system has slow dynamics at one of the bounds during its oscillations. However, claiming that the oscillations take place after the deterministic bifurcation point is not accurate. None of the diagrams in Figure 5.9 can be used to define the exact point that limit cycles start to appear. Examining Figure 5.9-(B) suggest that the stochastic Brusselators are always oscillating and increasing B only increase the bounds of the oscillation. Moreover, Figure 5.9-(B) shows that the probabilistic bifurcation diagram is centered around both the stable and unstable branches for Y_1. Therefore, the deterministic bifurcation diagram can predict where the probability of finding the system is highest with regard to Y_1 but fails to provide bounds of oscillations as shown by the probabilistic bifurcation diagram.

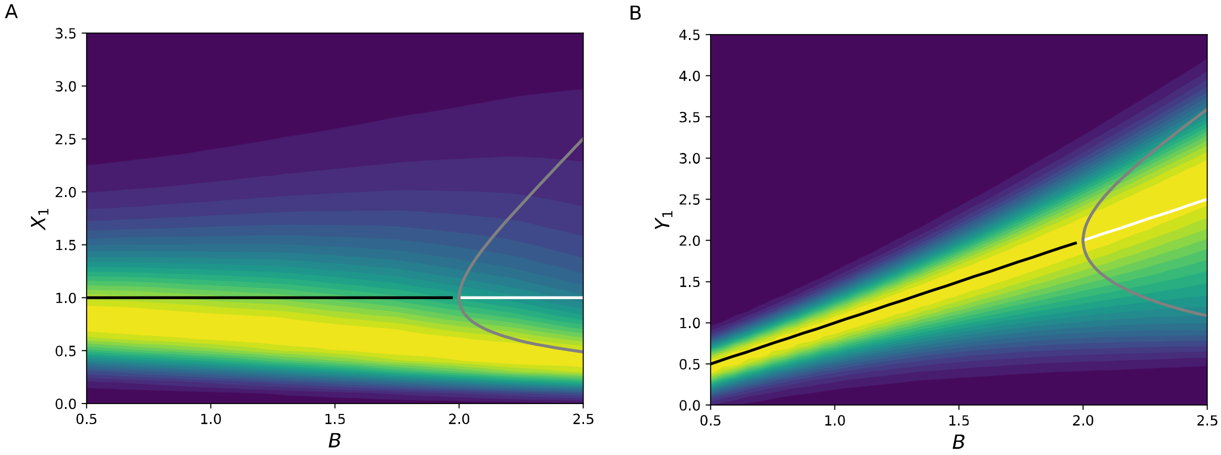

Figure 5.9- Probabilistic bifurcation digrams of coupled Brusselators in the presence noise. The noise is due to white noise in A and B. Black lines correspond to stable branches, white lines to unstable branches, and gray lines to extremums of limit cycles in the deterministic bifurcation diagram. The colorbars are removed because the values of the normalized PDF vary between 0 and 1 for all cases

5.4 Conclusions

Bifurcation diagrams provide essential information showing how nonlinear dynamical systems behave in a concise manner. However, such analysis is mostly limited to deterministic dynamical systems and there does not exist a unified approach to construct bifurcation diagrams for stochastic dynamical systems. Yet, noise is unavoidable in many real physical systems that are modeled using dynamical systems. We have demonstrated in this chapter that probabilistic bifurcation diagrams can be constructed for stochastic dynamical systems using the Fokker-Planck equation (FPE). The probabilistic bifurcation diagram provides the probability distribution for a state of the dynamical system for each value of bifurcation parameter. In the limit of noise going to zero, the PDF for a state becomes the delta function. Such delta function can also resemble stable fixed points of the deterministic dynamical system. However, when the noise is not zero, the PDF for a state of the dynamical system does not distinguish between stable or unstable fixed points. We have provided several examples of nonlinear dynamical systems in this chapter that shows how noise can affect the behavior of dynamical system.

Finding a closed form analytic solution of FPE is not usually tractable even when the stationary solution is sought. Hence, we have constructed such probabilistic bifurcation diagrams by finding the numerical stationary solution of the PFE that is associated with stochastic dynamical systems. However, we have provided analytic solution for the stationary FPE for the case of one-dimensional dynamical system that we have studied in this chapter. The comparison between the numerical solution and analytical solution shows that they match well.

We have considered a one-dimensional dynamical system with deterministic subcritical pitchfork bifurcation. Additive noise can change where the bifurcation occurs in such dynamical system depending on the strength of the noise because the system can switch between stable branches if the noise is strong enough. Hence, the system can jump to other equilibria before reaching the deterministic bifurcation point. Such change in the position where bifurcation can lead to dramatic consequences in real systems in which such sudden large amplitude changes must be avoided. The change in the parameter where the bifurcation occurs in stochastic dynamical systems compared to deterministic systems was also observed in the other systems we studied in this chapter. Moreover, multiplicative noise can have greater impact on the behavior of dynamical systems compared to additive noise. For instance, we have provided evidence that multiplicative noise not only changes where pitchfork bifurcation occurs, it can also change subcritical bifurcation into supercritical bifurcation. Furthermore, we have provided another type of multiplicative noise that terminates pitchfork bifurcation altogether.

We have considered nonlinear system of equations beyond one-dimension. We have investigated dynamics of the FitzHugh-Nagumo (FHN) model that is simplified neuron model. We have provided probabilistic phase plane analysis and probabilistic bifurcation diagrams for the FHN model. The FHN model exhibits limit cycles and the FPE can accurately capture the presence of limit cycles. Moreover, joint PDFs obtained from FPE can be used to show how fast a dynamical system is at each point in its cycle. Noise also changes when limit cycles appear and disappear in FHN model. Moreover, we have applied noise in nonlinear terms of FHN model. For such noise, we have used Taylor series expansion of nonlinear terms to construct standard stochastic differential equations before they can be converted to FPE. The probabilistic bifurcation diagrams for such multiplicative noise can stabilizes the system by delaying when the bifurcation occurs and also reducing amplitude of oscillations.

We have studied Lorenz equations as a three-dimensional dynamical system. The probabilistic bifurcation diagram can be used to show the transition to chaos. The bifurcation parameter where such transition occurs depends on the magnitude of noise and the functional form of noise. We have shown that even changing the noise in one of the equations in Lorenz system from additive noise to multiplicative noise can change the parameter where the transition to chaos occurs significantly.

We have studied dynamics of a coupled Brusselators as a four-dimensional dynamical system. The probabilistic bifurcation diagram for one the states of Brusselators follow the deterministic bifurcation diagram closely while the other state shows complete disparity between the deterministic and probabilistic analysis. Moreover, analyzing the probabilistic phase planes of the system shows the oscillatory behavior of the dynamical system. However, such conclusion cannot be made from the probabilistic bifurcation diagrams.

All the examples that we have provided in this work emphasizes that noise must not be disregarded in nonlinear dynamical system because noise can change where the bifurcation occurs or change nature and type of the bifurcation. More accurate and faster solution to high dimensional

Fokker-Planck equation can provide a powerful tool that enables construction of probabilistic bifurcation diagrams for stochastic dynamical systems.

Chapter 6

Probabilistic Analysis of the Bifurcations and Nonlinear Dynamics of Stochastic Firing Rate Models

6.1 Introduction

Advances in the characterization of neurons and the increase in computational capacity has enabled researchers to build larger and more detailed models of neural networks. While such models have proven to be helpful, the interpretation of results obtained from such models is not straightforward due the lack of necessary analytical and mathematical tools [291]. Such detailed models have high degrees of freedom and spiking of each individual neuron is tracked separately. However, large networks of neurons can be modeled using a simplification models such as firing rate models. Firing rate models are attractive not only because they are computationally efficient, but they can also be analyzed based on a rich mathematical foundation of dynamical systems [267].

Firing rate models are sometimes referred to as population models because they represent activity of whole populations of neurons rather than spiking of single neurons. Such models can be used to model the activity of a single population or interaction of different population of neurons. For instance, the celebrated model by Wilson and Cowan [292] considered interaction between an excitatory and an inhibitory population.

Firing rate models can be utilized in context of various neural systems. Here, we consider the concept of working memory. Working memory is the ability of the brain to hold memories for short periods of time [293]. Working memory can be investigated based on its association with persistent activity (the ability of neural network to sustain its activity upon removal of the initial stimulus) [47]. However, working memory can also be studied in the context of attractor based memory models. The dynamics of such models have more than one stable state and a transient stimulus switch the dynamics of network between these states. The famous model proposed by Hopfield [294] is an example of such models. The Hopfield model for associative memory was not biologically plausible, but extremely advanced theories and models for memory. More biologically relevant models for attractor based memories were developed later. For example, the work by Wang [49] used dynamics of integrate-and-fire neurons with all-to-all connectivity to model working memory. Moreover, Wang [49] used mean-field analysis to derive firing rate equations for the average firing rate of the network. The firing rate model was shown to have bistability. However, Amit and Brunel [295,296] have demonstrated that multiple attractors can exist if the network consists of several clusters such that each cluster is selective to a certain stimulus. Such clustering can be achieved by online synaptic plasticity rules [297] or statically implemented higher synaptic weights in the cluster compared to rest of the network [298].

In this research, we use the probabilistic framework that was introduced in chapter 5 to study firing rate models. The firing rate models show bistability that can represent different states of memory. Noise is introduced to the firing rate model as the stimulus that can switch the dynamical states of the model (recalling the memory). We solve the Fokker-Planck equation (FPE) numerically to find the stationary solutions at various parameter values, hence building stochastic bifurcation diagrams. Namely, we are interested to investigate how different parameter values that can represent impairment of synapses can change the capability of the model to be bistable (exhibit working memory).

6.2 Methods

We consider firing rate models for interaction of population of inhibitory and excitatory neurons. The excitatory population is divided into two subpopulations: an active population that represents neurons that are selective to external stimulus, and a background population that is not selective to any stimulus. Figure 6.1 shows the schematic of the firing model used.

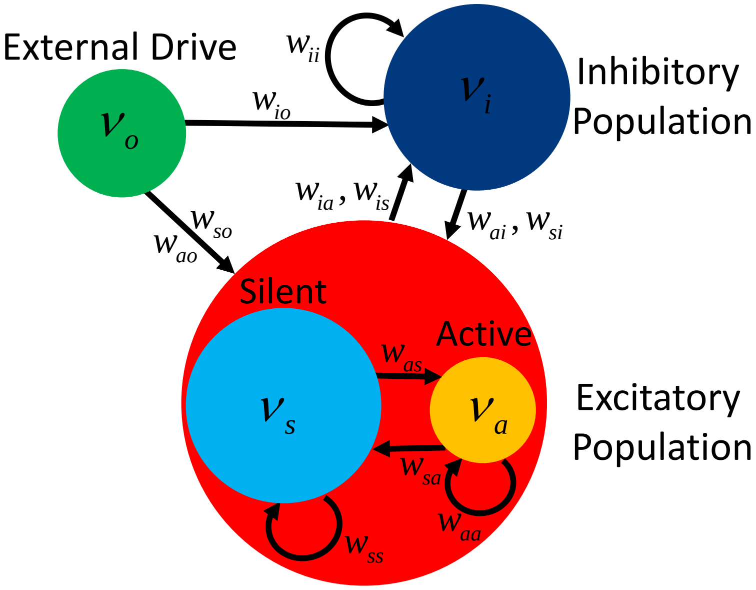

Figure 6.1- Schematic of the firing rate model. The excitatory population is divided to subpopulations of active and silent. The excitatory and inhibitory populations are driven by an external population. v_m is the firing rate of population m and w_{mn} is the weight of the connection that population m receives from population n.

Short-term synaptic plasticity has been shown to affect working memory [299]. A phenomenological model of short-term plasticity can be written as [300,301]:

$$\frac{dx}{dt}=\frac{1-x}{\tau_d}-ux\delta(t-t_{spike}), \tag{5.1}$$

$$\frac{du}{dt}=\frac{U_0-u}{\tau_f}+U_0(1-u)\delta(t-t_{spike}), \tag{5.2}$$

where x corresponds to amount of available synaptic resources (normalized so that $0<x<1$), and u is the fraction of resources used during each spike. τ_d and τ_f are two time constants that correspond to depression and facilitation, respectively. U_0 is the baseline release probability. δ is the Dirac delta function and t_{spikes} is arrival time of a presynaptic spike. For a firing rate model, the Dirac delta function (δ) is replaced with firing rate of the population (ν) [299]. Moreover, since we are only interested in steady state behavior of the system, the time derivatives are set equal to zero to obtain steady-state function for x and u as [302]:

$$x(\nu)=\frac{1}{1+\tau_d \nu u(\nu)}, \tag{5.3}$$

$$u(\nu)=U_0\frac{1+\nu\tau_f}{1+\nu\tau_f U_0}. \tag{5.4}$$

Then, the effective firing rate of a population (S) that is subjected to short-term plasticity can be written as:

$$S(\nu)=xu\nu. \tag{5.5}$$

Next, based on the schematic shown in Figure 6.1, the firing rates for each population can be written as [267]:

$$\tau_a\dot{\nu}_a=-\nu_a+\mathrm{F}\left(\nu_o w_{ao}+S(\nu_a)w_{aa}+S(\nu_s)w_{as}-\nu_i w_{ai}\right), \tag{5.6}$$

$$\tau_s\dot{\nu}_s=-\nu_s+\mathrm{F}\left(\nu_o w_{so}+S(\nu_a)w_{sa}+S(\nu_s)w_{ss}-\nu_i w_{si}\right), \tag{5.7}$$

$$\tau_i\dot{\nu}_i=-\nu_i+\mathrm{F}\left(\nu_o w_{io}+\nu_a w_{ia}+\nu_s w_{is}-\nu_i w_{ii}\right), \tag{5.8}$$

where the subscript o,a,s and i correspond to external, active, silent and inhibitory populations respectively. τ_m is the time constant that controls the time response of population m , ν_m is the firing rate of population m, and w_{mn} is the weight of the connections from population n to m. Also, the short-term synaptic plasticity is assumed to be present only in the connections of excitatory populations. F is the gain function that approximates the firing rate of a population based on the current it receives [267]:

$$F(y) = A\sqrt{\beta \log\left[1 + \exp\left((y - y_T)/\beta\right)\right]}, \tag{5.9}$$

where β is a measure of noise, A controls the magnitude of the gain function and y_T determines the minimum current that induces firing.

Next, we assume the transient stimulus that triggers the memory recall acts as white noise that is added to the external derive $\left(\nu_o + \mathcal{N}(0,\sigma^2)\right)$. Such noises will be added inside the nonlinear function of Eq. (5.9) for each of the population (Eqs. (5.6)-(5.8)). Since the noise is added inside the nonlinear gain function, the corresponding stochastic differential equations do not have the standard form of Ito process. However, assuming the noise to be small compared to the other terms in the gain function, we can linearize the gain function using Taylor's series as:

$$F\left(\nu_o + \mathcal{N}(0,\sigma^2)\right) \approx F\left(\nu_o\right) + \mathcal{N}(0,\sigma^2)\frac{dF(\nu_o)}{d\nu_o}. \tag{5.10}$$

Using Eq. (5.10), the standard stochastic differential equation for the firing rate of each population can be constructed. For example, the standard stochastic differential equation for the firing rate of active population (Eq. (5.6)) can be written as:

$$\begin{aligned} \tau_a d\nu_a = {} & \left[-\nu_a + \mathrm{F}\left(\nu_o w_{ao} + S(\nu_a) w_{aa} + S(\nu_s) w_{as} - \nu_i w_{ai}\right)\right] dt \\ & + \sigma_a{}^2 \frac{d}{d\nu_o}\left[\mathrm{F}\left(\nu_o w_{ao} + S(\nu_a) w_{aa} + S(\nu_s) w_{as} - \nu_i w_{ai}\right)\right] dW_t, \end{aligned} \tag{5.11}$$

where W_t is the standard Wiener process. Similar to Eq. (5.11), the standard stochastic differential equations can be constructed for firing rate of silent (Eq. (5.7)) and inhibitory (Eq.

(5.8)) populations. The multiplicative noise for each of the equations will have different functional form. Moreover, the variance of the white noise that translates to the strength of noise will be different for each population. However, we assume that the noise for the active population to be greater compared the silent and inhibitory populations. Next, we use the method introduced in Chapter 5 to form the Fokker-Planck equation (FPE) from the standard stochastic differential equations. Then, the stationary solution of the FPE is studied for rate models with different parameter values.

6.3 Results and Discussion

We investigated how different parameters of the model can affect the dynamics of the rate model. The rate model studied here can exhibit three different behaviors:

1) The system has only a stable state in which the active and inhibitory populations have high firing rate and the silent population has low firing rate (baseline activity).
2) The system has only a stable state in which the active and inhibitory populations low high firing rate and the silent population has high firing rate (persistent activity).
3) The system is bistable and switches between dynamics of baseline activity and persistent activity.

Figure 6.2 shows the marginal probability distribution for a bistable system. There are two regions of high probability. The one in which the firing rate of active population is low corresponds to the baseline activity. This state shows the dynamics of the system when the memory is not recalled. However, when the memory is recalled, the firing rate of the active state increases. Higher firing rate of the active population increases the firing rate inhibitory population. Consequently, the higher activity of inhibitory population suppresses the activity of silent population. Hence, the firing rate of silent population decreases during the memory recall. Such behavior is consistent with the dynamics observed in detailed models of working memory [299].

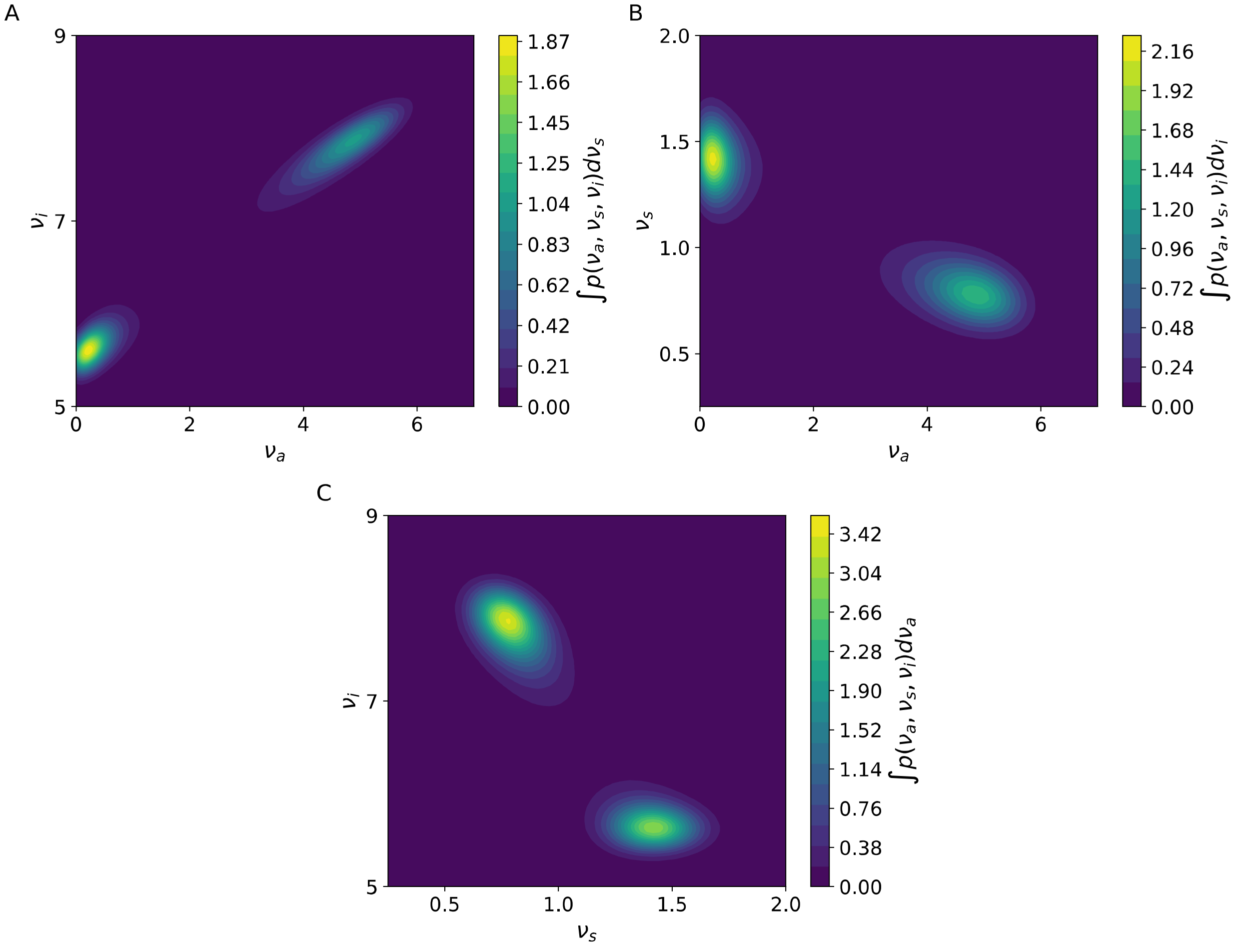

Figure 6.2- Firing rate model with bistability demonstrates characteristics of working memory. The stable state with high firing rate of active population corresponds to the persistent activity after a memory is recalled while the stable state with low firing rate of active population shows the system with baseline activity. The parameter values for the results shown here are $A = 2,\ B = 0.5,\ u_t = 3,\ U_0 = 0.2,$ $\tau_f = 0.5,\ \tau_d = 0.1,\ \nu_o = 8,\ w_{ao} = 0.5,\ w_{aa} = 4.75,\ w_{as} = 0.2,\ w_{ai} = 0.5,\ w_{so} = 0.75,\ w_{sa} = 0.2,$ $w_{ss} = 0.2,\ w_{si} = 0.5,\ w_{ia} = 2,\ w_{io} = 1,\ w_{is} = 2,$ and $w_{ii} = 0.1$.

Systems with bistability such as the one shown in Figure 6.2 can resemble networks with working memory. For such systems, a transient stimulus (here implemented as white noise), can switch the system from baseline activity to persistent activity. Therefore, changing the parameters of the system that leads to loss of bistability can be regarded as impairment. The parameter that is changed can be considered as a bifurcation parameter. Hence, probabilistic bifurcation diagrams of the rate model are constructed to study loss of bistability (the ability of the system to resemble working memory) for various scenarios of impairment. Figure 6.3 shows how the marginal probability distribution of the system changes when w_{aa} (the strength of the connection between neurons within the active population) varies.

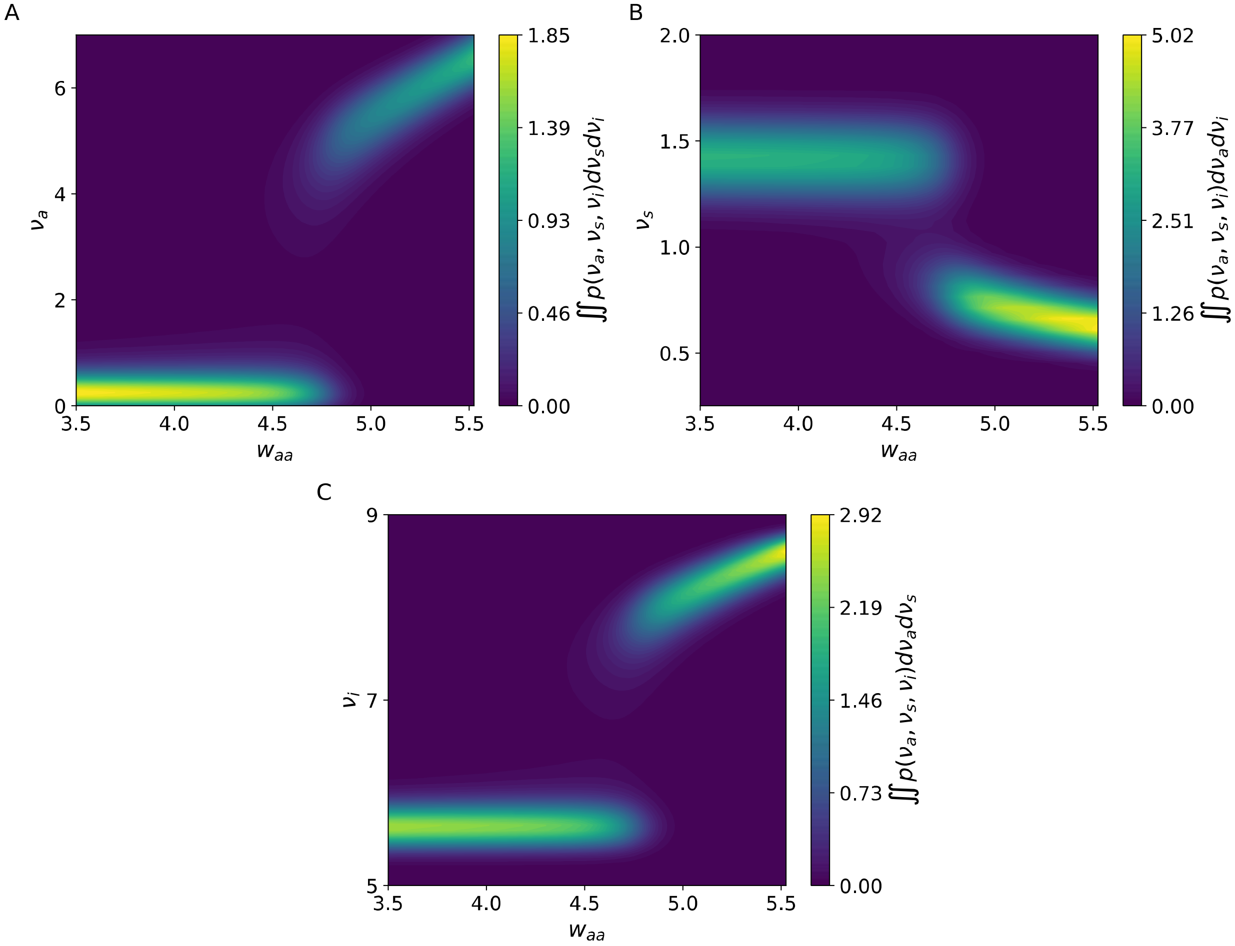

Figure 6.3- Probabilistic bifurcation diagrams of the rate model when w_{aa} (the strength of the connections between neurons within the active population) is changed. All the other parameters of the system are the same as the ones used in Figure 6.2.

A bistable system requires the strength of connections between neurons of active population (w_{aa}) needs to be higher compared to the strength of connections within and between other populations. Such property for w_{aa} is similar to having higher synaptic weight between neurons within a cluster in network models of working memory [295,296]. Therefore, for small w_{aa} the system cannot have persistent activity and the only stable state is the baseline firing.

However, when the strength of connections between the neurons within the active population is too high, the active population becomes dominant and the system only shows persistent activity. Between these two extremes, there is a region in which the system is bistable (the vicinity of $w_{aa} = 4.75$ as seen in Figure 6.3). The region of bistability observed in Figure 6.3 is small. Hence, small impairment of w_{aa} affect bistability of the system dramatically. Essentially, neurons within a cluster in detailed network models [295,296] are equivalent to the active population in the rate model. Therefore, impairment of w_{aa} is similar to impairment of neurons with higher outdegree [303], which was shown to be more detrimental compared to random impairment of synapses. Random impairment of synapses is not possible in the firing rate model. However, we can still compare the results when w_{aa} is impaired with changes in the strength of connection within and between different populations (Figure 6.1). Such comparison can demonstrate if impairment of connection within the active population is more harmful compared to impairment of connections elsewhere. Figure 6.4 shows probabilistic bifurcation diagrams when w_{as} varies.

The system is bistable for all the values of w_{as} explored in Figure 6.4. Therefore, unlike changing w_{aa} (Figure 6.3) the system is not sensitive to changes of w_{as}. Similar results are obtained when w_{sa} and w_{ss} are changed (supplementary Figure B.3 and Figure B.4). Hence, impairing of connections within the active population has greater impact than impairing the other connections of the system. Thus, random impairment that can affect any of the connections in the system with equal likelihood, is less destructive compared to targeted impairment of active population.

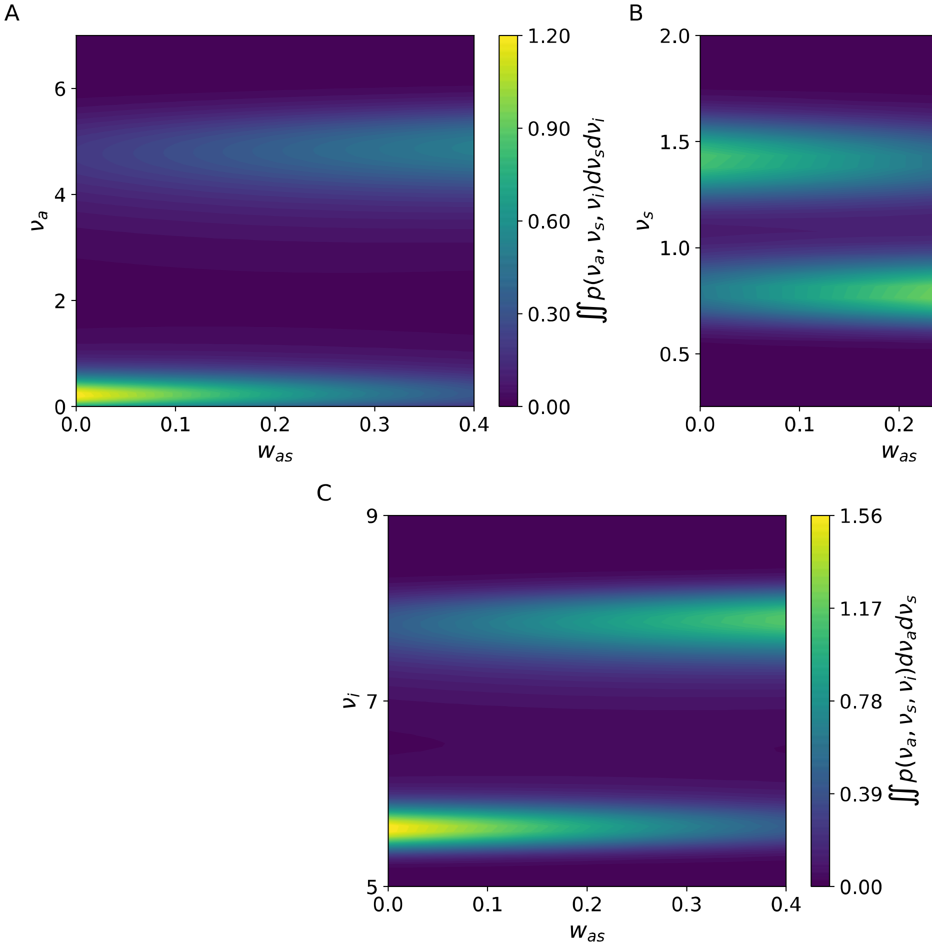

Figure 6.4- Probabilistic bifurcation diagrams of the rate model when w_{as} (the strength of the connections neurons in the active population receives from the silent population) is changed. All the other parameters of the system are the same as the ones used in Figure 6.2.

Next, we consider impairment scenarios that are related to activity of neurons. Such impairments are shown to have the largest impact on the activity of the network [303]. Here, we apply such impairments by changing the parameters of short-term synaptic plasticity (Eqs. (5.3) and (5.4)). Such impairments can be linked into subcellular dynamics such as axonal transport. When axonal transport is defected [22], less resources are delivered to synaptic terminals for producing and recycling of synaptic vesicles [31]. Therefore, axonal deficiency is expected to decrease the baseline release probability (U_0), speed up the rate that resources are consumed (decrease τ_f), and increase the time constant associated with recovery of resources (τ_d) at the synaptic terminal. However, synapses of a less active neuron should be affected less by such defects in axonal transport. A neuron that does not fire frequently consumes its synaptic resources slowly. Hence, even a deficient axonal transport might be able to maintain synapses of such neuron. Contrary, a highly active neuron consumes its synaptic resources quickly and requires a healthy and efficient axonal transport for maintaining it synapses. Therefore, impairments related to axonal transport should affect highly active neurons more than silent neurons. Figure 6.5 shows that changing parameters of the short-term synaptic plasticity model affects the effecting firing rate $(S(\nu))$ more when the firing rate (ν) is high. Therefore, changing parameters of the short-term plasticity model satisfies our hypothesize regarding impairments due to defects in axonal transport.

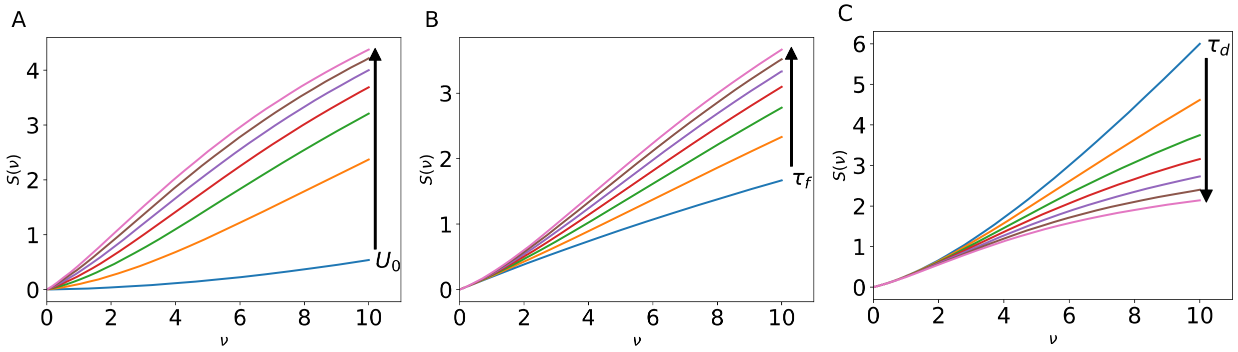

Figure 6.5- $S(\nu)$ (Eq. (5.5)) changes nonlinearly with the firing rate when parameters of the short-term plasticity (Eqs. (5.3) and (5.4)) are varied. The arrows show the direction in which each parameter increases.

Figure 6.6 shows the probabilistic bifurcation diagram when the baseline release probability in Eq. (5.4) changes. Similar to results in Figure 6.3 in which w_{aa} (the strength of connections within the active population) was changed, the regions of bistability is small when U_0 is changing. Therefore, the system is sensitive to changes of U_0. Similarly, changing the other parameters of the short-term synaptic plasticity (τ_f and τ_d) have visible impact on the bistability of the system (supplementary Figure B.5 an Figure B.6). Hence, impairments that are related to activity of populations and can be linked to defects in the subcellular dynamics (axonal transport), have harmful impact on the ability of the system to have working memory (show bistability).

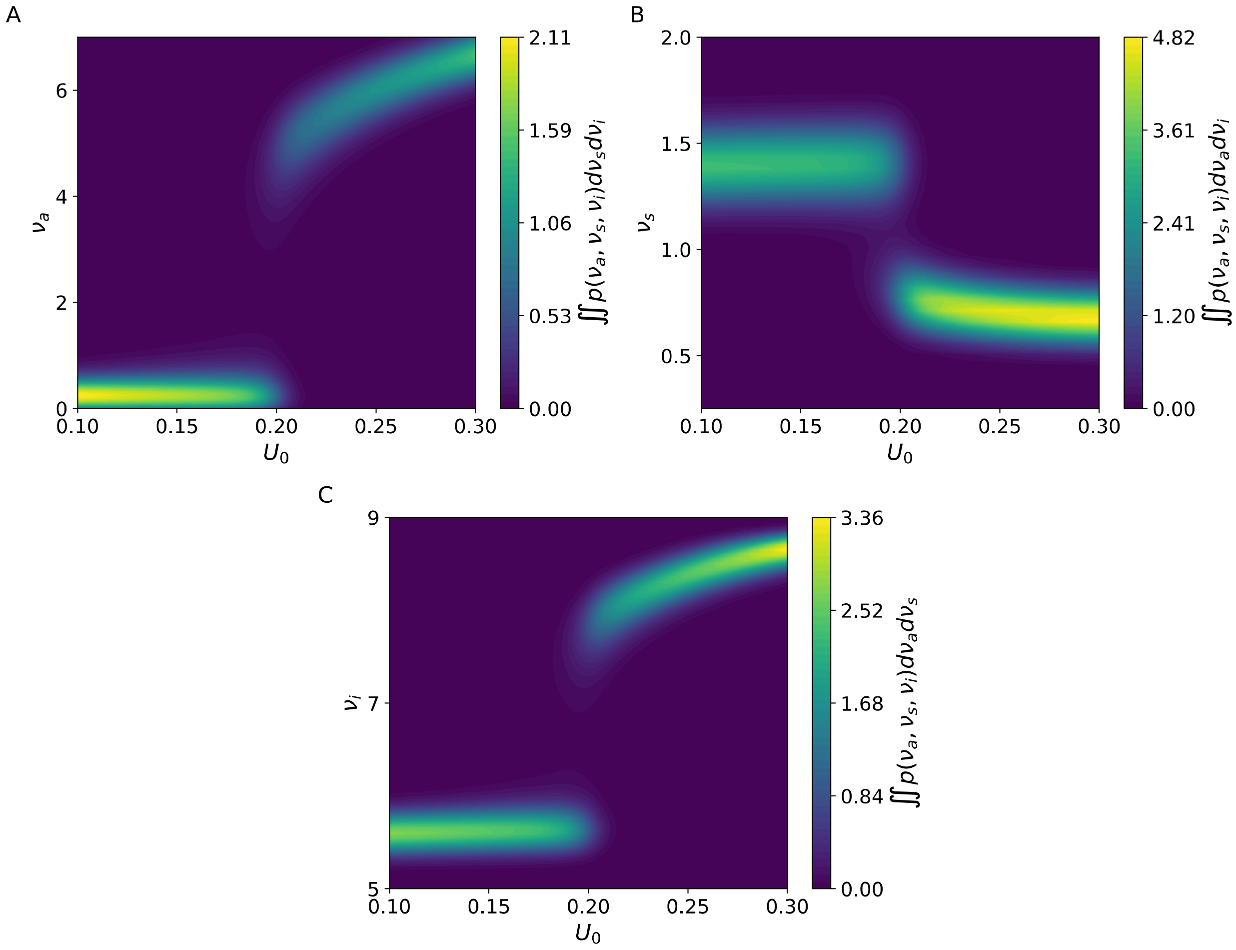

Figure 6.6- Probabilistic bifurcation diagrams of the rate model when U_0 (the baseline release probability in Eq. (5.4)) is changed. All the other parameters of the system are the same as the ones used in Figure 6.2.

All the probabilistic bifurcation diagrams shown so far are marginal probability density functions (PDF) in which the stationary PDF obtained from FPE is integrated twice. Integrating any of the marginal PDF equals to 1 because the integral of the PDF over the whole domain is 1. However, we can define “up” and “down” states and perform the integration only around the “up” and “down” state. We define the “down” state when the active population has low firing rate and the “up” state when the active population has high firing rate. Then, the probability function can be integrated in the vicinity of “up” and “down” states to determine the likelihood of finding the system near each of these states. To that end, we first find the local maximum of the PDF for $\nu_a < 2.5$(“down” state) and $\nu_a > 2.5$ (“up” state). The threshold is based on the bifurcation diagram shown in Figure 6.3- A that shows how the “up” and “down” states are separated for the firing rate of active population. Then, the PDF is integrated within a box that is centered around each local maximum. The size of the box is set equal to 2 in each direction. For the parameter values that the system shows only baseline firing rate, the resulting integral will be approximately equal to 1 for the “down” state and 0 for the “up” state. Similarly, the resulting integral will be approximately equal to 0 for the “down” state and 1 for the “up” state when the system only shows persistent activity. However, when the system is bistable, the integral is nonzero for either of the states. The value of the integral is closer to 1 for the state in which the system is more likely to found. The sum of the integrals obtained for the two states should be approximately equal to 1 because the likelihood of finding the system in transition between the “up” and “down” state is small (for example there is no region of high probability between the “up” and “down” states in Figure 6.2). The results of such analysis are presented in Figure 6.7 for the same parameters that their bifurcation diagrams were shown in Figure 6.3, Figure 6.4 and Figure 6.6 studied in this chapter.

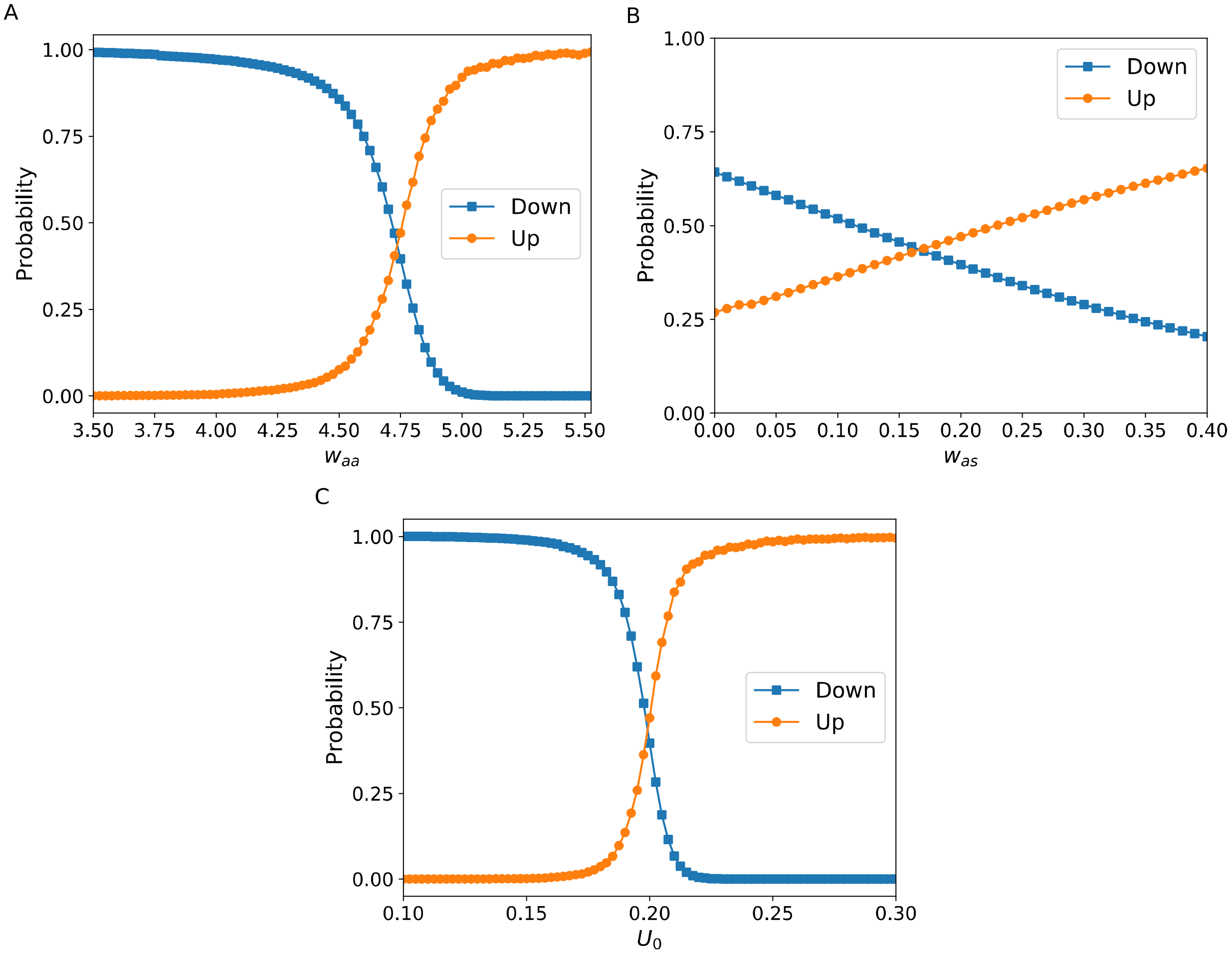

Figure 6.7- Probability of being in the “up” or “down” states when parameters of the model change.

The conclusion from Figure 6.7 is similar to what was observed in Figure 6.3, Figure 6.4 and Figure 6.6. For example, Figure 6.7-A shows w_{aa} has greater impact on the bistability of the system compared to w_{as} (Figure 6.7-B). However, the results shown in Figure 6.7 can be used to compare the sensitivity of the system when different parameters of the model are changed. To this end, we calculate how the absolute value of the normalized slope for the “up” state:

$$\text{Normalized Slope} = \left| \frac{(\max(p) - 0.1) - (\min(p) + 0.1)}{\left(\mu_{\max(p)-0.1} - \mu_{\min(p)+0.1}\right) / \mu_{p=0.5}} \right|, \tag{5.12}$$

where p is the probability, and $\mu_{p=P}$ is the bifurcation parameter at which $p = P$. We use points at which $(\max(p) - 0.1)$ and $(\min(p) + 0.1)$ to avoid the flat regions seen in Figure 6.7-A and C. We normalized the slope by the value of the bifurcation parameter at which the probability of being in the “up” state is same as the probability of being in “down” state $\mu_{p=0.5}$. The normalization is conducted to allow fair comparison between parameters that their scale and nature is different. Figure 6.8 shows how the normalized slope changes when different parameters of the model are changed.

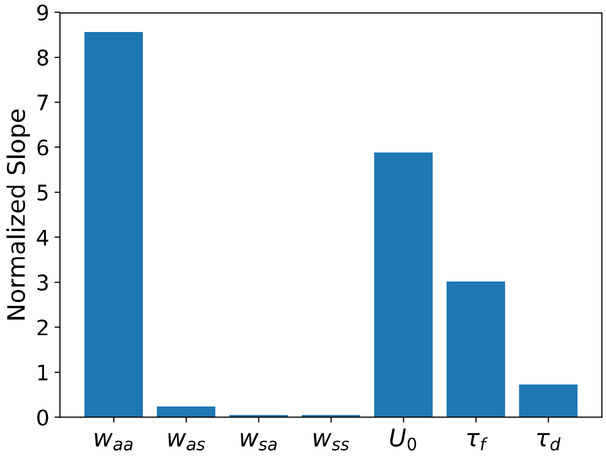

Figure 6.8- Sensitivity of the model to changes of different parameters. A Larger slope means that the system loses its bistability with a smaller change of a parameter

Figure 6.8 shows that strength of connections within the active population (w_{aa}) has the greatest impact on the bistability of the system. However, other strengths of connections have minimal effect on the bistability of the system. The parameters associated with short-term synaptic plasticity can affect the bistability of the system. The baseline probability of release (U_0) has the largest impact on the bistability of the system, which is comparable to changes in w_{aa}.

6.4 Conclusions

The firing rate models are computationally affordable but more importantly, they can be analyzed using mathematical techniques that are developed for dynamical systems. Here, we studied stochastic firing rate models that can represent models of working memory. The noise acts as the transient stimulus that recalls a stored memory. The stochastic differential equations associated with the firing rate model is used to construct the Fokker-Planck equation (FPE). The stationary solution of the FPE is obtained numerically in the presence of the multiplicative noise. Next, the stationary solution of the FPE is used probabilistic bifurcation diagrams of the firing rate model by changing different parameters of the model. The regions of bistability in the probabilistic bifurcation diagrams correspond to models that can represent working memory. Hence, changes in the parameters that diminish bistability can be considered as impairments that lead to loss of working memory. The strength of connections within the active population is shown to have the greatest impact on the bistability of the model. Such impairment is closely related to impairment of synapses in neuron with high degrees (introduced in Chapter 4). Moreover, impairment of parameters that are linked to dynamics of synapses is shown to lead to loss of bistability. Such parameters are connected to subcellular dynamics such as axonal transport. Hence, we have shown that impairments related to subcellular processes can manifest themselves in larger scale dynamics of neural systems such population of neurons firing rate.

Chapter 7

Summary and Future Research

7.1 Summary

Dynamics of neural system in different scales were studied. The goal at each step was to provide insight into how dynamics of neural systems can help with detecting malfunctions in the element of the neural system that was under investigation. Moreover, this effort tries to connect the dynamics of neural systems in different scales when possible. Specifically, how small-scale dynamics in neurons such as the axonal nanotransport can influence larger scale dynamics such as population activity of neurons. Addressing such questions are important because they can pave the way to solve inverse problems that connect observed dynamics of neural system on larger scales to otherwise undetectable subcellular neural processes.

At the smallest scale, axonal transport by kinesin motor protein was studied. Previously developed mechanistic models of kinesin dynamics were used to investigate dynamics of cargo transport in the presence of magnetic nanoparticles. The magnetic nanoparticles were used as a mean to perturb dynamics of kinesin by exerting forces on the cargo that can be altered dynamically by changing the external magnetic field. Traditional single-molecule methods that are used to exert forces on the cargo transported by kinesin have had only partial success to be extended from *in vitro* to *in vivo*. The alternate method proposed here has the possibility to be applied *in vivo*, to influence kinesin transport by indirectly applying external loads on cargoes using superparamagnetic nanoparticles. However, multiphysics models that capture the dynamics of both magnetic nanoparticles and biological phenomena such as axonal nanotransport are computationally expensive. Hence, a novel reduced order model (ROM) for the dynamics of magnetic nanoparticles was developed to study the interaction of superparamagnetic nanoparticles with cellular nanotransport upon delivery of these particles into cells. Superparamagnetic nanoparticles were shown to form chain-like structures in the presence of external magnetic fields. Such chains influence the nanotransport inside cells. The model included viscous and magnetic forces on the nanoparticles, and the formation of aggregates/structures composed of nanoparticles to construct the novel ROM. Further, the stochastic nanotransport coupled with the dynamics of the magnetic nanoparticles was established. The novel ROM was used to characterize the stochastic motion of a kinesin in the presence of magnetic nanoparticles by determining the force acting on cargoes for different aggregate shapes and sizes (without having to solve the full-order dynamics every time). The ROM coupled with kinesin model allows the quantification of the decreases in processivity of kinesin and in its average velocity under external loads caused by chains of superparamagnetic nanoparticles. Such changes can then be utilized to decipher healthy and impaired transport. However, the small scale of such analysis reduces its practicality and requires high spatial and temporal resolution. Nonetheless, study of dynamics of neural systems in larger scales can still provide vital information about subcellular mechanism in normal or pathological conditions.

Investigating dynamics of Ca^{2+} transients to indirectly assess a neuron's activation is a well-established approach. A mathematical and computational model is developed that captures the stimulus-generated Ca^{2+} transients in the *C. elegans* ASH sensory neuron. The model provides a tool that enables a cross-talk between modeling and experiments, using modeling results to guide targeted experimental efforts. The model is built based on biophysical events and molecular cascades known to unfold as part of neurons' Ca^{2+} homeostasis mechanism, as well as on Ca^{2+} signaling events. The state of ion channels is described by their probability of being activated or inactivated, and the remaining molecular states are based on biochemically defined kinetic equations or known biochemical motifs. The parameters of the model are estimated using experimental data of hyperosmotic stimulus-evoked Ca^{2+} transients detected with a FRET sensor in young and aged worms, unstressed and exposed to oxidative stress. A hybrid optimization method composed of a multi-objective genetic algorithm and nonlinear least-squares is used to estimate the model parameters. First, the model parameters are obtained for young unstressed worms. In addition, the established model is shown to be able to predict ASH response to complex combinations of stimulation pulses. The proposed model includes for the first time the ASH Ca^{2+} dynamics observed during both "on" and "off" responses. This mathematical and computational effort is the first to propose a dynamic model of the Ca^{2+} transients' mechanism in *C. elegans* neurons, based on biochemical pathways of the cell's Ca^{2+} homeostasis machinery. Most importantly, the model can explain potential changes in the components of the system induced by aging or oxidative stress that leads to alteration in the observed Ca^{2+} transients. The findings of the model for the changes that can explain aging or impact of oxidative stress agrees with available experimental results in the literature. However, some of the predictions made by the mathematical model has not been investigated in experiments yet. Indeed, one goal for the proposed model is to further elucidate the Ca^{2+} dynamics of a key *C. elegans* neuron by guiding future experiments on *C. elegans* neurobiology.

Study of cellular processes such as Ca^{2+} transients still requires high temporal and spatial precision. However, larger scales dynamics of neural systems can still provide valuable information regarding defects occurring in smaller scales. For instance, synaptic deficiencies are a known hallmark of neurodegenerative diseases, but the diagnosis of impaired synapses on the cellular level is not an easy task. Nonetheless, changes in the system-level dynamics of neuronal networks with damaged synapses can be detected using techniques that do not require high spatial resolution. The structure/topology of neuronal networks and how they influence their dynamics when they suffer from synaptic loss has been investigated. Different neuronal network structures/topologies were studied by specifying their degree distributions. The modes of the degree distribution can be used to construct networks that consist of rich clubs and resemble small world networks, as well. Two dynamical metrics were defined to compare the activity of networks with different structures: persistent activity (namely, the self-sustained activity of the network upon removal of the initial stimulus) and quality of activity (namely, percentage of neurons that participate in the persistent activity of the network). The results show that synaptic loss affects the persistent activity of networks with bimodal degree distributions less than random networks. The robustness of neuronal networks enhances when the distance between the modes of the degree distribution increases, suggesting that the rich clubs of networks with distinct modes keep the whole network active. In addition, a tradeoff is observed between the quality of activity and the persistent activity. For a range of distributions, both of these dynamical metrics are considerably high for networks with bimodal degree distribution compared to random networks. Also, three different scenarios of synaptic impairment were proposed, which may correspond to different pathological or biological conditions. Regardless of the network structure/topology, results demonstrate that synaptic loss has more severe effects on the activity of the network when impairments are correlated with the activity of the neurons.

Detailed models of neural networks are computationally expensive and interpretation of results obtained from detailed neural networks is not straightforward. Alternatively, firing rate models allow fast simulation of population of neurons and can be analyzed using mathematical tools that are accessible for dynamical systems. Firing rate models are considered to represent properties of working memory. To that end, a mechanistic model of short-term plasticity is incorporated into the rate model. Adding noise to the firing rate model with short-term plasticity allows investigating capability of the model to poses properties of working memory. The established stochastic firing rate model requires numerous simulations in order to draw meaningful statistical conclusions from the model. Instead, the stochastic differential equations of the firing rate model are used to construct the Fokker-Planck representation of the firing model. The Fokker-Planck equation is solved to directly find the probabilistic properties of the firing rate model. Specifically, the stationary solution of the Fokker-Planck equation is obtained by solving the discretized partial differential equations numerically. The interaction of excitatory and inhibitory populations is modeled. The excitatory population is divided into two subpopulations of active and silent neurons. The active subpopulation corresponds to neurons that participate in the memory recall by showing elevated activity and the silent subpopulation correspond to neurons that show low activity during the recall. The probability distributions obtained from the Fokker-Planck equation shows the state of each population for different parameters of the model. The probabilistic bifurcation diagrams of the stochastic rate model are constructed by changing parameters of the model. The regions of the bistability is considered where the model shows characteristics of working memory. Hence, changing the parameters from their nominal, where system is bistable, is considered as impairment. The results show that impairment of parameters that control the synaptic plasticity affects the region of bistability more than the other parameters of the model such as the strength of connections between the populations. Especially, the parameter related to synaptic availability of synaptic resources and rate of synaptic resource depletion. Such parameters are adversely affected by impairments of axonal transport. Hence, dynamics of homogenized models of neural systems such as firing rate models still inherent impairments occurring in smaller scales of the system.

7.2 Contributions

The major contributions of this dissertation are summarized as follows.

- A novel reduced-order model is constructed for the interaction of magnetic nanoparticles and kinesin meditated axonal transport to study effects of perturbation on dynamics of intracellular transport.
- A mathematical model is developed for Ca^{2+} dynamics in the ASH neuron of *C. elegans*. No previous model existed that could capture the full dynamics of Ca^{2+} transients in ASH neuron including its “on” and “off” response.
- The mathematical model for Ca^{2+} dynamics in the ASH neuron of *C. elegans* is used to propose potential changes in the cell, induced by aging or exposure to oxidative stress.
- Constructing networks with multiple modes in their degree distributions are proposed as a method to create networks with high rich-club coefficient.
- Neural networks with high rich-club coefficient are shown to be more robust to impairment of their synapses.

- Synaptic impairment scenarios are proposed that can reflect defects in subcellular dynamics of neurons specifically deficiencies in intracellular transport. Synaptic impairment scenarios that are correlated with topology or activity of the network are shown to be detrimental.
- Stationary solution of the Fokker-Planck equation is proposed as a mean to construct probabilistic bifurcation diagrams for stochastic nonlinear dynamical systems in the presence of additive and multiplicative noise.
- Stochastic firing rate model is used to study effects of impairment on working memory. Impairments related to synaptic dynamic that are linked to deficiencies in intracellular transport are shown to be most harmful.

7.3 Future Research

The proposed method of using magnetic nanoparticles to perturb transport of cargos by motor proteins needs to be tested experimentally. *In vitro* studies can be used to calibrate the model and test usefulness of the reduced-order model. *In vivo* studies will be more difficult because delivering enough particles into cells is challenging. Moreover, the size of the particles can also be a limiting factor. The particles need to be large enough to have enough magnetic material to create effective forces, yet they must not be too large to cause significant side effects by interfering with every aspect of the cell. Different characteristics of the external magnetic field can also be considered in experiments and in modeling. For instance, effects of spatial gradients or time varying magnetic fields on the behavior of the magnetic nanoparticles and their interaction with the transport of cargos can be studied. More importantly, the reduced-order-model should be coupled with models of impaired transport. The results of such study will show if healthy and defected axonal transport can be distinguished by perturbing transport of cargos by spatial and temporal varying forces (caused here by magnetic nanoparticles).

The findings of the mathematical model (those not already investigated in the available literature) of ASH neuron in *C. elegans* need to be verified experimentally. Such experiments can explore the complex stimuli that is investigated in the model. To that end, new experimental setups might be necessary in order to provide stimulus with complex transients such as those explored with the model. Moreover, knockouts in the actual model organism can be carried out to investigate if they agree with the *in silico* knockouts in the model. The model can also be expanded by incorporating interaction of other neurons with ASH. Moreover, the model can be more realistic if there were available data for fluxes of Ca^{2+} from different channels. Measurements for different ions other than Ca^{2+} is necessary if more realistic modeling of membrane voltage is also sought. Hence, electrophysiology experiments on *C. elegans* must be explored.

The network model used to study robustness of persistent activity only included excitatory neurons. Such network analysis can be improved by including inhibitory neurons and investigate how they can contribute to robustness against impairment of synapses. Moreover, more realistic models of working memory need to be implemented. To that end, long-term and short-term synaptic plasticity must be incorporated into the model. Then, similar analysis can be performed to determine how the dynamics and topology of the neural networks varies when synapses are impaired.

Models for axonal transport can be linked to dynamics of synapses. To that end, models of synapses must be developed that incorporate availability of synaptic resources at synaptic terminals. Then, the availability of the resources needs to be connected to precursor proteins that are provided by means of axonal transport. Establishing such interaction between axonal transport and synaptic dynamics will enable building multi-scale models of neural systems. Such models can be used to directly address how dynamics of neural systems in different scales affect each other.

Population models of neurons can be improved by expanding number of subpopulations. Then, each subpopulation will represent a different memory rather than state of the network (being active or silent). Then, the bifurcation analysis and effects of impairment can be investigated when network can store multiple memories. Moreover, the number of populations in the firing rate model that can adequately represent detailed network models needs to be determined. To that end, clustering algorithm and machine learning techniques can be utilized to determine which neurons have similar dynamical behavior to be grouped together. Such data-driven approach will be also applicable when real experimental data is available in order to construct the firing rate models.

Expanding number of populations is not computationally expensive when stochastic differential equations of firing rate model is considered. However, the dimension of the Fokker-Planck equation is the same as the number of populations in the firing rate models. Therefore, rate models with more population leads to high-dimensional partial differential equations. Finding the numerical solution of high-dimensional partial differential equations requires intensive computational resources. Therefore, more modern numerical schemes such as tensor decomposition methods should be utilized for higher-dimensional Fokker-Planck equations to prevent curse of dimensionality.

Appendices

Appendix A: Supplementary Tables and Figures for Chapter 3

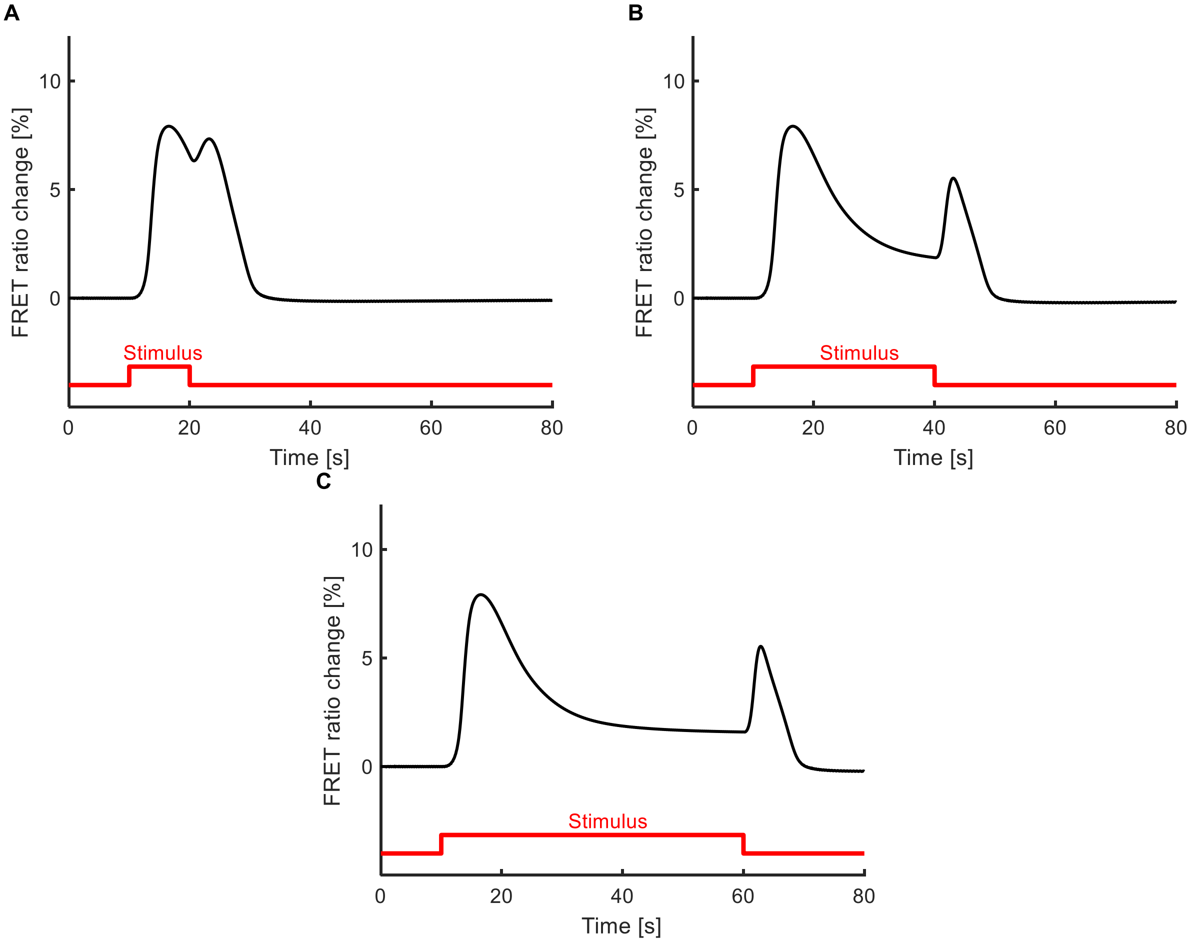

Figure A.1- The model generated Ca^{2+} transient, induced by square pulses of different durations and same strength. (A) A short pulse of 10sec still results in distinct peaks for “on” and “off” responses of different magnitudes, without the plateau region; (B) The Ca^{2+} transient induced by the pulse (30sec) delivered in the experimental data and the model results, presented here for comparison; (C) A long pulse of 50 sec results in a Ca^{2+} transient of similar shape with the one shown in (B). The response to the shorter stimulus in (A) includes an “off” response stronger than the one observed in (B) and (C), although still smaller than the “on” peak. All three Ca^{2+} transients are generated using the parameters estimated for young unstressed worms (reference case).

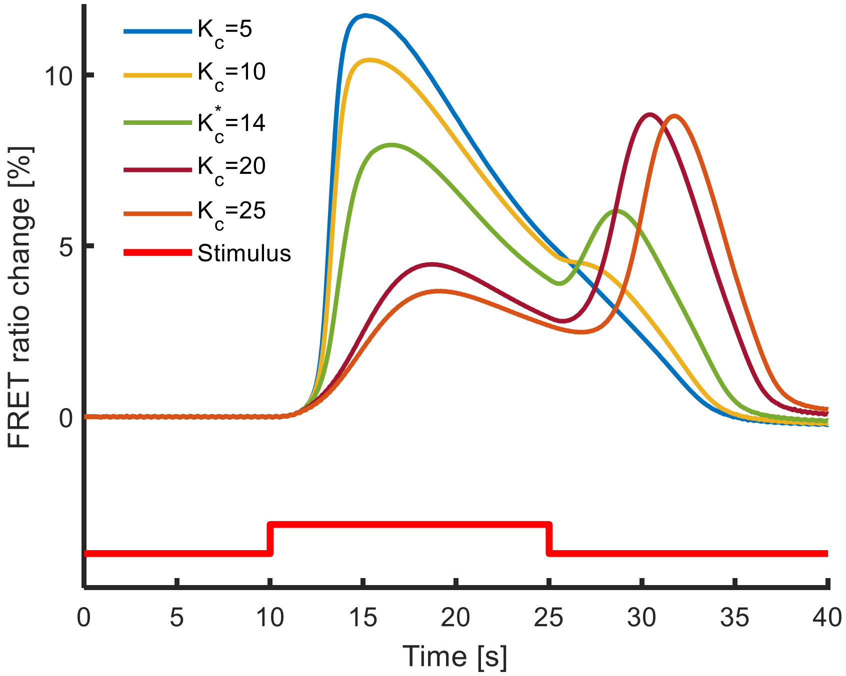

Figure A.2- The parameters of the mathematical model can be modified to capture variations in the transients that are observed experimentally. K_C in Eq. 16, which affects dynamics of IP3 , can be changed to control the relative magnitude of "on" and "off" response. A weaker "on" response leads to a stronger "off" response because when less Ca^{2+} is released from the ER during the "on" response, then there is more available to be released from ER during the "off" response. K_C^* corresponds to the value of this parameter used in the model for young unstressed worms (reference case).

Table A-1-Parameters descriptions, references, and values for young (Day 1) unstressed worms (reference case), as generated by the hybrid optimization algorithm. With bold are the selected parameters which are investigated for the aging and oxidative stress effect in the next three worm populations.

Parameters	Value	Units	Reference
G_{SERCA}	5.78	μMs^{-1}	This work
K_{SERCA}	0.10	μM	0.1-1 [304]
G_{PMCA}	14.81	μMs^{-1}	This work
K_{PMCA}	0.60	μM	0.1-1 [304]
G_{TRPV}	0.03	s^{-1}	This work
G_{IPR}	0.30	s^{-1}	This work
G_{VGCC}	0.00	$V^{-1}s^{-1}$	This work
K_{P_O}	11.77	-	This work
k_{P_o}	6.61	s^{-1}	This work
$k^-_{P_o}$	0.30	s^{-1}	This work
k_{P_1}	0.44	s^{-1}	This work
$k^-_{P_1}$	0.29	s^{-1}	This work
k_{P_2}	0.24	s^{-1}	This work
$k^-_{P_2}$	1.09	s^{-1}	This work
k_o	0.04	s^{-1}	This work
k^-_o	0.05	s^{-1}	This work
k_I	0.01	s^{-1}	This work
k^-_I	1.39	s^{-1}	This work
k_p	8.60	μMs^{-1}	This work
k^-_p	3.63	s^{-1}	This work
K_1	0.138	μM	[142]
K_2	1.05	μM	[142]
K_3	0.943	μM	[142]
K_4	0.144	μM	[142]
K_5	0.082	μM	[142]
k^-_2	0.21	s^{-1}	[142]
k^-_4	0.029	s^{-1}	[142]
K_c	0.23	μM	This work
K_p	14.04	-	This work
K_{P_2}	14.04	-	This work
$J_{Leak,ER}$	0.01	s^{-1}	[135]

J_{Leak}	0.39	s^{-1}	This work
γ	5.40	-	[135]
V_{rest}	-70.00	E	This work
c_{ES}	2000	$\mu\mathrm{M}$	[152]

Appendix B: Supplementary Tables and Figures for Chapter 6

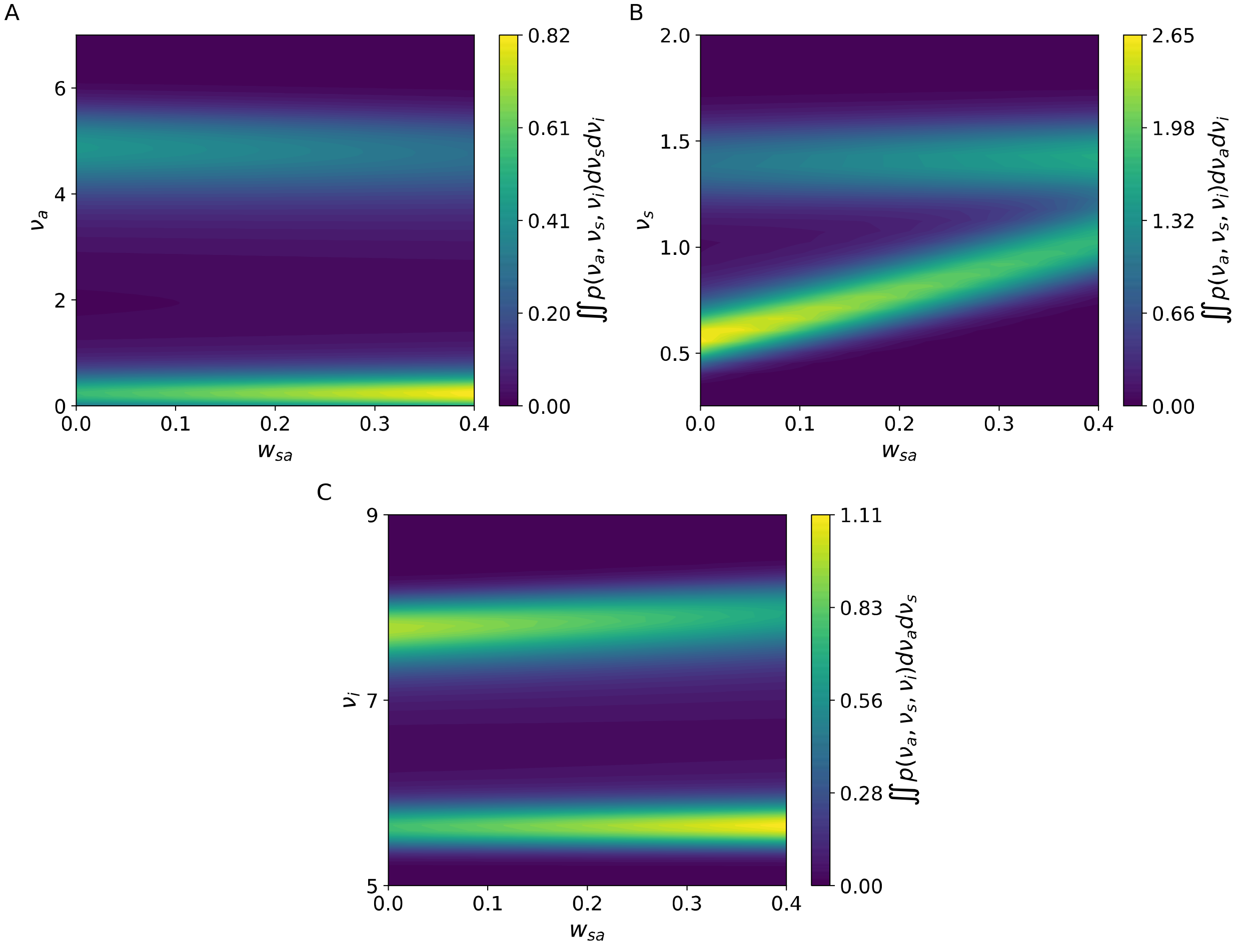

Figure B.3- Probabilistic bifurcation diagrams of the rate model when w_{sa} (the strength of the connections neurons in the silent population receives from the active population) is changed. All the other parameters of the system are the same as the ones used in Figure 6.2.

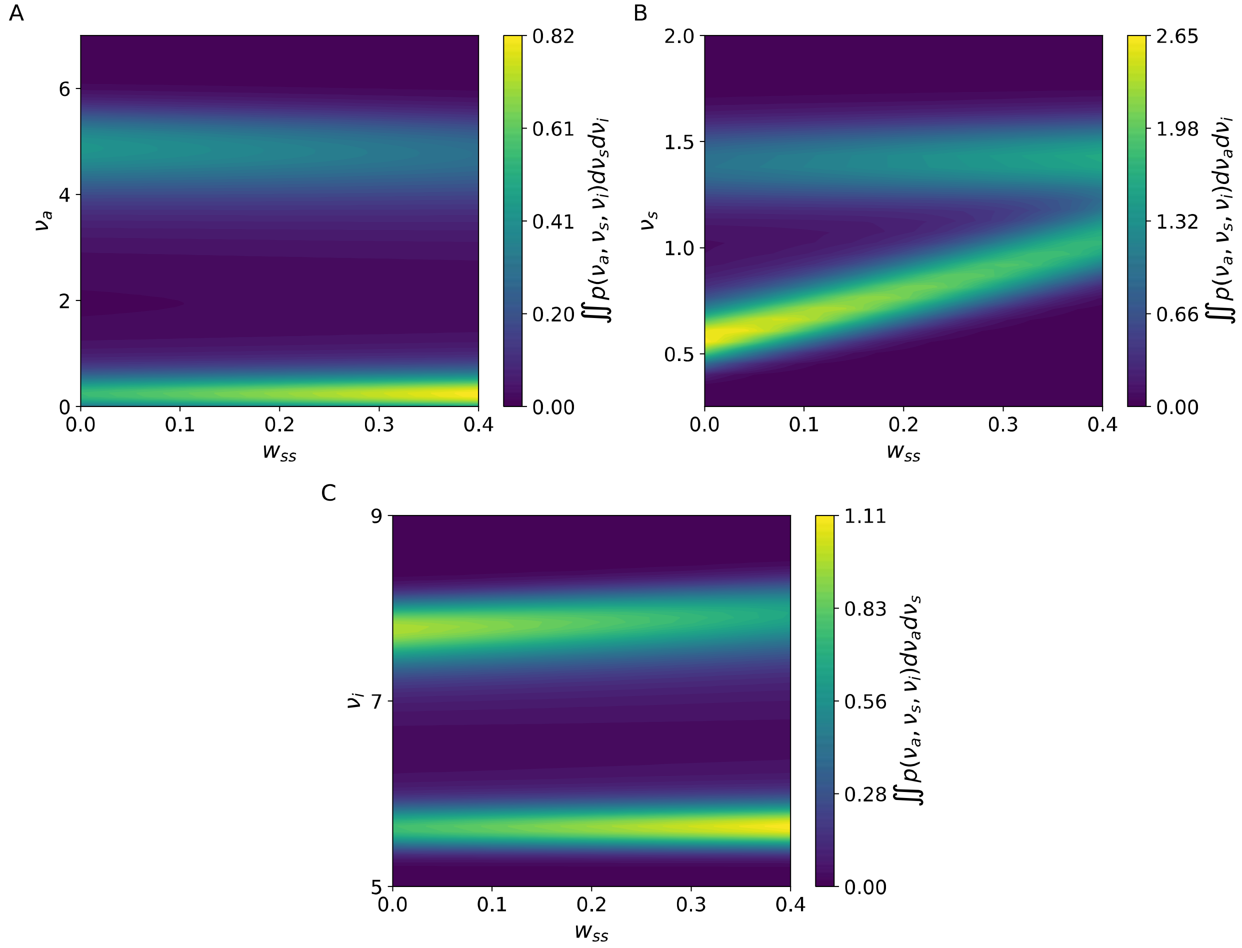

Figure B.4- Probabilistic bifurcation diagrams of the rate model when w_{ss} (the strength of the connections between neurons within the silent population) is changed. All the other parameters of the system are the same as the ones used in Figure 6.2.

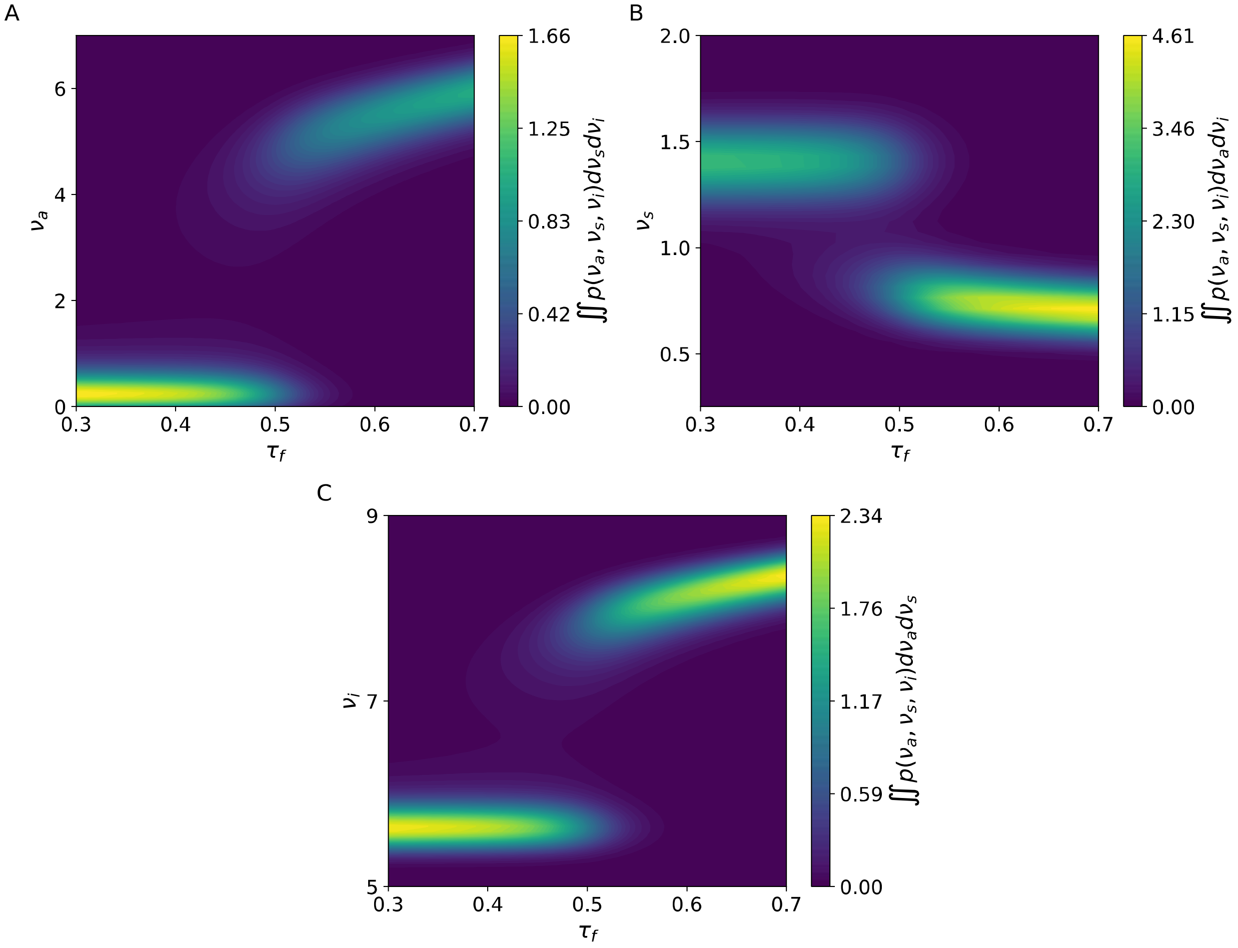

Figure B.5- Probabilistic bifurcation diagrams of the rate model when τ_f (the time constant associated with facilitation in Eq. (5.4)) is changed. All the other parameters of the system are the same as the ones used in Figure 6.2.

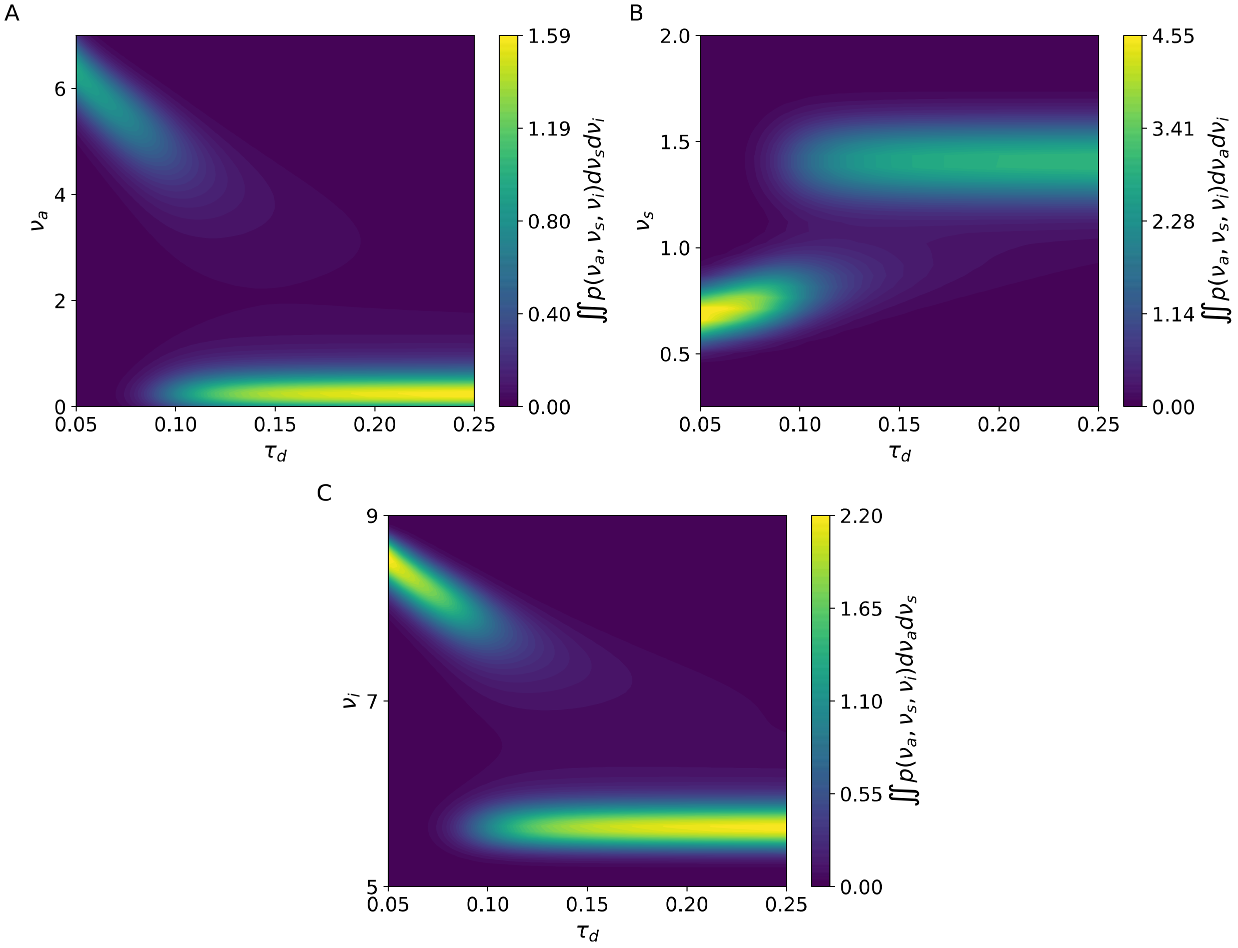

Figure B.6- Probabilistic bifurcation diagrams of the rate model when τ_d (the time constant associated with synaptic depression in Eq. (5.3)) is changed. All the other parameters of the system are the same as the ones used in Figure 6.2.

Bibliography

[1] Horner PJ, Gage FH. Regenerating the damaged central nervous system. Nature 2000;407:963–70. doi:10.1038/35039559.

[2] Dall TM, Gallo PD, Chakrabarti R, West T, Semilla AP, Storm M V. An aging population and growing disease burden will require a large and specialized health care workforce by 2025. Health Aff (Millwood) 2013;32:2013–20. doi:10.1377/hlthaff.2013.0714.

[3] de Souza/S. Nicolau E, Mendes Silva AP, Fiaux do Nascimento KK, Pereira KS, Ribeiro dos Santos G, Silva Barroso L, et al. Interaction network of tau protein, beta-amyloid protein, and amyloid protein precursor under oxidative stress in Alzheimer’s disease. Alzheimer’s Dement 2015;11:P651–2. doi:10.1016/j.jalz.2015.06.952.

[4] Selkoe DJ. Alzheimer’s Disease Is a Synaptic Failure. Science (80-) 2002;298:789–91. doi:10.1126/science.1074069.

[5] Rizzoli SO. Synaptic vesicle recycling: Steps and principles. EMBO J 2014;33:788–822. doi:10.1002/embj.201386357.

[6] Minoshima S, Cross D. In vivo imaging of axonal transport using MRI: Aging and Alzheimer’s disease. Eur J Nucl Med Mol Imaging 2008;35:89–92. doi:10.1007/s00259-007-0707-8.

[7] Milde S, Adalbert R, Elaman MH, Coleman MP. Axonal transport declines with age in two distinct phases separated by a period of relative stability. Neurobiol Aging 2015;36:971–81. doi:10.1016/j.neurobiolaging.2014.09.018.

[8] Takihara Y, Inatani M, Eto K, Inoue T, Kreymerman A, Miyake S, et al. In vivo imaging of axonal transport of mitochondria in the diseased and aged mammalian CNS. Proc Natl Acad Sci 2015;112:10515–20. doi:10.1073/pnas.1509879112.

[9] De Vos KJ, Grierson AJ, Ackerley S, Miller CCJ. Role of Axonal Transport in Neurodegenerative Diseases. Annu Rev Neurosci 2008;31:151–73. doi:10.1146/annurev.neuro.31.061307.090711.

[10] Sorbara CD, Wagner NE, Ladwig A, Nikić I, Merkler D, Kleele T, et al. Pervasive Axonal Transport Deficits in Multiple Sclerosis Models. Neuron 2014;84:1183–90. doi:10.1016/j.neuron.2014.11.006.

[11] Encalada SE, Goldstein LSB. Biophysical Challenges to Axonal Transport: Motor-Cargo Deficiencies and Neurodegeneration. Annu Rev Biophys 2014;43:141–69. doi:10.1146/annurev-biophys-051013-022746.

[12] Millecamps S, Julien JP. Axonal transport deficits and neurodegenerative diseases. Nat Rev Neurosci 2013;14:161–76. doi:10.1038/nrn3380.

[13] Hirokawa N, Takemura R. Molecular motors and mechanisms of directional transport in neurons. Nat Rev Neurosci 2005;6:201–14. doi:10.1038/nrn1624.

[14] VALE R, REESE T, SHEETZ M. Identification of a novel force-generating protein, kinesin, involved in microtubule-based motility. Cell 1985;42:39–50. doi:10.1016/S0092-8674(85)80099-4.

[15] Cai D, Verhey KJ, Meyhöfer E. Tracking single Kinesin molecules in the cytoplasm of mammalian cells. Biophys J 2007;92:4137–44. doi:10.1529/biophysj.106.100206.

[16] Uemura S, Ishiwata S. Loading direction regulates the affinity of ADP for kinesin. Nat Struct Biol 2003;10:308–11. doi:10.1038/nsb911.

[17] Schnitzer MJ, Visscher K, Block SM, Schnitzer MJ, Block SM. Force production by single kinesin motors. Nat Cell Biol 2000;2:718–23. doi:10.1038/35036345.

[18] Hendricks AG, Epureanu BI, Meyhöfer E. Collective dynamics of kinesin. Phys Rev E Stat Nonlin Soft Matter Phys 2009;79:31929. doi:10.1103/PhysRevE.79.031929.

[19] Nam W, Epureanu BI, Epurenau BI. Metrics for characterizing collective transport by multiple dimeric kinesins. Phys Rev E Stat Nonlin Soft Matter Phys 2012;86:51916. doi:10.1103/PhysRevE.86.051916.

[20] Kopeikina KJ, Wegmann S, Pitstick R, Carlson GA, Bacskai BJ, Betensky RA, et al. Tau Causes Synapse Loss without Disrupting Calcium Homeostasis in the rTg4510 Model of Tauopathy. PLoS One 2013;8:e80834. doi:10.1371/journal.pone.0080834.

[21] Shemesh OA, Erez H, Ginzburg I, Spira ME. Tau-Induced Traffic Jams Reflect Organelles Accumulation at Points of Microtubule Polar Mismatching. Traffic 2008;9:458–71. doi:10.1111/j.1600-0854.2007.00695.x.

[22] Jones R. Neurodegenerative disorders: Axonal traffic jams. Nat Rev Neurosci 2003;4:856–7. doi:10.1038/nrn1268.

[23] Liu X-A, Rizzo V, Puthanveettil S. Pathologies of axonal transport in neurodegenerative diseases. Transl Neurosci 2012;3:355–72. doi:10.2478/s13380-012-0044-7.

[24] Vershinin M, Carter BC, Razafsky DS, King SJ, Gross SP. Multiple-motor based transport and its regulation by Tau. Proc Natl Acad Sci U S A 2007;104:87–92. doi:10.1073/pnas.0607919104.

[25] Dixit R, Ross JL, Goldman YE, Holzbaur ELF. Differential regulation of dynein and kinesin motor proteins by tau. Science 2008;319:1086–9. doi:10.1126/science.1152993.

[26] Nam W, Epureanu BI. Highly loaded behavior of kinesins increases the robustness of transport under high resisting loads. PLoS Comput Biol 2015;11:e1003981. doi:10.1371/journal.pcbi.1003981.

[27] Nam W, Epureanu BI. Effects of Obstacles on the Dynamics of Kinesins, Including Velocity and Run Length, Predicted by a Model of Two Dimensional Motion. PLoS One 2016;11:e0147676. doi:10.1371/journal.pone.0147676.

[28] Nam W, Epureanu BI. Dynamic model for kinesin-mediated long-range transport and its local traffic jam caused by tau proteins. Phys Rev E 2017;95:12405. doi:10.1103/PhysRevE.95.012405.

[29] Leduc C, Padberg-Gehle K, Varga V, Helbing D, Diez S, Howard J. Molecular crowding creates traffic jams of kinesin motors on microtubules. Proc Natl Acad Sci U S A 2012;109:6100–5. doi:10.1073/pnas.1107281109.

[30] Miedema DM, Kushwaha VS, Denisov D V, Acar S, Nienhuis B, Peterman EJG, et al. Correlation Imaging Reveals Specific Crowding Dynamics of Kinesin Motor Proteins n.d. doi:10.1103/PhysRevX.7.041037.

[31] Goldstein AY, Wang X, Schwarz TL. Axonal transport and the delivery of pre-synaptic components. Curr Opin Neurobiol 2008;18:495–503. doi:10.1016/j.conb.2008.10.003.

[32] Stokin GB, Goldstein LSB. Axonal Transport and Alzheimer's Disease. Annu Rev Biochem 2006;75:607–27. doi:10.1146/annurev.biochem.75.103004.142637.

[33] Izhikevich EM. Which Model to Use for Cortical Spiking Neurons? IEEE Trans Neural Networks 2004;15:1063–70. doi:10.1109/TNN.2004.832719.

[34] Traub RD, Wong RK, Miles R, Michelson H. A model of a CA3 hippocampal pyramidal neuron incorporating voltage-clamp data on intrinsic conductances. J Neurophysiol 1991;66:635–50. doi:10.1152/jn.1991.66.2.635.

[35] Stein RB. Some models of neuronal variability. Biophys J 1967;7:37–68. doi:10.1016/S0006-3495(67)86574-3.

[36] Hodgkin a L, Huxley a F. A quantitative description of membrane current and its applicaiton to conduction and excitation in nerve. J Physiol 1952;117:500–44. doi:10.1016/S0092-8240(05)80004-7.

[37] Boccaletti S, Latora V, Moreno Y, Chavez M, Hwang D-U. Complex networks: Structure

and dynamics. Phys Rep 2006;424:175–308. doi:10.1016/J.PHYSREP.2005.10.009.

[38] Watts DJ, Strogatz SH. Collective dynamics of “small-world” networks. Nature 1998;393:440–2. doi:10.1038/30918.

[39] Netoff TI, Clewley R, Arno S, Keck T, White JA. Epilepsy in small-world networks. J Neurosci 2004;24:8075–83. doi:10.1523/JNEUROSCI.1509-04.2004.

[40] Percha B, Dzakpasu R, Żochowski M, Parent J. Transition from local to global phase synchrony in small world neural network and its possible implications for epilepsy. Phys Rev E 2005;72:31909. doi:10.1103/PhysRevE.72.031909.

[41] Towlson EK, Vertes PE, Ahnert SE, Schafer WR, Bullmore ET. The Rich Club of the C. elegans Neuronal Connectome. J Neurosci 2013;33:6380–7. doi:10.1523/JNEUROSCI.3784-12.2013.

[42] White JG, Southgate E, Thomson JN, Brenner S. The Structure of the Nervous System of the Nematode Caenorhabditis elegans. Philos Trans R Soc B Biol Sci 1986;314:1–340. doi:10.1098/rstb.1986.0056.

[43] Varshney LR, Chen BL, Paniagua E, Hall DH, Chklovskii DB. Structural Properties of the Caenorhabditis elegans Neuronal Network. PLoS Comput Biol 2011;7:e1001066. doi:10.1371/journal.pcbi.1001066.

[44] van den Heuvel MP, Stam CJ, Boersma M, Hulshoff Pol HE. Small-world and scale-free organization of voxel-based resting-state functional connectivity in the human brain. Neuroimage 2008;43:528–39. doi:10.1016/j.neuroimage.2008.08.010.

[45] Sporns O. The human connectome: a complex network. Ann N Y Acad Sci 2011;1224:109–25. doi:10.1111/j.1749-6632.2010.05888.x.

[46] Stopford CL, Thompson JC, Neary D, Richardson AMT, Snowden JS. Working memory, attention, and executive function in Alzheimer’s disease and frontotemporal dementia. Cortex 2012;48:429–46. doi:10.1016/j.cortex.2010.12.002.

[47] Curtis CE, D’Esposito M. Persistent activity in the prefrontal cortex during working memory. Trends Cogn Sci 2003;7:415–23. doi:10.1016/S1364-6613(03)00197-9.

[48] Roxin A, Riecke H, Solla SA. Self-Sustained Activity in a Small-World Network of Excitable Neurons. Phys Rev Lett 2004;92:198101. doi:10.1103/PhysRevLett.92.198101.

[49] Wang XJ. Synaptic basis of cortical persistent activity: the importance of NMDA receptors to working memory. J Neurosci 1999;19:9587–603. doi:10.1523/JNEUROSCI.19-21-09587.1999.

[50] Gourgou E, Chronis N, Gourgou Chronis, N. E. Chemically induced oxidative stress affects ASH neuronal function and behavior in C. elegans. Sci Rep 2016;6:38147. doi:10.1038/srep38147.

[51] Neuberger T, Schöpf B, Hofmann H, Hofmann M, von Rechenberg B. Superparamagnetic nanoparticles for biomedical applications: Possibilities and limitations of a new drug delivery system. J Magn Magn Mater 2005;293:483–96. doi:10.1016/j.jmmm.2005.01.064.

[52] Thorek DLJ, Chen AK, Czupryna J, Tsourkas A. Superparamagnetic iron oxide nanoparticle probes for molecular imaging. Ann Biomed Eng 2006;34:23–38. doi:10.1007/s10439-005-9002-7.

[53] Laurent S, Dutz S, Häfeli UO, Mahmoudi M. Magnetic fluid hyperthermia: focus on superparamagnetic iron oxide nanoparticles. Adv Colloid Interface Sci 2011;166:8–23. doi:10.1016/j.cis.2011.04.003.

[54] Colombo M, Carregal-Romero S, Casula MF, Gutiérrez L, Morales MP, Böhm IB, et al. Biological applications of magnetic nanoparticles. Chem Soc Rev 2012;41:4306–34. doi:10.1039/c2cs15337h.

[55] Satoh A. Introduction to practice of molecular simulation : molecular dynamics, Monte Carlo, Brownian dynamics, Lattice Boltzmann, dissipative particle dynamics. Elsevier; 2011.

[56] Nayfeh AH. Reduced-Order Models of Weakly Nonlinear Spatially Continuous Systems. Nonlinear Dyn 1998;16:105–25. doi:10.1023/A:1008281121523.

[57] Lucia DJ, Beran PS, Silva WA. Reduced-order modeling: new approaches for computational physics. Prog Aerosp Sci 2004;40:51–117. doi:10.1016/j.paerosci.2003.12.001.

[58] Masri SF, Caffrey JP, Caughey TK, Smyth AW, Chassiakos AG. A General Data-Based Approach for Developing Reduced-Order Models of Nonlinear MDOF Systems. Nonlinear Dyn 2005;39:95–112. doi:10.1007/s11071-005-1916-y.

[59] Boukouvala F, Gao Y, Muzzio F, Ierapetritou MG. Reduced-order discrete element method modeling. Chem Eng Sci 2013;95:12–26. doi:10.1016/j.ces.2013.01.053.

[60] Rudenko O V, Hedberg CM. Nonlinear Dynamics of Grains in a Liquid-Saturated Soil. Nonlinear Dyn 2004;35:187–200.

[61] Shang L, Nienhaus K, Nienhaus GU. Engineered nanoparticles interacting with cells: size matters. J Nanobiotechnology 2014;12:5. doi:10.1186/1477-3155-12-5.

[62] Kettler K, Veltman K, van de Meent D, van Wezel A, Hendriks AJ. Cellular uptake of nanoparticles as determined by particle properties, experimental conditions, and cell type. Environ Toxicol Chem 2014;33:481–92. doi:10.1002/etc.2470.

[63] Adjei IM, Sharma B, Labhasetwar V. Nanoparticles: cellular uptake and cytotoxicity. Adv Exp Med Biol 2014;811:73–91. doi:10.1007/978-94-017-8739-0_5.

[64] Ong BH, Devaraj NK. Superparamagnetic Nanoparticles. vol. 5, Berlin, Heidelberg:

Springer Berlin Heidelberg; 2010, p. 375–93. doi:10.1007/8611_2010_24.

[65] Rouhana LL, Schlenoff JB. Aggregation resistant zwitterated superparamagnetic nanoparticles. J Nanoparticle Res 2012;14:835. doi:10.1007/s11051-012-0835-3.

[66] Nakata K, Hu Y, Uzun O, Bakr O, Stellacci F. Chains of Superparamagnetic Nanoparticles. Adv Mater 2008;20:4294–9. doi:10.1002/adma.200800022.

[67] Peng X, Min Y, Ma T, Luo W, Yan M. Two-dimensional Monte Carlo simulations of structures of a suspension comprised of magnetic and nonmagnetic particles in uniform magnetic fields. J Magn Magn Mater 2009;321:1221–6. doi:10.1016/j.jmmm.2008.11.011.

[68] Hirokawa N, Noda Y. Intracellular transport and kinesin superfamily proteins, KIFs: structure, function, and dynamics. Physiol Rev 2008;88:1089–118. doi:10.1152/physrev.00023.2007.

[69] Brady ST. A novel brain ATPase with properties expected for the fast axonal transport motor. Nature 1985;317:73–5. doi:10.1038317073a0.

[70] Hoyt MA. Cellular roles of kinesin and related proteins. Curr Opin Cell Biol 1994;6:63–8. doi:10.10160955-0674(94)90117-1.

[71] Fazal FM, Block SM. Optical tweezers study life under tension. Nat Photonics 2011;5:318–21. doi:10.1038/nphoton.2011.100.

[72] Block SM, Goldstein LSB, Schnapp BJ. Bead movement by single kinesin molecules studied with optical tweezers. Nature 1990;348:348–52. doi:10.1038/348348a0.

[73] Svoboda K, Schmidt CF, Schnapp BJ, Block SM. Direct observation of kinesin stepping by optical trapping interferometry. Nature 1993;365:721–7. doi:10.1038/365721a0.

[74] Vale RD, Funatsu T, Pierce DW, Romberg L, Harada Y, Yanagida T. Direct observation of single kinesin molecules moving along microtubules. Nature 1996;380:451–3. doi:10.1038/380451a0.

[75] Hendricks AG, Epureanu BI, Meyhöfer E. Mechanistic mathematical model of kinesin under time and space fluctuating loads. Nonlinear Dyn 2008;53:303–20. doi:10.1007/s11071-007-9315-1.

[76] Visscher K, Schnitzer MJ, Block SM. Single kinesin molecules studied with a molecular force clamp. Nature 1999;400:184–9. doi:10.1038/22146.

[77] Kojima H, Muto E, Higuchi H, Yanagida T. Mechanics of single kinesin molecules measured by optical trapping nanometry. Biophys J 1997;73:2012–22. doi:10.1016/S0006-3495(97)78231-6.

[78] Fallesen TL, Macosko JC, Holzwarth G. Force-velocity relationship for multiple kinesin motors pulling a magnetic bead. Eur Biophys J 2011;40:1071–9. doi:10.1007/s00249-011-

0724-1.

[79] Wei J, Kawaguchi Y, Yu B, Li F, Zhang C. Microstructures and rheology of micellar surfactant solution by Brownian dynamics simulation. Nonlinear Dyn 2010;61:503–15. doi:10.1007/s11071-010-9667-9.

[80] Satoh A. Practice of Dissipative Particle Dynamics Simulations. In: Satoh A, editor. Introd. to Pract. Mol. Simul., London: Elsevier; 2011, p. 187–218. doi:10.1016/B978-0-12-385148-2.00006-9.

[81] Satoh A, Chantrell RW, Kamiyama S-I, Coverdale GN. Two-Dimensional Monte Carlo Simulations to Capture Thick Chainlike Clusters of Ferromagnetic Particles in Colloidal Dispersions. J Colloid Interface Sci 1996;178:620–7. doi:10.1006/jcis.1996.0159.

[82] Aoshima M, Satoh A. Two-dimensional Monte Carlo simulations of a colloidal dispersion composed of polydisperse ferromagnetic particles in an applied magnetic field. J Colloid Interface Sci 2005;288:475–88. doi:httpdx.doi.org10.1016j.jcis.2005.02.093.

[83] Zhu Y, Umehara N, Ido Y, Sato A. Computer simulation of structures and distributions of particles in MAGIC fluid. J Magn Magn Mater 2006;302:96–104. doi:10.1016/j.jmmm.2005.08.015.

[84] Nam W, Epureanu BI. The effects of viscoelastic fluid on kinesin transport. J Phys Condens Matter 2012;24:375103. doi:10.1088/0953-8984/24/37/375103.

[85] Kou SC, Cherayil BJ, Min W, English BP, Xie XS. Single-molecule Michaelis-Menten equations. J Phys Chem B 2005;109:19068–81. doi:10.1021/jp051490q.

[86] Carter NJ, Cross RA. Mechanics of the kinesin step. Nature 2005;435:308–12. doi:10.1038/nature03528.

[87] Luby-Phelps K. Cytoarchitecture and Physical Properties of Cytoplasm: Volume, Viscosity, Diffusion, Intracellular Surface Area. Int. Rev. Cytol., vol. 192, 1999, p. 189–221. doi:10.1016/S0074-7696(08)60527-6.

[88] Kühn T, Ihalainen TO, Hyväluoma J, Dross N, Willman SF, Langowski J, et al. Protein Diffusion in Mammalian Cell Cytoplasm. PLoS One 2011;6:e22962. doi:10.1371/journal.pone.0022962.

[89] Svoboda K, Block SM. Force and velocity measured for single kinesin molecules. Cell 1994;77:773–84. doi:10.1016/0092-8674(94)90060-4.

[90] Nishiyama M, Higuchi H, Yanagida T. Chemomechanical coupling of the forward and backward steps of single kinesin molecules. Nat Cell Biol 2002;4:790–7. doi:10.1038/ncb857.

[91] Zucker RS, Regehr WG. Short-Term Synaptic Plasticity. Annu Rev Physiol 2002;64:355–405. doi:10.1146/annurev.physiol.64.092501.114547.

[92] Graupner M, Brunel N. Calcium-based plasticity model explains sensitivity of synaptic changes to spike pattern, rate, and dendritic location. Proc Natl Acad Sci 2012;109:3991–6. doi:10.1073/pnas.1109359109.

[93] Higgins D, Graupner M, Brunel N. Memory Maintenance in Synapses with Calcium-Based Plasticity in the Presence of Background Activity. PLoS Comput Biol 2014;10:e1003834. doi:10.1371/journal.pcbi.1003834.

[94] Zhang H, Liu J, Sun S, Pchitskaya E, Popugaeva E, Bezprozvanny I. Calcium Signaling, Excitability, and Synaptic Plasticity Defects in a Mouse Model of Alzheimer's Disease. J Alzheimer's Dis 2015;45:561–80. doi:10.3233/JAD-142427.

[95] Ye J, Rozdeba PJ, Morone UI, Daou A, Abarbanel HDI. Estimating the biophysical properties of neurons with intracellular calcium dynamics. Phys Rev E 2014;89:62714. doi:10.1103/PhysRevE.89.062714.

[96] Chalasani SH, Chronis N, Tsunozaki M, Gray JM, Ramot D, Goodman MB, et al. Dissecting a circuit for olfactory behaviour in Caenorhabditis elegans. Nature 2007;450:63–70.

[97] Hilliard MA, Apicella AJ, Kerr R, Suzuki H, Bazzicalupo P, Schafer WR. In vivo imaging of C. elegans ASH neurons: cellular response and adaptation to chemical repellents. EMBO J 2005;24:63–72. doi:10.1038/sj.emboj.7600493.

[98] Zahratka JA, Williams PD, Summers PJ, Komuniecki RW, Bamber BA. Serotonin differentially modulates Ca2+ transients and depolarization in a C. elegans nociceptor. J Neurophysiol 2015;113:1041–50. doi:10.1152/jn.00665.2014.

[99] Budde T, Meuth S, Pape H-C. Calcium-dependent inactivation of neuronal calcium channels. Nat Rev Neurosci 2002;3:873–83.

[100] Busch KE, Laurent P, Soltesz Z, Murphy RJ, Faivre O, Hedwig B, et al. Tonic signaling from O2 sensors sets neural circuit activity and behavioral state. Nat Neurosci 2012;15:581–91. doi:http://www.nature.com/neuro/journal/v15/n4/abs/nn.3061.html#supplementary-information.

[101] Kato HK, Kassai H, Watabe AM, Aiba A, Manabe T. Functional coupling of the metabotropic glutamate receptor, InsP3 receptor and L-type Ca2+ channel in mouse CA1 pyramidal cells. J Physiol 2012;590:3019–34. doi:10.1113/jphysiol.2012.232942.

[102] Williams PDE, Zahratka JA, Rodenbeck M, Wanamaker J, Linzie H, Bamber BA. Serotonin disinhibits a Caenorhabditis elegans sensory neuron by suppressing Ca ++ -dependent negative feedback. J Neurosci 2018;38:1908–17. doi:10.1523/JNEUROSCI.1908-17.2018.

[103] Chung SH, Sun L, Gabel C V. In vivo Neuronal Calcium Imaging in C. elegans 2013:e50357. doi:doi:10.3791/50357.

[104] Nguyen JP, Shipley FB, Linder AN, Plummer GS, Liu M, Setru SU, et al. Whole-brain

calcium imaging with cellular resolution in freely behaving Caenorhabditis elegans. Proc Natl Acad Sci 2016;113:E1074–81. doi:10.1073/pnas.1507110112.

[105] Guo M, Wu TH, Song YX, Ge MH, Su CM, Niu WP, et al. Reciprocal inhibition between sensory ASH and ASI neurons modulates nociception and avoidance in Caenorhabditis elegans. Nat Commun 2015;6:5655. doi:10.1038/ncomms6655.

[106] Li G, Gong J, Lei H, Liu J, Xu XZS. Promotion of behavior and neuronal function by reactive oxygen species in C. elegans. Nat Commun 2016;7:13234. doi:10.1038/ncomms13234http://www.nature.com/articles/ncomms13234#supplementary-information.

[107] Leinwand SG, Chalasani SH. Neuropeptide signaling remodels chemosensory circuit composition in Caenorhabditis elegans. Nat Neurosci 2013;16:1461–7. doi:10.1038/nn.3511.

[108] Tsunozaki M, Chalasani SH, Bargmann CI. A behavioral switch: cGMP and PKC signaling in olfactory neurons reverses odor preference in C. elegans. Neuron 2008;59:959–71. doi:10.1016/j.neuron.2008.07.038.

[109] Shipley F, Clark C, Alkema M, Leifer A. Simultaneous optogenetic manipulation and calcium imaging in freely moving C. elegans. Front Neural Circuits 2014;8. doi:10.3389/fncir.2014.00028.

[110] Kim E, Sun L, Gabel C V, Fang-Yen C. Long-Term Imaging of Caenorhabditis elegans Using Nanoparticle-Mediated Immobilization. PLoS One 2013;8:e53419. doi:10.1371/journal.pone.0053419.

[111] Gabel C V, Gabel H, Pavlichin D, Kao A, Clark DA, Samuel ADT. Neural Circuits Mediate Electrosensory Behavior in Caenorhabditis elegans. J Neurosci 2007;27:7586–96. doi:10.1523/jneurosci.0775-07.2007.

[112] Chokshi TV, Bazopoulou D, Chronis N. An automated microfluidic platform for calcium imaging of chemosensory neurons in Caenorhabditis elegans. Lab Chip 2010;10:2758. doi:10.1039/c004658b.

[113] Chronis N, Zimmer M, Bargmann CI. Microfluidics for in vivo imaging of neuronal and behavioral activity in Caenorhabditis elegans. Nat Meth 2007;4:727–31. doi:http://www.nature.com/nmeth/journal/v4/n9/suppinfo/nmeth1075_S1.html.

[114] Chung K, Crane MM, Lu H. Automated on-chip rapid microscopy, phenotyping and sorting of C. elegans. Nat Meth 2008;5:637–43. doi:http://www.nature.com/nmeth/journal/v5/n7/suppinfo/nmeth.1227_S1.html.

[115] Ben-Yakar A, Chronis N, Lu H. Microfluidics for the analysis of behavior, nerve regeneration, and neural cell biology in C. elegans. Curr Opin Neurobiol 2009;19:561–7. doi:10.1016/j.conb.2009.10.010.

[116] Chokshi TV, Bazopoulou D, Chronis N. Probing the physiology of ASH neuron in Caenorhabditis elegans using electric current stimulation. Appl Phys Lett 2011;99:53702–537023. doi:10.1063/1.3615821.

[117] Wang W, Xu ZJ, Wu YQ, Qin LW, Li ZY, Wu ZX. Off-response in ASH neurons evoked by CuSO4 requires the TRP channel OSM-9 in Caenorhabditis elegans. Biochem Biophys Res Commun 2015;461:463–8. doi:10.1016/j.bbrc.2015.04.017.

[118] Kato S, Xu Y, Cho CE, Abbott LF, Bargmann CI. Temporal Responses of C. elegans Chemosensory Neurons Are Preserved in Behavioral Dynamics. Neuron 2014;81:616–28. doi:10.1016/j.neuron.2013.11.020.

[119] Krzyzanowski MC, Brueggemann C, Ezak MJ, Wood JF, Michaels KL, Jackson CA, et al. The C. elegans cGMP-Dependent Protein Kinase EGL-4 Regulates Nociceptive Behavioral Sensitivity. PLOS Genet 2013;9:e1003619. doi:10.1371/journal.pgen.1003619.

[120] Rakowski F, Srinivasan J, Sternberg P, Karbowski J. Synaptic polarity of the interneuron circuit controlling C. elegans locomotion. Front Comput Neurosci 2013;7. doi:10.3389/fncom.2013.00128.

[121] Tanimoto Y, Yamazoe-Umemoto A, Fujita K, Kawazoe Y, Miyanishi Y, Yamazaki SJ, et al. Calcium dynamics regulating the timing of decision-making in C. elegans. Elife 2017;6:e21629. doi:10.7554/eLife.21629.

[122] Thiele TR, Faumont S, Lockery SR. The Neural Network for Chemotaxis to Tastants in Caenorhabditis elegans Is Specialized for Temporal Differentiation. J Neurosci 2009;29:11904–11. doi:10.1523/jneurosci.0594-09.2009.

[123] Ezcurra M, Tanizawa Y, Swoboda P, Schafer WR. Food sensitizes C. elegans avoidance behaviours through acute dopamine signalling. EMBO J 2011;30:1110–22. doi:10.1038/emboj.2011.22.

[124] Laurent P, Soltesz Z, Nelson GM, Chen C, Arellano-Carbajal F, Levy E, et al. Decoding a neural circuit controlling global animal state in C. elegans. Elife 2015;4:e04241. doi:10.7554/eLife.04241.

[125] Sassa T, Murayama T, Maruyama IN. Strongly alkaline pH avoidance mediated by ASH sensory neurons in C. elegans. Neurosci Lett 2013;555:248–52. doi:10.1016/j.neulet.2013.06.001.

[126] Kuramochi M, Doi M. A Computational Model Based on Multi-Regional Calcium Imaging Represents the Spatio-Temporal Dynamics in a Caenorhabditis elegans Sensory Neuron. PLoS One 2017;12:e0168415. doi:10.1371/journal.pone.0168415.

[127] Kahn-Kirby AH, Bargmann CI. TRP channels in C. elegans. Annu Rev Physiol 2006;68:719–36. doi:10.1146/annurev.physiol.68.040204.100715.

[128] Kahn-Kirby AH, Dantzker JL, Apicella AJ, Schafer WR, Browse J, Bargmann CI, et al. Specific polyunsaturated fatty acids drive TRPV-dependent sensory signaling in vivo. Cell 2004;119:889–900. doi:10.1016/j.cell.2004.11.005.

[129] Thibault O, Hadley R, Landfield PW. Elevated postsynaptic [Ca2+]i and L-type calcium channel activity in aged hippocampal neurons: relationship to impaired synaptic plasticity. J Neurosci 2001;21:9744–56.

[130] Thibault O, Gant JC, Landfield PW. Expansion of the calcium hypothesis of brain aging and Alzheimer's disease: minding the store. Aging Cell 2007;6:307–17. doi:10.1111/j.1474-9726.2007.00295.x.

[131] Bansaghi S, Golenar T, Madesh M, Csordas G, RamachandraRao S, Sharma K, et al. Isoform-and species-specific control of IP3 receptors by reactive oxygen species. J Biol Chem 2014. doi:10.1074/jbc.M113.504159.

[132] Gant JC, Sama MM, Landfield PW, Thibault O. Early and simultaneous emergence of multiple hippocampal biomarkers of aging is mediated by Ca2+-induced Ca2+ release. J Neurosci 2006;26:3482–90. doi:10.1523/jneurosci.4171-05.2006.

[133] Nikoletopoulou V, Tavernarakis N. Calcium homeostasis in aging neurons. Front Genet 2012;3. doi:10.3389/fgene.2012.00200.

[134] Keener JP, Sneyd J. Mathematical physiology. vol. 1. Springer; 2009.

[135] Croisier H, Tan X, Perez-Zoghbi JF, Sanderson MJ, Sneyd J, Brook BS. Activation of store-operated calcium entry in airway smooth muscle cells: insight from a mathematical model. PLoS One 2013;8:e69598. doi:10.1371/journal.pone.0069598.

[136] Nilius B, Talavera K, Owsianik G, Prenen J, Droogmans G, Voets T. Gating of TRP channels: a voltage connection? J Physiol 2005;567:35–44. doi:10.1113/jphysiol.2005.088377.

[137] Esposito G, Amoroso MR, Bergamasco C, Di Schiavi E, Bazzicalupo P. The G Protein regulators EGL-10 and EAT-16, the Giα GOA-1 and the Gqα EGL-30 modulate the response of the C. elegansASH polymodal nociceptive sensory neurons to repellents. BMC Biol 2010;8:138. doi:10.1186/1741-7007-8-138.

[138] Roayaie K, Crump JG, Sagasti A, Bargmann CI. The Gα Protein ODR-3 Mediates Olfactory and Nociceptive Function and Controls Cilium Morphogenesis in C. elegans Olfactory Neurons. Neuron 1998;20:55–67. doi:http://dx.doi.org/10.1016/S0896-6273(00)80434-1.

[139] Matta JA, Miyares RL, Ahern GP. TRPV1 is a novel target for omega-3 polyunsaturated fatty acids. J Physiol 2007;578:397–411. doi:10.1113/jphysiol.2006.121988.

[140] Li Y-X, Rinzel J. Equations for InsP3 Receptor-mediated [Ca2+]i Oscillations Derived from a Detailed Kinetic Model: A Hodgkin-Huxley Like Formalism. J Theor Biol 1994;166:461–73. doi:10.1006/jtbi.1994.1041.

[141] Tang Y, Stephenson JL, Othmer HG. Simplification and analysis of models of calcium dynamics based on IP3-sensitive calcium channel kinetics. Biophys J 1996;70:246–63. doi:10.1016/S0006-3495(96)79567-X.

[142] De Young GW, Keizer J. A single-pool inositol 1,4,5-trisphosphate-receptor-based model for agonist-stimulated oscillations in Ca2+ concentration. Proc Natl Acad Sci U S A 1992;89:9895–9. doi:10.1073/pnas.89.20.9895.

[143] Alon U. Network motifs: theory and experimental approaches. Nat Rev Genet 2007;8:450–61. doi:10.1038/nrg2102.

[144] ENDO M, TANAKA M, OGAWA Y. Calcium Induced Release of Calcium from the Sarcoplasmic Reticulum of Skinned Skeletal Muscle Fibres. Nature 1970;228:34–6. doi:10.1038/228034a0.

[145] McCormick DA, Huguenard JR. A model of the electrophysiological properties of thalamocortical relay neurons. J Neurophysiol 1992;68:1384–400.

[146] Kay AR, Wong RK. Calcium current activation kinetics in isolated pyramidal neurones of the Ca1 region of the mature guinea-pig hippocampus. J Physiol 1987;392:603–16.

[147] Lockery SR, Goodman MB. The quest for action potentials in C. elegans neurons hits a plateau. Nat Neurosci 2009;12:377–8. doi:10.1038/nn0409-377.

[148] Goodman MB, Lindsay TH, Lockery SR, Richmond JE. Electrophysiological Methods for C. elegans Neurobiology. Methods Cell Biol 2012;107:409–36. doi:10.1016/B978-0-12-394620-1.00014-X.

[149] Goodman MB, Hall DH, Avery L, Lockery SR. Active currents regulate sensitivity and dynamic range in C. elegans neurons. Neuron 1998;20:763–72.

[150] Mank M, Reiff DF, Heim N, Friedrich MW, Borst A, Griesbeck O. A FRET-Based Calcium Biosensor with Fast Signal Kinetics and High Fluorescence Change. Biophys J 2006;90:1790–6. doi:10.1529/biophysj.105.073536.

[151] Palmer AE, Tsien RY. Measuring calcium signaling using genetically targetable fluorescent indicators. Nat Protoc 2006;1:1057–65. doi:10.1038/nprot.2006.172.

[152] Egelman DM, Montague PR. Calcium dynamics in the extracellular space of mammalian neural tissue. Biophys J 1999;76:1856–67.

[153] Baylis HA, Furuichi T, Yoshikawa F, Mikoshiba K, Sattelle DB. Inositol 1,4,5-trisphosphate receptors are strongly expressed in the nervous system, pharynx, intestine, gonad and excretory cell of Caenorhabditis elegans and are encoded by a single gene (itr-1)1. J Mol Biol 1999;294:467–76. doi:https://doi.org/10.1006/jmbi.1999.3229.

[154] Mikoshiba K. IP3 receptor/Ca2+ channel: from discovery to new signaling concepts. J Neurochem 2007;102:1426–46. doi:10.1111/j.1471-4159.2007.04825.x.

[155] Di Leva F, Domi T, Fedrizzi L, Lim D, Carafoli E. The plasma membrane Ca2+ ATPase of animal cells: Structure, function and regulation. Arch Biochem Biophys 2008;476:65–74. doi:http://dx.doi.org/10.1016/j.abb.2008.02.026.

[156] Periasamy M, Kalyanasundaram A. SERCA pump isoforms: Their role in calcium transport and disease. Muscle Nerve 2007;35:430–42. doi:10.1002/mus.20745.

[157] Lockery SR, Goodman MB, Faumont S. First report of action potentials in a C. elegans neuron is premature. Nat Neurosci 2009;12:365–6; author reply 366. doi:10.1038/nn0409-365.

[158] Lindsay TH, Thiele TR, Lockery SR. Optogenetic analysis of synaptic transmission in the central nervous system of the nematode Caenorhabditis elegans. Nat Commun 2011;2:306. doi:10.1038/ncomms1304.

[159] Kraev A, Kraev N, Carafoli E. Identification and Functional Expression of the Plasma Membrane Calcium ATPase Gene Family from Caenorhabditis elegans. J Biol Chem 1999;274:4254–8. doi:10.1074/jbc.274.7.4254.

[160] Sharma V, He C, Sacca-Schaeffer J, Brzozowski E, Martin-Herranz DE, Mendelowitz Z, et al. Insight into the Family of Na(+)/Ca(2+) Exchangers of Caenorhabditis elegans. Genetics 2013;195:611–9. doi:10.1534/genetics.113.153106.

[161] Vandecaetsbeek I, Vangheluwe P, Raeymaekers L, Wuytack F, Vanoevelen J. The Ca(2+) Pumps of the Endoplasmic Reticulum and Golgi Apparatus. Cold Spring Harb Perspect Biol 2011;3:a004184. doi:10.1101/cshperspect.a004184.

[162] Vandecaetsbeek I, Raeymaekers L, Wuytack F, Vangheluwe P. Factors controlling the activity of the SERCA2a pump in the normal and failing heart. Biofactors 2009;35:484–99. doi:10.1002/biof.63.

[163] Dally S, Bredoux R, Corvazier E, Andersen JP, Clausen JD, Dode L, et al. Ca2+-ATPases in non-failing and failing heart: evidence for a novel cardiac sarco/endoplasmic reticulum Ca2+-ATPase 2 isoform (SERCA2c). Biochem J 2006;395:249–58. doi:10.1042/bj20051427.

[164] Kimura T, Nakamori M, Lueck JD, Pouliquin P, Aoike F, Fujimura H, et al. Altered mRNA splicing of the skeletal muscle ryanodine receptor and sarcoplasmic/endoplasmic reticulum Ca2+-ATPase in myotonic dystrophy type 1. Hum Mol Genet 2005;14:2189–200. doi:10.1093/hmg/ddi223.

[165] Zwaal RR, Van Baelen K, Groenen JTM, van Geel A, Rottiers V, Kaletta T, et al. The Sarco-Endoplasmic Reticulum Ca2+ ATPase Is Required for Development and Muscle Function in Caenorhabditis elegans. J Biol Chem 2001;276:43557–63. doi:10.1074/jbc.M104693200.

[166] Cho JH, Bandyopadhyay J, Lee J, Park CS, Ahnn J. Two isoforms of sarco/endoplasmic reticulum calcium ATPase (SERCA) are essential in Caenorhabditis elegans. Gene

2000;261:211–9.

[167] Van Baelen K, Vanoevelen J, Missiaen L, Raeymaekers L, Wuytack F. The Golgi PMR1 P-type ATPase of Caenorhabditis elegans. Identification of the gene and demonstration of calcium and manganese transport. J Biol Chem 2001;276:10683–91. doi:10.1074/jbc.M010553200.

[168] Cho JH, Ko KM, Singaravelu G, Ahnn J. Caenorhabditis elegans PMR1, a P-type calcium ATPase, is important for calcium/manganese homeostasis and oxidative stress response. FEBS Lett 2005;579:778–82. doi:10.1016/j.febslet.2004.12.032.

[169] Praitis V, Simske J, Kniss S, Mandt R, Imlay L, Feddersen C, et al. The Secretory Pathway Calcium ATPase PMR-1/SPCA1 Has Essential Roles in Cell Migration during Caenorhabditis elegans Embryonic Development. PLOS Genet 2013;9:e1003506. doi:10.1371/journal.pgen.1003506.

[170] Baylis HA, Vazquez-Manrique RP. Genetic analysis of IP3 and calcium signalling pathways in C. elegans. Biochim Biophys Acta 2012;1820:1253–68. doi:10.1016/j.bbagen.2011.11.009.

[171] Gower NJD, Temple GR, Schein JE, Marra M, Walker DS, Baylis HA. Dissection of the promoter region of the inositol 1,4,5-trisphosphate receptor gene, itr-1, in C. elegans: a molecular basis for cell-specific expression of IP3R isoforms1. J Mol Biol 2001;306:145–57. doi:https://doi.org/10.1006/jmbi.2000.4388.

[172] Iwasaki K, Liu DW, Thomas JH. Genes that control a temperature-compensated ultradian clock in Caenorhabditis elegans. Proc Natl Acad Sci 1995;92:10317–21.

[173] Zou W, Cheng H, Li S, Yue X, Xue Y, Chen S, et al. Polymodal Responses in C. elegans Phasmid Neurons Rely on Multiple Intracellular and Intercellular Signaling Pathways 2017;7:42295. doi:10.1038/srep42295.

[174] O'Leary T, Williams AH, Caplan JS, Marder E. Correlations in ion channel expression emerge from homeostatic tuning rules. Proc Natl Acad Sci 2013;110:E2645–54. doi:10.1073/pnas.1309966110.

[175] Kenyon C, Chang J, Gensch E, Rudner A, Tabtiang R. A C. elegans mutant that lives twice as long as wild type. Nature 1993;366:461–4. doi:10.1038/366461a0.

[176] Bargmann CI. Chemosensation in C. elegans. WormBook 2006:1–29. doi:10.1895/wormbook.1.123.1.

[177] Xiao R, Xu XZ. C. elegans TRP channels. Adv Exp Med Biol 2011;704:323–39. doi:10.1007/978-94-007-0265-3_18.

[178] Lombardi MS, Kavelaars A, Penela P, Scholtens EJ, Roccio M, Schmidt RE, et al. Oxidative stress decreases G protein-coupled receptor kinase 2 in lymphocytes via a calpain-dependent mechanism. Mol Pharmacol 2002;62:379–88.

[179] Ushio-Fukai M. Vascular signaling through G protein coupled receptors - new concepts. Curr Opin Nephrol Hypertens 2009;18:153–9. doi:10.1097/MNH.0b013e3283252efe.

[180] Alemany R, Perona JS, Sánchez-Dominguez JM, Montero E, Cañizares J, Bressani R, et al. G protein-coupled receptor systems and their lipid environment in health disorders during aging. Biochim Biophys Acta - Biomembr 2007;1768:964–75. doi:https://doi.org/10.1016/j.bbamem.2006.09.024.

[181] Kilts JD, Akazawa T, Richardson MD, Kwatra MM. Age Increases Cardiac Gαi2 Expression, Resulting in Enhanced Coupling to G Protein-coupled Receptors. J Biol Chem 2002;277:31257–62. doi:10.1074/jbc.M203640200.

[182] Zhao J, Deng Y, Jiang Z, Qing H. G Protein-Coupled Receptors (GPCRs) in Alzheimer's Disease: A Focus on BACE1 Related GPCRs. Front Aging Neurosci 2016;8. doi:10.3389/fnagi.2016.00058.

[183] Xiao R, Zhang B, Dong Y, Gong J, Xu T, Liu J, et al. A genetic program promotes C. elegans longevity at cold temperatures via a thermosensitive TRP channel. Cell 2013;152:806–17. doi:10.1016/j.cell.2013.01.020.

[184] Riera CE, Huising MO, Follett P, Leblanc M, Halloran J, Van Andel R, et al. TRPV1 pain receptors regulate longevity and metabolism by neuropeptide signaling. Cell 2014;157:1023–36. doi:10.1016/j.cell.2014.03.051.

[185] Lee JC, Choe SY. Age-related changes in the distribution of transient receptor potential vanilloid 4 channel (TRPV4) in the central nervous system of rats. J Mol Histol 2014;45:497–505. doi:10.1007/s10735-014-9578-z.

[186] Chuang HH, Lin S. Oxidative challenges sensitize the capsaicin receptor by covalent cysteine modification. Proc Natl Acad Sci U S A 2009;106:20097–102. doi:10.1073/pnas.0902675106.

[187] Ogawa N, Kurokawa T, Fujiwara K, Polat OK, Badr H, Takahashi N, et al. Functional and Structural Divergence in Human TRPV1 Channel Subunits by Oxidative Cysteine Modification. J Biol Chem 2016;291:4197–210. doi:10.1074/jbc.M115.700278.

[188] Kahya MC, Nazıroğlu M, Övey İS. Modulation of Diabetes-Induced Oxidative Stress, Apoptosis, and Ca2+ Entry Through TRPM2 and TRPV1 Channels in Dorsal Root Ganglion and Hippocampus of Diabetic Rats by Melatonin and Selenium. Mol Neurobiol 2017;54:2345–60. doi:10.1007/s12035-016-9727-3.

[189] Görlach A, Bertram K, Hudecova S, Krizanova O. Calcium and ROS: A mutual interplay. Redox Biol 2015;6:260–71. doi:http://dx.doi.org/10.1016/j.redox.2015.08.010.

[190] Todorovic SM, Jevtovic-Todorovic V. Redox Regulation of Neuronal Voltage-Gated Calcium Channels. Antioxid Redox Signal 2014;21:880–91. doi:10.1089/ars.2013.5610.

[191] Nishida M, Ishikawa T, Saiki S, Sunggip C, Aritomi S, Harada E, et al. Voltage-dependent

N-type Ca2+ channels in endothelial cells contribute to oxidative stress-related endothelial dysfunction induced by angiotensin II in mice. Biochem Biophys Res Commun 2013;434:210–6. doi:https://doi.org/10.1016/j.bbrc.2013.03.040.

[192] Thibault O, Landfield PW. Increase in single L-type calcium channels in hippocampal neurons during aging. Science (80-) 1996;272:1017–20.

[193] Zhang J, Wang X, Vikash V, Ye Q, Wu D, Liu Y, et al. ROS and ROS-Mediated Cellular Signaling. Oxid Med Cell Longev 2016;2016:18. doi:10.1155/2016/4350965.

[194] Bogeski I, Niemeyer BA. Redox regulation of ion channels. Antioxid Redox Signal 2014;21:859–62. doi:10.1089/ars.2014.6019.

[195] Lushington GH, Zaidi A, Michaelis ML. Theoretically predicted structures of plasma membrane Ca2+-ATPase and their susceptibilities to oxidation. J Mol Graph Model 2005;24:175–85. doi:https://doi.org/10.1016/j.jmgm.2005.07.003.

[196] Michaelis ML, Bigelow DJ, Schoneich C, Williams TD, Ramonda L, Yin D, et al. Decreased plasma membrane calcium transport activity in aging brain. Life Sci 1996;59:405–12.

[197] Gao J, Cohen IS, Mathias RT, Baldo GJ. The inhibitory effect of beta-stimulation on the Na/K pump current in guinea pig ventricular myocytes is mediated by a cAMP-dependent PKA pathway. Pflugers Arch 1998;435:479–84.

[198] Kaplan P, Babusikova E, Lehotsky J, Dobrota D. Free radical-induced protein modification and inhibition of Ca2+-ATPase of cardiac sarcoplasmic reticulum. Mol Cell Biochem 2003;248:41–7. doi:10.1023/A:1024145212616.

[199] Murchison D, Griffith WH. Age-related alterations in caffeine-sensitive calcium stores and mitochondrial buffering in rat basal forebrain. Cell Calcium 1999;25:439–52. doi:10.1054/ceca.1999.0048.

[200] Larsch J, Ventimiglia D, Bargmann CI, Albrecht DR. High-throughput imaging of neuronal activity in Caenorhabditis elegans. Proc Natl Acad Sci U S A 2013;110:E4266–73. doi:10.1073/pnas.1318325110.

[201] Albrecht DR, Bargmann CI. High-content behavioral analysis of Caenorhabditis elegans in precise spatiotemporal chemical environments. Nat Meth 2011;8:599–605. doi:http://www.nature.com/nmeth/journal/v8/n7/abs/nmeth.1630.html#supplementary-information.

[202] Larsch J, Flavell SW, Liu Q, Gordus A, Albrecht DR, Bargmann CI. A Circuit for Gradient Climbing in C. elegans Chemotaxis. Cell Rep 2015;12:1748–60. doi:http://dx.doi.org/10.1016/j.celrep.2015.08.032.

[203] Sporns O. Networks of the Brain. MIT press; 2010.

[204] Morgan RJ, Soltesz I. Nonrandom connectivity of the epileptic dentate gyrus predicts a major role for neuronal hubs in seizures. Proc Natl Acad Sci 2008;105:6179–84. doi:10.1073/pnas.0801372105.

[205] Crossley NA, Mechelli A, Scott J, Carletti F, Fox PT, McGuire P, et al. The hubs of the human connectome are generally implicated in the anatomy of brain disorders. Brain 2014;137:2382–95. doi:10.1093/brain/awu132.

[206] Van Essen DC, Smith SM, Barch DM, Behrens TEJ, Yacoub E, Ugurbil K. The WU-Minn Human Connectome Project: An overview. Neuroimage 2013;80:62–79. doi:10.1016/j.neuroimage.2013.05.041.

[207] Hodge MR, Horton W, Brown T, Herrick R, Olsen T, Hileman ME, et al. ConnectomeDB—Sharing human brain connectivity data. Neuroimage 2016;124:1102–7. doi:10.1016/j.neuroimage.2015.04.046.

[208] Eguíluz VM, Chialvo DR, Cecchi GA, Baliki M, Apkarian AV. Scale-Free Brain Functional Networks. Phys Rev Lett 2005;94:18102. doi:10.1103/PhysRevLett.94.018102.

[209] He Y, Chen ZJ, Evans AC. Small-World Anatomical Networks in the Human Brain Revealed by Cortical Thickness from MRI. Cereb Cortex 2007;17:2407–19. doi:10.1093/cercor/bhl149.

[210] Achard S. A Resilient, Low-Frequency, Small-World Human Brain Functional Network with Highly Connected Association Cortical Hubs. J Neurosci 2006;26:63–72. doi:10.1523/JNEUROSCI.3874-05.2006.

[211] van den Heuvel MP, Sporns O. Rich-Club Organization of the Human Connectome. J Neurosci 2011;31:15775–86. doi:10.1523/JNEUROSCI.3539-11.2011.

[212] Oh SW, Harris JA, Ng L, Winslow B, Cain N, Mihalas S, et al. A mesoscale connectome of the mouse brain. Nature 2014;508:207–14. doi:10.1038/nature13186.

[213] de Reus MA, van den Heuvel MP. Rich Club Organization and Intermodule Communication in the Cat Connectome. J Neurosci 2013;33:12929–39. doi:10.1523/JNEUROSCI.1448-13.2013.

[214] Downes JH, Hammond MW, Xydas D, Spencer MC, Becerra VM, Warwick K, et al. Emergence of a Small-World Functional Network in Cultured Neurons. PLoS Comput Biol 2012;8:e1002522. doi:10.1371/journal.pcbi.1002522.

[215] Schroeter MS, Charlesworth P, Kitzbichler MG, Paulsen O, Bullmore ET. Emergence of Rich-Club Topology and Coordinated Dynamics in Development of Hippocampal Functional Networks In Vitro. J Neurosci 2015;35:5459–70. doi:10.1523/JNEUROSCI.4259-14.2015.

[216] Fornito A, Zalesky A, Breakspear M. Graph analysis of the human connectome: Promise, progress, and pitfalls. Neuroimage 2013;80:426–44.

doi:10.1016/j.neuroimage.2013.04.087.

[217] Abbott LF, Nelson SB. Synaptic plasticity: taming the beast. Nat Neurosci 2000;3:1178–83. doi:10.1038/81453.

[218] Marder E, Thirumalai V. Cellular, synaptic and network effects of neuromodulation. Neural Networks 2002;15:479–93. doi:10.1016/S0893-6080(02)00043-6.

[219] Shankar GM, Walsh DM. Alzheimer's disease: synaptic dysfunction and Aβ. Mol Neurodegener 2009;4:48. doi:10.1186/1750-1326-4-48.

[220] Sheng M, Sabatini BL, Sudhof TC. Synapses and Alzheimer's Disease. Cold Spring Harb Perspect Biol 2012;4:a005777–a005777. doi:10.1101/cshperspect.a005777.

[221] Abuhassan K, Coyle D, Maguire L. Compensating for thalamocortical synaptic loss in Alzheimer's disease. Front Comput Neurosci 2014;8:65. doi:10.3389/fncom.2014.00065.

[222] Kamat PK, Kalani A, Rai S, Swarnkar S, Tota S, Nath C, et al. Mechanism of Oxidative Stress and Synapse Dysfunction in the Pathogenesis of Alzheimer's Disease: Understanding the Therapeutics Strategies. Mol Neurobiol 2016;53:648–61. doi:10.1007/s12035-014-9053-6.

[223] Gaál ZA, Boha R, Stam CJ, Molnár M. Age-dependent features of EEG-reactivity—Spectral, complexity, and network characteristics. vol. 479. 2010. doi:10.1016/j.neulet.2010.05.037.

[224] Smit DJA, Boersma M, van Beijsterveldt CEM, Posthuma D, Boomsma DI, Stam CJ, et al. Endophenotypes in a Dynamically Connected Brain. Behav Genet 2010;40:167–77. doi:10.1007/s10519-009-9330-8.

[225] Wang L, Li Y, Metzak P, He Y, Woodward TS. Age-related changes in topological patterns of large-scale brain functional networks during memory encoding and recognition. Neuroimage 2010;50:862–72. doi:10.1016/j.neuroimage.2010.01.044.

[226] Zhu W, Wen W, He Y, Xia A, Anstey KJ, Sachdev P, et al. Changing topological patterns in normal aging using large-scale structural networks. Neurobiol Aging 2012;33:899–913. doi:10.1016/j.neurobiolaging.2010.06.022.

[227] Wu K, Taki Y, Sato K, Qi H, Kawashima R, Fukuda H. A longitudinal study of structural brain network changes with normal aging. Front Hum Neurosci 2013;7:113. doi:10.3389/fnhum.2013.00113.

[228] Palop JJ, Chin J, Mucke L. A network dysfunction perspective on neurodegenerative diseases. Nature 2006;443:768–73. doi:10.1038/nature05289.

[229] Kosik KS. Diseases: Study neuron networks to tackle Alzheimer's. Nature 2013;503:31–2. doi:10.1038/503031a.

[230] Kocher M, Gleichgerrcht E, Nesland T, Rorden C, Fridriksson J, Spampinato M V., et al. Individual variability in the anatomical distribution of nodes participating in rich club structural networks. Front Neural Circuits 2015;9:16. doi:10.3389/fncir.2015.00016.

[231] Petersen PC, Vestergaard M, Jensen KHR, Berg RW. Premotor Spinal Network with Balanced Excitation and Inhibition during Motor Patterns Has High Resilience to Structural Division. J Neurosci 2014;34:2774–84. doi:10.1523/JNEUROSCI.3349-13.2014.

[232] Baddeley A. Working memory. Science 1992;255:556–9. doi:10.1126/science.1736359.

[233] Sakai K, Rowe JB, Passingham RE. Active maintenance in prefrontal area 46 creates distractor-resistant memory. Nat Neurosci 2002;5:479–84. doi:10.1038/nn846.

[234] Baddeley AD, Bressi S, Della Sala S, Logie R, Spinnler H. The decline of working memory in Alzheimer's disease. A longitudinal study. Brain 1991;114 (Pt 6:2521–42.

[235] Baddeley AD, Baddeley HA, Bucks RS, Wilcock GK. Attentional control in Alzheimer's disease. Brain 2001;124:1492–508. doi:10.1093/brain/124.8.1492.

[236] Shanahan M. Dynamical complexity in small-world networks of spiking neurons. Phys Rev E 2008;78:41924. doi:10.1103/PhysRevE.78.041924.

[237] Roxin A. The Role of Degree Distribution in Shaping the Dynamics in Networks of Sparsely Connected Spiking Neurons. Front Comput Neurosci 2011;5:1–15. doi:10.3389/fncom.2011.00008.

[238] Amitai Y. Membrane potential oscillations underlying firing patterns in neocortical neurons. Neuroscience 1994;63:151–61. doi:10.1016/0306-4522(94)90013-2.

[239] Stiefel KM, Gutkin BS, Sejnowski TJ. The effects of cholinergic neuromodulation on neuronal phase-response curves of modeled cortical neurons. J Comput Neurosci 2009;26:289–301. doi:10.1007/s10827-008-0111-9.

[240] Rich S, Booth V, Zochowski M. Intrinsic Cellular Properties and Connectivity Density Determine Variable Clustering Patterns in Randomly Connected Inhibitory Neural Networks. Front Neural Circuits 2016;10:82. doi:10.3389/fncir.2016.00082.

[241] Fink CG, Booth V, Zochowski M. Cellularly-Driven Differences in Network Synchronization Propensity Are Differentially Modulated by Firing Frequency. PLoS Comput Biol 2011;7:e1002062. doi:10.1371/journal.pcbi.1002062.

[242] Destexhe A, Mainen ZF, Sejnowski TJ. Kinetic models of synaptic transmission: From Ions to Networks. Methods Neural Model from Ions to Networks 1998:1–25.

[243] Hass J, Hertäg L, Durstewitz D. A Detailed Data-Driven Network Model of Prefrontal Cortex Reproduces Key Features of In Vivo Activity. PLOS Comput Biol 2016;12:e1004930. doi:10.1371/journal.pcbi.1004930.

[244] Erdös P, Rényi A. On random graphs. Publ Math 1959;6:290–7. doi:10.2307/1999405.

[245] Pozzo-Miller LD, Gottschalk W, Zhang L, McDermott K, Du J, Gopalakrishnan R, et al. Impairments in high-frequency transmission, synaptic vesicle docking, and synaptic protein distribution in the hippocampus of BDNF knockout mice. J Neurosci 1999;19:4972–83.

[246] Rubinov M, Sporns O. Complex network measures of brain connectivity: Uses and interpretations. Neuroimage 2010;52:1059–69. doi:10.1016/j.neuroimage.2009.10.003.

[247] Newman M. Networks. Oxford University Press; 2010. doi:10.1093/acprof:oso/9780199206650.001.0001.

[248] Zhou S, Mondragon RJ. The Rich-Club Phenomenon in the Internet Topology. IEEE Commun Lett 2004;8:180–2. doi:10.1109/LCOMM.2004.823426.

[249] Colizza V, Flammini A, Serrano MA, Vespignani A. Detecting rich-club ordering in complex networks. Nat Phys 2006;2:110–5. doi:10.1038/nphys209.

[250] McAuley JJ, da Fontoura Costa L, Caetano TS. Rich-club phenomenon across complex network hierarchies. Appl Phys Lett 2007;91:84103. doi:10.1063/1.2773951.

[251] Barrat A, Barthelemy M, Vespignani A. Dynamical processes on complex networks. Cambridge university press; 2008.

[252] Fransén E, Tahvildari B, Egorov A V, Hasselmo ME, Alonso AA, Stern CE. Mechanism of graded persistent cellular activity of entorhinal cortex layer v neurons. Neuron 2006;49:735–46. doi:10.1016/j.neuron.2006.01.036.

[253] Neymotin SA, McDougal RA, Bulanova AS, Zeki M, Lakatos P, Terman D, et al. Calcium regulation of HCN channels supports persistent activity in a multiscale model of neocortex. Neuroscience 2016;316:344–66. doi:10.1016/j.neuroscience.2015.12.043.

[254] Ball G, Aljabar P, Zebari S, Tusor N, Arichi T, Merchant N, et al. Rich-club organization of the newborn human brain. Proc Natl Acad Sci 2014;111:7456–61. doi:10.1073/pnas.1324118111.

[255] Izhikevich EM, Edelman GM. Large-scale model of mammalian thalamocortical systems. Proc Natl Acad Sci 2008;105:3593–8. doi:10.1073/pnas.0712231105.

[256] Holland JH. Adaptation in natural and artificial systems: an introductory analysis with applications to biology, control, and artificial intelligence. Bradford Books, MIT Press 1992:183.

[257] Hiratani N, Fukai T. Hebbian Wiring Plasticity Generates Efficient Network Structures for Robust Inference with Synaptic Weight Plasticity. Front Neural Circuits 2016;10:41. doi:10.3389/fncir.2016.00041.

[258] Sporns O, Tononi G, Edelman GM. Theoretical Neuroanatomy: Relating Anatomical and

Functional Connectivity in Graphs and Cortical Connection Matrices. Cereb Cortex 2000;10:127–41. doi:10.1093/cercor/10.2.127.

[259] Buckner RL, Sepulcre J, Talukdar T, Krienen FM, Liu H, Hedden T, et al. Cortical Hubs Revealed by Intrinsic Functional Connectivity: Mapping, Assessment of Stability, and Relation to Alzheimer's Disease. J Neurosci 2009;29:1860–73. doi:10.1523/JNEUROSCI.5062-08.2009.

[260] Wang X, Michaelis EK. Selective neuronal vulnerability to oxidative stress in the brain. Front Aging Neurosci 2010;2:12. doi:10.3389/fnagi.2010.00012.

[261] Knyazev GG, Volf N V., Belousova L V. Age-related differences in electroencephalogram connectivity and network topology. Neurobiol Aging 2015;36:1849–59. doi:10.1016/j.neurobiolaging.2015.02.007.

[262] Horsthemke W, Lefever R. Noise-Induced Transitions: Theory and Applications in Physics, Chemistry, and Biology. vol. 15. Springer Berlin Heidelberg; 2006. doi:10.1007/3-540-36852-3.

[263] Lindner B. Effects of noise in excitable systems. Phys Rep 2004;392:321–424. doi:10.1016/j.physrep.2003.10.015.

[264] Scheffer M, Bascompte J, Brock WA, Brovkin V, Carpenter SR, Dakos V, et al. Early-warning signals for critical transitions. Nature 2009;461:53–9. doi:10.1038/nature08227.

[265] Song C, Phenix H, Abedi V, Scott M, Ingalls BP, Kærn M, et al. Estimating the Stochastic Bifurcation Structure of Cellular Networks. PLoS Comput Biol 2010;6:e1000699. doi:10.1371/journal.pcbi.1000699.

[266] Kærn M, Elston TC, Blake WJ, Collins JJ. Stochasticity in gene expression: from theories to phenotypes. Nat Rev Genet 2005;6:451–64. doi:10.1038/nrg1615.

[267] Ermentrout GB, Terman DH. Mathematical Foundations of Neuroscience. vol. 35. New York, NY: Springer New York; 2010. doi:10.1007/978-0-387-87708-2.

[268] Shu Y, Hasenstaub A, McCormick DA. Turning on and off recurrent balanced cortical activity. Nature 2003;423:288–93. doi:10.1038/nature01616.

[269] Gardiner C. Stochastic Methods: A Handbook for the Natural and Social Sciences. vol. 13. Berlin, Heidelberg: Springer Berlin Heidelberg; 2009. doi:10.1007/978-3-662-02377-8.

[270] Spencer BF, Bergman LA. On the numerical solution of the Fokker-Planck equation for nonlinear stochastic systems. Nonlinear Dyn 1993;4:357–72. doi:10.1007/BF00120671.

[271] Kumar P, Narayanan S. Solution of Fokker-Planck equation by finite element and finite difference methods for nonlinear systems. Sadhana 2006;31:445–61. doi:10.1007/BF02716786.

[272] Pichler L, Masud A, Bergman LA. Numerical Solution of the Fokker–Planck Equation by Finite Difference and Finite Element Methods—A Comparative Study, 2013, p. 69–85. doi:10.1007/978-94-007-5134-7_5.

[273] Kumar M, Chakravorty S, Singla P, Junkins JL. The partition of unity finite element approach with hp-refinement for the stationary Fokker–Planck equation. J Sound Vib 2009;327:144–62. doi:10.1016/J.JSV.2009.05.033.

[274] Sun Y, Kumar M. Numerical solution of high dimensional stationary Fokker–Planck equations via tensor decomposition and Chebyshev spectral differentiation. Comput Math with Appl 2014;67:1960–77. doi:10.1016/j.camwa.2014.04.017.

[275] Sun Y, Kumar M. A numerical solver for high dimensional transient Fokker–Planck equation in modeling polymeric fluids. J Comput Phys 2015;289:149–68. doi:10.1016/j.jcp.2015.02.026.

[276] Liao S, Vejchodský T, Erban R. Tensor methods for parameter estimation and bifurcation analysis of stochastic reaction networks. J R Soc Interface 2015;12:20150233. doi:10.1098/rsif.2015.0233.

[277] Khoromskij BN. Tensors-structured numerical methods in scientific computing: Survey on recent advances. Chemom Intell Lab Syst 2012;110:1–19. doi:10.1016/j.chemolab.2011.09.001.

[278] Chen N, Majda AJ. Efficient statistically accurate algorithms for the Fokker–Planck equation in large dimensions. J Comput Phys 2018;354:242–68. doi:10.1016/j.jcp.2017.10.022.

[279] Grant M, Boyd S, Ye Y. CVX: Matlab software for disciplined convex programming 2008.

[280] CPLEX IBMI. V12. 1: User's Manual for CPLEX. Int Bus Mach Corp 2009;46:157.

[281] Jones E, Oliphant T, Peterson P. {SciPy}: Open source scientific tools for {Python} 2001.

[282] Dhooge A, Govaerts W, Kuznetsov YA. MATCONT. ACM Trans Math Softw 2003;29:141–64. doi:10.1145/779359.779362.

[283] Fitzhugh R. Impulses and Physiological States in Theoretical Models of Nerve Membrane. Biophys J 1961;1:445–66. doi:10.1109/JRPROC.1962.288235.

[284] Izhikevich EM. Dynamical systems in neuroscience : the geometry of excitability and bursting. MIT Press; 2007.

[285] KOSTUR M, SAILER X, SCHIMANSKY-GEIER L. STATIONARY PROBABILITY DISTRIBUTIONS FOR FITZHUGH-NAGUMO SYSTEMS. Fluct Noise Lett 2003;3:L155–66. doi:10.1142/S0219477503001221.

[286] Lorenz EN. Deterministic Nonperiodic Flow. J Atmos Sci 1963;20:130–41.

doi:10.1175/1520-0469(1963)020<0130:DNF>2.0.CO;2.

[287] Thuburn J. Climate sensitivities via a Fokker–Planck adjoint approach. Q J R Meteorol Soc 2005;131:73–92. doi:10.1256/qj.04.46.

[288] Allawala A, Marston JB. Statistics of the stochastically forced Lorenz attractor by the Fokker-Planck equation and cumulant expansions. Phys Rev E 2016;94:52218. doi:10.1103/PhysRevE.94.052218.

[289] Prigogine I, Lefever R. Symmetry breaking instabilities in dissipative systems. II. J Chem Phys 1968;48:1695–700. doi:10.1063/1.1668896.

[290] Arnold L, Bleckert G, Schenk-Hoppé KR. The Stochastic Brusselator: Parametric Noise Destroys Hoft Bifurcation. Stoch. Dyn., New York, NY: Springer New York; 1999, p. 71–92. doi:10.1007/0-387-22655-9_4.

[291] Montbrió E, Pazó D, Roxin A. Macroscopic Description for Networks of Spiking Neurons. Phys Rev X 2015;5:21028. doi:10.1103/PhysRevX.5.021028.

[292] Wilson HR, Cowan JD. Excitatory and Inhibitory Interactions in Localized Populations of Model Neurons. Biophys J 1972;12:1–24. doi:10.1016/S0006-3495(72)86068-5.

[293] Baddeley A. Working memory: looking back and looking forward. Nat Rev Neurosci 2003;4:829–39. doi:10.1038/nrn1201.

[294] Hopfield JJ. Neural networks and physical systems with emergent collective computational abilities. Proc Natl Acad Sci 1982;79:2554–8. doi:10.1073/pnas.79.8.2554.

[295] Amit DJ, Brunel N. Dynamics of a recurrent network of spiking neurons before and following learning. Netw Comput Neural Syst 1997;8:373–404. doi:10.1088/0954-898X_8_4_003.

[296] Amit DJ, Brunel N. Model of global spontaneous activity and local structured activity during delay periods in the cerebral cortex. Cereb Cortex n.d.;7:237–52.

[297] Del Giudice P, Fusi S, Mattia M. Modelling the formation of working memory with networks of integrate-and-fire neurons connected by plastic synapses. J Physiol 2003;97:659–81. doi:10.1016/j.jphysparis.2004.01.021.

[298] Litwin-Kumar A, Doiron B. Slow dynamics and high variability in balanced cortical networks with clustered connections. Nat Neurosci 2012;15:1498–505. doi:10.1038/nn.3220.

[299] Mongillo G, Barak O, Tsodyks M. Synaptic Theory of Working Memory. Science (80-) 2008;319:1543–6. doi:10.1126/science.1150769.

[300] Markram H, Wang Y, Tsodyks M. Differential signaling via the same axon of neocortical pyramidal neurons. Proc Natl Acad Sci U S A 1998;95:5323–8.

doi:10.1073/PNAS.95.9.5323.

[301] Tsodyks M, Pawelzik K, Markram H. Neural networks with dynamic synapses. Neural Comput 1998;10:821–35.

[302] Zenke F, Agnes EJ, Gerstner W. Diverse synaptic plasticity mechanisms orchestrated to form and retrieve memories in spiking neural networks. Nat Commun 2015;6:6922. doi:10.1038/ncomms7922.

[303] Mirzakhalili E, Gourgou E, Booth V, Epureanu B. Synaptic Impairment and Robustness of Excitatory Neuronal Networks with Different Topologies. Front Neural Circuits 2017;11:38. doi:10.3389/fncir.2017.00038.

[304] Lytton J, Westlin M, Burk SE, Shull GE, MacLennan DH. Functional comparisons between isoforms of the sarcoplasmic or endoplasmic reticulum family of calcium pumps. J Biol Chem 1992;267:14483–9.